TADF in Copper(I) Complexes bearing an Anionic *N*-Heterocyclic Carbene

Dissertation

Philipp Schmeinck

August 2023

TADF in Copper(I) Complexes bearing an Anionic *N*-Heterocyclic Carbene

Inaugural-Dissertation

zur Erlangung des Doktorgrades
der Mathematisch-Naturwissenschaftlichen Fakultät
der Heinrich-Heine-Universität Düsseldorf

vorgelegt von

Philipp Schmeinck

aus Düsseldorf

Düsseldorf, August 2023

aus dem Institut für Anorganische Chemie I
der Heinrich-Heine-Universität Düsseldorf

Gedruckt mit der Genehmigung der
Mathematisch-Naturwissenschaftlichen Fakultät der
Heinrich-Heine-Universität Düsseldorf

Berichterstatter:

1. Prof. Dr. Christian Ganter

2. Jun.-Prof. Dr. Markus Suta

Tag der mündlichen Prüfung: 22.08.2023

Perfection is achieved, not when there is nothing left to add,
but when there is nothing left to take away.

Antoine de Saint-Exupéry

Eidesstattliche Erklärung

Ich versichere an Eides Statt, dass die Dissertation von mir selbständig und ohne unzulässige fremde Hilfe unter Beachtung der „Grundsätze zur Sicherung guter wissenschaftlicher Praxis an der Heinrich-Heine-Universität Düsseldorf“ erstellt worden ist. Die Dissertation wurde in der vorgelegten oder in ähnlicher Form noch bei keiner anderen Institution eingereicht und ich habe bisher keine erfolglosen Promotionsversuche unternommen.

Düsseldorf, den 28.08.2023

Philipp Schmeinck

Diese Arbeit wurde in der Zeit von August 2019 bis August 2023 am Institut für Anorganische Chemie I in der Abteilung für Metallorganische Chemie im Arbeitskreis von Herrn Prof. Dr. Christian Ganter angefertigt. In der Zeit von Oktober 2019 bis März 2023 wurde diese Arbeit, im Rahmen des Graduiertenkollegs 2482 (ModISC), durch die Deutsche Forschungsgemeinschaft (DFG) finanziert.

Veröffentlichungen

1) Philipp Schmeinck, Dragana Sretenović, Jasper Guhl, Ralf Kühnemuth, Claus A. M. Seidel, Christel M. Marian, Markus Suta, Christian Ganter, *Eur. J. Inorg. Chem.* **2023**, e202300416.

   Luminescent Copper(I)-Complexes with an Anionic NHC obtained via a Coordination Polymer as Versatile Precursor

   Eigenanteil: Synthese und Charakterisierung der untersuchten Komplexe, Messung, Verfeinerung und Analyse der Einkristall-Röntgenstrukturdaten, Messung der spektroskopischen Daten am Feststoff unter Anweisung von M.S. und in Suspension in Zusammenarbeit mit D.S., Verfassen von Teilen des Manuskripts (Synthese und Diskussion, Experimenteller Teil, Visualisierung).

2) Oliver Nolden, Jennifer Kremper, Wiebke Haselbach, Mahbobeh Morshedi, Jasper Guhl, Philipp Schmeinck, Christel M. Marian, Christian Ganter, Peter Gilch, *ChemPhotoChem* **2023**, *7*, e20220023.

   Femtosecond Spectroscopy and Quantum Chemistry of a Linearly Coordinated Copper(I) Carbene Complex

   Eigenanteil: Synthese der untersuchten Verbindung.

3) Julia Wiefermann, Philipp Schmeinck, Christian Ganter, Thomas J. J. Müller, *Chem. Eur. J.* **2022**, *28*, e2022005.

   Highly Deep-Blue Luminescent Twisted Diphenylamino Terphenyl Emitters by Bromine-Lithium Exchange Borylation-Suzuki Sequence

   Eigenanteil: Messung, Verfeinerung und Analyse der Einkristall-Röntgenstrukturdaten.

Posterbeiträge

Philipp Schmeinck, Dragana Sretenović, Jasper Guhl, Markus Suta, Claus A. M. Seidel, Christel M. Marian, Christian Ganter, 28. Lecture Conference on Photochemistry, Düsseldorf, Deutschland.

Luminescent Copper(I)-Complexes bearing an Anionic N-Heterocyclic Carbene

Betreute Abschlussarbeiten

Leonard Karl, B.Sc., **2019/2020**

Eignen sich Übergangsmetall-Amidinatkomplexe als Vorläufer N-Heterocyclischer Carbene?

Aaron Hoffmann, B.Sc., **2021**

Beiträge zur Chemie von Kupfer(I)-Komplexen mit rückgratmodifizierten NHCs

Florian Picken, B.Sc., **2022**

Thio- und Selenoharnstoffe als Liganden für Kupfer-NHC-Komplexe

Weitere Anmerkungen

Ergebnisse zu Kupfer(I)-Komplexen mit Pniktogenliganden wurden bereits teilweise in der o. g. Veröffentlichung (*Eur. J. Inorg. Chem.* **2023**, e202300416) publiziert.

Ergebnisse zu Kupfer(I)-Komplexen mit Chalkogenliganden wurden in Zusammenarbeit mit Florian Picken während der Betreuung seiner Bachelorarbeit erhalten und sind in dieser bereits zum Teil niedergeschrieben.

Quantenchemische Rechnungen, die diese Arbeit unterstützen, wurden von Jasper Guhl im Arbeitskreis von Frau Prof. Dr. Christel Marian durchgeführt.

Danksagung

An dieser Stelle spreche ich meinen Dank gegenüber vielen Personen aus, die mich bei der Anfertigung dieser Arbeit unterstützt haben.

Herrn Prof. Dr. Christian Ganter danke ich einerseits für die Aufnahme in den Arbeitskreis der Metallorganischen Chemie sowie die interessante Themenstellung. Andererseits danke ich ihm für die sehr gute Arbeitsatmosphäre, die gute Erreichbarkeit und seine Philosophie, auftretende Probleme auf die *Rheinische Art* zu lösen.

Herrn Jun.-Prof. Dr. Markus Suta danke ich sowohl für die Anfertigung des Zweitgutachtens, als auch für einige fachliche Diskussionen und Hilfestellungen.

Des Weiteren danke ich meinen derzeitigen und ehemaligen Arbeitskollegen Meryem Terzi, Leonard Karl, Joscha Nellesen, Maurice Pütz, Linda Kronenberg, Peter Brüggemann und Torsten Hölzel für die angenehme Arbeitsatmosphäre.

Meinen Bachelorstudenten Leonard Karl, Florian Picken und Aaron Hoffmann danke ich für das Engagement in der Anfertigung ihrer Abschlussarbeit.

Meinen Kollegen aus dem Graduiertenkolleg ModISC danke ich für aufschlussreiche fachliche Diskussionen, viele neue Perspektiven und insbesondere für einige tolle Feiern und lange Abende. Frau Dr. Martina Holz danke ich im Besonderen für die Administration dieses Graduiertenkollegs.

Für zahlreiche Analytik der hergestellten Verbindungen danke ich Herrn Mohanad Aian und Herrn PD Dr. Klaus Schaper (NMR-Spektroskopie), Herrn Ralf Bürgel und Herrn Dr. Peter Tommes (Massenspektrometrie) und Frau Gaby Zerta (Elementaranalyse). Herrn Dr. Suren Felekyan danke ich für die Bereitstellung der speziell entwickelten Software *Batch Fitting* für globale Fits der Lumineszenzabklingkurven.

Meinen Kollaboratoren Dragana Sretenović, Jasper Guhl, Oliver Nolden, Julia Wiefermann und Dr. Ralf Kühnemuth danke ich für eine sehr angenehme und gelungene Zusammenarbeit, sowie für viele lange aber nie langweilige Diskussionsrunden.

Meinen Freunden Peter Brüggemann, Torsten Hölzel, Leonard Karl, Moritz Klischan, Karol Mzyk, Sven Polle, Vanessa Reichel-Deland und Meryem Terzi möchte ich ebenfalls danken.

Christian Wulkesch, meinem Kommilitonen erster Stunde, Laborpartner, Stimmungsmacher und zukünftigem Trauzeugen, spreche ich meinen besonderen Dank aus.

Meiner Familie möchte ich ebenfalls herzlich danken. Meinen Eltern Gaby und Klaus, meiner Oma Hannelore, des Weiteren Udo, insbesondere für das Korrekturlesen und Birte, Frank und Vincent, sowie Vesna, Ljuban und Duško. Danke für eure großartige Unterstützung!

Dragana, dir möchte ich schließlich von ganzem Herzen danken, dafür dass du an meiner Seite bist und mit mir eine gemeinsame Zukunft aufbaust. Dafür, dass du mir privat als auch fachlich immer zur Seite stehst und mich nicht selten erdest. Und dafür, dass du mein Leben durch so viele neue Erlebnisse, Eindrücke, tolle Freunde und Liebe komplettiert hast. Danke!

List of Abbreviations

1D	One dimensional
bpy	Bipyridine
CAAC	Cyclic alkyl amino carbene
DAS	Decay associated spectroscopy
DCM	Dichloromethane
DF	Delayed fluorescence
Dipp	2,6-Diisopropylphenyl
DMAP	Dimethyl amino pyridine
eq.	Equivalent
ESI	Electrospray ionization
HMDS	Bis(trimethylsilyl)amide
HOMO	Highest occupied molecular orbital
HSAB	Hard and soft acids and bases
IC	Internal conversion
IR	Infrared
IRF	Instrument response function
ISC	Intersystem crossing
KO^tBu	Potassium tert-butoxide
L	Ligand
LC / LE	Local(ly centered) excitation
LED	Light emitting diode
LLCT	Ligand to ligand charge transfer
LUMO	Lowest unoccupied molecular orbital
M	Metal
MALDI-TOF	matrix-assisted laser desorption/ionization
MLCT	Metal to ligand charge transfer
MS	Mass spectrometry
n-BuLi	n-Butyl lithium
NHC	N-Heterocyclic carbene
NMR	Nuclear magnetic resonance
OLEC	Organic light emitting cell
OLED	Organic light emitting diode
PF	Prompt fluorescence
Ph	Phosphorescence
PLQY	Photoluminescence quantum yield
PXRD	Powder X-ray diffraction
rISC	reverse intersystem crossing
S_0	A molecule's ground state
S_1	First excited singlet state
SC-XRD	Single crystal X-ray diffraction
T_1	First excited triplet state
TADF	Thermally activated delayed fluorescence
TCSPC	Time correlated single photon counting
TEP	Tolman electronic parameter

THF	Tetrahydrofuran
TRES	Time resolved emission spectroscopy
TTA	Triplet-triplet annihilation
UV	Ultraviolet
UV-Vis	Ultraviolet and visible light
VR	Vibronic relaxation

Table of Contents

Abstract

The present work investigates the coordination chemistry of an anionic diamido-NHC with copper(I) and explores the photophysical properties of such complexes with particular reference to possible TADF behaviour. Several heteroleptic linear and trigonal planar copper(I) complexes incorporating pnictogen- or chalcogen-based ligands such as pyridines, triphenylphosphine, and seleno ureas were synthesized. The synthetic route begins with a 1D coordination polymer, composed of the NHC and copper(I) ions in a linear coordination arrangement. Addition of ligands to suspensions of this polymer generates the respective monomeric target complexes. The synthesis and the identity of the complexes in solution is subject to an equilibrium between them and oligomeric material. Molecular structures of the pnictogen-based complexes obtained via SC-XRD reveal intermolecular contacts between the electron-rich carbene backbone and electron-deficient pyridine moieties in solid state. These contacts are attributed to the high dipole moments of the complexes. An in-depth photophysical analysis was conducted with four selected compounds. Due to the equilibrium in solution, spectroscopic methods are adapted to ensure defined and reproducible sample compositions. In solution, addition of excess ligand is needed to push the equilibrium towards the monomeric complexes, while measurements on solid-state samples were conducted both on neat powders and on their suspensions in liquid or solid cyclohexane, the latter allowing measurements in standard cuvettes. The obtained results from the suspensions align well with those from powdered samples. Steady-state and time-resolved spectroscopy techniques were employed to investigate excitation behaviour and confirm potential TADF properties. The emission spectra of the complexes range from blue (451 nm) to orange (591 nm), covering a significant portion of the visible light spectrum. Time-resolved spectroscopy reveals a highly diverse emission behaviour, with one compound relaxing predominantly via the prompt fluorescence pathway and another via a long-lived phosphorescence. Temperature-dependent steady-state and time-resolved spectroscopy suggests delayed fluorescence for two complexes incorporating electron-poor pyridines, indicated by a spectral redshift and elongated lifetimes in the µs domain upon cooling. Excitation power dependant measurements indicate an emission kinetic of first order, excluding TTA as source of this emission. Time-resolved emission spectroscopy (TRES) provides a detailed insight into the types of emission involved from early nanoseconds to

late milliseconds and from 270 K down to 10 K. It provides a comprehensive overview of the processes involved and sheds light on the excited-state's intricate nature of the compounds analysed.

1 Introduction

Every year, about 1700 TWh of energy is expended for the generation of light, which is about seven per cent of mankind's total annual energy consumption.[1,2] As this is a considerable fraction, the pursuit of more efficient and less costly technologies is subject to intense research both at the basic level, i.e., the physics and chemistry of devices, as well as on advanced levels, such as the actual production of lighting technologies with lower costs, higher lifetimes, deeper colours, shorter response times and more.

A widely used measure of the ratio between the energy uptake and the visible light generated by a device is the luminous efficacy, expressed in lumen per watt. It considers the luminous flux of a light source and thereby accounts for the changing sensitivity of the human eye to different parts of the visible light spectrum.[3] The theoretical limit for the luminous efficacy is a totally loss-free and ideally monochromatic light source at 555 nm with around 683 lm/W, since the human eye is most sensitive to that wavelength.[4] Conversely, a likewise ideal, monochromatic UV-source would have a luminous efficacy of zero, since UV light is invisible to the human eye.

With ongoing research, well-established lighting technologies with low luminous efficacies had to give way for their more energy efficient successors, with one prominent example being the incandescent light bulb, whose simple principle of light generation is an electrically heated tungsten wire. Besides the desired visible light emission though, an incandescent light bulb converts 95 – 98% of its energy uptake into heat; the luminous efficacy is around 10 lm/W.[5] As a consequence, such technologies have been entirely banned from private use in the European Union since 2012.

A successor technology is the *light-emitting diode* (LED). Its core principle is an inorganic semiconducting layer with a defined band gap. When voltage is applied, electrons and holes recombine in this layer, thereby jumping the band gap and emitting a photon of a specific wavelength.[6] Around 30% of the energy uptake is converted desirably into light, with luminous efficacies of up to 200 lm/W.[7]

The use of inorganic semiconductors in LEDs relies on the construction of a crystalline layer with a low defect density, which is restricted to a very small region, typically spanning a few square millimetres. As a consequence, the current size of advanced inorganic LEDs remains confined within this range, resulting in a point source of light that exhibits strong directionality. Conversely, *Organic Light Emitting Diodes* (OLEDs) employ amorphous organic layers, which are not subject to such limitations. These organic layers can be coated across extensive areas, potentially spanning thousands of square millimetres, with the main constraint being the cleanliness of the manufacturing process, since the employed luminophores are typically more sensitive to oxygen and water. Consequently, OLEDs produce diffuse emissions independent from the viewing angle, they can be much larger and even flexible.[8] Nevertheless, the luminous efficacy does not reach values of LEDs yet, with current record holders being around 100 lm/W.[9]

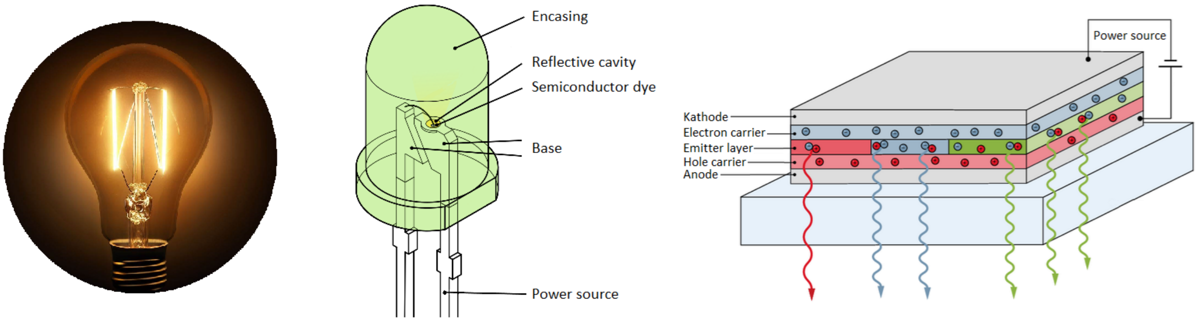

Figure 1. Evolution of lighting technologies from incandescent light bulbs (left[10]) via LEDs (middle[11]) to OLEDs (right[12]).

The emitters in OLEDs are excited electrically by the recombination of electrons and holes, which form excitons nearby a fluorophore molecule. Opposed to photon excitation, which exclusively results in excited singlet states, electrical excitation is subject to spin statistics, resulting in 75% excited triplet states. Therefore, the main goal of OLED research is to make both types of excitations usable by keeping non-radiative deactivation to a minimum, especially in the triplet manifold. The evolution of OLEDs can be divided into three stages[13], with the basic research beginning in the 1950s using anthracene, a typical fluorescent molecule.[14] Until 1997, only such fluorescent molecules were employed in these OLEDs of the first generation, thereby losing all energy of the triplet states as heat. OLEDs of the second generation are based on purely phosphorescent emitters, typically heavy metal complexes featuring large spin-orbit-coupling and therefore fast ISC rates. This approach is known as triplet harvesting, since the initially created 25% of singlet states are converted to light via the triplet manifold.[15] For the third generation, the opposite approach has gained attention, meaning that the generated 75% of triplet states are harvested via the singlet manifold. This is possible due to thermally activated delayed fluorescence (TADF), a process undergone by certain molecules featuring both fast intersystem crossing as well as reverse intersystem crossing between thermally efficiently coupled S_1 and T_1 states.[16]

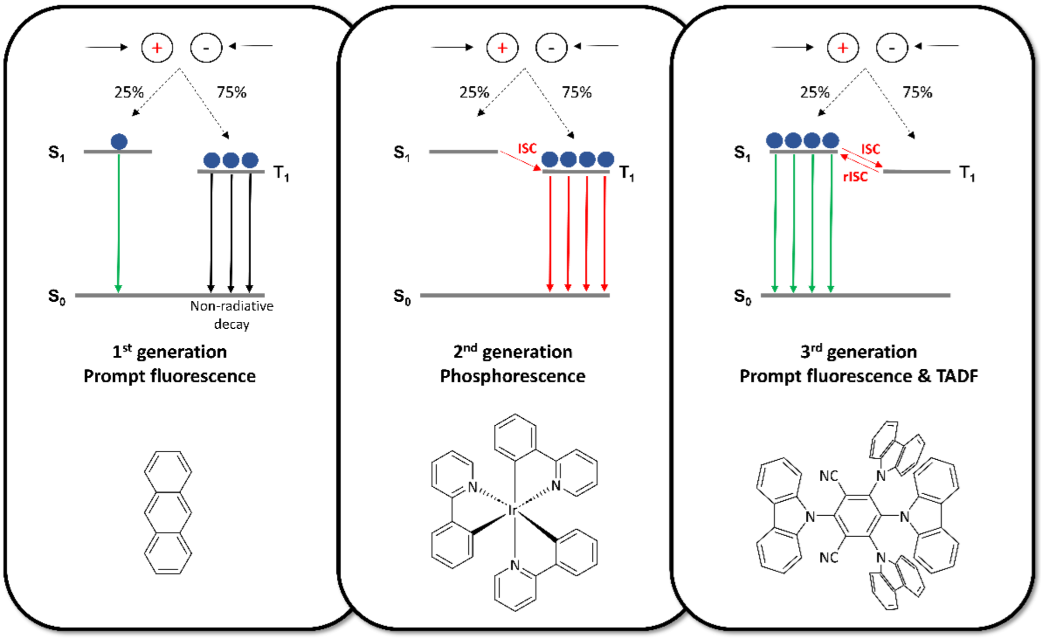

Figure 2. Mechanisms of excitation and (non-)radiative deactivation of the fluorophores in the different generations of OLEDs, adapted from [17].

In recent years, copper(I) complexes have gained attention as potential candidates for third-generation OLEDs. They possess comparatively high spin-orbit-coupling constants for efficient intersystem crossing, and in some cases, small energetic gaps between S_1 and T_1, enabling TADF to occur.[18] Moreover, they captivate with lower costs than noble metal complexes containing iridium, osmium or platinum, as well as often more feasible synthetic routes compared to the fully organic donor-acceptor-conjugates.

The present work is divided into two main parts. The first part deals with the synthesis of new copper(I) containing complexes incorporating an *N*-heterocyclic carbene (NHC). The anionic nature of the chosen NHC causes overall charge-neutrality of the synthesized compounds, which is favourable for the production of OLEDs, since the emitters are typically introduced via the gas phase. Along the line, the obtained substances were characterized by standard analytical methods, as well as by structure clarification techniques, such as single crystal X-ray diffraction. The work was closely linked with rational design conducted by the department of theoretical chemistry, focusing the synthetic efforts towards small energetic distances between the first excited singlet and triplet states of the complexes, as well as large intersystem crossing (ISC) rate constants. The second part focuses on an in-depth experimental analysis of the excited state behaviour and resultant photophysical properties of selected compounds. The main focus lies on finding irrefutable, experimental evidence for thermally activated delayed fluorescence (TADF), caused by the small energetic distance between S_1 and T_1 and large ISC rates. Furthermore, the effect of the molecular geometries and the substitution pattern of the secondary ligands is to be analysed. The general molecular structures targeted by this work are shown in Scheme 1.

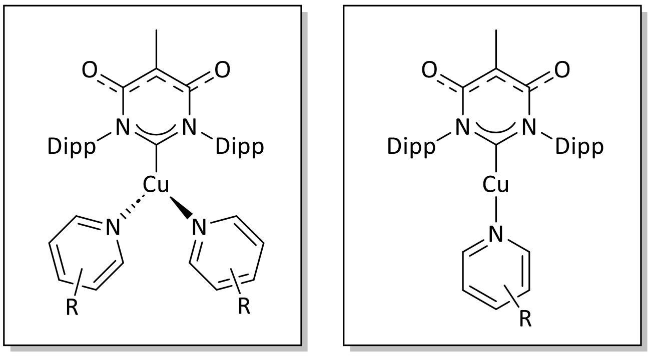

Trigonal planar **Linear**

Scheme 1. Target molecules of this work.

2 Scientific Background

This chapter contains the underlying scientific foundations, on which the research presented in this thesis is based. The chapter is divided into two parts, important aspects of carbene chemistry and the phenomenon of luminescence in materials.

2.1 Carbenes

Carbenes are defined as molecules that contain an uncharged, divalent carbon atom with an electron sextet. Since the vast majority of organic compounds contain only carbon atoms with an electron octet, carbenes were formerly considered as unstable and merely transient species. In recent decades though, considerable progress has been made in the field of carbene chemistry, such that even bench-stable representatives are known today. These singlet carbenes feature a filled sp^2-hybrid orbital accompanied by an empty p-orbital at the carbene carbon, leading to excellent ligand properties of such compounds. Their metal complexes have been established for homogeneous catalysis, e.g., the *Grubbs* catalyst II for olefin metathesis[19] or carbene palladium complexes for cross coupling reactions.[20,21,22] A deeper insight into this fascinating class of compounds is given in the following subchapters.

2.1.1 History of carbene chemistry

The history of carbene chemistry dates back to 1835, when *Dumas* and *Péligot* tried to obtain the simplest possible carbene, methylene ($:CH_2$), by dehydrating methanol with sulphuric acid.[23] From today's perspective it is clear that their efforts could not have been fruitful. Rather than isolating methylene, they instead obtained dimethyl ether among other by-products such as ethylene and dimethyl sulphate. Even if this experiment did not yield the intended carbene, it can still be regarded as the first intentional attempt to produce one. In the late 19th century, *Nef* followed up on this series of experiments. In 1892, he again tried to obtain methylene by dehydrating methanol, with the same outcome as in 1835.[24]

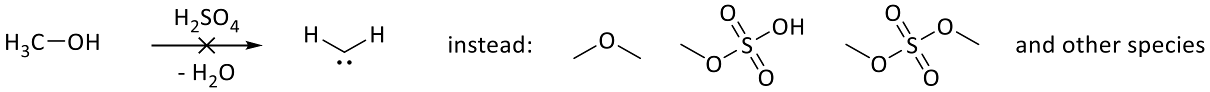

Scheme 2. Unsuccessful strategy for obtaining methylene from methanol.

The synthesis of the first carbene complex dates back to 1915. *Chugaev* reacted tetrachloroplatinate(II) with methyl isocyanide and hydrazine, obtaining a *red salt*. This was in fact a platinum diamino carbene complex, although this was not correctly assigned until 55 years later.[25,26,27]

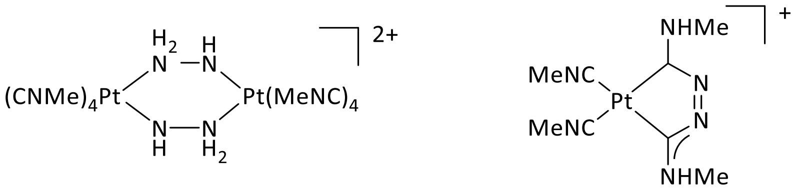

Scheme 3. The initially proposed structure for *Chugaevs red salt* (left) versus the actual structure verified by SC-XRD (right).

Entering the 1960s, carbene research was rekindled by *Wanzlick*, who experimented with a 2-trichloromethyl imidazolidine, which he suspected to produce the respective imidazolidine-ylidene via thermal α-elimination of chloroform. However, he isolated the carbene dimer, the enetetramine, which he recognized by its molar weight.[28] He postulated an equilibrium involving this molecule and the free carbene, a hypothesis that was however falsified in 1964/65 by Lemal[29] and Winberg.[30]

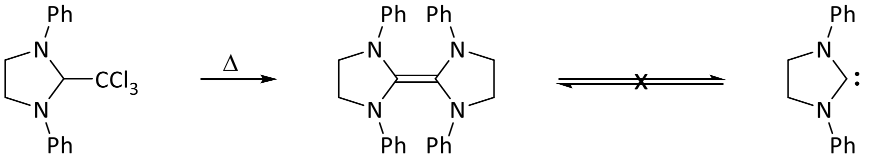

Scheme 4. Thermolysis of a trichloromethyl imidazolidine to an enetetramine. The subsequent equilibrium to a free carbene was disproven.

A major breakthrough was achieved by Fischer in 1964 with the successful synthesis and recognition of a transition metal carbene complex, the type of which was later named after him. He treated tungsten hexacarbonyl with methyl lithium and subsequently methylated the product using diazo methane, giving rise to a complex with a composition of $(CO)_5W(COCH_3)(CH_3)$. He was able to show that the methyl group is indeed not bonded to the tungsten core but is rather part of a methoxymethylcarbene ligand, later verified by single crystal X-ray diffraction.[31]

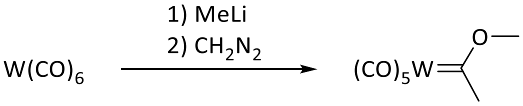

Scheme 5. First synthesis of a *Fischer type* carbene complex starting from tungsten hexacarbonyl.

The first synthesis of transition metal complexes of *N*-heterocyclic carbenes are ascribed to *Wanzlick* and *Öfele*, both in 1968. *Wanzlick* pioneered the classical deprotonation of an imidazolium cation in the presence of a transition metal, which is still the most used method for generating carbenes today.[32] Specifically, he reacted diphenyl imidazolium perchlorate with mercury(II) acetate, the acetate hereby functioning as internal base, giving rise to the bis(NHC) mercury(II) perchlorate.[33]

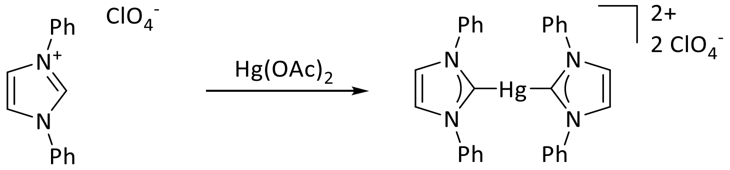

Scheme 6. Synthesis of a bis(NHC) mercury(II) complex starting from an imidazolium salt and mercury(II) acetate, the acetate functioning as internal base for deprotonation of the imidazolium salt.

Öfele chose a different approach; thermal treatment of an imidazolium salt with a pentacarbonyl chromium hydride anion resulted in the formation of the respective NHC-chromium complex under concomitant release of dihydrogen.[34]

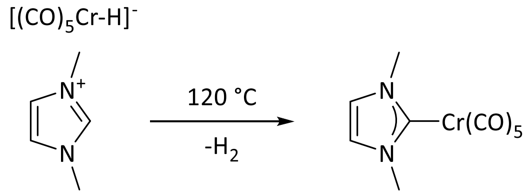

Scheme 7. Thermolysis of an imidazolium salt containing a pentacarbonyl chromium hydride anion under formation of the NHC chromium(0) complex and concomitant release of dihydrogen.

Further achievements were gained by *Lappert* in the early 70s, who succeeded in the thermal cleavage of an NHC-dimer in the presence of Di-µ-chlorodichlorobis(triethylphosphine)diplatinum(II), resulting in a platinum NHC complex; an outcome postulated but never observed by *Wanzlick*.[35,36]

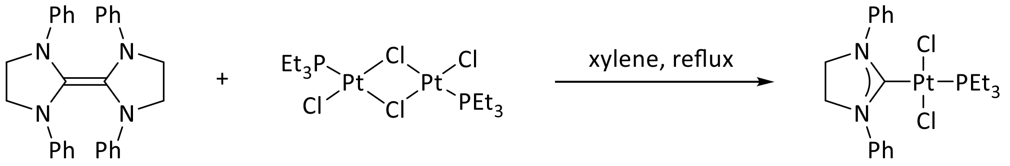

Scheme 8. Thermolysis of an enetetramine in xylene under reflux conditions. The platinum dimer complex is cleaved, resulting in a mononuclear carbene platinum(II) NHC complex.

From today's point of view, the first bench-stable carbene stabilized by heteroatoms was synthesized in 1988 by *Bertrand*, although again, proof was given in the form of the molecular structure of a derivative only in 2000.[37,38] He thermally cleaved a diazo compound under removal of dinitrogen and generation of a carbene, neighboured by a trimethylsilyl- and a diaminophosphane-group to either side.

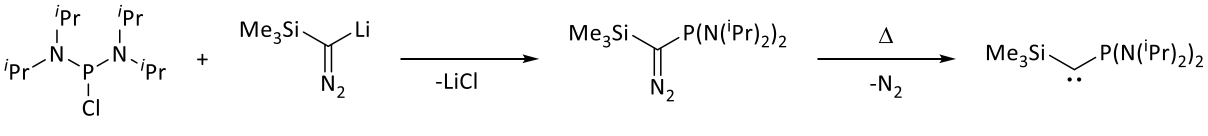

Scheme 9. Synthetic route to the first bench-stable free carbene stabilized by heteroatoms.

The first literature appearance and simultaneously the final breakthrough in the field of carbene chemistry corresponds to the ground-breaking work of *Arduengo* in 1991, who synthesized and characterized the first bench-stable, free NHC, the bis(adamantyl) imidazole ylidene, today informally known as the *Arduengo carbene*.[39]

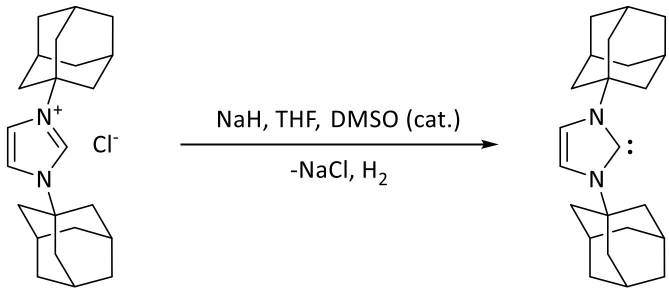

Scheme 10. The first literature appearance of a bench-stable carbene, the bis(adamantyl) imidazole ylidene.

From this point on, the field of carbene research was extended far beyond the laboratory curiosities to which the first reports were attributed, experiencing a steady growth in the number of publications until 2014.

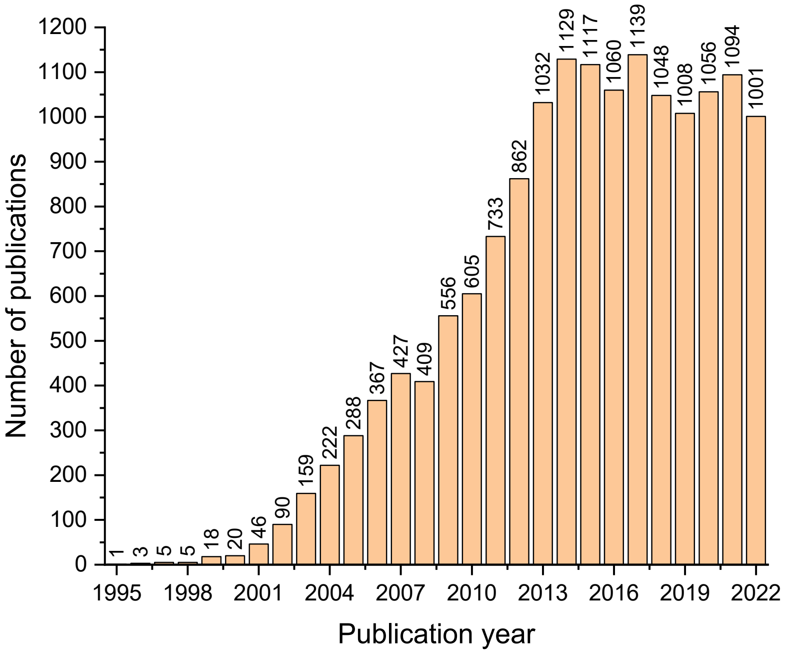

Figure 3. Number of publications containing the keyword *N-heterocyclic carbene* since 1995.[40]

2.1.2 From transient species to isolable compounds

The remarkable stability of some carbene derivatives like the *Arduengo carbene* is caused by several thermodynamic and kinetic effects. Compared to the simplest carbene, methylene, bench-stable carbenes typically benefit from at least one of the following stabilizing properties.

In first approximation, the construction of a carbene from an isolated carbon atom and two single-bonded substituents results in a linear arrangement. Two electrons engage in bonding with the neighbouring substituents via an sp-hybrid orbital. The other two electrons occupy the remaining, degenerate p-orbitals of the carbon following the *Pauli principle* and *Hund's rule*, resulting in a triplet ground state. Such carbenes approaching linearity are typically highly reactive intermediates featuring radical reactivity and electrophilicity.

Bending the substituents away from linearity results in nucleophilic carbenes, in which the carbon is present in an sp^2 hybridisation. The degeneracy between the p_y and p_z orbitals is broken by this angulation, since the orbital parallel to the R-C-R plane receives a higher s-portion, while the p-orbital orthogonal to it remains almost unchanged. If their distance becomes larger than about 2 eV, the singlet state is finally preferred.[41] These singlet carbenes are much more stable and less reactive than their diradical relatives. NHCs belong to this class. Figure 4 gives an overview of the electronic nature of singlet and triplet carbenes.[42]

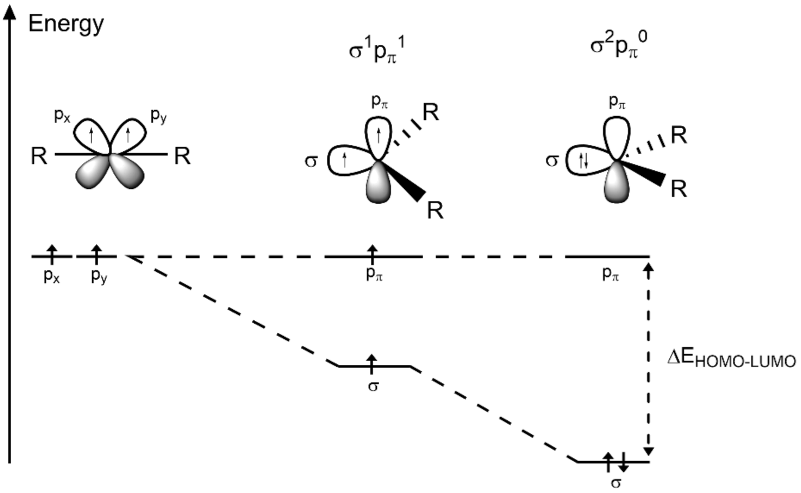

Figure 4. Bending of a carbene and the influence on its electronic configuration. With increased angulation, ΔE becomes larger, ultimately giving rise to singlet carbenes (right).

NHCs in particular are further stabilized by other properties. Among them, the most important is the push-pull effect caused by the nitrogen atoms to either side of the carbene carbon atom, which exert a negative inductive effect on the filled σ-orbital through its higher electronegativity on the one hand, which leads to its energetic lowering. On the other hand, they contribute with a positive, mesomeric effect via its free electron pair, which energetically raises the empty p_z orbital of the carbene. As a result, the HOMO-LUMO gap of the carbene increases even further, again leading to a preferred singlet ground state.

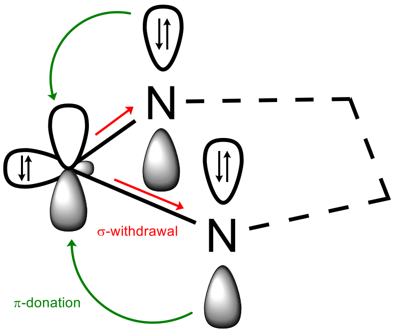

Figure 5. The push-pull effect increases the HOMO-LUMO gap of an NHC even further.

Some carbenes benefit from aromaticity, if the ring containing the carbene is fully conjugated with 4n + 2 π-electrons, fulfilling the *Hückel rule*. While such carbenes are generally more stable, the *Arduengo carbene* being one of them featuring 6 π-electrons, there are plenty examples known that are not aromatic.

Besides thermodynamic stabilization, kinetic effects can heavily contribute to a carbenes' stability as well, most importantly steric protection of the carbene carbon atom. The prime example again being the *Arduengo carbene*, which contains two adamantyl groups bonded to each of the nitrogen atoms. The geometry of NHCs places these bulky substituents right in front of the carbene, shielding it from collisions with other molecules, that might result in a chemical reaction.

2.1.3 Carbenes in coordination chemistry

Since carbenes are excellent ligands, with carbene complexes known for almost every metal in the periodic system[43], there are a few well-established methods in order to understand and quantify their coordination chemistry.

The combination of the σ-donor and π-acceptor capability of an NHC can be measured by the TEP value (Tolman Electronic Parameter) developed by *Tolman*[44] and based on the work by *Müller*[45] and *Bigorgne*[46]. Originally, this quantification was developed for phosphines and it allows conclusions about the electron density of the metal atom or ion, to which an investigated ligand is bonded. For this purpose, the IR spectrum of a carbonyl complex, originally of the form $Ni^0(CO)_3L$, is measured. The energy of the CO stretching vibration ($\tilde{\nu}_{CO}$)

is found to be dependent on the electronic properties of the ligand L. This dependence results from the increasing strength of the π-backbonding of the metal's d-orbitals into the antibonding orbitals of the CO ligands as the donor character of the ligand increases. Strongly donating ligands thus weaken the CO bond, the CO stretching vibration can be excited at lower energy and $\tilde{\nu}_{CO}$ decreases. Conversely, $\tilde{\nu}_{CO}$ increases by strongly π-accepting ligands for the same causality. This method was later extended to the characterisation of NHC ligands. The originally employed $Ni^0(CO)_3NHC$ complexes require nickel tetracarbonyl as educt though, which holds drawbacks due to synthetic difficulties and commercial availability. Therefore, they were soon replaced by square planar rhodium(I) and iridium(I) complexes of the type NHC-$M(CO)_2Cl$.

To characterise the pure π-acceptor character of an NHC ligand, *Ganter* developed the method of ^{77}Se-NMR-spectroscopy on selenoureas, which can be obtained from the reaction of an in situ generated carbene with elemental selenium.[47,48] The shielding of the selenium is directly dependent on the π-acidity of the NHC. The more π-acidic the NHC, i.e., the more electron-deficient, the further down-field the signal for the selenium nucleus will appear in the ^{77}Se-NMR-spectrum. This method is based on studies by *Bertrand*, who in 2013 established the ^{31}P-NMR-spectroscopy on phenylphosphinidene-carbene adducts as a measure for the π-acceptor character of a carbene ligand.[49] The chemical shift of the phosphorus in such phosphinidenes is subject to the same dependency as that of selenium in selenoureas. This method is applicable to fewer carbenes than the method developed by *Ganter* though, since a prerequisite is that the carbene is stable in solution.

The quantification of steric factors of NHC ligands is carried out by the determination of their *buried volume*.[50,51,52] Based on the Tolman cone angle for phosphines[53], it is defined as the fraction of a sphere, centred at the metal core of an NHC complex, that is covered by atoms of the NHC.

2.2 Luminescence

Luminescence is a phenomenon observed in materials that can relax from an electronically excited state to the ground state via emission of photons. It is opposed by non-radiative relaxation, a pathway undergone by the vast majority of materials, by which the energy of their excitation is converted to heat.

The energy used to initially excite a material can be of various forms, the two most important ones are photoexcitation and electric excitation, i.e., absorption of a photon by a molecule or recombination of an electron and a hole nearby a molecule respectively. The major difference between photoexcitation and electric excitation lies in the multiplicity of the resulting excited states. While for photoexcitation the rule of conservation of multiplicity enforces the generation of exclusively excited singlet states, the recombination of an electron and a hole will result in a statistical distribution of singlets to triplets of 1:3, due to spin statistics.[54] The following processes are independent of the form of excitation and will therefore be discussed for photoexcitation. A graphical representation is given by the Jablonski diagram in Figure 6.[55]

The absorption of a photon by a molecule in its electronic ground state (S_0) and the concomitant rearrangement of its electrons happens in the domain of late attoseconds to early femtoseconds. Usually, the energy of the absorbed photon is greater than the energy gap between the molecule's ground state (S_0) and first excited state (S_1), exciting the molecule into a higher singlet state S_n. From there, two processes relax the molecule quickly to its first excited state S_1. The non-radiative vibronic relaxation will bring the molecule to its lowest vibrational mode within one electronic state and convert this excess energy into heat, whereas the isoenergetic internal conversion bridges between higher and lower lying electronic states, enabling the molecule to reach the S_1 state. Since higher electronic states are generally well admixed with each other, these processes happen in the range of picoseconds. Emission processes cannot compete with this speed, resulting in the *Rule of Kasha*, stating that the emission energy is independent of the excitation energy. Secondly, the *Stokes shift* is a direct consequence of these processes, since the absorption will generally occur at higher energy than the emission.

A molecule in the S_1 state can undergo two processes. The first is relaxation to the ground state under conservation of its spin multiplicity and emission of a photon, which is called *prompt fluorescence*. Since the rule of spin conservation, a consequence of the law of conservation of momentum, is not violated, this process is efficient, usually in range of 1 - 100 nanoseconds. Another possibility is an *intersystem crossing* (ISC), a related process to the internal conversion, likewise isoenergetic, however bridging between states of different multiplicity, e.g., S_1 and T_1. This process is normally forbidden, since a spin-flip is involved. It can occur on a broad time scale between a few nanoseconds up to milliseconds, strongly depending on the spin-orbit-coupling constants, which are typically high for molecules containing heavy atoms.[56,57] Since the T_1 is most often energetically lower than the S_1, an ISC is followed again by vibronic relaxation.

A molecule in its first triplet state T_1 has yet again two possibilities. Relaxation to S_0 with concomitant emission of a photon would now involve a change of multiplicity, which is why this so-called *phosphorescence* is inefficient, ranging from late microseconds to even seconds and beyond. The T_1 is almost always energetically lower than the S_1, leading to a redshift of phosphorescence compared to prompt fluorescence. The other possibility is the counterpart to ISC. This *reverse intersystem crossing* (rISC) plays a central role in this work, since it enables a way back to the excited singlet domain. Nevertheless, this process is also isoenergetic and therefore cannot occur from the lowest vibronic state of the T_1. Consequently, the system must reach higher vibrational modes, which can be achieved by uptake of surrounding thermal energy. Provided the energy gap between S_1 and T_1 is small enough, rISC can occur, finally enabling *thermally activated delayed fluorescence* (TADF), which will be discussed in detail in a later chapter.

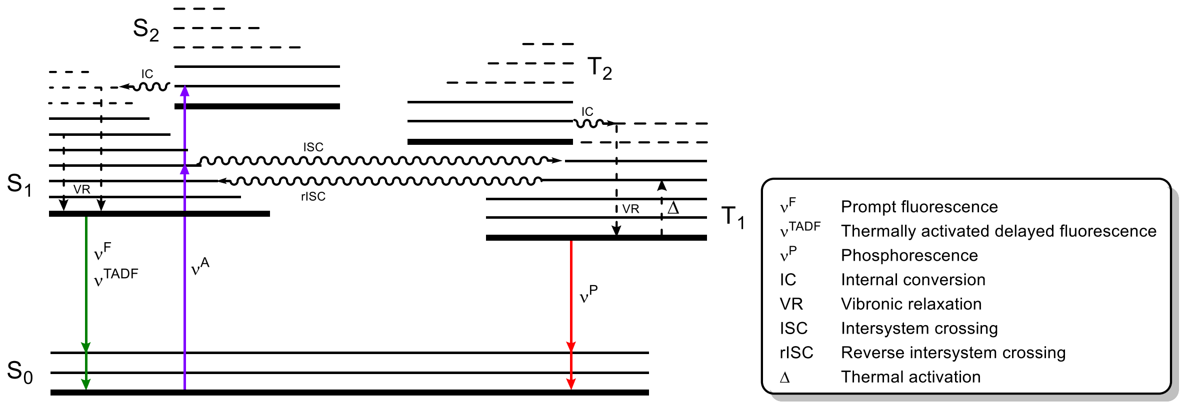

Figure 6. A simplified Jablonski diagram displaying the most important processes of an excited molecule, adapted from [55,58].

2.2.1 Luminescence in copper(I)-complexes

Emissive copper(I) complexes gained a lot of attention in recent years due to the still challenging task of obtaining efficient and long-lived, phosphorescent blue light emitters based on the well-established noble-metal phosphors, e.g., complexes of platinum(II) or iridium(III). This property heavily relies on the energy difference between the emitting triplet state and higher-lying metal-centred states with dd* character. If these states are thermally accessible at room temperature and the energy separation to the T_1 state is less than approximately 3000 cm^{-1}, they can significantly quench the emission.[59] In this regard, investigations have focused on Cu(I) complexes, possessing a d^{10} ground state configuration, therefore lacking low-lying unoccupied d* orbitals. Consequently, emission quenching resulting from the population of dd* states is not a concern. Moreover, copper(I) is favourable since it is inexpensive due to its 1200- and 6000- times greater earth crust abundance compared to platinum and iridium respectively.[60]

Before copper(I) complexes were able to compete with their predecessors though, several challenges had to be overcome. One of them concerns tetrahedral complexes, featuring metal-to-ligand charge transfer states (^{1}MLCT) after excitation. These formally oxidize the copper(I) to copper(II), causing a Jahn-Teller distortion of the d^9-Cu(II). The hereby enforced approach to a square planar configuration, the so-called *flattening distortion*, dramatically quenches the emission by opening non-radiative decay pathways. This problem, first observed by McMillin in 1985[61], was later solved by introducing steric protection to prevent the distortion.[62]

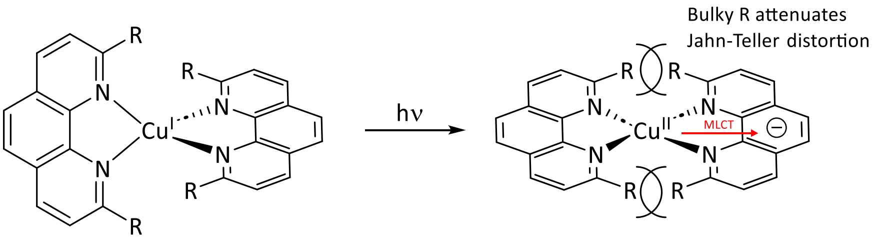

Scheme 11. Flattening distortion of a tetrahedral bis(phenanthroline) copper(I) complex upon photoexcitation.

Furthermore, phosphorescence in copper(I) complexes is often very inefficient, since non-radiative decay dominates the deactivation of excited triplet states at room temperature. Moreover, the typical phosphorescence decay times for copper(I) compounds are often very long, ranging from hundreds of microseconds to milliseconds.[63,64] Such long decay times make these compounds unsuitable as emitters in OLEDs due to a dramatically decreased response time of the resulting display. Furthermore, with longer lifetimes of the excited states, the chance of non-radiative decay increases. Nonetheless, specific Cu(I) complexes can exhibit thermally activated delayed fluorescence (TADF) from the lowest excited singlet state at room temperature. This not only reduces the emission lifetime and therefore makes them potential candidates for efficient emitters in OLEDs, it also makes the otherwise lost 75% of triplet energy, generated upon electric excitation, usable through singlet harvesting. This interesting process is illuminated in the following chapter.

2.2.2 Thermally activated delayed fluorescence

Thermally activated delayed fluorescence (TADF) is defined as photon emission from an excited molecule via S_1-relaxation, that at some point after initial excitation existed in an excited triplet state and overcame the barrier back to the S_1 state using surrounding thermal energy. In its simplest form, TADF is a special case of delayed fluorescence that arises in molecules featuring energetically close lying singlet and triplet excited states, enabling thermal coupling and therefore reverse intersystem crossing (rISC) between the S_1 and the

T_1 state. Intrinsic to classic TADF phosphors is a third luminescence lifetime, typically in the range of microseconds, besides a lifetime of prompt fluorescence and one of phosphorescence at lower temperatures, when the thermal energy does not support rISC anymore.

The occurrence of a third lifetime with only two involved excited states can be rationalized by the fact that for TADF to occur, the system needs a rate of ISC that can compete with the rate of prompt fluorescence and in turn a rate of rISC being able to compete with the rate of phosphorescence. With such properties, an excited molecule will spend time in the T_1 state or even shift back and forth between the S_1 and the T_1 state, depending on the involved rate constants. These processes create a third "pseudo-state" with a lifetime between the one of prompt fluorescence and phosphorescence.[65,66]

This work deals with TADF involving the lowest excited states S_1 and T_1 but it should be briefly mentioned, that the so called *hot rISC* between higher lying states S_n and T_n might also enable TADF in some specific systems, if the higher triplets are sufficiently long lived due to restricted internal conversion down to T_1. [67,68] Nevertheless, those instances are quite rare, since rISC of higher states is typically orders of magnitude slower than internal conversion.[69]

Typical TADF emitters are conjugated systems featuring excited states of charge transfer (CT) type, since the large spatial displacement of one electron and its mesomeric stabilization ensures long lifetimes of the excited state. These so-called *donor-acceptor-conjugates* might be complexes containing metal ions, but even small organic molecules without heteroatoms are known to show TADF. A narrow gap between the S_1 and the T_1 is typically ensured by deconjugation of the donor and the acceptor moiety, resulting in a smaller overlap between the molecules' frontier orbitals (HOMO and LUMO),[70,71] a decrease in the electronic exchange energy and ultimately a small energy gap between the S_1 and the T_1 state, which is vital for an efficient thermal coupling with high rISC rates.[72] Besides a small $\Delta E_{S1\text{-}T1}$ it is also important to ensure that the excited triplet states live long enough, i.e., to minimize non-radiative decay from T_1. This especially hampers the design of red TADF emitters, since here the T_1 state is typically quite low in energy, allowing efficient non-radiative relaxation down to the ground state, in accordance with the energy gap law.[73]

TADF is indeed a long known photophysical phenomenon that was first described in the pioneering work of *J. Perrin* in 1926, who established the term *E-type fluorescence* for this mechanism.[74] He correctly interpreted this process as thermally activated and accurately recognised the involved electronic states.[75] Nevertheless, the topic has received only very little attention for the following 83 years. It was *Adachi* in 2011[76] and 2012[16], who reinvigorated it with two consecutive studies on purely organic donor-acceptor-conjugates that efficiently emit from S_1 by means of TADF and their application in OLEDs. He was then the first to recognize the potential of TADF phosphors in electroluminescent lighting technologies as an elegant way of harvesting triplet excitons via the pathway of fluorescence.

The first time that TADF was recognized in copper(I) complexes dates back to 1983, when McMillin observed a decreased luminescence intensity upon cooling a solution of bis(2,9-dimethylphenanthroline) copper(I) tetrafluoroborate ($Cu(dmp)_2BF_4$) and related compounds.[77] Two distinct emissions were detected while measuring the luminescence at different temperature, one with a rate constant of 10^7 s^{-1} ascribed to a prompt fluorescence as well as a redshifted emission with a rate constant of 10^3 s^{-1} ascribed to a phosphorescence. The energetic distance between the two states was reported to be 220 meV, which is small enough for TADF to occur.

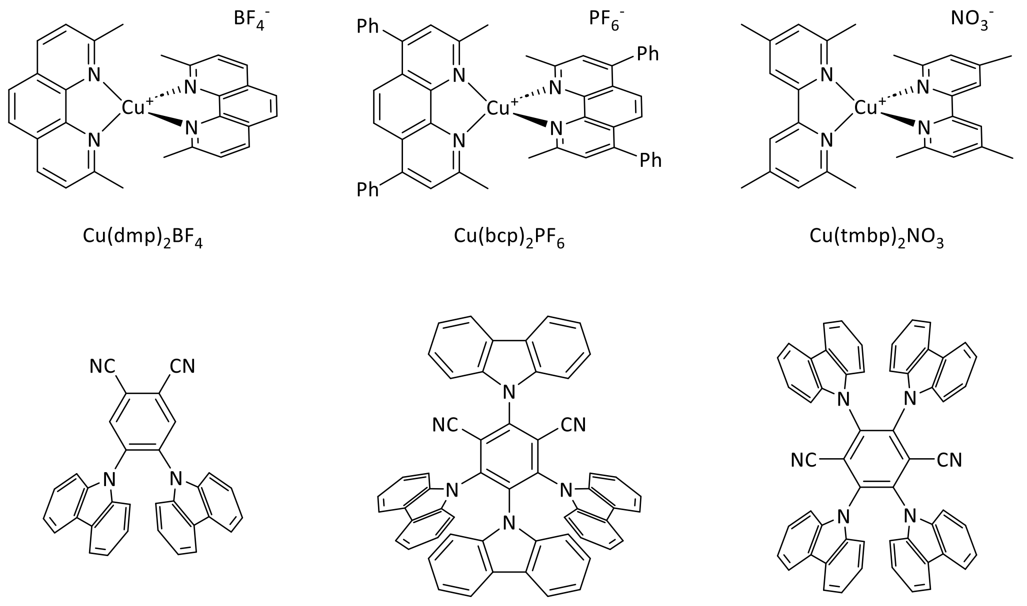

$Cu(dmp)_2BF_4$ $Cu(bcp)_2PF_6$ $Cu(tmbp)_2NO_3$

2CzBN 4CzIPN 4CzTPN

Figure 7. Early TADF emitters by *McMillin* (top) and *Adachi* (bottom).

2.2.2.1 Detecting TADF

It is quite challenging to irrefutably detect TADF, since it is a very unremarkable phenomenon. Many emission properties might be mistakenly assigned to TADF and it is therefore not easy to confirm its presence in a material. Broadly speaking, there exist five distinct features that are typically found in TADF emitters. Nevertheless, neither of these criteria alone is sufficient to confirm TADF and for any given system, edge-cases must always be carefully evaluated before making a final statement.[78]

1. Solvatochromic shift of the emission

As discussed earlier, charge transfer type excited states are inherent to TADF phosphors, since they allow for a small $\Delta E_{S1\text{-}T1}$. This is typically accompanied with substantial changes of the molecules' dipole moment in its excited state compared to its ground state, which affects the solvent molecules in the close surrounding. For solvents of high polarity, e. g. alcohols, a greater rearrangement is to be expected, as for non-polar ones like alkanes. Thus, in polar solvents, the excited states can be better stabilized, which results in a decrease in their energy and leads to an emission shift towards longer wavelengths compared to that observed in non-polar solvents. This behaviour can be used as experimental evidence for charge transfer type excited states.

2. Lifetime on the microsecond timescale

A lifetime in the microsecond range might also be a suitable hint towards TADF, especially paired with an even longer lifetime once the sample is cooled down to prevent rISC. Nevertheless, this might as well be a short-lived phosphorescence.

3. Temperature dependence of the emission spectrum and the lifetimes

The steady-state emission of a TADF emitter will show a red shift upon cooling, since the reduced thermal energy hampers the rISC, trapping the molecules in their triplet state. This results in increased phosphorescence, which is usually red shifted compared to fluorescence.

The time resolved decay curve of a TADF emitter will show an elongation upon cooling, with the slow component, i.e., the delayed fluorescence, having a smaller amplitude compared to high temperatures, again attributed to the hampered rISC.

For an ideal system with only one contributing emissive state, the *Arrhenius Equation* (Equation 1) describes the dependence of the rate constant k from the temperature T

$$k = A \cdot e^{-\frac{\Delta \mathrm{E}_{S_1-T_1}}{k_B \cdot T}} \qquad \text{Equation 1}$$

with A being a constant pre-exponential factor and k_B being the Boltzmann constant. With $k = \frac{1}{\tau}$ Equation 1 can be rewritten as Equation 2, illustrating a linear dependency between the natural logarithm of the reciprocal time constant τ and the reciprocal temperature.

$$\ln\left(\frac{1}{\tau}\right) = \ln(A) - \frac{1}{T} \cdot \frac{\Delta \mathrm{E}_{S_1-T_1}}{k_B} \qquad \text{Equation 2}$$

By quantifying the lifetime τ of the delayed fluorescence at different temperatures T and plotting $\ln\left(\frac{1}{\tau}\right)$ versus $\frac{1}{T}$ the resulting *Arrhenius Plot* yields an experimental value for $\Delta E_{S1\text{-}T1}$, since the slope of this linear equation is $-\frac{\Delta \mathrm{E}_{S_1-T_1}}{k_B}$.

4. Equality of prompt fluorescence and TADF

Since prompt and delayed fluorescence both arise from the S_1 state and just differ in their time constants, once the time information is ignored, their steady state emission spectra must match. Experimentally, the independent spectra of different time ranges can be obtained by performing time resolved emission spectroscopy (TRES). The details of this method are discussed in section 4.3.5.

5. Exclusion of triplet-triplet-annihilation

Triplet-triplet-annihilation (TTA) is a type of radical recombination that involves two excited molecules in their triplet state colliding and resulting in a dexter-type transfer of the energy from one molecule to the other. The former is thereby relaxed to its ground state, whereas the latter is pushed to a higher singlet state. After internal conversion, this molecule might emit from the S_1 state, resulting in a delayed fluorescence signal[79]. It is clear, that such an emission pathway can falsely satisfy point 4. Furthermore, TTA can react to temperature change in the same way as TADF, since it is diffusion controlled which is slowed down upon cooling, leading to longer lifetimes, falsely satisfying point 3. A first hint that TTA is not operative might be a mono-exponential decay of the delayed fluorescence signal, since emission stemming from radical recombination is prone to be intricate and therefore multi-exponential.

Experimentally, it is possible to distinguish between TADF and TTA by analysing the order of the kinetics of the emission. For TADF, a first order kinetic is to be expected, since it is only depending on the concentration of triplet excited states $c[T_1]$. A linear increase in $c[T_1]$ leads to a linear increase of TADF photons. In contrast, TTA follows a second order kinetic, since two molecules are involved in its mechanism, which collide due to diffusion. Therefore, it depends on $c^2[T_1]$, leading to a quadratic increase of TTA photon emission with linearly increasing $c[T_1]$.[73]

Since $c[T_1]$ cannot be quantified directly, it is assumed that doubling the energy fluence H_e, a measure of photon count, leads to a doubling of the concentration of excited molecules. This assumption is reasonable, since the oscillator strength is independent of the photon count. ISC follows a first order kinetic as well, therefore $c[T_1]$ is linearly proportional to H_e. With these considerations, the integral of a TADF emission band will scale linearly with H_e, whereas the one of TTA emission will scale quadratically.

To avoid TTA in the first place, a low laser power and high sample dilution should be employed, lowering the probability of triplet formation and of two triplets colliding.

3 State of the Art

In order to place the results of this thesis in a broader context, this chapter presents some of the most important milestones in the fields of luminescent copper(I) complexes as well as anionic carbenes.

3.1 Modern copper(I) luminophores

The discoveries of the first copper(I) TADF complex[77] and bulky substituents as remedy for the flattening distortion for tetrahedral copper(I) complexes[62], both by *McMillin*, only marked the beginning of a fruitful journey towards a diverse field of modern copper(I) containing luminophores.[80]

The first use of a copper(I) complex in an electroluminescent cell is reported by *Fu* in 2005.[81] The group employed $[Cu_2(triphos)_2(4,4'\text{-}bpy)][BF_4]_2$ **(3.1)**, a binuclear complex, η^3-coordinated by the tridentate chelate triphos and bridged by 4,4'-bipyridine.

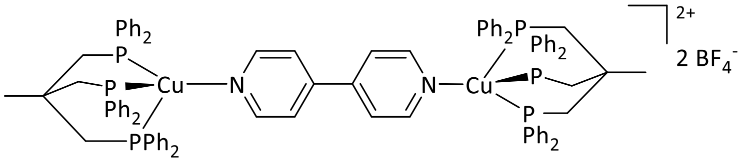

3.1

Scheme 12. The first copper(I) complex used in an electroluminescent cell.

In particular, this work reports a solvatochromic shift of this compound's emission. In polar solvents, a redshift is observed as well as a blueshift in non-polar solvents, in line with LLCT states being stabilized in polar solvents. Nevertheless, the authors do not investigate this observation further regarding possible TADF properties.

Armaroli followed up in 2006, by employing mononuclear, tetrahedral copper(I) complexes in an *Organic Light Emitting Cell* (OLEC).[82] They specifically emphasize the fit of charged complexes in such cells; the use in OLEDs is not feasible due to charge migration. These cationic, heteroleptic complexes consist of a P^P and an N^N chelate with a tetrafluoroborate anion. The N^N chelates are of phenanthroline type, substituted in 2- and 9-position by a variety of substituents, to prevent flattening distortion, giving rise to the three compounds **3.2** – **3.4**. Surprisingly, compound **3.3** and **3.4** showcase a PLQY of over 30% in dichloromethane solution, highlighting structural rigidity even in solubilized state. This quantum yield was the highest reported to that date. Since the involved excited states are reported to be of MLCT character, which are typically long-lived, and the luminescence intensity is extremely sensitive to oxygen, this type of compound seems to exhibit phosphorescence or even TADF, although the authors do not make a statement in this direction.

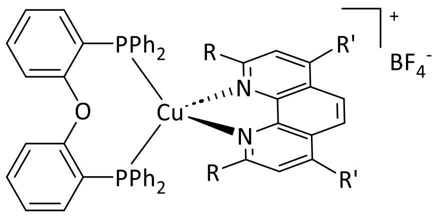

3.2 R = phenethyl, R' = H
3.3 R = Bu, R' = H
3.4 R = Me, R' = Ph

Scheme 13. The three heteroleptic complexes employed by *Armaroli*.

The first literature example of a copper(I) complex being investigated towards TADF appeared in 2011. *Yersin* and co-workers synthesized and characterized compounds incorporating the same P^P type ligand employed by *Armaroli*, but introduced a bis(pyrazolyl) ligand with a negatively charged borate backbone, resulting in overall charge neutral complexes.[83] The compounds exhibit strong emission, displaying impressive solid-state photoluminescence quantum yields of 45% **(3.5)** and 90% (**3.6** and **3.7**). The authors suggest that the responsible excited state in this type of complexes is of MLCT character. Below 100 K, phosphorescence from T_1 is observed. At extremely low temperatures of around 2 K, the emission bands broaden and lose their distinct structure, with peak wavelengths spanning from 436 nm (**3.5**) to 464 nm (**3.7**) across the three compounds. The decay times range from 450 ms to 610 ms (30 – 100 K). As the temperature rises beyond 100 K, the emissions blueshift, accompanied by shorter decay times, which aligns with the emission originating from the lowest excited singlet state, S_1. At room temperature, S_1

becomes the primary source of emission. The energy gap between S_1 and T_1 states is 1300 cm^{-1} **(3.5)**, 1000 cm^{-1} **(3.6)**, and 800 cm^{-1} **(3.7),** respectively equivalent to 160 meV, 120 meV, and 100 meV. These small energy differences allow the occurrence of thermally activated delayed fluorescence (TADF).

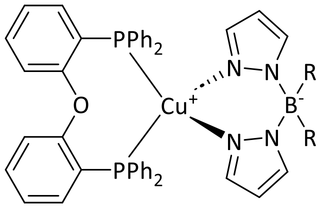

3.5 R = H
3.6 R = pyrazol-1-yl
3.7 R = Ph

Scheme 14. The three neutral copper(I) complexes employed by *Yersin*, which show TADF.

Due to the d^{10} configuration of the Cu(I) ion in its complexes, the coordination geometry of copper(I) is not restricted to a tetrahedron. In fact, complexes with the coordination numbers 2 or 3 amount to over 65% of the known copper(I) complexes.[84] The advantage of such geometries is that flattening distortion does not play a huge role anymore. Nevertheless, there is experimental and computational evidence that with regard to TADF properties, LLCT states are vital in order to facilitate a strong thermal coupling between the S_1 and the T_1 state. MLCT type excitations tend to decay via the phosphorescence pathway.[85] Furthermore, such low-valent complexes bear the risk of impaired structural uniformity, often undergoing chemical equilibria in solution. One such example was reported by *Ganter* in 2019. Bi- and tricoordinate copper(I) complexes with the IPr carbene and pyridine ligands were investigated with regard to their luminescence properties.[86] It was shown that while the linear representatives with only one pyridine moiety are dark in their crystalline state, the trigonal counterparts show PLQYs of up to 83%. Nevertheless, grinding or reprecipitating solid material of the linear complex **3.9** resulted in a dramatic increase of its luminescence efficiency to 87%, exceeding the ones of the trigonal derivatives. This behaviour was attributed to the tetrafluoroborate anion coordinating to the copper(I).

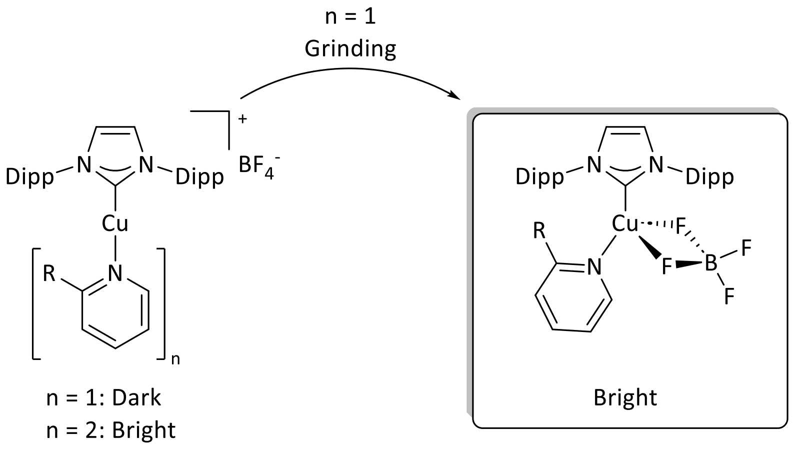

3.8 n = 1, R = H
3.9 n = 1, R = Me
3.10 n = 1, R = Ph
3.11 n = 2, R = H
3.12 n = 2, R = Me
3.13 n = 2, R = Ph

Scheme 15. Heteroleptic IPr copper(I) complexes by *Ganter*, the linear representatives showing luminescence only after grinding due to anion coordination.

A follow-up publication of *Gilch* in 2023 shed light on compound **3.9**, investigating the chemical dynamics of its solutions in various solvents.[87] They were not only able to give a comprehensive description of the excited state behaviour of this compound via femtosecond spectroscopy techniques, but could also give chemical evidence that even in solution, an equilibrium is present between the linear complex **3.9** and BF_4^- coordinated species. Addition of a tetrafluoroborate salt to a solution of **3.9** in dichloromethane resulted in increased band intensity of the steady-state emission spectrum. In line with the preceding work, they confirmed the MLCT character of the S_1 state being swiftly transferred to a locally excited triplet state located on the Dipp substituents.

Precisely this excitation prevents efficient luminescence of this family of complexes, as was reported by *Marian* in 2019.[88] Specifically, introducing aliphatic substituents instead of the aromatic Dipp groups would be a remedy for the undesirable non-radiative decay pathways, according to their calculations. Nevertheless, such aliphatic substituents proved to be inferior to the aromatic ones, providing much lower chemical stability for the resulting complexes. The research in this direction is still ongoing today.

In 2021, a study in this direction was published again by *Ganter*.[89] They reported the synthesis and photophysical characterization of similar complexes **3.14** - **3.20**, in which the Dipp substituents are replaced by triphenylmethyl- (trityl) substituents. These extremely bulky moieties feature an sp^3-carbon atom neighbouring the carbene nitrogen atoms.

As secondary ligands, pyridine and quinoline derivatives were chosen. In dichloromethane solution, the pyridine-based complexes **(3.14 – 3.18)** exhibit absorption bands below 300 nm and show broad emission spectra with colours ranging from yellow at 550 nm **(3.14)** to red at 665 nm **(3.16)**. The emission shifts bathochromically with acceptor-substituted pyridine ligands. The emission of the 6-methylquinoline complex **(3.19)** appears with 525 nm at lower wavelengths, with visible vibrational progression, indicating the presence of a localized state.

The emission properties of the complexes are further investigated at lower temperature. The pyridine complexes **3.14** and **3.17** show emission with rate constants around 10^3 s^{-1} that does not change significantly upon cooling, typical for phosphorescence. On the other hand, the acceptor-substituted complexes **3.15** and **3.16** exhibit features characteristic of thermally activated delayed fluorescence, in that the emission colour shifts to longer wavelengths under concomitant elongation of the lifetimes with decreasing temperature. Nevertheless, the paper refrains from a definite conclusion towards TADF properties, since the obtained results are ambiguous and the excited state behaviour are probably much more complicated.

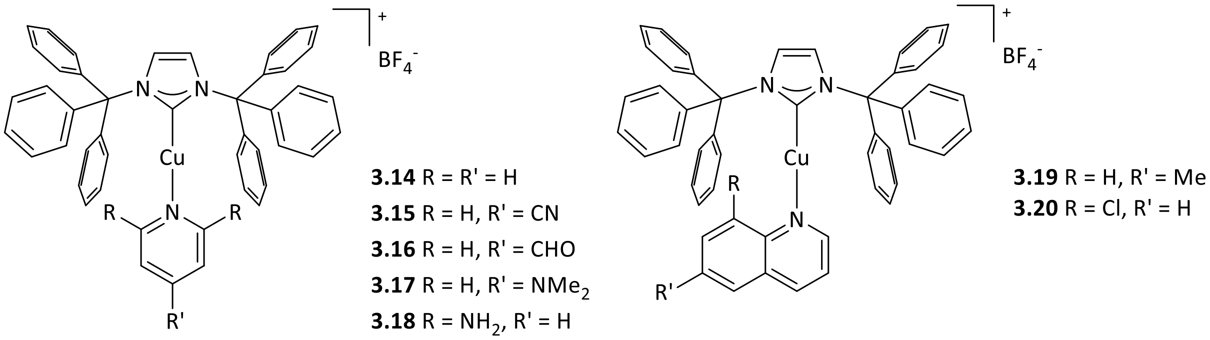

3.14 R = R' = H
3.15 R = H, R' = CN
3.16 R = H, R' = CHO
3.17 R = H, R' = NMe_2
3.18 R = NH_2, R' = H

3.19 R = H, R' = Me
3.20 R = Cl, R' = H

Scheme 16. Strictly linear NHC copper(I) complexes by *Ganter*, the linearity being enforced by sterically demanding trityl substituents.

This previously discussed research dealt with charged complexes combined with non-coordinating anions. This can not only lead to unexpected chemical behaviour (vide supra) but is also not desirable for the fabrication of OLEDs. In 2019, *Thompson* reported ground-breaking work towards neutral copper(I) complexes and their employment in OLEDs.[90] This was achieved by carbazolate anions as secondary ligands. These highly donating anions were coupled with a strongly accepting (di)amido carbene, resulting in copper(I) luminophores covering a wide range of the visible spectrum with their emission, ranging from deep blue 430 nm **(3.21)** to deep red 700 nm **(3.26)**. The six compounds, **3.21** – **3.26**, all show TADF at room temperature, with remarkably low lifetimes of the delayed fluorescence of maximally 2.3 µs in 2-methyltetrahydrofuran solution **(3.21)** and exceptionally low $\Delta E_{S1\text{-}T1}$ of down to 62 meV. Moreover, for compound **3.22** a PLQY of 1 was found in 2-methyltetrahydrofuran solution as well as in a polystyrene film.

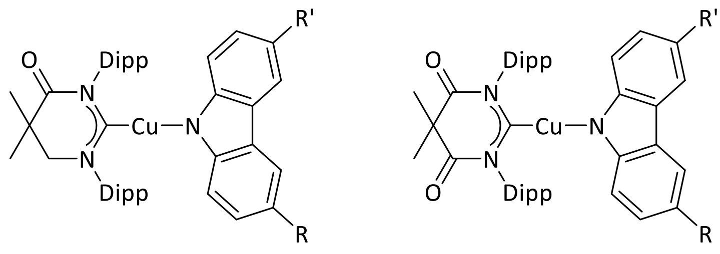

3.21 R = R' = CN
3.22 R = CN, R' = H
3.23 R = R' = H

3.24 R = R' = CN
3.25 R = CN, R' = H
3.26 R = R' = H

Scheme 17. Overall charge-neutral copper(I) complexes by *Thomspons* employed in OLEDs, covering a vast range of the visible light spectrum.

In the same year, *Bochmann* employed a structurally related carbene, but with an anionic malonate backbone. This is of particular interest, since it is the same carbene employed in this work. The group focused on only one linear copper(I) complex incorporating this carbene together with a cyclic alkyl amino carbene (CAAC) and compared it with the structural analogues containing the higher homologues silver and gold instead of copper.[91] With the increasing size of the central metal ion, the spin-orbit coupling coefficients become larger, resulting in decreased phosphorescence lifetimes. The article reports 400 µs, 350 µs and 50 µs in the row Cu > Ag > Au for the solid samples, consistent with the lifetimes of typical phosphorescent copper(I) emitters. The emission maxima are not heavily influenced by the metal ion, ranging between 440 nm **(3.28)** and 460 nm **(3.29)**. Such complexes were also tested with regard to their catalytic activity in hydrosilylation reactions of acetophenones. César and co-workers found that these bis(carbene) complexes show low catalytic activity but concomitantly reported much better results for the respective copper(I)-chloride complex of the anionic carbene.[92]

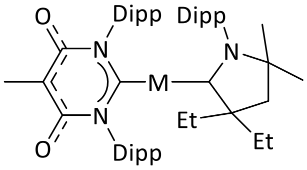

3.27 M = Cu
3.28 M = Ag
3.29 M = Au

Scheme 18. Heteroleptic NHC CAAC copper(I) complexes with the coinage metals by *Bochmann*.

3.2 Anionic carbenes

Carbenes containing an anionic charge are a recent branch of research in the field of carbene chemistry. The first literature appearance is ascribed to *Fehlhammer* in 1996[93], five years after the first stable carbene was reported by *Arduengo*. He connected three methylimidazolium moieties via their nitrogen atoms to a boranate backbone. Subsequently, he reported the coordination of the liberated tricarbene to various transition metal ions, such as Fe(III) and Co(III)[94], the complexes manifesting themselves as remarkably stable.

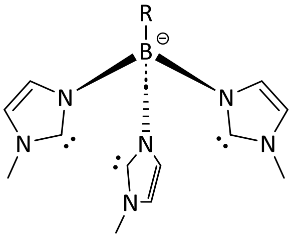

3.30 R = H
3.31 R = Ph

Scheme 19. The first literature appearance of an anionic carbene by *Fehlhammer*.

In the following chapter, some recent advancements in this topic of research are collected. The anionic carbenes are sorted according to the incorporation of the anionic charge, whether it is endo- or exocyclic.[95]

3.2.1 Exocyclic charge

In 2009, Lavigne reported the synthesis of a mono-amido imidazolidinium cation **3.32** via the reaction of the corresponding formamidine with 2-chloroacetyl chloride.[96] This compound is in equilibrium with its tautomer **3.33**, featuring a hydroxy functionality in the backbone; a major tautomer due to its aromaticity, which they were able to deprotonate to the carbene precursor **3.34**. Liberation of the carbene was possible with LiHMDS and besides the thio urea **3.35**, coordination of this carbene to a chlorodicarbonyl rhodium (I) fragment was achieved, resulting in the overall negatively charged complex **3.36** with a lithium counterion. The TEP value was subsequently determined to be 2030 cm^{-1}.

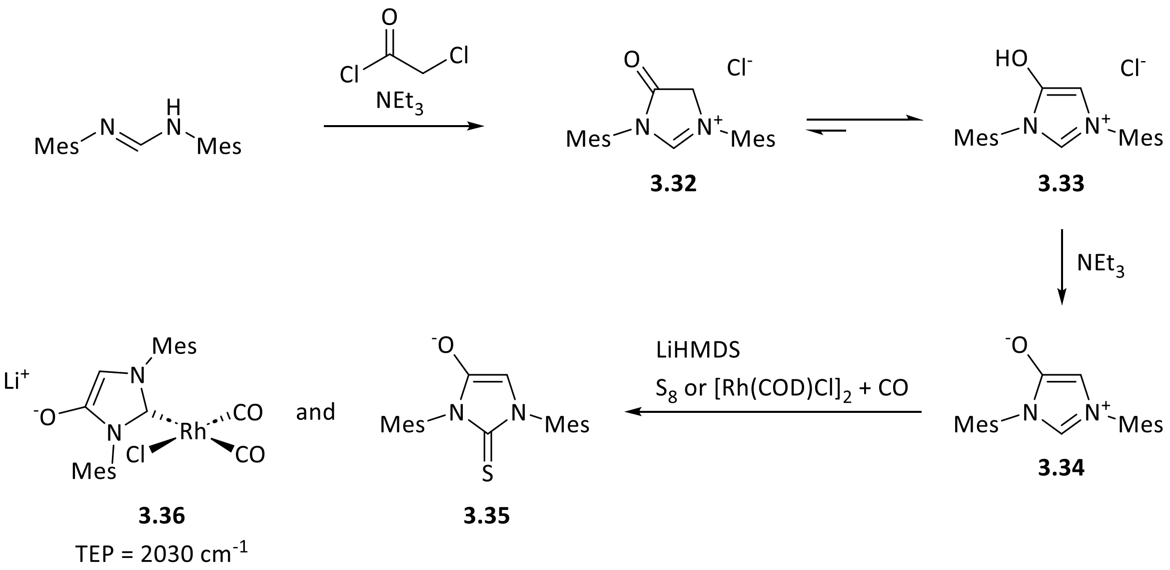

Scheme 20. Synthetic route to anionic carbenes with an exocyclic charge delivered by an alcoholate.

Later in that year, the group of *Glorius* developed a way to generate the same anionic carbene precursor in only one step with the concomitant possibility of functionalizing it in 4-position.[97] They found that the above formamidine reacts cleanly with methyl-2-bromoacetate and DIPEA as a base via a nucleophilic substitution and then undergoes an intramolecular nucleophilic attack with closure of the ring and removal of the methanolate. This in turn serves as internal base, generating zwitterionic, functionalized carbene precursors of the type **3.37**. Exemplary, the TEP value of the phenyl derivative has been determined to be 2044 cm^{-1}.

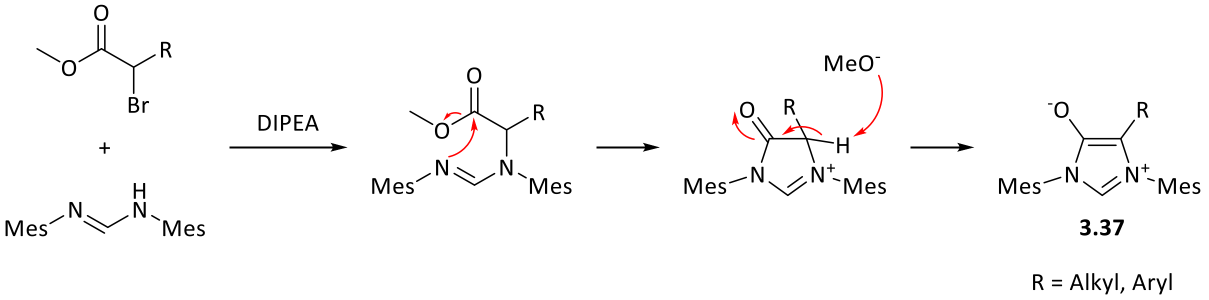

Scheme 21. One-Pot reaction developed by *Glorius*, yielding anionic carbene precursors in one step.

In 2012, *Lavigne* established the family of amido carbenes, that feature an anionic amide in their backbone.[98] This research was initially driven by the commercially available reagent Nitron©, which was reported to show typical reactivity of a carbene, with which it is in tautomeric equilibrium. Synthetically, the precursor **3.38** is accessible by condensation of *N*-isopropyl-2-chloroacetamide with a formamidine, followed by treatment with triflic anhydride.

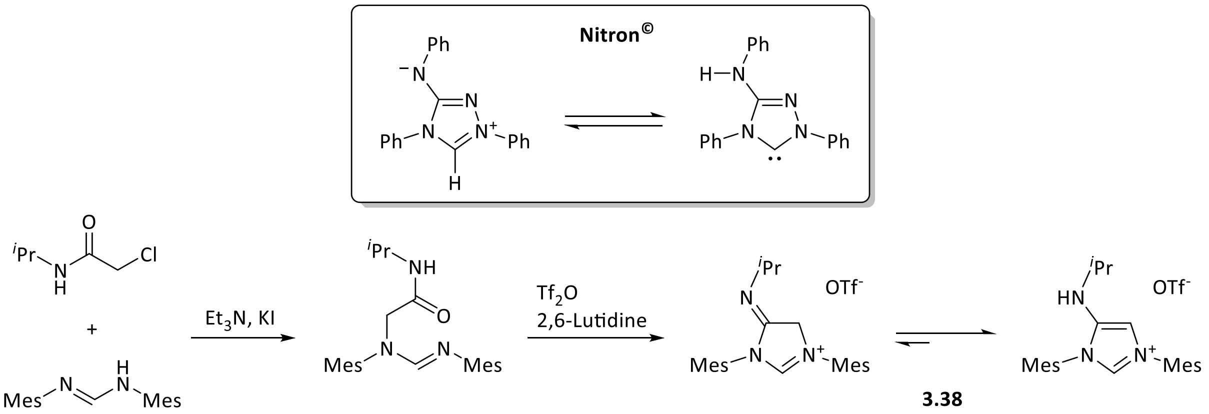

Scheme 22. The synthetic route to the precursors of anionic amido carbenes and the tautomeric equilibrium of Nitron©.

Subsequently, **3.38** might be deprotonated once or even twice, the latter leading to the free anionic carbene **3.39**. Nevertheless, also mono-deprotonation leads to carbene reactivity, since the mesoionic imidazolium-aminide **3.40** is in tautomeric equilibrium with the corresponding NHC. This was shown in the ^{1}H-NMR-spectrum, since the signal for the amine proton as well as the NCN proton is missing at room temperature, only below 180 K it becomes visible as a broad singlet, indicating a fast exchange between the two tautomers.

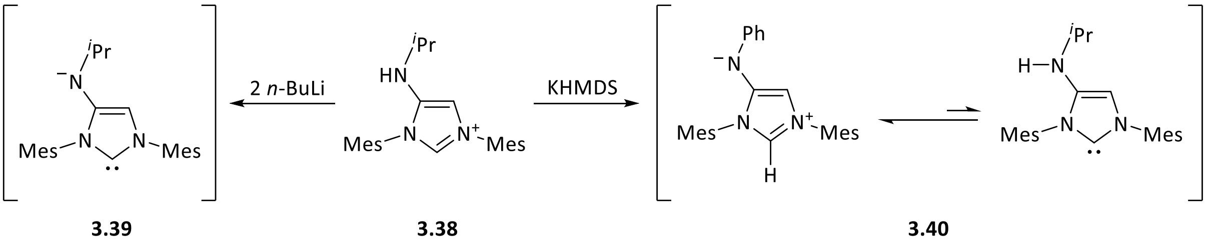

Scheme 23. Single and double deprotonation of the amido carbene precursor **3.38**.

In the following year, *Streubel* extended this chemistry to the higher homologue phosphorus, leading to the class of phosphanido carbenes.[99] The synthetic route is not as straight-forward as for the nitrogen analogues. The zwitterionic precursor **3.42** is obtained by deprotonation of thiourea **3.41** and subsequent reaction with dichlorophenylphosphine, followed by a reduction with elemental potassium. Treatment with *n*-butyllithium liberates the anionic carbene **3.43**. These carbene precursors are also in equilibrium with their NHC tautomers, even with a much lower barrier, suggested by calculations. Nevertheless, the research into their coordination chemistry has not been reported to date.

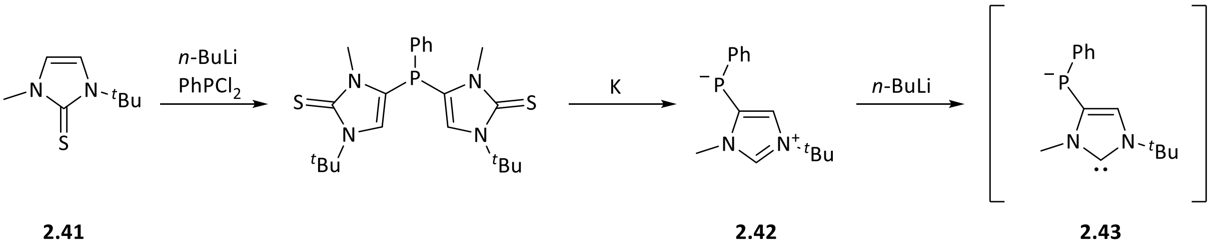

Scheme 24. Synthetic route of phosphanido carbenes.

3.2.2 Endocyclic charge

The first appearance of an anionic carbene incorporating the charge within the heterocycle was reported by *Roesler* in 2006.[100] The group synthesized the precursor **3.44** with an inorganic boron backbone by reaction of a trimethylsilyl-formamidine with 1,1-bis(chloromethylboryl)ethane and trimethylsilyltriflate. This reaction produces the zwitterionic iminium borate **3.43** with the triflate coordinating to one of the boron atoms, as clarified by X-ray diffraction on a single crystal. Dual treatment with strong bases leads to the anionic carbene **3.45**, first KHMDS deprotonates the backbone, then *n*-butyllithium liberates the carbene. The molecular structure of the carbene was only obtained indirectly, since a coordination to the lithium cation is established in solid state. The article gives a comparison of the anionic carbene to the classic imidazolylidene I and a terphenyl anion III. Computational studies indicate that the anionic carbene **3.45** falls into place between these two edge cases, with the σ-donating ability increasing from I << **3.45** < III and the π-accepting ability decreasing in reverse order: I > **3.45** > III.

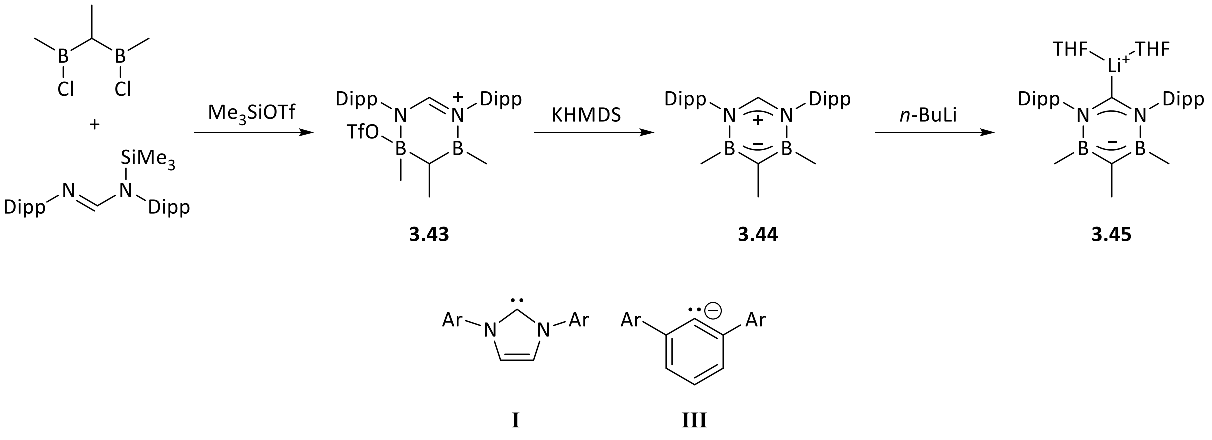

Scheme 25. The lithium complex of the first anionic carbene with an endocyclic charge in its inorganic backbone **(3.45)**, and the two edge cases I and III it was compared to.

The carbene studied in the present work was first reported by *Lavigne* in 2008.[101] The group established the name *maloNHC* for this type of compounds, related to their synthesis involving a malonic acid or the respective dichloride reacting with a formamidine in the presence of DCC for the acid or triethylamine for the acid chloride. The deprotonation of the acidic backbone proton is achieved in situ by an excess of base. The TEP value of **3.46** was determined to be 2043 cm^{-1} in 2010[102], the ^{77}Se-NMR-shift is 348 ppm reported in 2017 by *César*.[103] These constants were reported for a variety of compounds differing in their cations, this overview is therefore restricted to the triethylammonium salt in both cases, since the least influence from this weakly coordinating ion is to be expected.

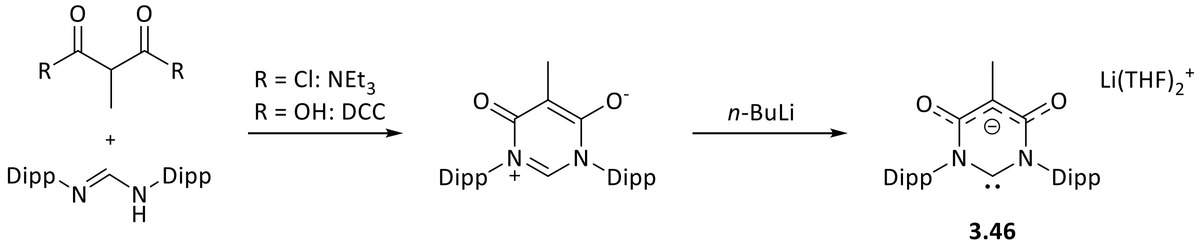

3.46

Scheme 26. The anionic maloNHC by *Lavigne*.

In 2020, an interesting coordination mode of this NHC was discovered by *Dias*.[104] They found that the malonate backbone can undergo coordination to mercury(II) ions, leading to the 1D-coordination polymer **3.47**, with the mercury atoms being trigonally coordinated by the carbene, the backbone oxygen atom and one chloride ion. This is of particular interest for the present work, since a similar motif was found for copper(I).

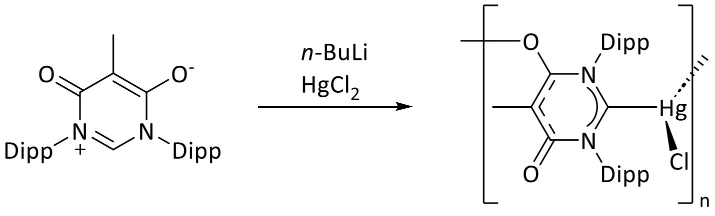

3.47

Scheme 27. Coordination mode of the *maloNHC* to mercury(II) chloride, resulting in a 1D coordination polymer.

Lastly, in 2015, *Ganter* reported the synthesis of an anionic NHC in the scope of backbone modification of triazolone ylidenes.[105] They found that diphenyl carbazide can yield the zwitterionic carbene precursor **3.48** via refluxing in triethyl orthoformate, the CH fragment thereby being delivered by the solvent. Neither NMR nor reactivity studies towards chalcogens or CS_2 indicate the presence of the carbene tautomer **3.49**. Nevertheless, deprotonation with KO^{t}Bu or NaHMDS liberates the anionic carbene **3.50**, which was then able to undergo the typical reaction with the abovementioned trapping reagents. The TEP value of this carbene was determined to be 2050 cm^{-1}.

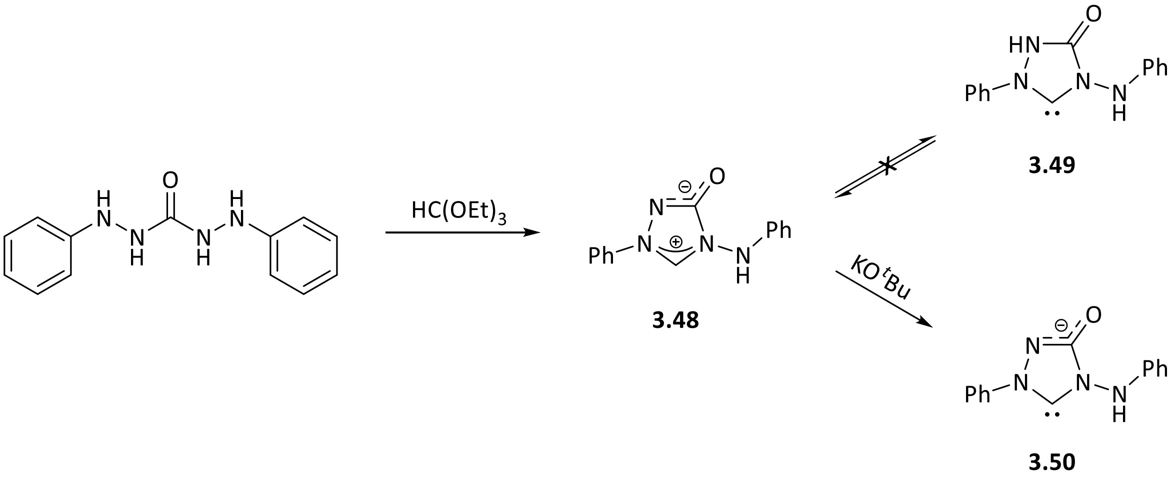

Scheme 28. Reaction of diphenyl carbazide with triethyl orthoformate to a meso-ionic carbene precursor. While this is not in equilibrium with a carbene, it can be liberated using a base.

4 Results and Discussion

In the course of this work, several copper(I) complexes containing the anionic diamido carbene **1** have been synthesised and fully characterised. In the following chapter, their synthetic route as well as their chemical and physical properties in solution and in solid state will be presented in detail. Moreover, a selection of four compounds was scrutinized regarding their photophysical properties with the aim to understand the nature of their excited state behaviour. These compounds were chosen according to rational design suggested by quantum chemical calculations. The class of linear and trigonal copper(I) complexes presented in this work is depicted in Figure 8.

General structure	**Ligand**	**Nomenclature**
linear	***Pnictogen based***	
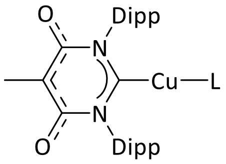	L = 2,6-lutidine	**1 · Cu · Lut**
	L = 4-formyl-2,6-lutidine	**1 · Cu · FLut**
	L = 4-dimethylamino pyridine	**1 · Cu · DMAP**
	L = acridine	**1 · Cu · Acr**
	L = triphenyl phosphine	**1 · Cu · TPP**
	Chalcogen based	
	L = ^{Me}ImSe	**1 · Cu · ^{Me}ImSe**
	L = ^{iPr}ImSe	**1 · Cu · ^{iPr}ImSe**
	L = ^{tBu}ImSe	**1 · Cu · ^{tBu}ImSe**
trigonal-planar	***Pnictogen based***	
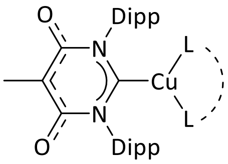	L = pyridine	**1 · Cu · Py$_2$**
	L = 4-formyl pyridine	**1 · Cu · FPy$_2$**
	L = 4-acetyl pyridine	**1 · Cu · 4AcPy$_2$**
	L^L = 2-acetyl pyridine	**1 · Cu · ^{N,O}2AcPy**
	L^L = 2,2'-bipyridine	**1 · Cu · Bpy**
	Chalcogen based	
	L = ^{Me}BenzImSe	**1 · Cu · ^{Me}BenzImSe$_2$**

Figure 8. Target molecules presented in this work, their respective secondary ligands and the employed nomenclature.

4.1 Synthesis

4.1.1 Preparation of the carbene precursor

The synthesis of the zwitterionic carbene precursor **1^H** and the corresponding carbene has already been described by *César* in 2013.[92] In this work, it has been prepared in the same fashion, only the purification has been adjusted to larger scales. Originally, the product is purified by column chromatography, which is generally less feasible on larger scales. Therefore, the purification was achieved via a filtration through silica, removing the triethylammonium chloride, followed by a recrystallization from an ethyl acetate / *n*-hexane mixture. This was successfully done with scales up to 30 g with a yield of 85%. The yield is lower than reported in the original publication (97%) although the ^{1}H-NMR-spectrum indicates a higher purity.

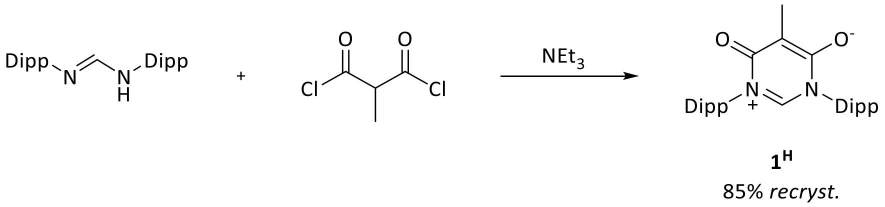

Scheme 29. Synthesis of the zwitterionic precursor **1^H**.

4.1.2 Forming the carbon-copper bond

The coordination of the carbene **1** to copper(I) starts with the liberation of **1** with *n*-butyl lithium. The proton bonded to the future carbene carbon atom is much less acidic due to the zwitterionic nature of the precursor, requiring stronger bases, opposed to the cationic imidazolium salts. The carbon-copper bond is then formed by the reaction of **1** in tetrahydrofuran solution with a solid copper(I) halide, leading to the anionic complexes of the general motif **$1{\cdot}CuX^M$**. This route has been described in several articles, mainly for X = Cl and M = Li, and the nature of such complexes is well understood.[92,106] Therefore, this approach has been maintained as the working basis in the present investigation.

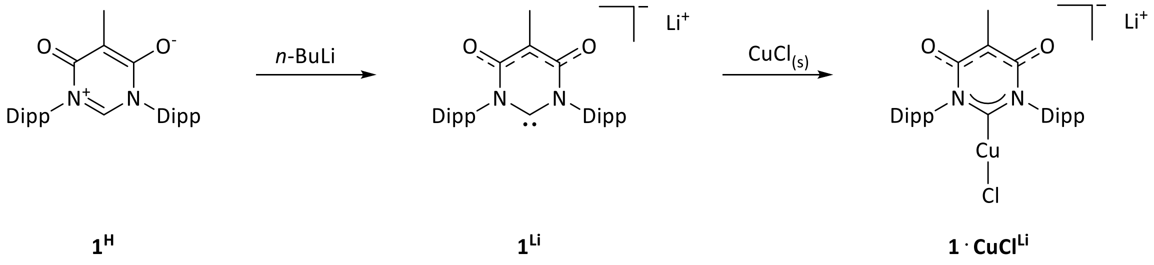

Scheme 30. Reaction cascade from the zwitterionic precursor $\mathbf{1^{H}}$ to the copper(I) halide complex $\mathbf{1{\cdot}CuCl^{Li}}$ via the free carbene route.

4.1.3 Preliminary attempts towards heteroleptic complexes

Before the final synthesis procedures of the targeted copper(I) complexes are discussed, it is beneficial to present the preceding work that did not or only partly yield the desired compounds, yet has been inevitable for eventually understanding a unique property of the chemistry of **1** towards Cu(I). The coordination chemistry of the anionic NHC **1** in the scope of this work is largely dominated by its possibility to form a one-dimensional coordination polymer with Cu(I). Due to the anionic charge, which is predominantly located in the carbenes' backbone, its reactivity can be compared to that of an enolate. According to the HSAB concept, Cu(I) is a borderline case between hard and soft metal ions[107], ultimately leading to a favourable coordination of the carbenes' backbone oxygen to the copper and the possibility of polymer generation. This finding has been crucial for this project, since this polymer can easily be formed unknowingly, if the conditions are not set carefully. An in-depth discussion of this coordination polymer will follow in a later chapter.

4.1.3.1 Abstraction of the halide from $1{\cdot}CuX^{M}$

NHC-Cu-X complexes (X = Cl, Br, I) are often employed as starting materials in copper(I) chemistry, since the halide is easily abstracted with a silver(I) salt, leaving space for other secondary ligands.[86,89] In the scope of this work, $\mathbf{1{\cdot}CuCl^{Li}}$ was employed as starting material which is prepared as previously described.[92] The carbene is generated in situ by deprotonation of $\mathbf{1^{H}}$ with *n*-butyllithium in dry tetrahydrofuran at -80 °C whereupon solid cuprous chloride is added. After work-up, this colourless solid is dissolved in tetrahydrofuran and treated with silver(I) tetrafluoroborate solution in the presence of a desired ligand. For these preliminary studies, two ligands have been tested, pyridine and 4-formylpyridine. After filtering off the silver chloride, the resulting solutions are concentrated *in vacuo* and a colourless solid is precipitated by addition of *n*-hexane in case of pyridine.

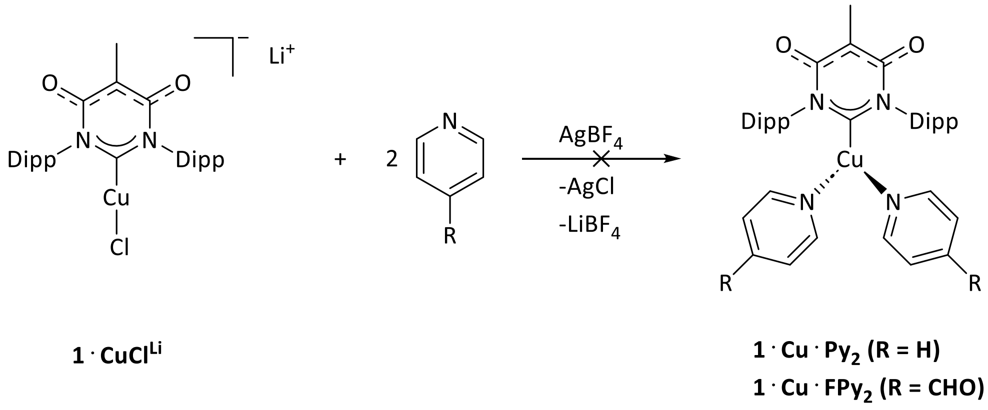

Scheme 31. The reaction of **1·CuCl^{Li}** with pyridines under precipitation of the chloride with silver(I) does not yield the expected products.

The resulting proton NMR-spectrum reveals the presence of the carbene as well as pyridine, although not in an expected whole integer ratio. In fact, this method yields consistently too low and not reproducible contents of pyridine with an average of 0.8 equivalents with respect to the carbene-copper moiety. In case of 4-formyl pyridine, a colourless precipitate is generated after filtration without any addition of *n*-hexane. Its ^{1}H-NMR reveals that 4-formylpyridine is not at all present in it, only the signal set of the carbene is found. Interestingly, the obtained powders did not show any sign of degradation, which is uncommon for under-coordinated copper(I) compounds. Removal of a halide ligand by silver(I) addition with too little secondary ligand to substitute the vacant coordination spot on the copper usually leads to a green to brown discoloration of the resulting product.

Ultimately, this finding is explained by build-up of oligomeric material of **[1·Cu]$_n$**. In case of pyridine, the length on these oligomers remains small enough for them to remain in solution, whereas for 4-formyl pyridine, they apparently become so large, that they precipitate instantaneously. The chain ending copper atom is presumably coordinated by one or two pyridine molecules.

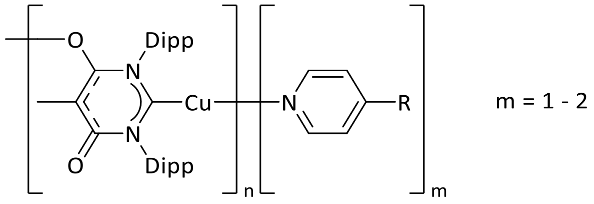

Scheme 32. Suspected compounds obtained from precipitation of pyridine-based heteroleptic complexes from tetrahydrofuran solution by addition of *n*-hexane, as evidenced by ^{1}H-NMR-spectroscopy.

Another challenge encountered in this process is the by-product lithium tetrafluoroborate which is detected as residual impurity via ^{19}F-NMR-spectroscopy. Like many lithium salts, it is quite soluble in organic solvents which makes its removal exceptionally hard.[108] Reprecipitation or washing yielded unsatisfactory results because of the very similar solubility properties of the lithium salt and the desired complex. Likewise, column chromatography was not applicable since the complexes apparently do not withstand these conditions.

4.1.3.2 Change of the counter ion

To circumvent the difficult removal of the lithium salts, the alkali metal ion was substituted. Sodium was chosen, since its inorganic salts are much less soluble than the respective lithium derivatives. Besides organolithium bases, also amides are strong enough to deprotonate the carbene precursor, such that NaHMDS was employed as readily available sodium containing base.

However, it was found that the derivative **1·CuCl**$^{\mathbf{Na}}$ is unstable in solution. It readily decomposes directly after the addition of CuCl to the solution of **1**$^{\mathbf{Na}}$ under formation of a colourless precipitate. Presumably, the strongly donating carbene results in the anionic chloride being rather weakly bonded. Together with the low solubility of sodium chloride in tetrahydrofuran, the equilibrium shown in Scheme 33 is shifted in favour of **[1·Cu]**$_{\mathbf{n}}$, leading to its precipitation together with the inorganic salt.

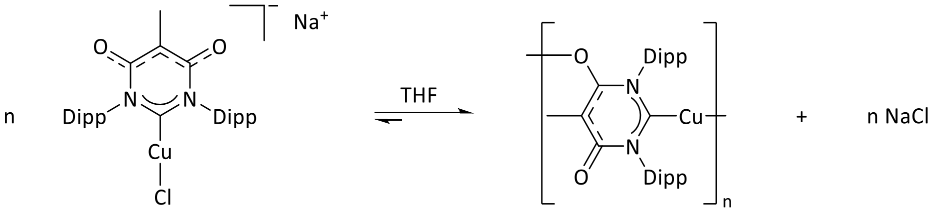

$1\cdot\mathrm{CuCl}^{\mathrm{Na}}$

$[1\cdot\mathrm{Cu}]_n$

Scheme 33. The equilibrium between **1·CuCl**$^{\mathbf{Na}}$ and **[1·Cu]**$_{\mathbf{n}}$ is shifted far to the side of the polymeric material in tetrahydrofuran solution.

4.1.3.3 Change of the halide

In order to gain a stable compound of the motif **1·CuX**$^{\mathbf{Na}}$, X was chosen to be iodide, since sodium iodide has a much higher solubility in tetrahydrofuran caused by its lower lattice energy. Indeed, adding solid CuI to a solution of **1**$^{\mathbf{Na}}$ in tetrahydrofuran, as depicted in Scheme 34, showed no visible decomposition and **1·CuI**$^{\mathbf{Na}}$ was obtained with a yield of 87% as colourless powder. Moreover, experiments involving the halide abstraction by silver(I) did in fact yield products without contamination of sodium tetrafluoroborate after precipitation. Nevertheless, build-up of oligomeric material, as depicted in Scheme 32, still caused products undersaturated with pyridine.

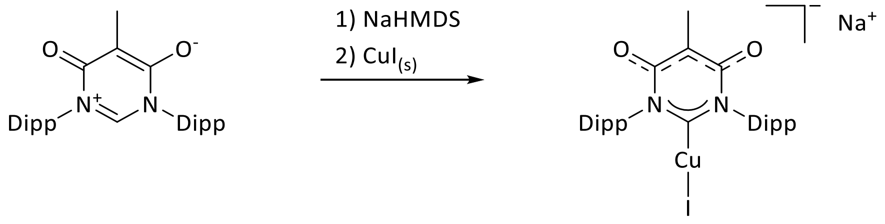

1^{H}

$1\cdot\mathrm{CuI}^{\mathrm{Na}}$
87 %

Scheme 34. Synthesis of **1·CuI**$^{\mathbf{Na}}$ in a similar fashion as **1·CuCl**$^{\mathbf{Li}}$.

4.1.3.4 Elimination of the halide

Due to the equilibrium depicted in Scheme 33, it is reasonable to assume that the elimination of an iodide anion from **1·CuI**$^{\mathbf{Na}}$ is favoured. Therefore, it was anticipated to achieve this by adding a large excess of desired pyridine derivative, presumably better suited due to its charge neutrality. Dichloromethane is chosen as the solvent since the by-product sodium iodide is mostly insoluble in it, shifting the equilibrium towards the desired complex by precipitation.

Indeed, employing this strategy, compound **1·Cu·Py₂** was successfully generated by slow diffusion of diethyl ether into a solution of **1·CuI$^{\mathbf{Na}}$** and 30 equivalents of pyridine in dichloromethane, which was verified by the ^{1}H-NMR-spectrum, showing an expected ratio of carbene to pyridine of 1 : 2. Also, the molecular structure was determined, illustrating its trigonal geometry. An in-depth discussion of its structural properties is given in a later chapter.

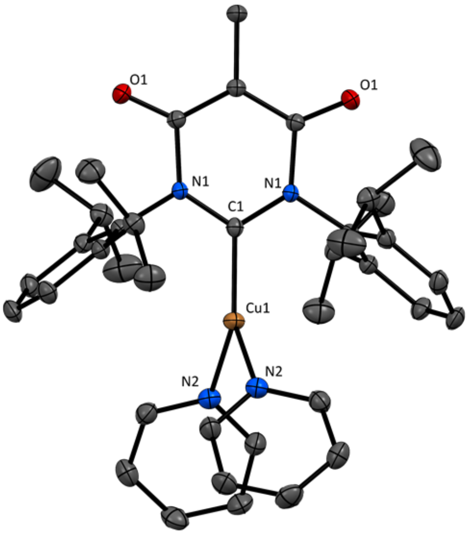

Figure 9. Molecular structure of compound **1·Cu·Py₂**. Thermal ellipsoids for 50% probability. Hydrogen atoms are omitted for clarity. The molecule resides on a crystallographic C_2-axis propagating through C1 and Cu1.

With **1·Cu·Py₂** successfully generated, the same strategy was pursued using the electron poor ligand 4-formyl pyridine, once again yielding single crystalline material. X-ray diffraction revealed though, that the ligand did not substitute the iodide. Instead, it coordinates to the sodium ions, resulting in infinite chains of [4-formylpyridine]$_2$Na[1·CuI]. Apparently, 4-formylpyridine is not able to compete with the coordination of the iodide, in contrast to pyridine.

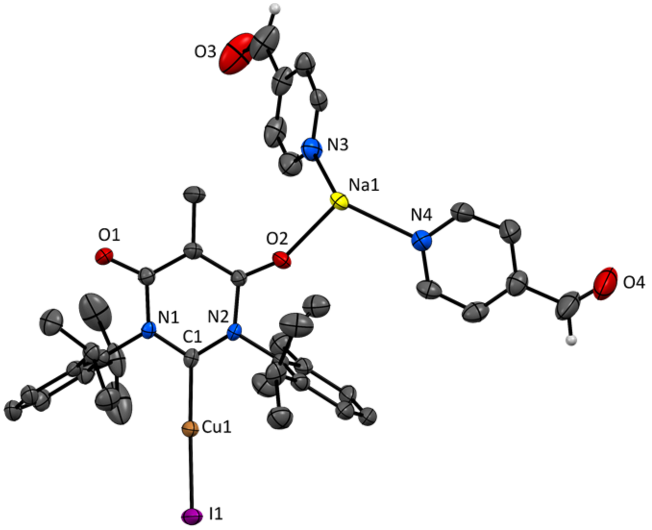

Figure 10. Asymmetric unit of the molecular structure of **1·CuI^{Na}** with two 4-formylpyridine ligands coordinated to the sodium ions. Thermal ellipsoids for 50% probability. Hydrogen atoms, except formyl protons, are omitted for clarity.

This complex crystallizes in one-dimensional chains, with the sodium ions being tetrahedrally coordinated by two carbene backbone oxygen atoms and two formylpyridine ligands. This structural motif is already known for **1·CuCl^{Li}**, which adopts the same constitution with two acetone molecules coordinating to the lithium ions.[92]

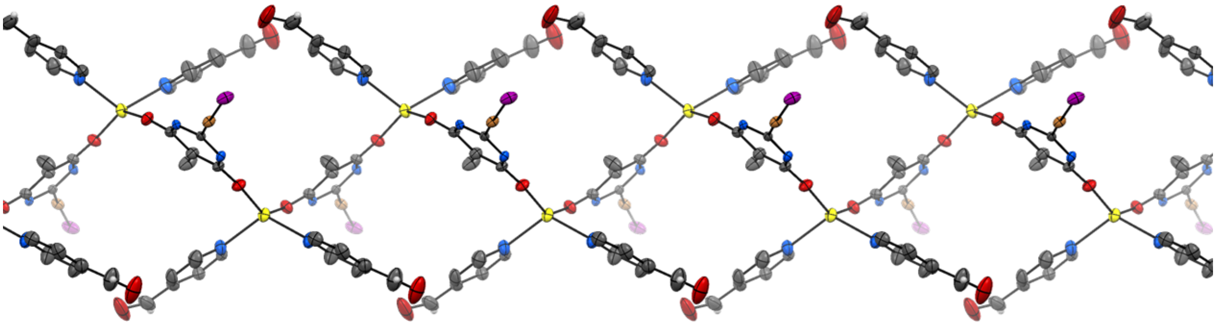

Figure 11. Crystallographic expansion of the structure shown in Figure 10. Thermal ellipsoids for 50% probability. Dipp-substituents and hydrogen atoms, except formyl protons, are omitted for clarity. Depth cueing indicates moieties pointing away from the paper plane.

4.1.4 The coordination polymer [1·Cu]ₙ

The unremarkable nature of the colourless precipitate that was received during many of the preliminary experiments hampered its correct characterization. Since its ^{1}H-NMR-spectrum revealed only the signal set of the carbene, efforts were made to receive single crystalline material, which turned out to be challenging due to its high insolubility in virtually all commonly used organic solvents and very poor quality of the received crystals. Eventually, acetonitrile was recognized to dissolve up to 1 mg/ml of the compound and slow evaporation of saturated solutions yielded crystals of moderate quality. X-ray diffraction studies revealed the polymeric nature of the compound, although with a data quality that does not allow more than constitutional clarification.

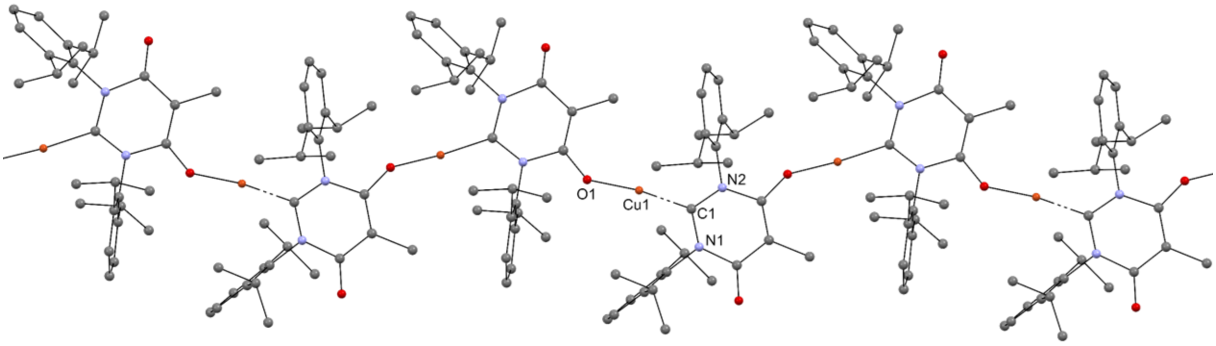

Figure 12. Expanded Ball-and-Stick representation of **[1·Cu]ₙ**. Hydrogen atoms are omitted for clarity.

Intentionally synthesizing **[1·Cu]ₙ** turned out to be straightforward. In a first approximation, the previously discussed compounds of the type **1·CuX^{M}** consist of monomers of **[1·Cu]ₙ** and an inorganic salt MX. According to Scheme 33, such compounds are already in an equilibrium with oligomeric material of **[1·Cu]ₙ** in solution and depending on the solubility of either of the two materials, this equilibrium might even be far on the side of the desired compound. Therefore, as shown in Scheme 35, concentrated solutions of **1·CuCl^{Li}** in acetonitrile were treated with a large excess of degassed water, precipitating **[1·Cu]ₙ** and bringing the lithium chloride into the aqueous phase. The product was received as a very fine, amorphous powder and was collected by centrifugation of the suspension with a yield of 60%. All side products are easily removed during the synthesis of **[1·Cu]ₙ**, due to its insolubility and remarkable stability towards moisture and air. Thus, it was washed with deionized water, methanol and diethyl ether, removing any organic and inorganic impurities.

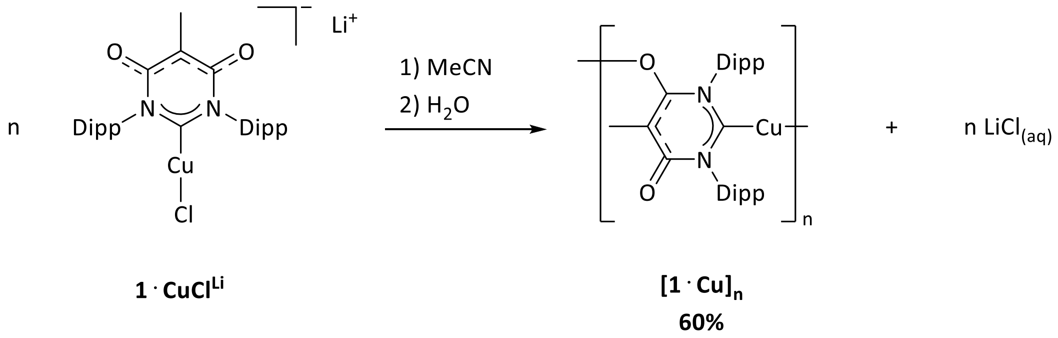

Scheme 35. Synthesis procedure for **[1·Cu]n**.

4.1.5 Preparation of heteroleptic complexes

As outlined above, the build-up of **[1·Cu]n** disturbed the successful formation of the desired heteroleptic Cu(I) complexes since it is removed from the equilibrium due to its high insolubility. Nevertheless, it concomitantly holds the invaluable advantage of containing only building blocks that are part of the final target complexes. Comparing the two incorporated coordinative bonds, the Cu-C^{Carbene} and the Cu-O^{Backbone} bond, the latter will be the weaker one according to the HSAB concept, since the rather soft Cu(I) ion will thermodynamically favour the likewise soft carbene carbon. Therefore, cleavage of the Cu-O bond might be possible by providing a more suitable ligand.

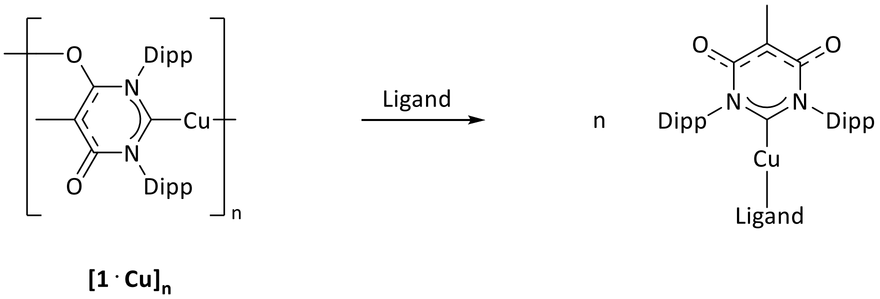

Scheme 36. Expected cleavage of **[1·Cu]n** by addition of a ligand more favourable for coordination to the copper ion.

In the following chapter, not only the general synthesis procedure for the heteroleptic copper(I) complexes containing the NHC **1** is described, but also which criteria led to the selection of the secondary ligands used for the cleavage of **[1·Cu]$_n$** and how the system behaves depending on the electronic and steric properties of these ligands.

4.1.5.1 Choice of secondary ligands

Firstly, common pnictogen ligands, i.e., pyridines and triphenylphosphine, were chosen as secondary ligands, since their behaviour in luminescent Cu(I) complexes is well investigated in the chemical literature.[86,89] As described above, a high dipole moment within a molecule is one important prerequisite for TADF to occur, since excited LLCT states are stabilized in such systems. Therefore, the choice of electron withdrawing ligands was of special importance, since pairing them with an electron rich, anionic carbene presumably achieves that. Rational design strategies provided by the department of theoretical chemistry focused the attention to either cyano- or acyl-groups as electron withdrawing substituents. Other common electron-withdrawing moieties, like nitro-groups, are not applicable due to non-radiative relaxation pathways that are opened. From a chemical point of view, cyano-substituted pyridines are not desirable, since they tend to form polymeric chains by coordination of the cyano-N to the Cu(I).[89] Therefore, acyl groups were chosen as electron withdrawing substituents.

Compound **[1·Cu]$_n$** was first subjected to preliminary solubility experiments to verify the hypothesis of cleaving the Cu-O$^{\text{Backbone}}$ bond in order to generate monomeric complexes. For this, it was suspended in the non-coordinating solvent dichloromethane, in which it is virtually insoluble, and one equivalent of ligand, related to the repeating unit of **[1·Cu]$_n$**, was added to it. Depending on the electronic and steric properties of the added ligands, a trend in reaction speed has been observed phenomenologically. Addition of one equivalent of ligand indeed led to dissolution of **[1·Cu]$_n$** within a few seconds, although only for the most electron-rich or chelating ligands, such as DMAP, triphenylphosphine, acridine or 2,2'-bipyridine. In case of 2,6-lutidine, addition of one equivalent does eventually dissolve **[1·Cu]$_n$** but several minutes are required to do so. Decreasing the electron donating ability of the pyridines further, full dissolution was not observed by addition of 1 equivalent anymore.

Here, an excess is needed in order to guarantee full conversion, which ranges from 10 equivalents in case of pyridine up to 50 equivalents for 4-formylpyridine. For extremely electron-poor ligands, such as pentafluoropyridine, no dissolution was observed regardless of the added excess, which indicates that it cannot compete with the coordination of the backbone oxygen of the carbene anymore. A chemical discussion for this behaviour is given in chapter 4.2.

Table 1. Molar equivalents needed to fully dissolve **[1·Cu]$_n$** in dichloromethane for some pyridines.

Ligand	**Equivalents needed**
Pentafluoropyridine	no complex formation
4-Formylpyridine	50
4-Acetylpyridine	30
2-Acetylpyridine	20
Pyridine	10
2,6-Lutidine	1
Acridine	1
DMAP	1
2,2'-Bipyridine	1

The behaviour of **[1·Cu]$_n$** towards ligand addition in solution allowed for a straightforward and highly versatile synthesis procedure. A variety of ligands are able to cleave the polymer under formation of monomeric complexes. For electron-rich ligands, even one equivalent is sufficient to generate a pure solution of the respective complex and, apart from solvent removal, no further manipulation is needed to obtain the pure material. For ligands that only fully cleave the polymer after addition of an excess, the solid was washed with diethyl ether, removing the excess ligand without harming the compound's integrity.

Besides pyridine derivatives, also more unconventional compounds have been screened for their ability to cleave **[1·Cu]$_n$** under formation of monomeric complexes. In 2020, *Nolan* has investigated the ligand properties of seleno ureas towards coinage metals.[109] Due to the close relation to carbene chemistry, some representatives of this class of compounds have been screened in their ability to cleave **[1·Cu]$_n$** into monomeric complexes. Indeed, successful coordination could be achieved for small and electron rich seleno ureas, which are shown in Scheme 37.

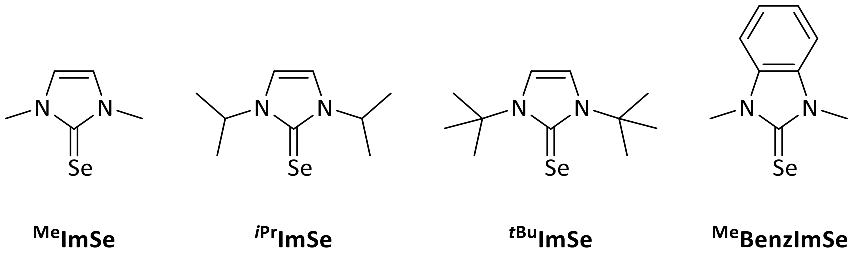

Scheme 37. Seleno ureas able to cleave **[1·Cu]$_n$** under concomitant formation of monomeric complexes.

4.1.5.2 Stoichiometric control

Accompanying the need for an excess of ligand in case of electron poor pyridines, the stoichiometry of the obtained complexes cannot be controlled by the amount of ligand added. This implies, that for pyridine, 4-formyl pyridine or 4-acetyl pyridine, the respective complexes can only be obtained in their trigonal form, a linear complex with only one molecule of pyridine coordinated to the copper cannot be synthesized under the given conditions.

Nevertheless, stoichiometric control is possible by other means. Steric hindrance of the secondary ligand, as it is provided by 2,6-lutidine, acridine or triphenylphosphine, only allows the mono-coordination to the copper, giving rise to linear complexes. Furthermore, regardless of its small size, the highly electron rich DMAP also coordinates only once to the copper. Presumably, the already strongly donating carbene results in an electronic mismatch between **1·Cu·DMAP** and a second DMAP molecule.[102] Even for a large excess of ligand, the trigonal representative was never obtained and no indication of its formation was found.

In order to obtain a linear representative of the pnictogen-based complexes, which incorporates an electron-poor pyridine, the synthesis of the 2,6-lutidine derivative with a formyl group in 4-position was envisaged. This molecule has previously been described, although with more complicated synthesis procedures.[110,111,112] In the present work, a simplified approach was realized.

As depicted in Scheme 38, 4-bromo-2,6-lutidine was subjected to a bromine-lithium exchange at -80 °C with *n*-butyl lithium in dry tetrahydrofuran. The resulting 4-lithio-2,6-lutidine was then reacted with dry dimethyl formamide. Protic work-up and recondensation into a flask cooled with liquid nitrogen results in a pale-yellow oil with a yield of 70%. The chemical shifts of its ^{1}H-NMR signals are identical to the ones reported in the original publication.

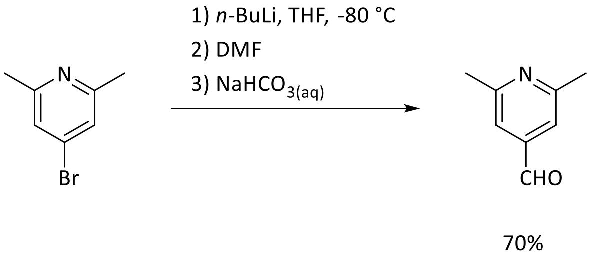

Scheme 38. Reaction cascade towards 4-formyl-2,6-lutidine.

For the chalcogen-based ligands, an unintuitive trend in stoichiometry was observed. The molecular structures, which are discussed in detail in a later chapter, reveal that **1·Cu·MeImSe** incorporates one urea ligand, while **1·Cu·MeBenzImSe** contains two ligands. This behaviour follows the trend found for the pnictogen based ligands. The methylbenzimidazole seleno urea can be considered a less electron rich ligand, since the underlying carbene has a ^{77}Se-NMR-shift of 80 ppm[113], while the methylimidazole seleno urea has one of -6 ppm[114], both in acetone-d_6. Even though this difference is small, considering the vast spectroscopic range of the ^{77}Se-NMR-spectroscopy, it might be an explanation for the sterically unintuitive coordination of two benzimidazole seleno urea ligands. The ligand without benz-annelation might be slightly more electron-rich, leading to a situation comparable to the one found in **1·Cu·DMAP**, where the donor strength of the DMAP prevents its second coordination.

4.2 Chemical and structural properties

The synthesized complexes possess interesting properties that make them stand out from related compounds. This chapter first summarizes their behaviour in solution, whereafter the data obtained from SC-XRD are presented and discussed.

4.2.1 The complexes in solution

The situation of the herein presented copper(I) complexes of the anionic carbene **1** in solution is intricate. Due to the ability of the carbenes' backbone to compete for the coordination to the copper ion with the secondary ligands, an equilibrium is operative, whose position depends strongly on the nature of said ligand. The trend found in the preliminary tests of the solubility of **[1·Cu]$_n$** in dependence on ligand addition is resembled, once a solid compound is resolubilized in an organic solvent. Complexes containing electron-poor pyridines instantaneously dissociate upon dissolution, leaving behind a white precipitate of **[1·Cu]$_n$**. Accordingly, the NMR spectrum after removal of the precipitate shows only very weak signals of the carbene moiety, whereas very strong signals of the respective ligand are found. This is the reason, why for some of the complexes presented herein, analytical investigation requiring solutions, such as MS or NMR studies, could not be performed. More information is given in the experimental section. Scheme 39 depicts the equilibrium that is assumed in solution.

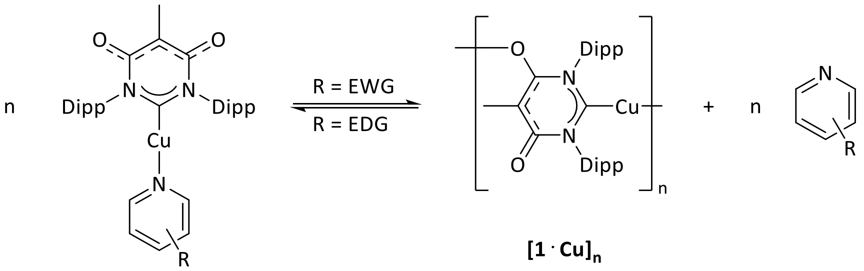

Scheme 39. Assumed equilibrium in solution, shown exemplary for a linear complex. For trigonal complexes, the same situation occurs.

In order to confirm the presence of oligomeric material of **[1·Cu]$_n$**, MALDI-TOF MS experiments were carried out on all presented complexes that do not instantaneously dissociate in solution. This type of mass spectrometry has the advantage that the matrix is typically made of small aromatic carboxylic acids and therefore contains no strongly coordinating molecules, as it is the case in ESI-MS, which employs a mixture of acetonitrile and water.[115] Such a medium might distort the results due to additional coordination to the copper. Indeed, the MALDI-TOF mass spectra indicate the presence of oligomeric material for all probed compounds. Even for **1·Cu·DMAP**, one of the most stable compounds in solution of the presented series, **[1·Cu]$_n$** was detected up to a chain length of n = 5. The relative abundances of each oligomer follow a negative exponential trend. Whether this resembles the actual distribution in solution cannot be deduced, since it might also be due to instability of larger oligomers under the measurement conditions. The MALDI-TOF mass spectrum of **1·Cu·DMAP** is shown in Figure 13 together with a close-up of each oligomer's measured and predicted isotope pattern.

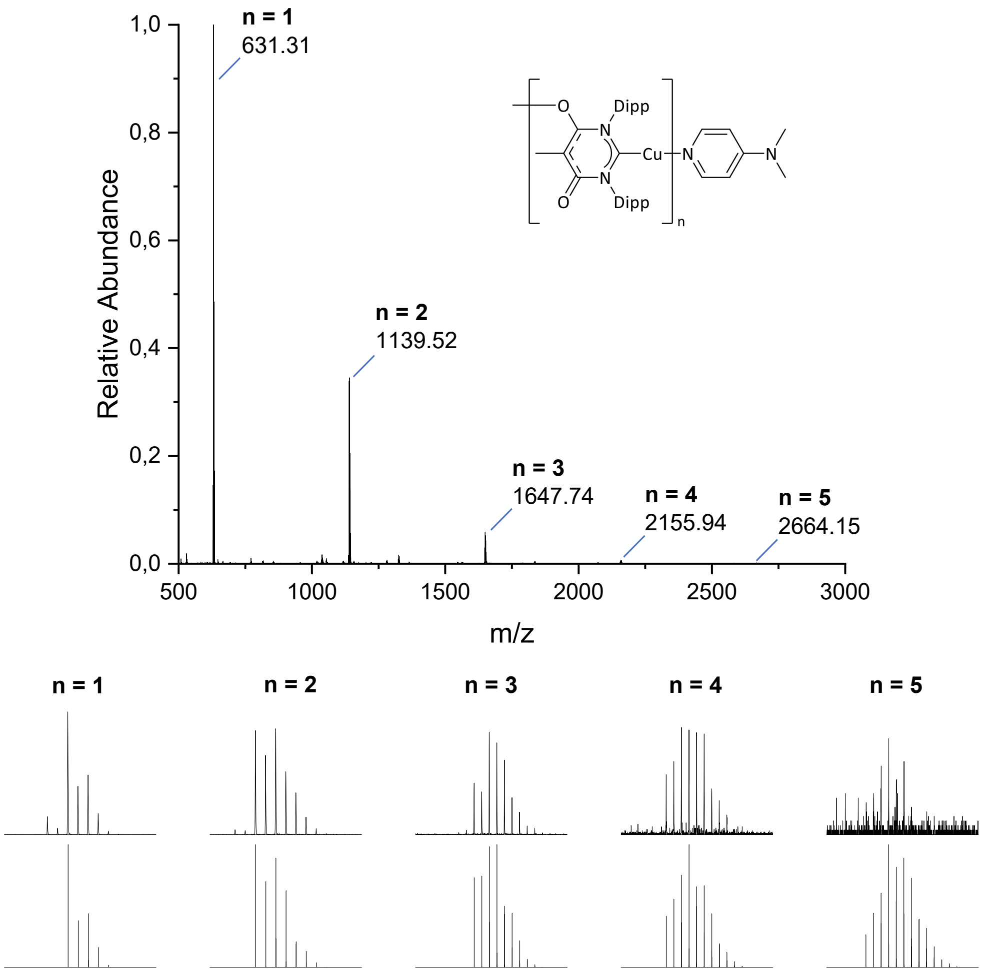

Figure 13. MALDI-TOF mass spectrum of compound **1·Cu·DMAP** in dichloromethane (top) and a close-up on each visible oligomer (middle) with the respective predicted isotope pattern (bottom).

That this process is indeed an equilibrium was confirmed by NMR studies conducted on **1·Cu·DMAP**. Its ^{1}H-NMR-spectrum, in contrast to its mass spectrum, does not suggest that several different species are present in solution. This indicates an equilibrium between the present species, which is fast on the NMR timescale. Also, with addition of more equivalents of DMAP, the NMR spectrum does not show more than one signal set for it. Instead, the broad singlet, which comprises the merged signals of the aromatic DMAP protons, is divided into its separate components, with their positions approaching those of free DMAP, as depicted in Figure 14. The peaks marked in red and blue experience the largest influence on the DMAP concentration. Therefore, a fast equilibrium between the monomeric complex and short oligomers of **[1·Cu]$_n$** end-capped by DMAP is verified.

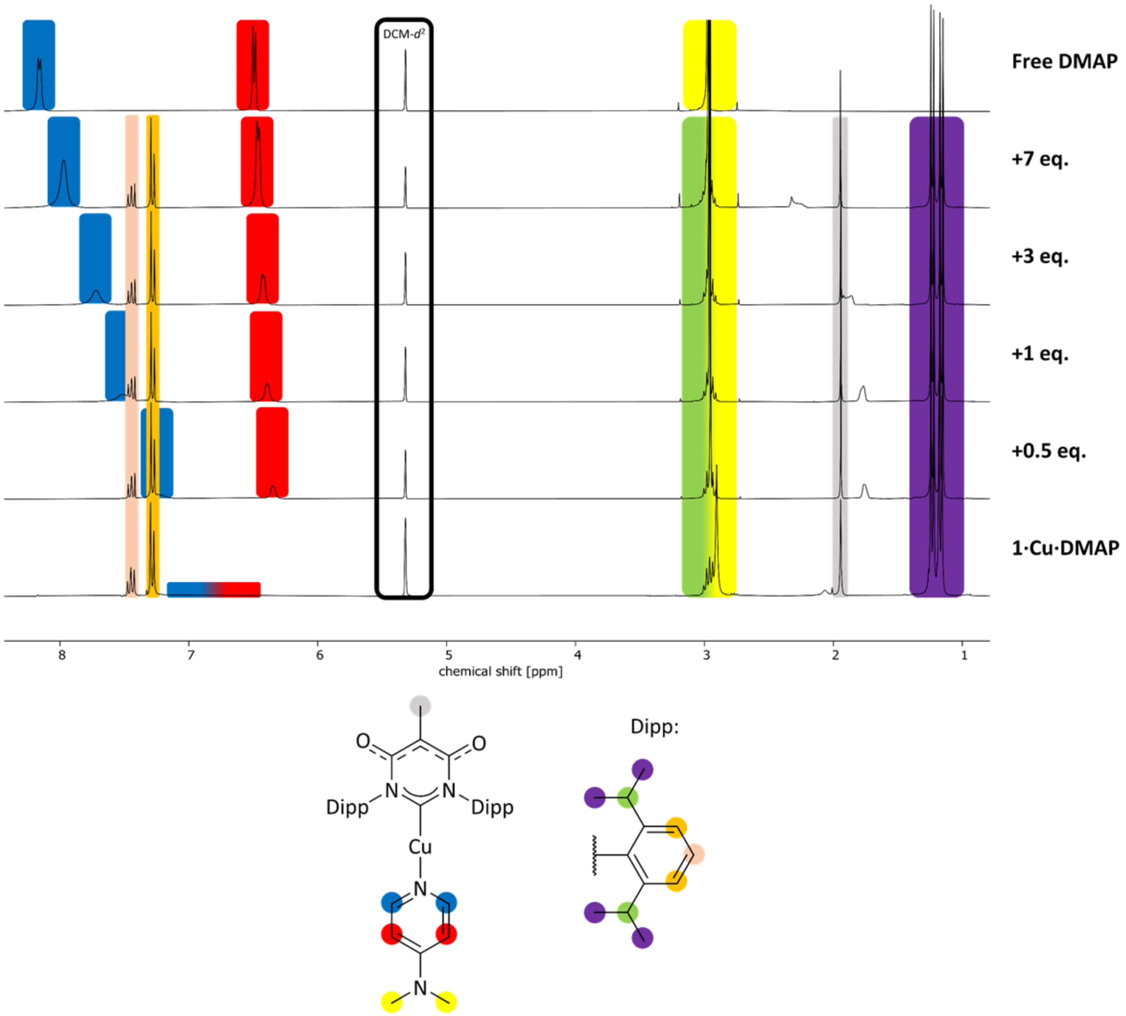

Figure 14. ^{1}H-NMR-spectrum of **1·Cu·DMAP** in deuterated dichloromethane (bottom), spectra of the same sample with further equivalents of DMAP added and the spectrum of free DMAP under the same conditions (top).

A chemical understanding of these processes might be given by the electron donating capability of the involved secondary ligands, which is reduced by introducing electron-withdrawing substituents. In such cases, a bond formation between the electron rich carbene backbone oxygen atom and the copper(I) centre is favoured.

The weighting of the individual components in solution could not be quantified. It must be assumed that for all neutral copper(I) complexes of the type **1·Cu·L**, a different situation will be encountered, inevitably leading to the conclusion that their identity cannot be guaranteed, once solubilized.

4.2.2 The complexes in solid state

Opposed to the instability in solution, the **1·Cu·L** type complexes show a remarkable stability in solid state towards oxidation or other disintegration by air. Storage under non-inert conditions is possible without jeopardizing the compounds' chemical or physical integrity.

As indicated in previous chapters, the structures of all compounds presented herein were determined by X-ray diffraction experiments. Obtaining suitable single crystalline material was possible from solutions containing an excess of secondary ligand, in order to keep the equilibrium (Scheme 39) on the side of the monomeric complexes. An overview of the molecular structures of the pnictogen-based complexes is given in Figure 15 and selected geometrical data are compiled in Table 2.

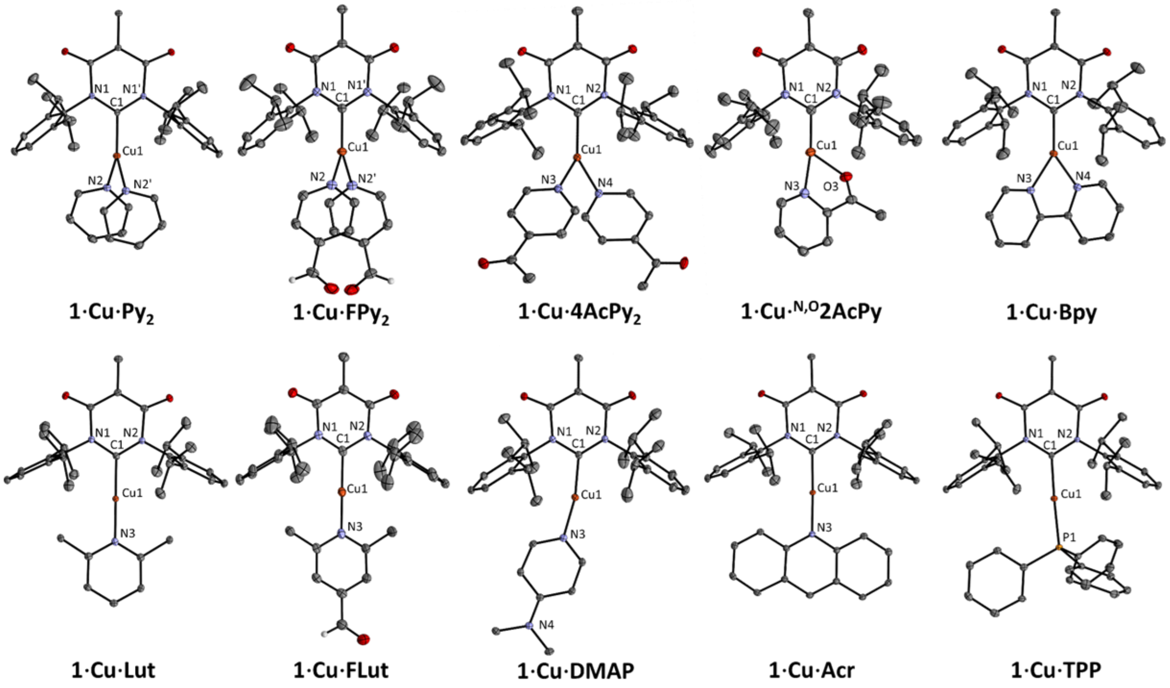

1·Cu·Py$_2$ **1·Cu·FPy$_2$** **1·Cu·4AcPy$_2$** **1·Cu·^{N,O}2AcPy** **1·Cu·Bpy**

1·Cu·Lut **1·Cu·FLut** **1·Cu·DMAP** **1·Cu·Acr** **1·Cu·TPP**

Figure 15. Thermal ellipsoid plots of the pnictogen based complexes. Thermal ellipsoids are drawn at the 30% probability level. Hydrogen atoms (except formyl protons) and solvent molecules (if present) are omitted for clarity.

Table 2. Selected distances and angles for the pnictogen-based complexes.

	NHC-Cu [Å]	L-Cu [Å]	Angle sum at copper (trig.)	Angle at copper (lin.)	Torsion NHC-pyridine
1·Cu·Py$_2$	1.910(2)	2.046(1)	360.0(1)	-	-
1·Cu·FPy$_2$	1.897(2)	2.031(1)	360.0(1)	-	-
1·Cu·4AcPy$_2$	1.927(3)	2.054(1)[a]	360.0(2)	-	-
1·Cu·^{N,O}2AcPy	1.889(3)	1.937(2)	357.3(2)	-	30.73(8)
1·Cu·Bpy	1.905(2)	2.046(2)[a]	360.0(1)	-	40.03(4)
1·Cu·Lut	1.918(3)	1.925(2)[b]	-	178.58(9)[b]	10.07(7)[b]
1·Cu·FLut	1.901(4)	1.926(3)	-	178.53(1)	10.54(1)
1·Cu·DMAP	1.894(2)	1.880(2)	-	169.01(9)	0(0)
1·Cu·Acr	1.905(1)	1.918(1)	-	177.91(6)	11.73(5)
1·Cu·TPP	1.927(4)	2.203(1)	-	177.36(1)	-

[a] Average between the two coordinating pyridine moieties.

[b] Average between the two independent molecules in the asymmetric unit.

These compounds fall well into place with similar substances. The coordination bond lengths and angles are in line with previously reported, similar systems in almost all cases.[86,92] Deviations worth discussing are found in two compounds. Firstly, the angle at the copper atom in **1·Cu·DMAP** is unusually small in comparison to the other linear representatives. An explanation for this is found by examining the surrounding of the individual molecules. As seen in Figure 16, a close intermolecular contact between one oxygen atom of the NHC backbone and one aromatic proton of a DMAP ligand is formed, pushing the DMAP ligand further away from the ideal linear coordination angle of 180°. A deeper view into this unusual structural motif is given later in this chapter.

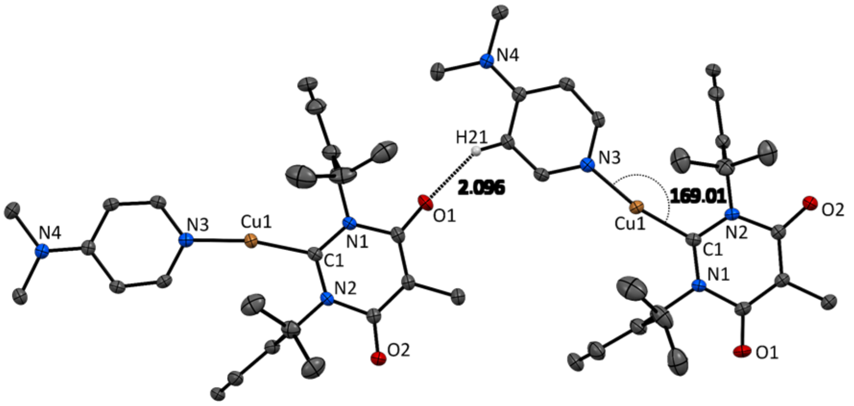

Figure 16. Thermal ellipsoid plot of **1·Cu·DMAP** indicating a close contact between two molecules. Thermal ellipsoids are drawn at the 50% probability level. Hydrogen atoms, except the one engaging in the contact, are omitted for clarity.

Secondly, in **1·Cu·^{N,O}2AcPy**, the angle sum at the copper atom deviates the most from ideal planarity with 360°, as found in the other trigonal complexes. On closer inspection, a distorted T-shape is found, rather than a trigonal geometry. In this molecule, the oxygen atom of the acetyl pyridine engages in coordination, although forming an inferior bond to the copper with 2.272(2) Å, compared to the main interaction with the nitrogen, measuring 1.937(2) Å (Figure 17).

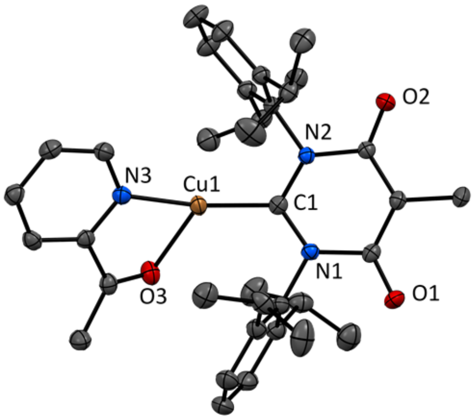

Figure 17. Thermal ellipsoid plot of **1·Cu· ^{N,O}2AcPy** showing the chelating coordination mode of the pyridine. Thermal ellipsoids are drawn at the 50% probability level. Hydrogen atoms are omitted for clarity.

Moreover, two molecular structures of the chalcogen based complexes were clarified via SC-XRD. Their molecular structures are given in Figure 18, important distances and angles are summarized in Table 3.

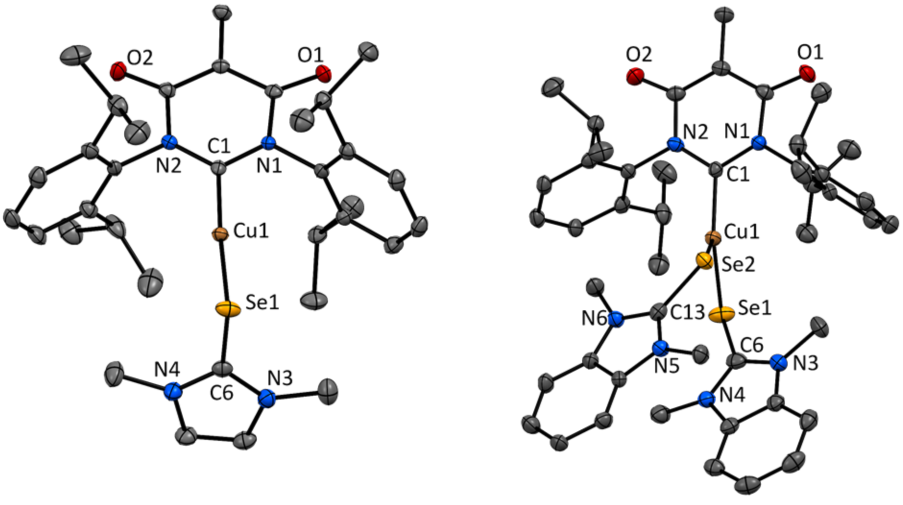

1·Cu·^{Me}ImSe **1·Cu·^{Me}BenzImSe**

Figure 18. Thermal ellipsoid plots of the chalcogen based complexes. Thermal ellipsoids are drawn at the 50% probability level. Hydrogen atoms and solvent molecules (if present) are omitted for clarity.

Table 3. Selected distances and angles for the chalcogen based complexes.

	NHC-Cu [Å]	**Se-Cu [Å]**	**Angle sum at copper (trig.)**	**Angle at copper (lin.)**	**Angle Cu-Se-C^{Se}**
1·Cu·^{Me}ImSe	1.918(3)	2.270(1)	-	175.15(8)	96.15(8)
1·Cu·^{Me}BenzIm	1.951(3)	2.425(1)	359.93(2)	-	105.35(1)[a]

[a] Average between the two coordinating urea moieties.

The most striking difference to the pnictogen based complexes is the angle of coordination of the selenium atom compared to the one of the nitrogen atom in the pyridine derivatives. While the lone pair engaged in bonding to the copper in a pyridine is of sp^2-character, a p-orbital of the selenium takes this place in the seleno ureas. This leads to a more acute angle between the mean planes of the NHC and the urea, approaching almost 90° in **1·Cu·MeImSe**. In the trigonal representative **1·Cu·^{Me}BenzImSe$_2$**, this angle is widened, possibly due to repulsion between the two urea moieties. A comparison is shown in Figure 19.

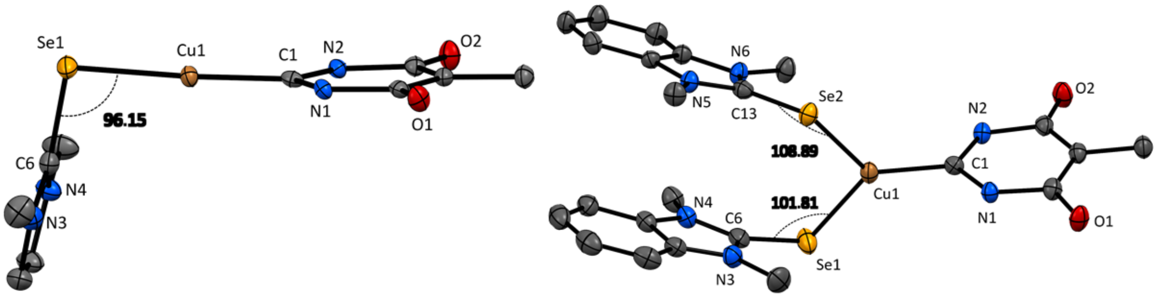

Figure 19. Thermal ellipsoid plot of **1·Cu·^{Me}ImSe** (left) and **1·Cu·^{Me}BenzImSe$_2$** (right), indicating the acute angle at the selenium atoms. Thermal ellipsoids are drawn at the 50% probability level. Hydrogen atoms, Dipp substituents and solvents (if present) are omitted for clarity.

4.2.2.1 Crystal packing

A close look at the crystal environments of the pnictogen-based complexes reveals that all of them exhibit intermolecular interactions, as was already seen in Figure 16 for **1·Cu·DMAP**. Surprisingly, these contacts do not only form between molecular moieties expected to have high charge densities, such as the carbenes' anionic backbone or incorporated polar solvents like methanol. Also, usually non-polar moieties like the protons or π-systems of aromatic rings engage in contact formation. Such an interaction is exemplary shown on the crystal packing of **1·Cu·FPy$_2$** in Figure 20.

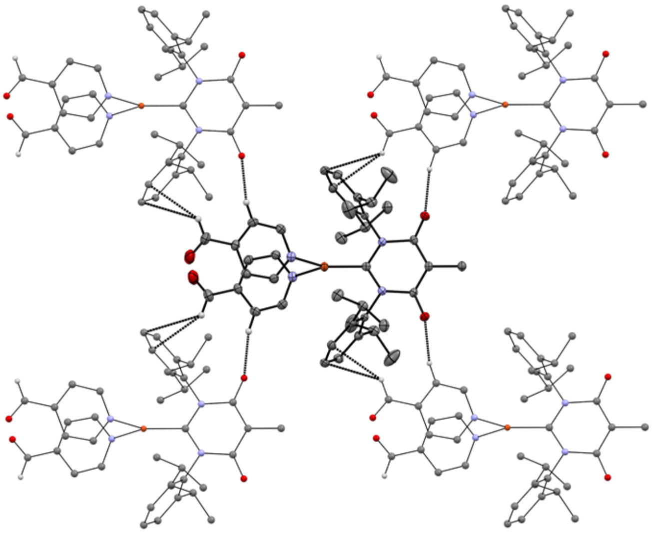

Figure 20. Compound **1·Cu·FPy$_2$** with the four closest surrounding molecules contacting it.

The main bond between the molecules is formed between the H atoms in *meta* position pointing outward and the backbone-oxygen of the carbene with a distance of 2.133 Å. This is continued in two dimensions, leading to a sheet-like structure, with no contacts between one sheet and the next. Additionally, an inferior interaction is observed in the form of a two-electron-three-centre contact involving the formyl protons and two aromatic carbon atoms of a Dipp-substituent. In the formed triangle, one bond is shorter than the other with 2.745 Å and 2.843 Å, respectively.

Surprisingly, compound **1·Cu·Lut** does not only show interactions between the backbone-oxygen and the aromatic protons of its 2,6-lutidine ligand, also the aliphatic methyl protons engage in such, which are even less Lewis-acidic. Moreover, the contacts to the aliphatic protons are even shorter than to the aromatic ones, with 2.377 Å and 2.346 Å, respectively.

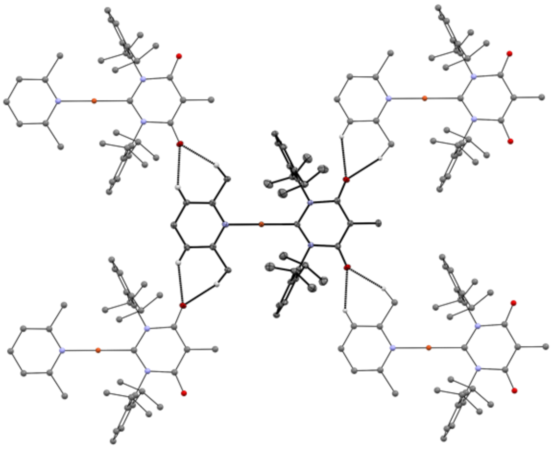

Figure 21. Compound **1·Cu·Lut** with the four closest surrounding molecules contacting it.

Such interactions might be considered as non-classical hydrogen bonds, although this has to be evaluated carefully.[116] A simple comparison of the contact lengths to the combined van-der-Waals radii of the involved atoms[117] is not always sufficient, since *Van-der-Waals* radii are no reliably defined constants. There are various approaches for their determination and they can be strongly influenced by the molecular environment. Moreover, intermolecular contacts within crystal cages are generally consequences of Coulomb attractions, which are strongest between positions of particularly high charge densities and not necessarily specific atoms, as was seen in the inferior interaction between the Dipp rings and the formyl protons in **1·Cu·4FP**. Any comparison to van-der-Waals radii is not beneficial in that case.[118]

The chalcogen-based complexes do not form such pronounced intermolecular contacts, being an indication that these complexes possess lower dipole moments. Only in compound **1·Cu·$^{\mathrm{Me}}$ImSe**, an intermolecular interaction of 2.970 Å between the selenium atom and the isopropyl proton of a neighbouring molecules' Dipp substituent is observed (Figure 22). Given that the combined Van der Waals radii of selenium and hydrogen is 3 Å, this interaction is barely below that distance, indicating that it is rather insignificant.

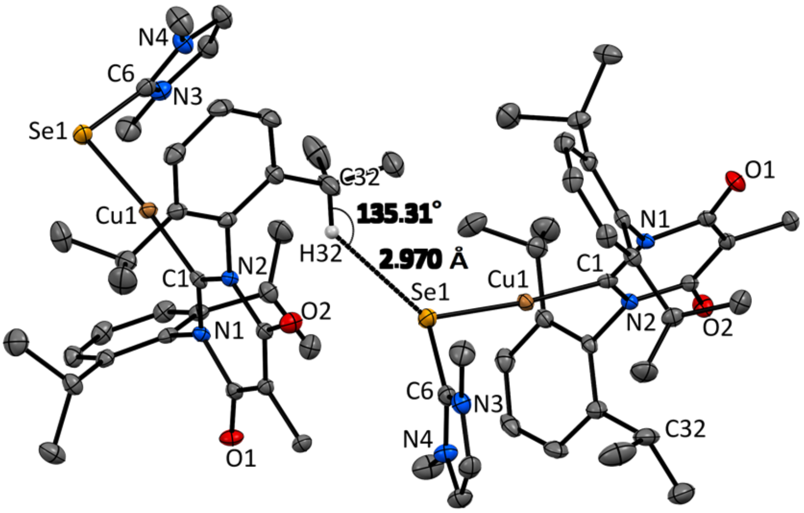

Figure 22. Compound **1·Cu·^{Me}ImSe** with its intermolecular contact between the selenium atom and one isopropyl proton.

A similar interaction was already reported in the literature, where intramolecular contacts within seleno ureas and aliphatic protons of their substituents in the range of 2.5 Å were observed. *Bertrand* showed in this work that such interactions also affect the ^{77}Se-NMR shift and therefore result in unexpected π-acceptor quantifications.[119] In this compound though, this should not play a role, since this intermolecular contact will most likely only persist in solid state, not in solution.

For compound **1·Cu·FPy$_2$**, the thermal lability of its intermolecular contacts was examined. This was achieved by measuring its PXRD histogram before and after heating the native sample to 50 °C for 30 min. A comparison to the simulated pattern, obtained from the SC-XRD data, not only revealed a high phase purity of the native compound but also an irreversible phase transition after the heating process. Nevertheless, its crystallinity was retained, since sharp peaks are still visible and the baseline-offset, an indicator for amorphous portions, did not increase significantly.

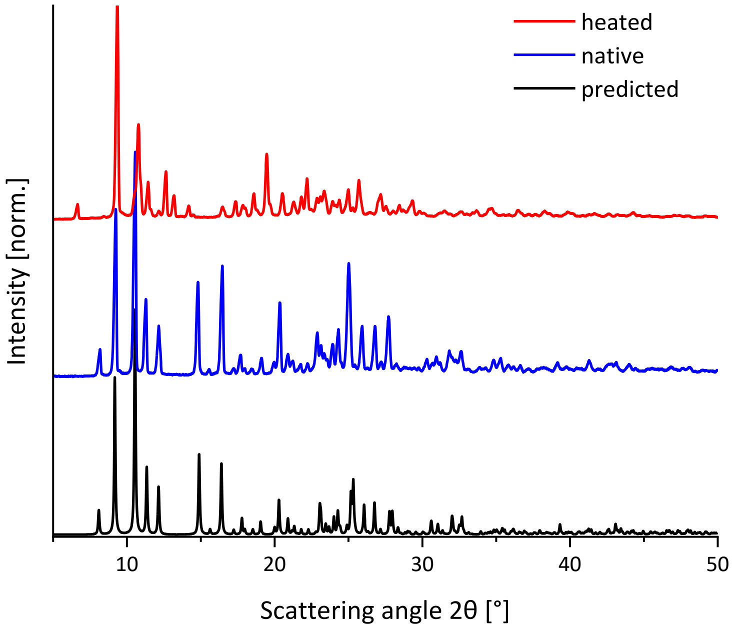

Figure 23. PXRD patterns of the same powder samples of **1·Cu·FPy$_2$** directly after synthesis (blue) and after heating it to 50 °C for 30 min (red), acquired with Cu K$_\alpha$ radiation, in comparison to the simulated pattern obtained from the SC-XRD data (black).

The observed molecular structures already allow preliminary expectations to be made in view of the photophysical properties. The presented pnictogen complexes are designed like donor-acceptor-conjugates with the carbene being the donating and the pyridines the accepting unit, allowing for LLCT excitations to be the lowest excited states. The thereby generated strong intra-molecular charge separations, i.e., high dipole moments of the complexes, are illustrated by their tendency to form intermolecular contacts. Most importantly, the contacts are shortest in the compounds incorporating electron-poor pyridines, such as in **1·Cu·FPy$_2$** and **1·Cu·FLut**, which feature contact lengths between the NHC's backbone oxygen atom and one aromatic pyridine proton of 2.13 Å and 2.15 Å compared to their counterparts **1·Cu·Py$_2$** and **1·Cu·Lut** with 2.47 Å and 2.35 Å, respectively. This is a good indicator for those complexes allowing delocalized excitations, i.e., LLCT transitions from the electron-rich carbene to the electron-poor pyridine moieties, which is a prerequisite for the intended TADF property. Furthermore, a greater torsion between donor and acceptor lowers their orbital overlap, thereby also stabilizing CT-states *(vide supra)*. With this in mind, the trigonal complexes should have lower lying CT-states than their respective linear counterparts, since in the trigonal complexes a rotation of the pyridines away from collinearity with the carbene is enforced. In conclusion, due to the trigonal nature and presumably high dipole moment of **1·Cu·FPy$_2$**, this compound seems to be the most promising candidate for TADF, followed by **1·Cu·FLut**.

4.3 Photophysical investigations

Based on rational design obtained from quantum chemical calculations, a selection of four related compounds from the family of pnictogen based complexes has been chosen for an in-depth analysis of their photophysical properties, in particular towards possible TADF behaviour. These compounds are shown in Scheme 40.

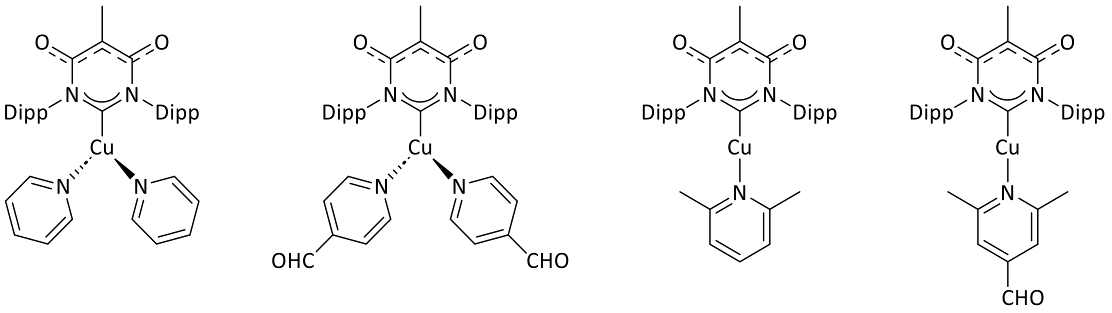

1·Cu·Py$_2$ **1·Cu·FPy$_2$** **1·Cu·Lut** **1·Cu·FLut**

Scheme 40. The compounds in focus for the photophysical analysis.

This selection combines several interesting properties. There are two trigonal-planar and two linear complexes, and each of these subgroups consists of one representative with an electron-deficient and one with an electron-rich pyridine derivative. Therefore, the aim of this work is not only to examine each compound individually, but to gain an understanding of the properties arising from these factors by comparison.

4.3.1 Sample preparation

Due to the unique chemical and physical properties characterizing these molecules, the sample preparation was not straightforward. The compounds are not only heat sensitive but also undergo an equilibrium in solution, as presented in chapter 4.2. This made less common techniques necessary, which are described in the following chapter.

4.3.1.1 In solution

Optical measurements on solubilized compounds represent the most common technique of photophysical assessments. Most importantly, absorption experiments are virtually exclusively conducted in solutions since uniformity and homogeneity of the sample is crucial. Nevertheless, the intricate equilibria that are present in solutions of the copper(I) complexes lead to chaotic compositions of their solutions, which is why they could not be employed as is. Therefore, stabilization with an excess of the respective ligand was intended, since according to the principle of *Le Châtelier*, this drives the equilibrium shown in Scheme 39 towards the desired complex and keeps the concentration of any oligomeric material of **[1·Cu]$_n$** to a minimum.

4.3.1.2 In solid state

Besides the assessment of solutions, the employment of solid-state material for optical measurements is another common approach. The easy sample preparation and lack of any environmental factors stand out compared to solutions, ensuring reproducible results. However, one major drawback is that classical absorption measurements are inapplicable on powdered samples. Furthermore, the setup needs to be suitable for solid samples, since they usually require special sample holders, that do not fit into a common cuvette-based spectrometer. In the course of this work, a new approach for solid-state measurements was developed, that makes use of powdered samples suspended in an inert medium. This had the invaluable advantage, that both problems were addressed simultaneously. Firstly, such suspensions can be employed in standard cuvettes and secondly, even real absorption measurements can be carried out on diluted suspensions. In the course of the following chapter, this approach is discussed in detail.

4.3.2 Absorption, excitation and reflectance

4.3.2.1 Absorption

UV-Vis absorption measurements were employed not only to get an understanding of the excited states that are in reach of photon energies in the ultraviolet and visible wavelength range, but also to shed light on the chemical dynamics, that are present in solution.

As depicted in Figure 24, the absorption spectrum of **1·Cu·Py$_2$** in dichloromethane shows a low-energetic band at 340 nm with an extinction coefficient of 2725 $M^{-1}cm^{-1}$, corresponding to the transition into the S_1 state of the molecule, that is later responsible for the emission. Its position is in good accordance with the theoretical absorption spectrum, suggesting that this transition is a local excitation on the carbene, which is the lowest excited state of **1·Cu·Py$_2$**.[120] Increased photon energy accesses a shoulder at 250 nm that is part of the very strong absorption of the aromatic moieties like the pyridine and the Dipp-substituents.[121] For **1·Cu·Lut**, the situation is very similar. The lowest excited state is accessible at a slightly lower energy, with a band at 330 nm and an extinction coefficient of 2720 $M^{-1}cm^{-1}$. Similarly, it corresponds to a local excitation on the carbene, simultaneously the S_1 state of the molecule. The absorption of the aromatic moieties again begins in a shoulder at 250 nm, increasing strongly with degreasing wavelength from there on. **1·Cu·FPy$_2$** and **1·Cu·FLut** could not be subjected to simple UV-Vis absorption experiments in solution, since the chemical equilibrium is almost fully on the side of **[1·Cu]$_n$** and free pyridine. As stated above, these compounds were stabilized by an excess of their respective pyridine ligand. The absolute concentration of the ligand in dichloromethane was matched in the reference cuvette, thereby subtracting any signal stemming from it. The S_1 band of **1·Cu·FPy$_2$** is much broader than for the previously discussed compounds, resembling its yellow colour at ambient light. The maximum lies at 350 nm with an extinction coefficient of 3195 $M^{-1}cm^{-1}$. Yet for **1·Cu·FLut**, the absorption spectrum is again very similar to the first two compounds, with its S_1 band peaking at 344 nm and an extinction coefficient of 2672 $M^{-1}cm^{-1}$. Both lowest excited states are of LLCT type between the carbene and the pyridine moieties.

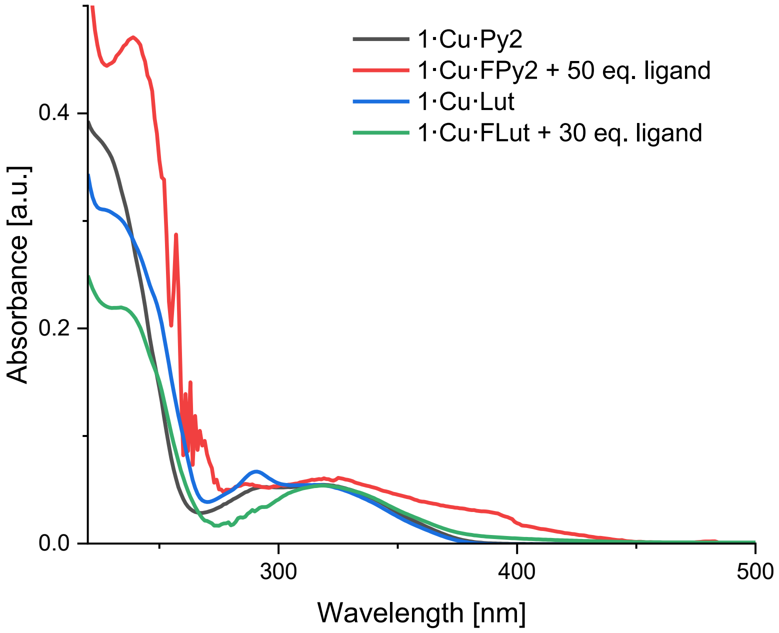

Figure 24. UV-Vis absorption spectra of **1·Cu·Py₂** (20.0 µM) and **1·Cu·Lut** (20.0 µM) as well as **1·Cu·FPy₂** (19.0 µM) and **1·Cu·FLut** (20.1 µM), both stabilized with an excess of ligand, all in dichloromethane. Note, that the artifacts in the spectra of the stabilized compounds arise from the referencing to the ligand solution, which absorb strongly in these regions. Nevertheless, the S_1 bands are not affected by that.

To assess, if this equilibrium is also present in solutions of the other compounds, that do not visibly dissociate, the parent compound **1·Cu·Py₂** was subjected to a titration experiment. To a diluted solution of it in acetonitrile, equivalents of pyridine were titrated. If an equilibrium is present, the absorption bands corresponding to the complex should intensify, as more ligand is shifting it to that side. Indeed, this effect is visible as shown by Figure 25. The band that corresponds to the S_1 state becomes gradually larger with increased pyridine concentration, even though free pyridine does not show absorbance in this wavelength range.

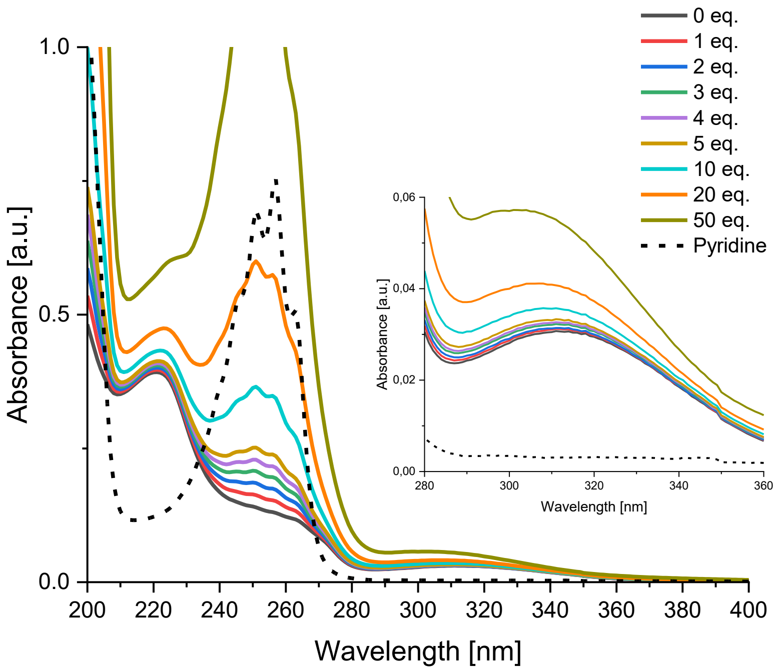

Figure 25. UV-Vis absorption spectra of **1·Cu·Py₂** in acetonitrile at c = 27.0 µM, in dependence on added pyridine. The inset shows a close-up on the S_1 band, indicating an increase of its intensity and therefore a shift of the equilibrium towards **1·Cu·Py₂**.

In solid state, meaningful absorption experiments are more difficult to achieve, since solids, especially powders, normally do not provide a homogenous light path. Many more effects become significant, such as diffuse reflection, scattering or interference. Two methods are generally established in the literature, one is absorption of thin films, the other employs suspensions. In the context of this project, thin films are not applicable, since they are prepared from evaporating solutions or by vapour deposition. Moreover, ensuring reproducibility is challenging, since the layer thickness is not easily controlled. Therefore, absorption in suspension was applied. According to *Duysens*, the *Lambert-Beer* law does apply to suspensions, provided they are diluted.[122] In that case, the absorption data need to be corrected only for scattering. This effect is inversely proportional to the fourth power of the wavelength, meaning that the light scattering has a much higher impact in the blue spectral region, according to Equation 3.

$$I_{Scatter} = \frac{C_1}{\lambda^4} + C_2 \qquad \text{Equation 3}$$

To compensate this effect, the individual scattering function, with C_1 and C_2, needs to be determined by two points within a region of no sample absorption (Figure 26).

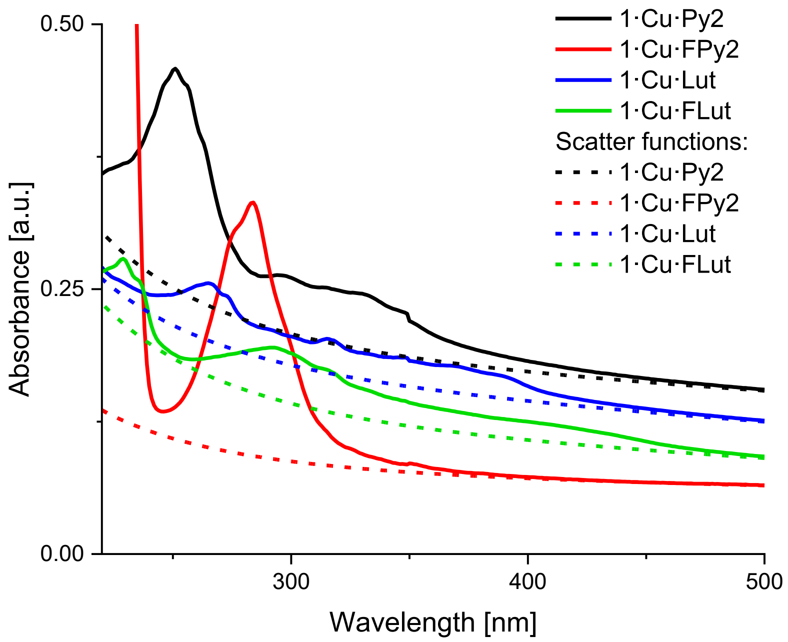

Figure 26. Uncorrected absorption data of **1·Cu·Py$_2$** (86.91 µM), **1·Cu·FPy$_2$** (102.29 µM), **1·Cu·Lut** (129.80 µM) and **1·Cu·FLut** (145.37 µM) in cyclohexane with their respective scatter function.

Subtraction of the scatter function from the original data creates the corrected baseline. The results and a comparison to the expected absorption according to calculations are shown in Figure 27.

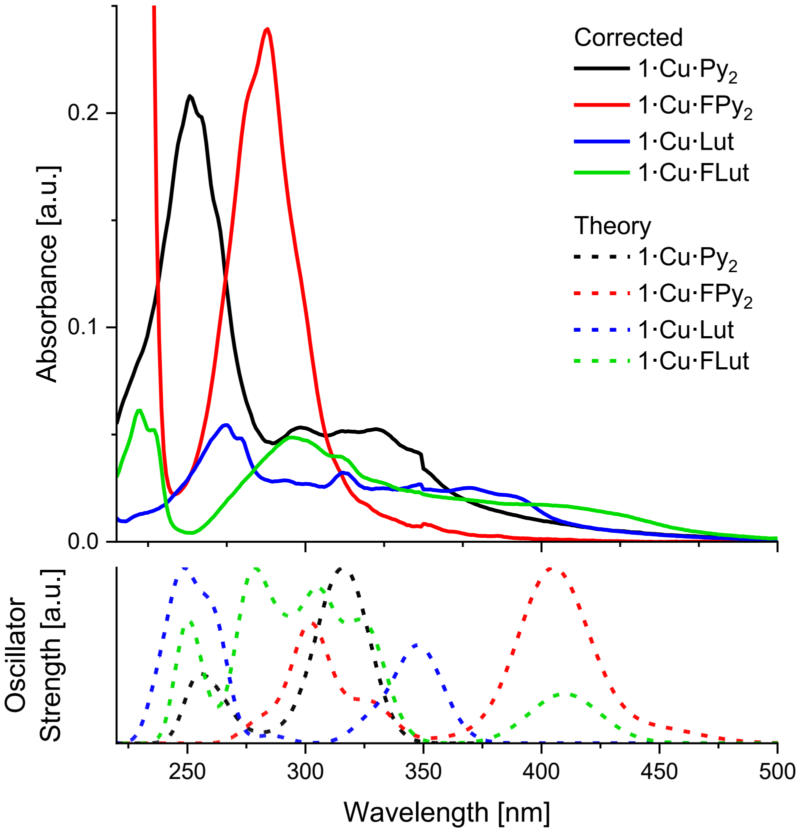

Figure 27. Absorption spectra of **1·Cu·Py₂** (86.91 µM), **1·Cu·FPy₂** (102.29 µM), **1·Cu·Lut** (129.80 µM) and **1·Cu·FLut** (145.37 µM) after correction for scattering (top) and expected absorption bands according to theoretical calculations (bottom).

The positions of the absorption bands are in good accordance with both the absorption data in solution as well as theoretical calculations for all compounds except **1·Cu·FPy₂**. Here, the most intense absorption band is expected at 405 nm, which is missing entirely in the experimental data. A possible explanation for this is that even in suspension, **1·Cu·FPy₂** has a strong tendency to dissociate, especially at such low sample concentrations. The extinction coefficients were not calculated from these experiments, since a concentration for suspensions is not meaningfully defined.

4.3.2.2 Excitation

Excitation experiments are another way of revealing excited state behaviour that, in first approximation, yield similar results compared to absorption data. Nevertheless, the technique relies on the emission of the sample and not its absorption, which in this context excluded solutions, since they are not emissive at room temperature. For excitation spectra, a fixed detection wavelength is defined and the sample is excited over a wavelength range. In principle, excitation at an absorption maximum results in the brightest emission, provided the absorption maximum belongs to an emissive state. Therefore, the excitation band is generally closely related to the S_1 absorption band of an emissive molecule, if *Kasha's* rule is not violated.

Excitation spectra were recorded both of the powders and of cyclohexane suspensions for the four respective complexes. A comparison is given in Figure 28. In first approximation, in both cases the data lead to the same conclusion. The complexes substituted with electron-poor pyridines (**1·Cu·FPy$_2$** and **1·Cu·FLut**) show much broader excitation bands than their counterparts **1·Cu·Py$_2$** and **1·Cu·Lut**. Furthermore, their onset begins at higher wavelengths, being in accordance with the expectations according to calculations.

One important difference between the two approaches is the spectral resolution. The excitation in powdered samples yields rather featureless and broad bands, whereas the data obtained from diluted cyclohexane suspensions show much narrower bands, even resolving some of the underlying excited states, to which the bands belong. This is seen very well in **1·Cu·FPy$_2$** and **1·Cu·FLut**, whose excitation bands feature weak shoulders at higher wavelengths.

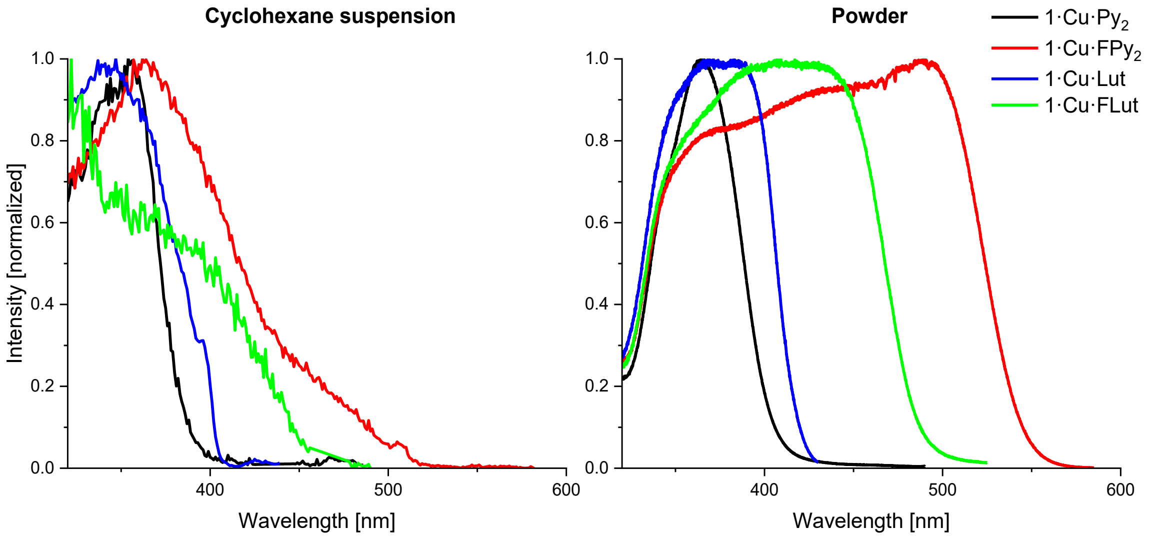

Figure 28. Excitation spectra of **1·Cu·Py₂** (λ_{Em} = 500 nm), **1·Cu·FPy₂** (λ_{Em} = 595 nm), **1·Cu·Lut** (λ_{Em} = 450 nm) and **1·Cu·FLut** (λ_{Em} = 540 nm) in cyclohexane suspension (left) and in solid state (right) at 298 K. The concentrations in cyclohexane are 86.91 µM, 102.29 µM, 129.80 µM and 145.37 µM, respectively. The Raman peak of the cyclohexane, produced by *anti-Stokes scattering*, is removed for clarity, if visible in the suspension measurements.

4.3.2.3 Diffuse Reflectance

Opposed to all other spectroscopic techniques discussed thus far, relying on light transmission through a material, diffuse reflection of light from a material represents yet another way of gathering excited state information. It should be noted, that diffuse reflectance spectroscopy is generally inferior to the classical transmission spectroscopy in many ways. Firstly, it requires a far more sophisticated, thus more expensive experimental setup and furthermore usually yields data with worse resolution and signal to noise ratios. Therefore, it is only a valid alternative, if transmission UV-Vis spectroscopy is not applicable.[123]

Experimentally, the powdered samples were placed into an integrating sphere (*Ulbricht Sphere*), ensuring that all diffusely reflected light is directed to the detector. The excitation source covers a range between 300 nm and 800 nm, with the detection wavelength always being equal to the excitation. This yields a radiation intensity I at any given wavelength, that is divided by the intensity of the incident beam I_0 at this wavelength, obtained from a blank measurement, finally resulting in the absolute remittance R_∞ according to Equation 4.

$$R_{\infty} = \frac{I}{I_0}$$ Equation 4

In order to obtain a data format that is comparable to UV-Vis transmission spectra, an empirical theory for diffuse reflectance, devised by *Kubelka* and *Munk* in 1931, is employed.[124] The absorbance in *Kubelka-Munk* units A_{KM} is attained from the absolute remittance R_{∞} according to Equation 5.

$$A_{KM} = \frac{(1 - R_{\infty})^2}{2R_{\infty}}$$ Equation 5

The results of this analysis are depicted in Figure 29. The inhomogeneous broadening is again limiting the spectral resolution, as it was the case for excitation spectra in solid state. Additionally, an inherent problem of this type of analysis limits the significance of the data at lower wavelengths, as the *Kubelka-Munk* theory is only valid in a range of the absolute remittance of $0.2 < R_{\infty} < 0.7$.[123]

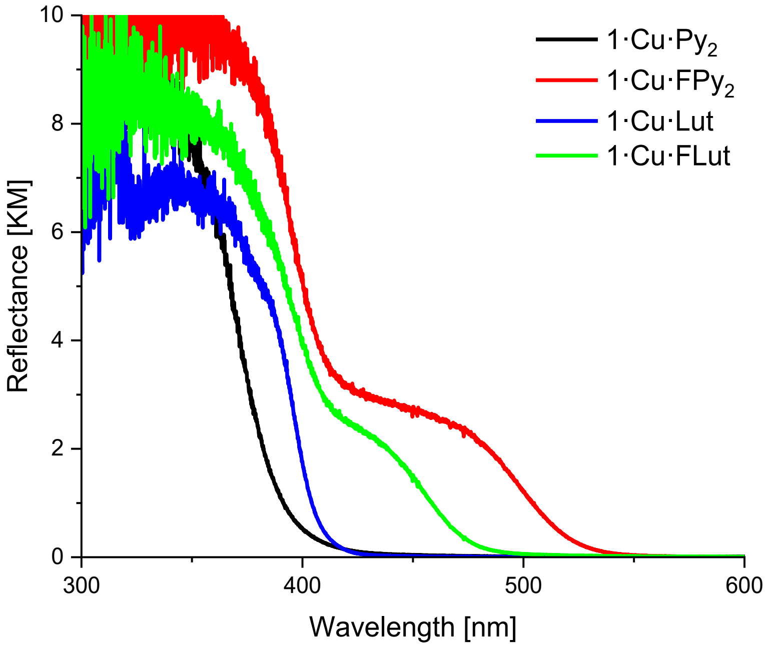

Figure 29. Diffuse reflectance spectra for **1·Cu·Py₂**, **1·Cu·FPy₂**, **1·Cu·Lut** and **1·Cu·FLut** in *Kubelka-Munk* units.

Due to these restrictions, the discussion of these data will be limited to the onset of the reflection. The complexes coordinated by electron-rich pyridines (**1·Cu·Py$_2$** and **1·Cu·Lut**) show the earliest onset of their reflection bands at 410 nm and 420 nm respectively, whereas the onset of reflection for the complexes with electron-poor pyridines (**1·Cu·FPy$_2$** and **1·Cu·FLut**) are visible at much higher wavelengths of 540 nm and 490 nm respectively. The trend follows the theoretically expected onset of the absorption very well. Moreover, the visible colour of the four complexes is well reproduced by the results.

4.3.3 Steady state spectroscopy

Meaningful emission spectra of the four compounds **1·Cu·Py$_2$**, **1·Cu·FPy$_2$**, **1·Cu·Lut** and **1·Cu·FLut** were obtained again from powdered samples as well as their cyclohexane suspensions. As discussed earlier, spectroscopy in solid state bears the advantage of not having any environmental factors possibly interfering with the sample's integrity, which is why these data are treated as standard for comparison in this context. The results of the solid-state emission spectroscopy are depicted in Figure 30.

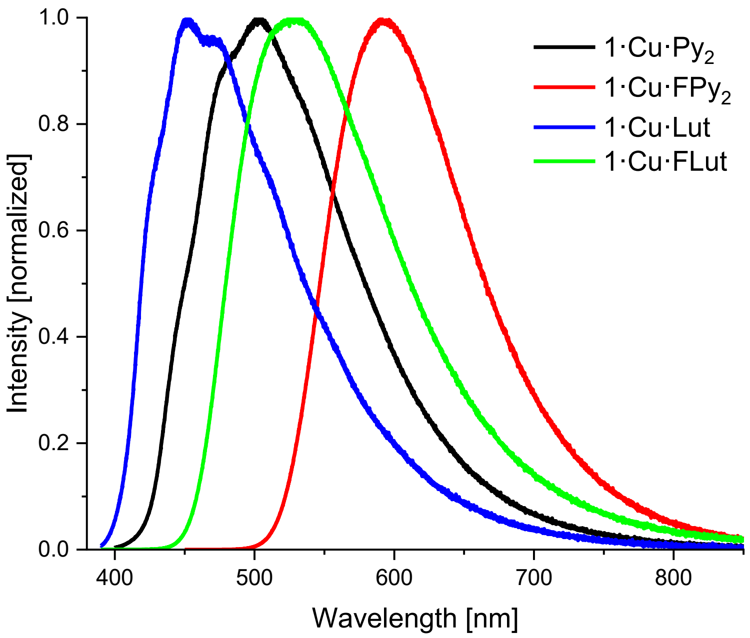

Figure 30. Steady-state emission spectra of **1·Cu·Py$_2$**, **1·Cu·FPy$_2$**, **1·Cu·Lut** and **1·Cu·FLut** obtained from powdered samples at λ_{Ex} = 375 nm and 298 K.

The steady state spectra of the analysed compounds span a range of roughly 140 nm, with **1·Cu·Lut** having its emission maximum at 451 nm in the blue region and **1·Cu·FPy₂** at 591 nm in the orange. **1·Cu·Py₂** has its maximum at 504 nm, **1·Cu·FLut** at 527 nm. The electron-accepting formyl groups shift the emission bathochromically, this trend is observed between **1·Cu·Lut** and **1·Cu·FLut** as well as **1·Cu·Py₂** and **1·Cu·FPy₂**. Among **1·Cu·Lut** and **1·Cu·Py₂**, the former exhibits a bluer emission than the latter due to both the alkyl-substitution in 2,6-position as well as the second pyridine ligand, presumably shifting the emission bathochromically.

Steady-state emission spectroscopy in cyclohexane suspensions resulted in reliable bands that nearly perfectly superimpose with their respective counterpart obtained from solid samples. The results and a comparison are given in Figure 31.

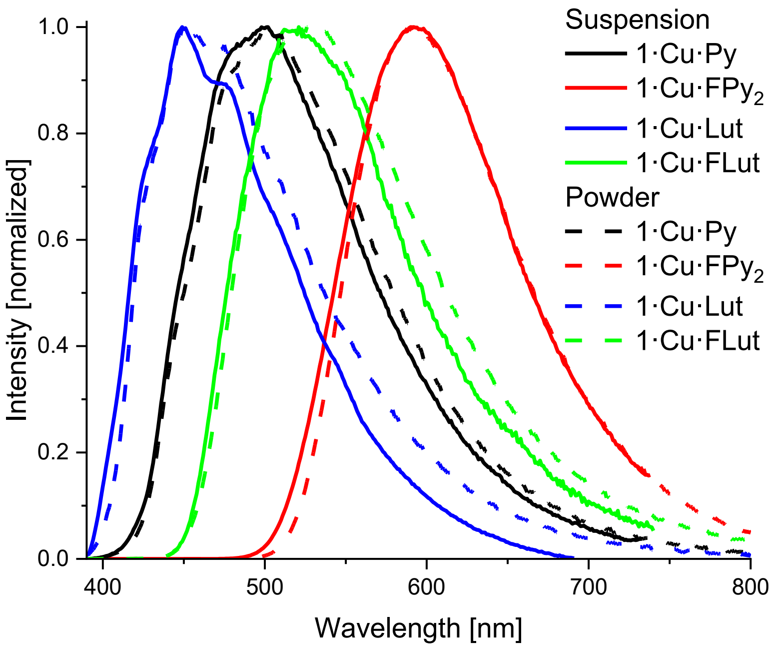

Figure 31. Steady-State emission spectra of **1·Cu·Py₂** (86.91 µM), **1·Cu·FPy₂** (102.29 µM), **1·Cu·Lut** (129.80 µM) and **1·Cu·FLut** (145.37 µM), obtained from cyclohexane suspension at λ_{Ex} = 375 nm and 298 K, superimposed with the respective counterpart from powdered samples.

4.3.3.1 Temperature dependence

The analysis of the temperature dependence of the steady-state emission is a first tool to assess possible TADF properties. As already outlined in 2.2.2.1, a spectral red shift upon cooling due to higher contribution of phosphorescence is to be expected, if TADF is operative. A first overview is given by Figure 32, which depicts the steady-state emission spectra of **1·Cu·Py₂**, **1·Cu·FPy₂**, **1·Cu·Lut** and **1·Cu·FLut** at 298 K and at 80 K.

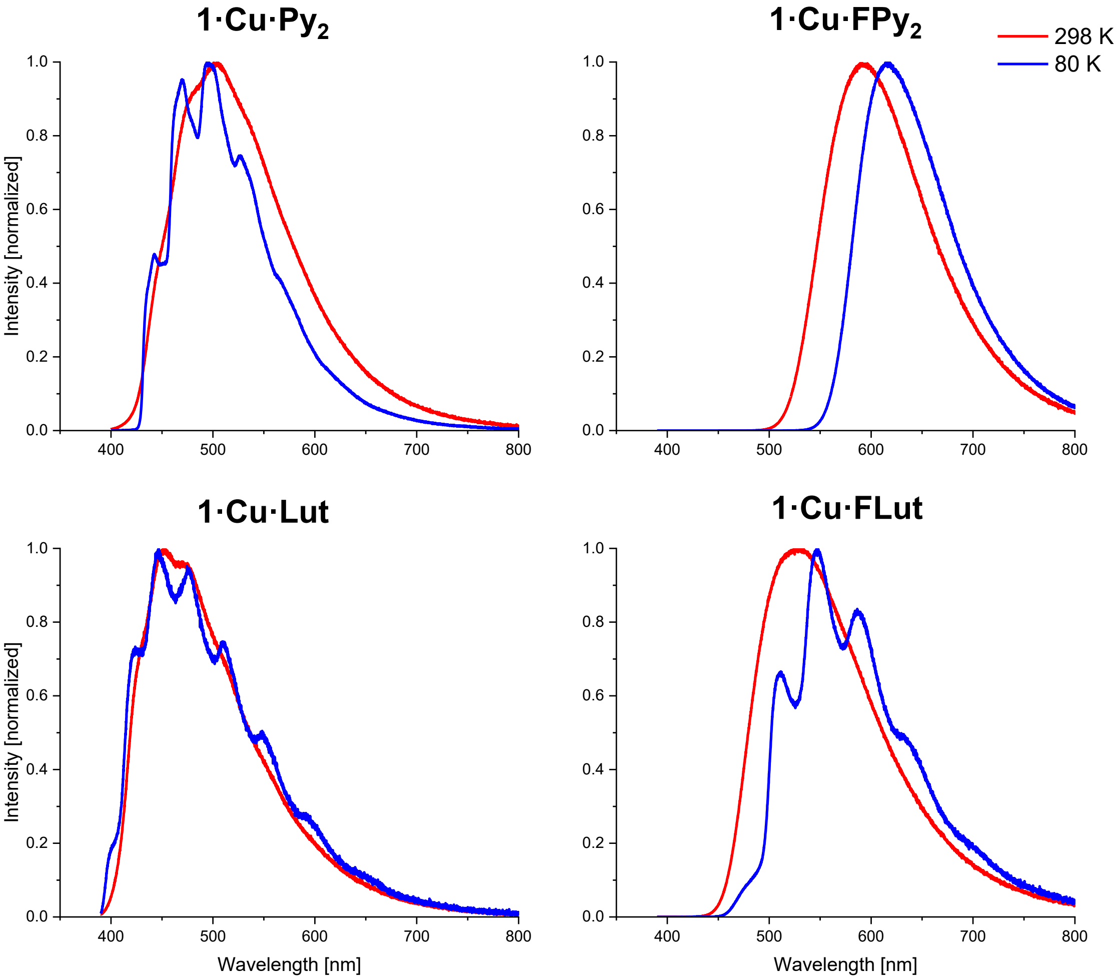

Figure 32. Steady-state emission spectra of **1·Cu·Py₂**, **1·Cu·FPy₂**, **1·Cu·Lut** and **1·Cu·FLut** at 298 K and 80 K, λ_{Ex} = 375 nm.

For the two compounds **1·Cu·Py₂** and **1·Cu·Lut**, only a weak spectral blueshift of 10 nm and 4 nm, respectively, was detected upon cooling. This phenomenon is possibly explained by rigidification of the emitters at 80 K, hampering their self-stabilization via rearrangement in the excited state. This hypothesis is supported by **1·Cu·Py$_2$** being more flexible due to its trigonal geometry, explaining its slightly larger blueshift upon rigidification. Nevertheless, for **1·Cu·FPy$_2$** and **1·Cu·FLut,** a substantial spectral red shift of 24 nm and 20 nm, respectively, is observed upon cooling, indicating an increased phosphorescence contribution. Assuming primarily S_1 emission in the high temperature case and T_1 emission in the low temperature case, the ΔE_{S1-T1} can be determined via the energetic distance of the emission maxima, which is 639 cm^{-1} (79 meV) for **1·Cu·FPy$_2$** and 758 cm^{-1} (93 meV) for **1·Cu·FLut**. These values are well below the threshold for efficient rISC of 200 meV.[125] It should be noted that this determination assumes that the systems reach the upper limit of their spectral shift at 298 K. No experiments have been conducted at higher temperatures, given the thermal lability of the complexes *(vide supra)* and the thereby caused uncertainties of spectral information at temperatures above ambient conditions.

Another observation that can be extracted from the presented data is the vibronic fine structure of the emission bands of **1·Cu·Py$_2$**, **1·Cu·Lut** and **1·Cu·FLut** at 80 K. Such a feature is generally an indication for a localized excitation, from which emission occurs. Transfer of the wavelength axis to wavenumbers, a determination of the local maxima's energetic distance reveals that they are strictly equidistant with an average distance of 1300 cm^{-1}. This energy is in good accordance with an aromatic C=N vibration and likely stems from a vibration of the carbene moiety.[126] This leads to the conclusion that the S_1 state of the aforementioned three compounds is a localized excitation on the carbene. Vice versa, the absence of such a vibronic progression in the emission of **1·Cu·FPy$_2$** at 80 K implies that the excited state is of delocalized nature, such as an LLCT transition. As discussed earlier, this is an important prerequisite for TADF to be operative, making **1·Cu·FPy$_2$** the most promising candidate for that.

In addition to these preliminary experiments, a more detailed temperature series was obtained from cyclohexane suspensions for **1·Cu·FPy$_2$** and **1·Cu·FLut**. For this, a diluted suspension was prepared in both cases and placed into a cryogenic cuvette inside a cryostat. The temperature was varied over a range from 60 K to 270 K, ensuring a solid cyclohexane matrix over the whole experiment, in order to prevent agglomeration or precipitation of the suspended sample. Figure 33 depicts the results of this experiment.

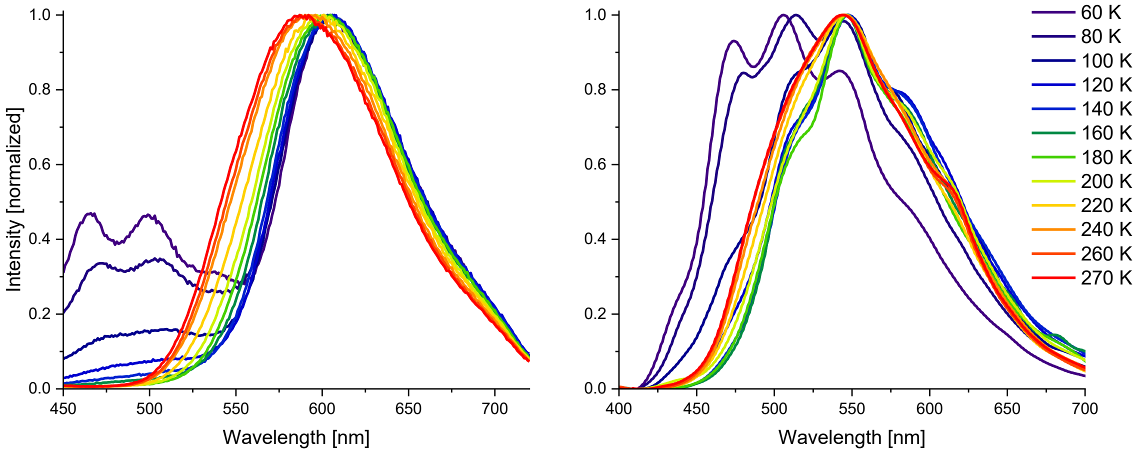

Figure 33. Steady-state emission spectra of **1·Cu·FPy₂** (left, c = 1.38 mM) and **1·Cu·FLut** (right, c = 5.17 mM) in cyclohexane suspension in a temperature range of 60 K – 270 K. λ_{Ex} = 375 nm. The spectra of **1·Cu·FLut** are shown after smoothing, since the raw data were very noisy. The original data and more information are given in chapter 6.3.

At first glance, the results are more intricate than expected. In comparison to the screening data obtained from powdered samples, depicted in Figure 32, the spectra in cyclohexane suspension show new emission bands that become visible at temperatures below 160 K in both cases, with emission maxima of 470 nm **(1·Cu·FPy₂)** and approximately 500 nm **(1·Cu·FLut)**.

For **1·Cu·FPy₂**, this second band is clearly separated from the compounds' emission band, whereas in **1·Cu·FLut**, admixing occurs between the two bands, given the more pronounced blue shift of **1·Cu·FLut** compared to **1·Cu·FPy₂**. The new bands' vibronic structure indicates a relation to the 4-formyl pyridine moieties coordinated to the Cu(I). Although it was first hypothesized that an emission of a higher lying excited state of **1·Cu·FPy₂** or **1·Cu·FLut**, localized on the coordinated pyridine moieties, was responsible for this emission, this could not be justified by theoretical calculations. In the end, steady-state emission spectroscopy on free 4-formyl pyridine in cyclohexane verified that this new emission band actually stems from free ligand in case of **1·Cu·FPy₂**, apparently leached from the microcrystals by the cyclohexane. At ambient temperatures, this ligand is non-emissive, cooling below 160 K activates its radiative relaxation, which was verified by steady-state emission spectroscopy. Figure 34 shows a comparison of the steady-state spectra of **1·Cu·FPy₂** and 4-formylpyridine, both at 60 K.

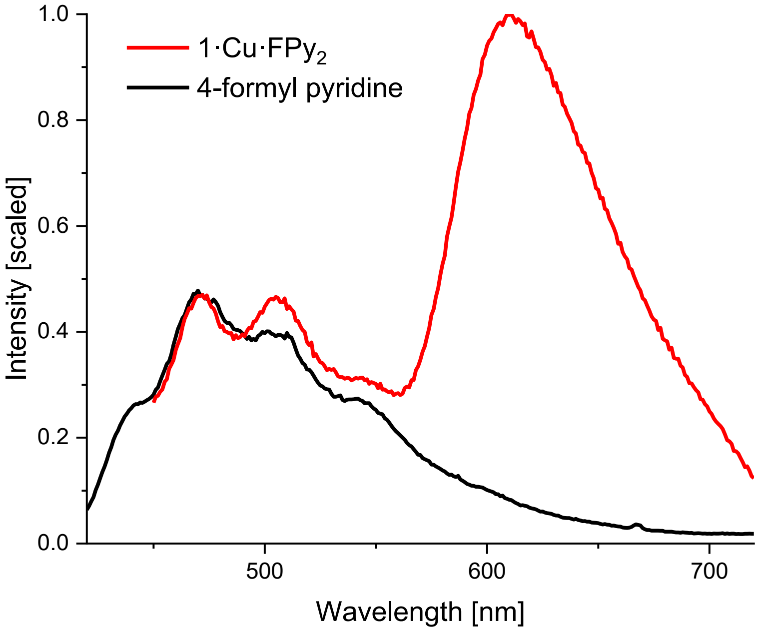

Figure 34. Comparison of the steady-state spectra of **1·Cu·FPy₂** in cyclohexane suspension (c = 1.38 mM) and 4-formyl pyridine in cyclohexane solution (c = 0.14 mM) at λ_{Ex} = 375 nm and 60 K. The emission spectrum of **1·Cu·FPy₂** is normalized to the compounds' emission maximum, whereas the emission of the free ligand is scaled to match the new emission band in **1·Cu·FPy₂**.

For **1·Cu·FLut**, such an easy comparison was not feasible, given the aforementioned admixing of the two emission bands. This problem will be addressed in a later chapter.

The better resolved emission bands of **1·Cu·FPy₂** allow a deeper analysis of the spectral information. The obtained data verify the gradual red shift of the emission band of **1·Cu·FPy₂** over the analysed temperature range. Moreover, the spectral shift is limited to the temperature range between 270 K and 180 K, further cooling does not lead to a red shift anymore, as depicted in Figure 35.

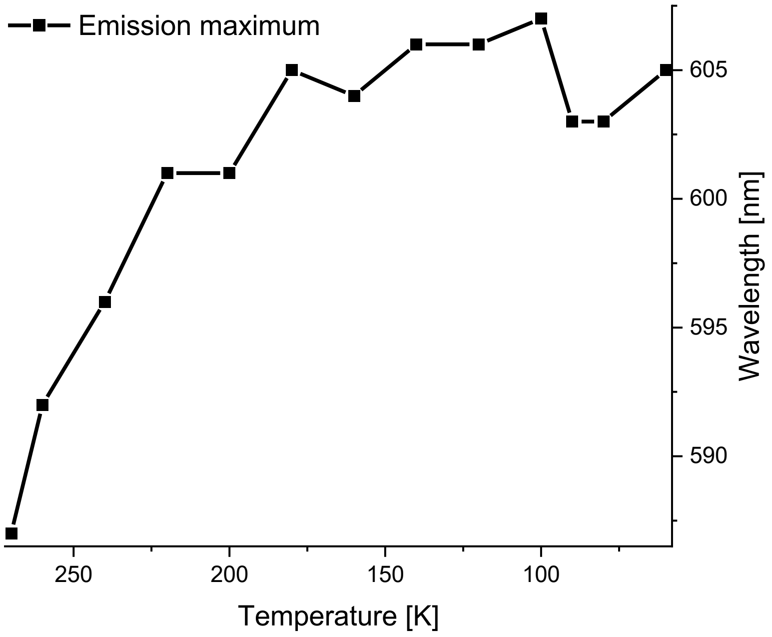

Figure 35. The emission maximum of compound **1·Cu·FPy₂** in dependence on the temperature.

Fortunately, the temperature range in which the spectral shift occurs does not coincide with the one, in which the free ligand is emissive. Therefore, Figure 36 depicts an updated version of the temperature dependent spectral shift, omitting the spectra obtained below 180 K.

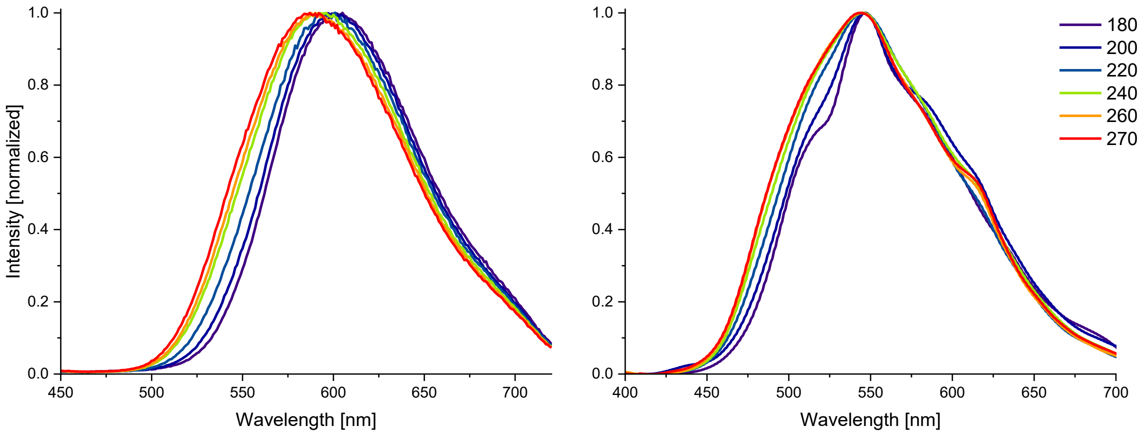

Figure 36. Steady-state emission spectra of **1·Cu·FPy₂** (left, c = 1.38 mM) and **1·Cu·FLut** (right, c = 5.17 mM) in cyclohexane suspension in a temperature range of 180 K – 270 K.

4.3.3.2 Dependence on energy fluence

In the context of TADF validation, excluding TTA is a necessary matter. Especially for the compounds studied in this work, TTA is a reasonable possibility for the emission pathway, since they are analysed in solid state. In light of the previously discussed crystal lattices of the complexes, indicating very close contact between the molecules, an energy transfer between two excited triplets next to each other is likely to be very efficient. Therefore, the room temperature steady state emission spectrum of **1·Cu·FPy₂** was obtained at varying energy fluences and the emission band was integrated. A plot of the band intensity versus the energy fluence H_e in a doubly logarithmic coordinate system enlightens the emission kinetics. H_e is derived by the laser power P_L, the area of the laser beam A_L and the irradiation time t_I. Since the emission band stretches over a range of 240 nm (480 nm – 720 nm), at an integration time of 1 s/nm, t_I amounts to 240 s. The irradiation area of the laser is fixed at $A_L = 1.77 \times 10^{-2}$ cm^2. For a given laser power P_L, the energy fluence is therefore obtained from Equation 6. Figure 37 depicts the results of this experiment.

$$H_e = \frac{P_L \cdot t_I}{A_L} \qquad \text{Equation 6}$$

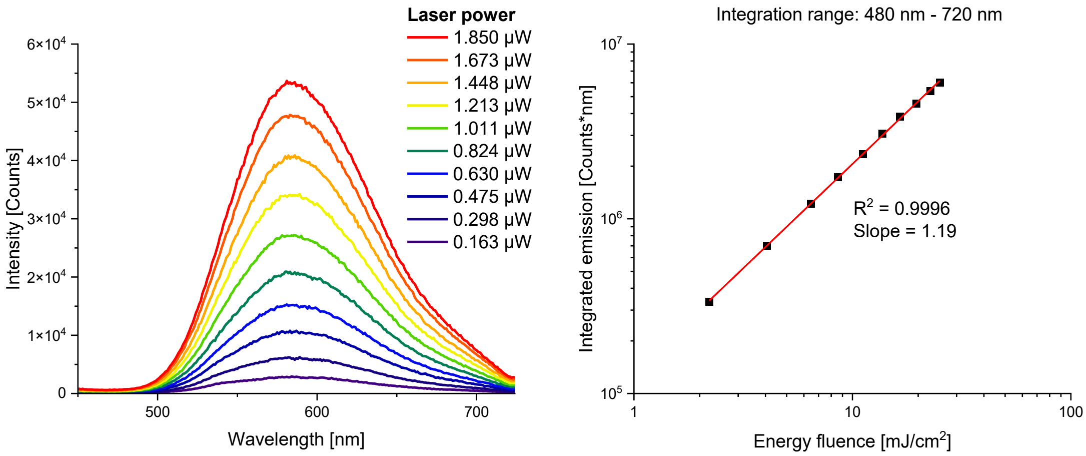

Figure 37. Steady-state emission spectra of **1·Cu·FPy₂** in cyclohexane suspension (c = 1.38 mM, λ_{Ex} = 375 nm) at various laser powers (left) and energy fluence versus integrated emission (right).

The linear dependence between emission intensity and energy fluence with a slope close to 1 highlights the strict first order kinetic of the underlying mechanism.[73] TTA is hereby excluded in the analysed excitation power range. Given the conditions of this experiment, this is an expected outcome for several reasons. Firstly, the setup for *time correlated single photon counting* (TCSPC), which was used to gain these data, is designed for low laser powers, typically in the range of microwatts[127], while TTA requires much higher powers to be efficient. Furthermore, the rigid crystal environment holding the molecules in very close proximity might indeed improve TTA between two triplet states next to each other *(vide supra)*, nevertheless, it disables the diffusion control of TTA, since the molecules are not able to move independently. Therefore, TTA would most likely not be temperature dependant under these circumstances, since this temperature dependence is a consequence of diffusion being faster at high temperature.

4.3.3.3 Photoluminescence quantum yields

The efficiency of the emission was determined as absolute photoluminescence quantum yield (^{Abs}PLQY) employing an integrating sphere loaded with the powdered samples. The quantum yield in general is the ratio of absorbed photons during excitation to the emitted photons during relaxation. It is a measure of how efficient the energy uptake is converted to the desired emission and can to a certain degree be translated to the situation in an OLED, where the excitation is carried out electrically.

During the measurement, the samples **1·Cu·Py$_2$**, **1·Cu·FPy$_2$**, **1·Cu·Lut** and **1·Cu·FLut** were irradiated with a 350 nm laser inside an *Ulbricht sphere*, and a steady-state emission spectrum was recorded, including both the excitation band of the laser and the sample emission. Additionally, a blank spectrum without sample was recorded in the same spectral interval prior to the measurements. Figure 38 depicts the experimental quantities that were extracted from these measurements.

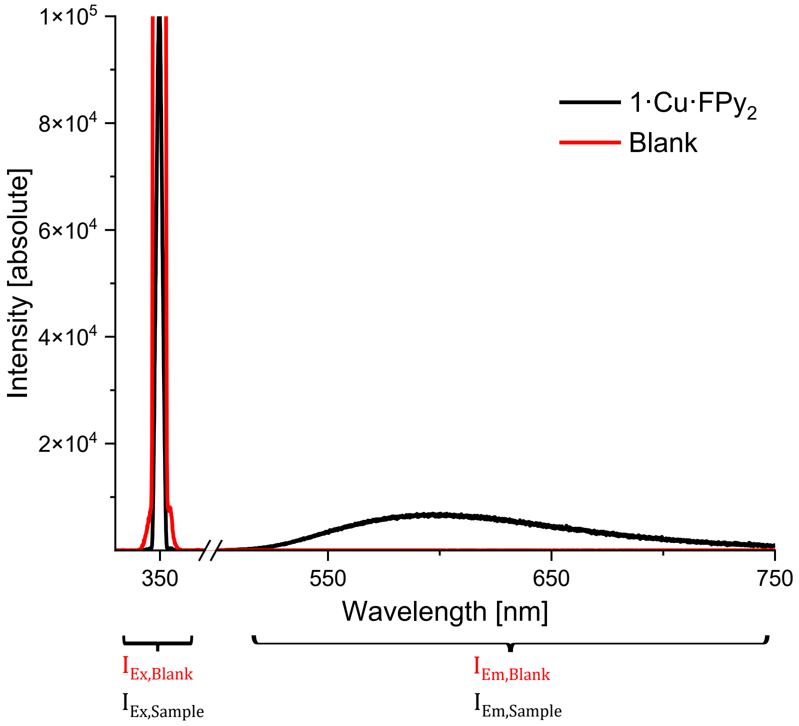

Figure 38. Exemplary measurement for the ^{Abs}PLQY on compound **1·Cu·FPy$_2$** versus the blank spectrum at λ_{Ex} = 350 nm and 298 K. The wavelength region between 370 nm and 500 nm and the intensity region above 10^5 (residual blank excitation band) are omitted for clarity. The integrated band intensities used for the ^{Abs}PLQY determination are highlighted.

The ratio of the intensities of the excitation band in the blank and the sample spectrum yields the absolute absorption Abs$_{350}$ of the samples at 350 nm, according to Equation 7. It turns out that for all four compounds, more than 90% of excitation photons were absorbed.

$$Abs_{350} = \frac{I_{Ex,Sample}}{I_{Ex,Blank}} \qquad \text{Equation 7}$$

The difference of the excitation band intensities in blank and sample spectrum in ratio to the difference of the emission band intensities in blank and sample spectrum is the ^{Abs}PLQY, according to Equation 8. For the four given compounds, the highest ^{Abs}PLQY was observed for **1·Cu·FPy$_2$** with 13%, followed by **1·Cu·Lut**, **1·Cu·Py$_2$** and **1·Cu·FLut** with 4%, 2% and 1% respectively.

$$^{Abs}\mathrm{PLQY} = \frac{I_{Em,Sample} - I_{Em,Blank}}{I_{Ex,Blank} - I_{Ex,Sample}}$$ Equation 8

Table 4. Absolute absorption and ^{Abs}PLQY of **1·Cu·Py$_2$**, **1·Cu·FPy$_2$**, **1·Cu·Lut** and **1·Cu·FLut**.

Compound	Absolute absorption$_{350}$ [%]	^{Abs}PLQY $_{350}$ [%]
1·Cu·Py$_2$	94	2
1·Cu·FPy$_2$	95	13
1·Cu·Lut	93	4
1·Cu·FLut	94	1

The remarkable subjective brightness of the compounds in contrast to their comparably low ^{Abs}PLQY can be understood by the efficient photon absorption of over 90% in all four cases. Although the compounds do not emit efficiently, the initial high photon uptake still results in subjectively bright emission.

4.3.4 Time resolved spectroscopy

The following chapter will discuss the time frames, in which the emission of **1·Cu·Py$_2$**, **1·Cu·FPy$_2$**, **1·Cu·Lut** and **1·Cu·FLut** occurs. The time-resolved emission data of the powdered samples will be discussed first. The compounds were placed onto quartz dishes into an external illumination cell, which is connected to the excitation source and the detector via optical fibre cables. Figure 39 depicts the emission decay curves of the four compounds at 298 K.

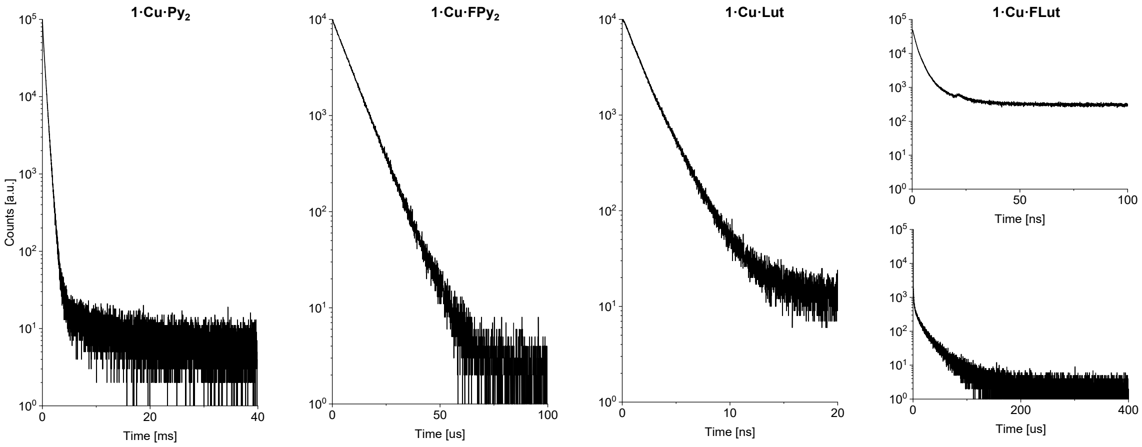

Figure 39. Decay curves for the main emissions of **1·Cu·Py₂**, **1·Cu·FPy₂**, **1·Cu·Lut** and **1·Cu·FLut** at 298 K. The excitation wavelength was 375 nm for **1·Cu·Py₂**, **1·Cu·Lut** and **1·Cu·FLut** (ns-range) or 420 nm for **1·Cu·FPy₂** and **1·Cu·FLut** (µs-range). The detection wavelength was chosen to be close to the respective emission maximum, at 500 nm **(1·Cu·Py₂)**, 590 nm **(1·Cu·FPy₂)**, 450 nm **(1·Cu·Lut)**, 540 nm (**1·Cu·FLut**, ns-range), or 480 nm (**1·Cu·FLut**, µs-range).

It is immediately clear that the emission of the four compounds occur in vastly different time domains. For **1·Cu·Py₂**, a very long decay time in the range of milliseconds was observed, likely corresponding to phosphorescence. The main emission is bi-exponential with a fluorescence averaged lifetime of 0.37 ms. In the tail of said decay, a very long and very weak component is visible. Its lifetime was fitted to be 7.45 ms with its amplitude being 0.01% of the total emission. In contrast, for **1·Cu·Lut** only a very short lifetime of 2.10 ns was observed, which is assigned to prompt fluorescence. The emission of **1·Cu·FPy₂** occurs entirely in the microsecond domain, no fractions were observed in the nanosecond or millisecond range. It shows a bi-exponential decay, with a lifetime of 7.58 µs. Lastly, **1·Cu·FLut** does not fall into the same pattern as before. Its main emission is tri-exponential with a fluorescence averaged lifetime of merely 2.11 ns, with an offset already indicating a much longer time component. Indeed, a longer and darker mono-exponential emission decay was observed with 0.35 µs. This emission contributes with approximately 0.1% to the overall brightness.

The absence of a prompt component in **1·Cu·FPy₂** is an interesting observation. An explanation for this might be a very large ISC rate constant, not allowing prompt fluorescence to occur. The concomitant absence of a millisecond component allows the assumption that the observed emission in microseconds is either a fast phosphorescence or indeed stems from TADF. Assuming the latter to be true, a complete absence of prompt fluorescence would be mathematically impossible, since for this, the ISC rate constant would have to be infinitely large. For real systems, even with large ISC rates compared to the rate of prompt fluorescence, a small fraction will always emit via prompt singlet decay. Therefore, efforts were made to resolve the prompt fluorescence of **1·Cu·FPy₂**. Figure 40 shows a comparison of the decay in the nanosecond range of **1·Cu·FPy₂** versus the *instrument response function* (IRF) of the TCSPC-device, which represents the decay curve of the laser light, being scattered into the detector. This is the lower threshold for reliably determined emission decay times. The direct comparison shows that the prompt fluorescence of **1·Cu·FPy₂** is only slightly longer than the IRF, making a statement about its lifetime less reliable. Nevertheless, promptly emitted photons are indeed present and detectable.

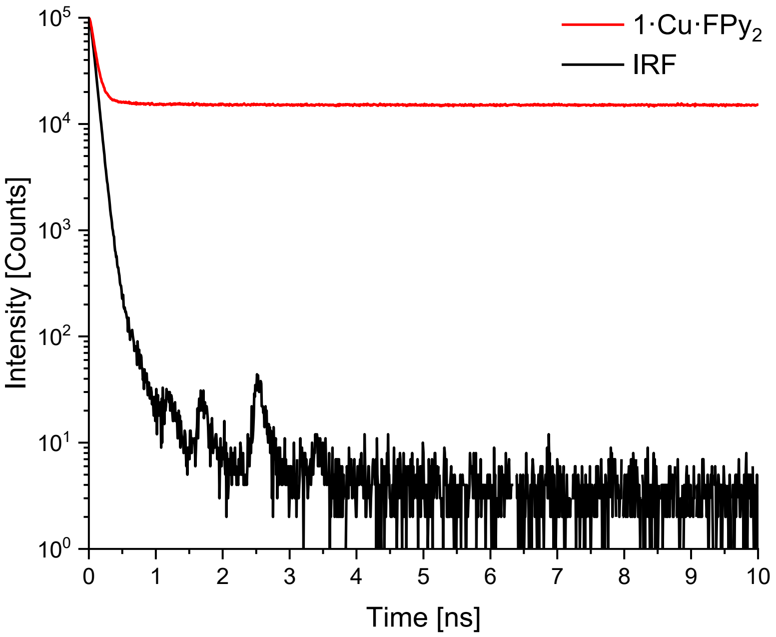

Figure 40. Emission decay histogram of **1·Cu·FPy₂** at 270 K in cyclohexane suspension in a time range of 10 ns versus the instrument response function.

4.3.4.1 Temperature dependence

To further investigate the temperature dependence of the emission, time-resolved data were recorded at 80 K, at otherwise the same experimental conditions. The results are depicted in Figure 41 and are compared to the respective decay curve at 298 K.

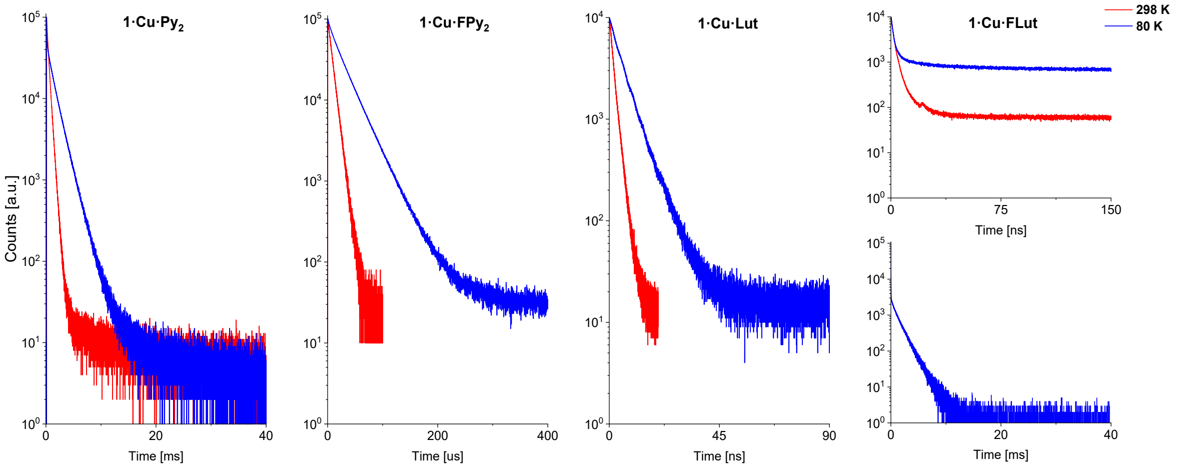

Figure 41. Decay curves for the main emissions of **1·Cu·Py₂**, **1·Cu·FPy₂**, **1·Cu·Lut** and **1·Cu·FLut** at 80 K (blue) in comparison to the previously shown data at 298 K (red). The excitation wavelength is 375 nm for **1·Cu·Py₂**, **1·Cu·Lut** and **1·Cu·FLut** or 450 nm for **1·Cu·FPy₂**. The detection wavelength was chosen to be close to the respective emission maximum, at 500 nm **(1·Cu·Py₂)**, 595 nm (**1·Cu·FPy₂**), 450 nm **(1·Cu·Lut)** and 540 nm (**1·Cu·FLut**). The decay curves at 298 K are scaled to match the measured initial amplitude of the 80 K data.

It is immediately visible that all emission decays are elongated upon cooling to 80 K. For **1·Cu·Py₂**, a fluorescence averaged lifetime of 0.97 ms is found, an increase by a factor of 2.6 compared to the 298 K data. The decay time of **1·Cu·Lut** increased to 5.76 ns, which corresponds to a factor of 2.7. In both cases, this elongation of the decay time is likely to be caused by a rigidification of the molecules and their crystal cage, hampering non-radiative decay due to vibrational relaxation and internal conversion. For **1·Cu·Py₂**, the tail of its decay curve at 80 K suggests an even longer component that was resolved by collecting more photons and increasing the time window. The histogram is depicted in Figure 42. Fitting of its tail results in an astonishing lifetime of 42.2 ms, naturally very dark with a contribution of only 0.008%.

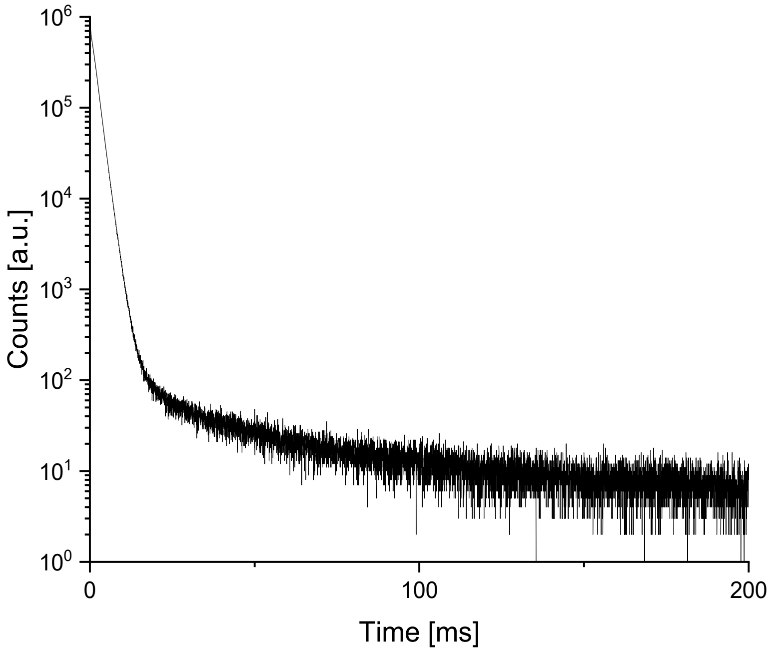

Figure 42. Decay curve of **1·Cu·Py$_2$** at 80 K with a maximum photon count of 10^6 in a range of 200 ms, resolving its longest component.

Compound **1·Cu·FLut** shows only a minor influence of cooling in its prompt fluorescence lifetime, which increases to 3.13 ns. The emission in the microsecond domain entirely vanishes though, being replaced by a much brighter millisecond decay of 1.11 ms. Although not being an irrefutable proof, this would be an expected behaviour for a TADF emitter, since this could be explained by the rISC being disabled and phosphorescence being enabled at low temperature.

For compound **1·Cu·FPy$_2$**, a rather intricate situation is observed upon cooling. Instead of losing its microsecond decay in favour of a long phosphorescence in milliseconds, as observed in **1·Cu·FLut**, it retains the former, which is elongated to 25.13 µs. For a simple TADF emitter, involving an rISC from T_1 to S_1, this would be highly unlikely, since the thermal energy at 80 K, estimated via $k_b \times T$, would allow a thermal coupling only if the $\Delta E_{S1\text{-}T1}$ is approximately 7 meV, almost ten times lower than the $\Delta E_{S1\text{-}T1}$ determined via the spectral shift upon cooling. This discrepancy will be addressed in a later chapter.

Table 5. Summary of the time-resolved data of the emission of **1·Cu·Py$_2$**, **1·Cu·FPy$_2$**, **1·Cu·Lut** and **1·Cu·FLut** at 80 K and 298 K obtained from powdered samples.

	1·Cu·Py$_2$			**1·Cu·FPy$_2$**			**1·Cu·Lut**			**1·Cu·FLut**		
	[ns]	[µs]	[ms]	[ns]	[µs]	[ms]	[ns]	[µs]	[ms]	[ns]	[µs]	[ms]
λ$_{Em}$ [nm]			500		590		450			540	540	540
298 K			0.37		7.58		2.10			2.11	0.39	
80 K			0.97		25.13		5.76			3.13		1.11

Furthermore, complementary, time-resolved data in cyclohexane suspension were gathered to compare it to the data of powdered samples. Table 6 contains the results of measurements at 270 K and 80 K. Note that in order to ensure a solid matrix, no data at 298 K were recorded, since cyclohexane melts at 6.5 °C (280 K).

Table 6. Summary of the time-resolved data of the emission of **1·Cu·Py$_2$**, **1·Cu·FPy$_2$**, **1·Cu·Lut** and **1·Cu·FLut** at 80 K and 270 K obtained from samples suspended in cyclohexane.

	1·Cu·Py$_2$			**1·Cu·FPy$_2$**			**1·Cu·Lut**			**1·Cu·FLut**		
	[ns]	[µs]	[ms]	[ns]	[µs]	[ms]	[ns]	[µs]	[ms]	[ns]	[µs]	[ms]
λ$_{Em}$ [nm]			500		595		450			540	540	540
270 K			0.41		10.44		2.20			1.97	2.71	
80 K			1.79		26.26		5.51			2.27		1.78

Taking into account the different measurement temperatures, a very good agreement can be reported between the two different techniques of sample preparation. The temperature trend extracted from only powdered samples explains the slight deviations very well, since the same trend is observed for all compounds comparing the 298 K data of powdered samples to the 270 K data in cyclohexane suspension.

For **1·Cu·FPy$_2$** and **1·Cu·FLut**, additional temperature dependant measurement series in a range from 60 K to 270 K were recorded to explore the decay behaviour in microseconds in more detail. The collection of histograms is depicted in Figure 43.

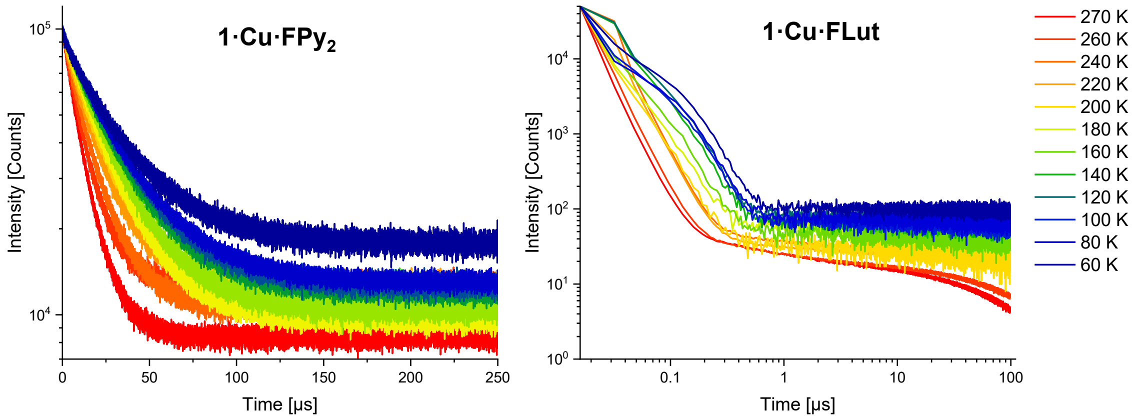

Figure 43. Decay histograms at varying temperature for **1·Cu·FPy$_2$** (c = 1.38 mM) and **1·Cu·FLut** (5.17 mM) in cyclohexane suspension. λ_{Ex} = 375 nm, λ_{Em} = 595 nm **(1·Cu·FPy$_2$)** and 540 nm **(1·Cu·FLut)**. Note that the data for **1·Cu·FLut** at 270 K and 260 K were gathered for a longer measurement time than the others. These two histograms are scaled down to match the other amplitudes.

The dataset of **1·Cu·FLut** is shown in a double logarithmic fashion, whereas **1·Cu·FPy$_2$** is not. This is to show also the prompt fluorescence that is present in **1·Cu·FLut**, but not in **1·Cu·FPy$_2$**, as also observed in the measurements on powdered samples. Besides an elongation of the decay times upon cooling, the compounds share an increase in their offset of the decay histograms, indicating a longer component becoming brighter, which is assigned to the phosphorescence of the molecules. Both these observations are also in line with the measurements on the powdered samples.

Assuming a kinetic of first order for the rISC, an Arrhenius plot might serve as second source for the $\Delta E_{S1\text{-}T1}$, besides the analysis of the spectral shift upon temperature variation (see 4.3.3.1). As described in 2.2.2.1, the natural logarithm of the delayed fluorescence's rate constant is plotted against the inverse temperature for **1·Cu·FPy$_2$** and **1·Cu·FLut** in Figure 44. Only the high temperature measurements between 270 K and 220 K were selected for constructing the *Arrhenius* plots since only in this range, linearity can be expected. This is because other triplet depopulating mechanisms become meaningful at both too high and too low temperatures.[78] Table 7 shows a comparison of the $\Delta E_{S1\text{-}T1}$ values extracted from the spectral shifts upon temperature variation and the *Arrhenius* plots.

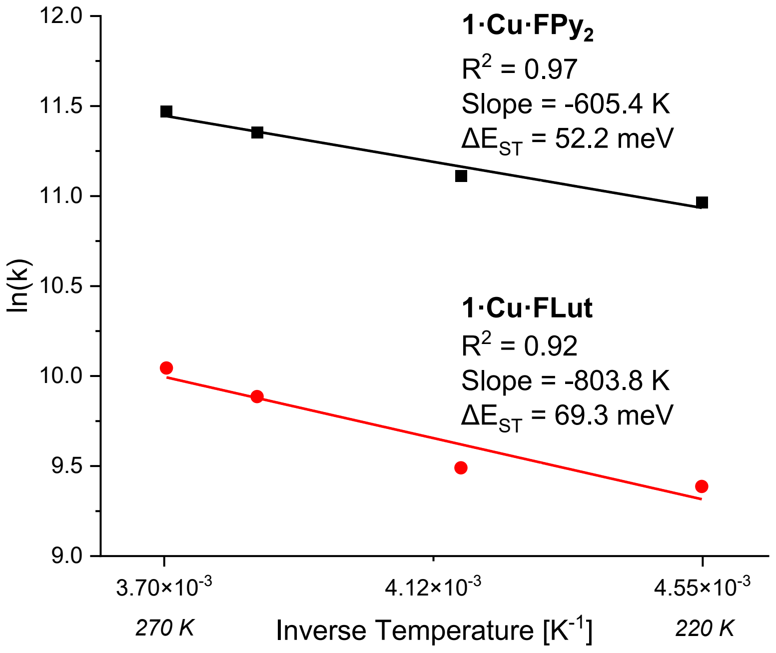

Figure 44. Arrhenius plot for **1·Cu·FPy₂** and **1·Cu·FLut** in the temperature range between 270 K and 220 K.

Table 7. Comparison of the $\Delta E_{S1\text{-}T1}$ extracted from the spectral shifts and the *Arrhenius* plots for **1·Cu·FPy₂** and **1·Cu·FLut**.

$\Delta E_{S1\text{-}T1}$ [meV]	Spectral shift	Arrhenius
1·Cu·FPy₂	79	52
1·Cu·FLut	93	69

Upon comparison of these two different techniques, it becomes apparent that the $\Delta E_{S1\text{-}T1}$ obtained from the spectral shift is systematically higher than the one from the *Arrhenius* plots. As already indicated before, there are other types of T_1 depopulating processes. Most importantly these are phosphorescence and quenching of the triplets by molecular oxygen. It is important to note that these types of depopulation mechanisms exhibit temperature dependence as well, which directly affects the slope of the *Arrhenius* plot and subsequently influences the $\Delta E_{S1\text{-}T1}$, while the spectral shift is not affected by these mechanisms. Therefore, the $\Delta E_{S1\text{-}T1}$ obtained by that is considered to be more reliable or at least to set a lower boundary for the energy gap. Ultimately, this reasoning renders the energy gap obtained from the *Arrhenius* plots as unreliable, since the observed temperature dependence must follow a kinetic of first order to yield reliable results. Nevertheless, it is possible to extract valuable information about the excited state behaviour from the *Arrhenius* plots, by understanding how they are affected by the processes stated above.

At higher temperatures, oxygen quenching becomes more effective, since the diffusion of oxygen is faster. As a result, points on the left side of the plot, which represent the higher temperature range, are increased due to an increase in the rate constant of T_1 depopulation. This leads to a larger overall slope, indicating a larger $\Delta E_{S1\text{-}T1}$. Conversely, at lower temperatures, phosphorescence becomes more active. In this case, the combined T_1 depopulating rate constant becomes larger for points on the right side of the plot, corresponding to the lower temperature range. This results in the overall slope being smaller, suggesting a smaller $\Delta E_{S1\text{-}T1}$. A graphical representation of these effects is given in Figure 45.

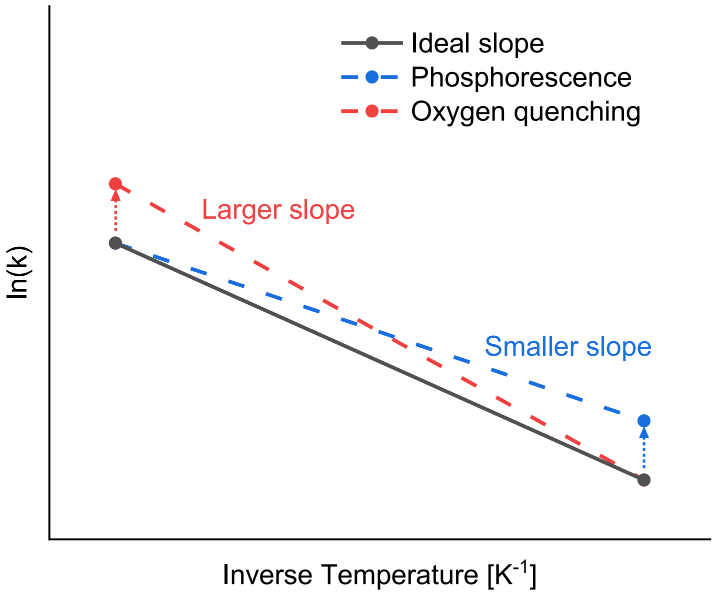

Figure 45. Effect of other T_1 depopulating processes on the slope of an Arrhenius plot.

Considering that the measurements used for constructing the *Arrhenius* plots were carried out in a solid matrix, diffusion of oxygen and its effect on the triplet lifetime can be considered negligible. Fittingly, a decreased $\Delta E_{S1\text{-}T1}$ is observed compared to the one obtained from spectral shift, in line with a phosphorescence distorting the results. By that reasoning, it is very likely that actually a mixture of TADF and phosphorescence is observed at or slightly above 220 K, which will be further justified in the next chapter.

4.3.5 Time resolved emission spectroscopy

Time resolved emission spectroscopy (TRES) is a powerful technique that revolves around creating steady-state spectra using time-resolved emission data. Essentially, with TRES, steady-state spectra are obtained by counting all photons detected within a specific time window. However, by adjusting this time window, even deeper insights into the behaviour of excited states within a system can be gained. By focusing only on the photons detected during the prompt fluorescence or phosphorescence time frame, individual spectra for each emission type can be constructed. Conducting TRES experiments can be quite costly in terms of resources. To gather a single dataset, emission decay histograms need to be recorded in dependence on the detection wavelength. Naturally, choosing a smaller detection interval leads to higher resolution in the obtained results. Figure 46 provides an approximation of the structure and information contained within such a histogram.

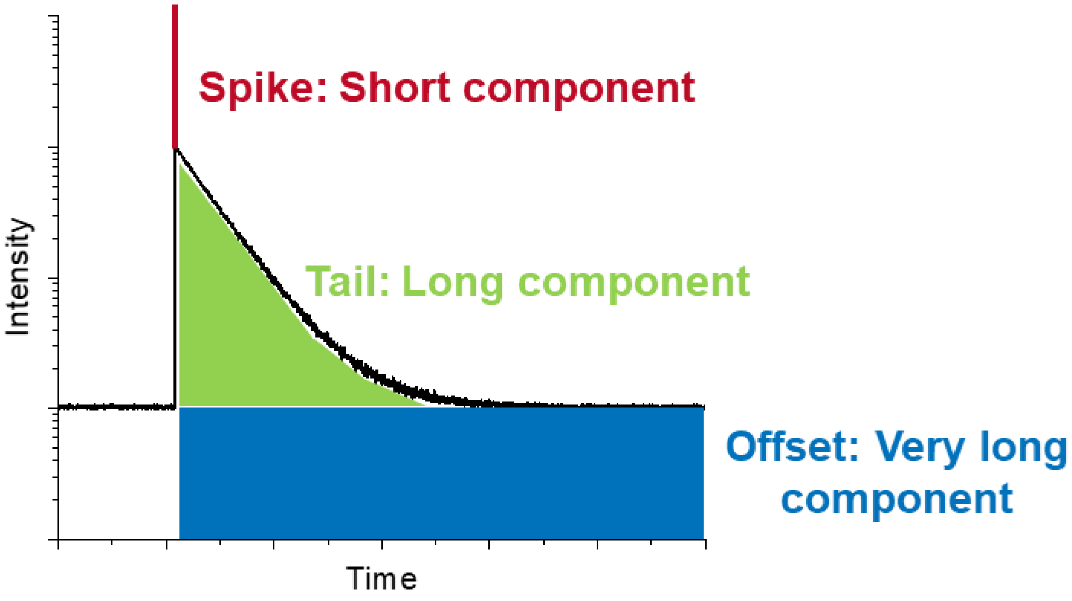

Figure 46. Individual components of an emission decay histogram. The coloured areas correspond to the integrated count rates.

Obtaining the histograms not only for each wavelength but beyond that also for each time range, where emission is expected, i.e., ns-, µs-, and ms-range, the collected photons in each area will origin from different types of emission, as summarized in Table 8.

Table 8. Photon origin per integrated area (see Figure 46) depending on the time window in which the histogram was recorded. [Sc] = scattered light, PF = prompt fluorescence, DF = delayed fluorescence, Ph = phosphorescence, [DC] = dark count rate of the detector.

	Spike	**Tail**	**Offset**
ns	[Sc]	PF	DF + Ph + [DC]
µs	[Sc] + PF	DF	Ph + [DC]
ms	[Sc] + PF + DF	Ph	[DC]

It becomes clear that the *tail* of each histogram contains the photons of PF, DF and Ph. In order to omit the photons that do not origin from the sample, i.e., the scattered laser light and the detector's dark count rate, the *spike* and the *offset* need to be excluded from integration. The distinguishment of these areas is done by finding a global fit function that matches all decay curves in the selected detection wavelength range, corresponding to one time window. In contrast to the fitting of a single decay curve, a global fit assumes the same lifetime of each emitting species in every decay curve, only their respective amplitudes differ depending on the detection wavelength. Moreover, the global fit allows for each species contributing to the overall emission to be separately analysed regarding their individual amplitude in dependence on the detection wavelength. This specific method of TRES is known as *decay associated spectroscopy* (DAS). It grants the most detailed analysis of the emission.

TRES was conducted for compounds **1·Cu·FPy$_2$** and **1·Cu·FLut** in cyclohexane suspension, for three time-ranges (ns, µs, ms), four different temperatures (10 K, 180 K, 220 K, 270 K) and 57 detection wavelengths (450 nm – 730 nm), amounting to a total of 1026 individual decay curves. The photon collection time was set to 30 min per decay, resulting in over 20 days of pure measurement time. The data are obtained in the form of the individual species with their corresponding lifetime τ and amplitude A per detection wavelength λ. The actual intensity at each detection wavelength is obtained by the sum of all products of the individual amplitudes and lifetimes divided by the time bin, which is the resolution of the time resolved histogram, according to Equation 9.

$$I_\lambda = \frac{\sum_i A_i \cdot \tau_i}{timebin} \qquad \text{Equation 9}$$

Subtracting the time trace of free ligand

As already indicated in Figure 34 and thereafter, for the two analysed compounds, small portions of ligand are leached off in suspension of cyclohexane, which is itself emissive at low temperatures. Therefore, it was the intention to remove their emission from the spectra by omitting their respective amplitudes and lifetimes from Equation 9. Since their emission properties are known and their spectra very characteristic, in that they show a strong vibronic progression and long-lived ms-phosphorescence, this is easily achieved. Figure 47 shows the individual spectra of all species detected in the ms-range.

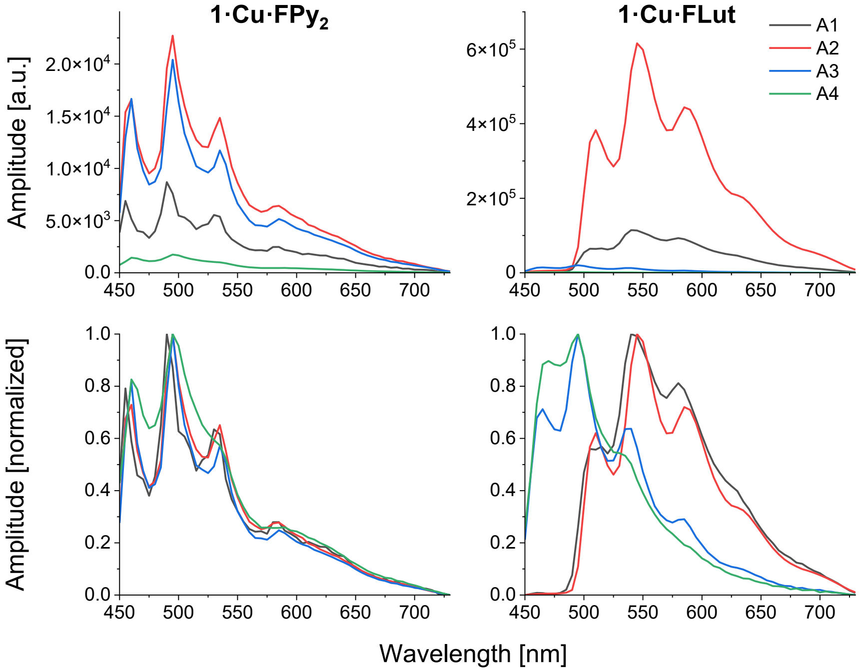

Figure 47. Decay associated spectra obtained from TRES data in the ms-range at 10 K in cyclohexane suspension of **1·Cu·FPy₂** and **1·Cu·FLut**. Shown are the intensity spectra of the individual amplitudes A1 – A4 (top) and their normalization (bottom).

For both compounds, four individual lifetimes are found in that time range. Interestingly, in **1·Cu·FPy$_2$**, all of them correspond only to the ligand. This observation is in line with the decay curves obtained from powdered samples, where no free ligand is expected (see Figure 41). For **1·Cu·FLut**, the situation is different. The strongest emissions indeed stem from the sample and only very weak bands corresponding to free ligands are observed. This is again in good agreement with the data of powdered sample and is also chemically intuitive, since ligand dissociation should be more favourable for the trigonal representative **1·Cu·FPy$_2$** than for the linear **1·Cu·FLut**. For the following analyses, the ligand emission was omitted.

Presentation of the refined data

With the ligand being removed, the pure emission stemming from the investigated compounds were resolved. These individual spectra are depicted in the following two figures. In Figure 48, the temperature dependence of the spectra in each time range is depicted, i.e., the shape and position of the band as well as its intensity. In contrast, Figure 49 shows the time dependence of the emission at each temperature. This representation allows to detect similarities between the emission types, e.g., between prompt and delayed fluorescence, which is a prerequisite for TADF.

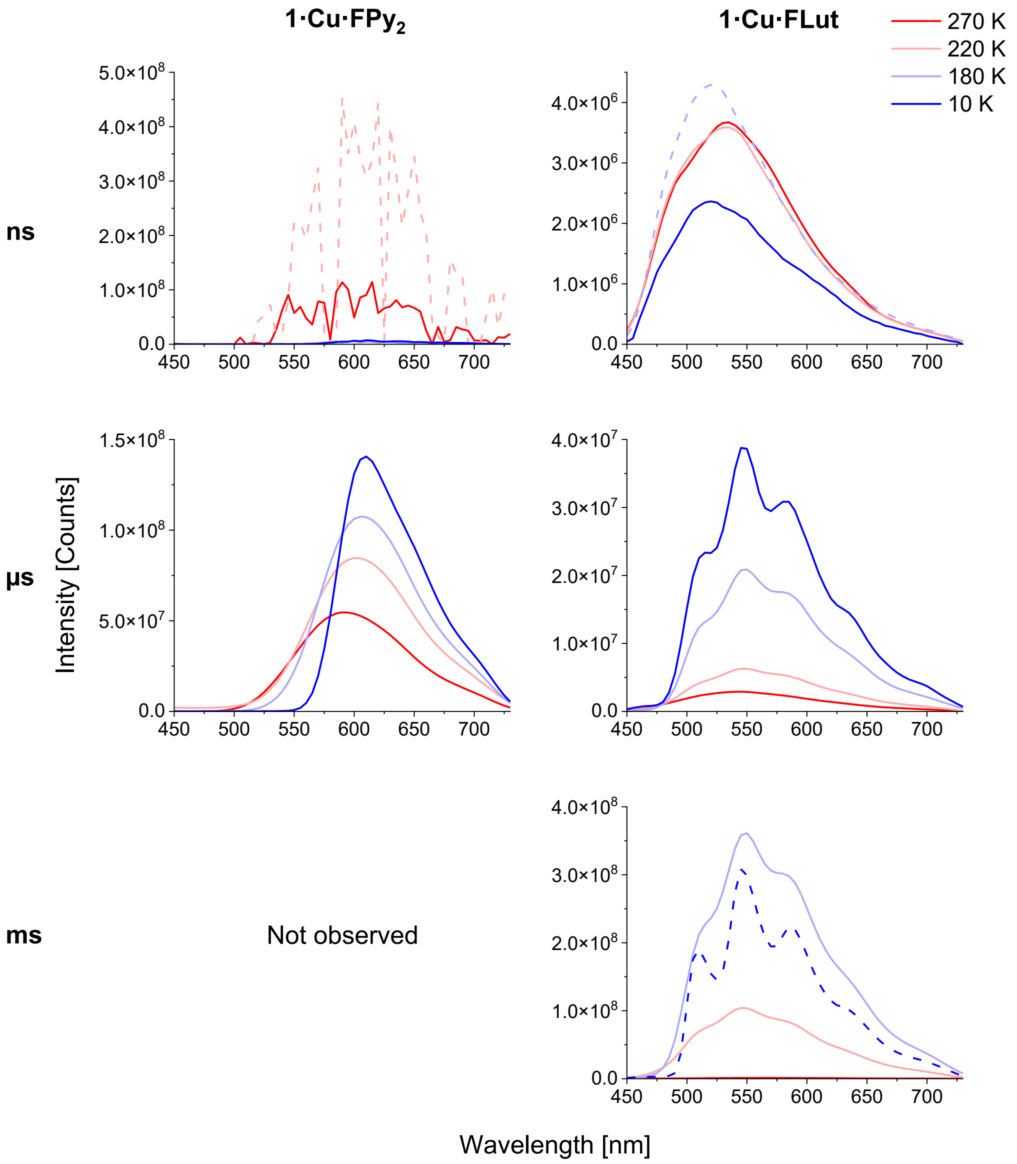

Figure 48. Dependence of the time-resolved emission spectra of **1·Cu·FPy₂** and **1·Cu·FLut** per time range on the temperature. Dotted lines indicate those spectra which do not fall in line with the apparent trend of intensity.

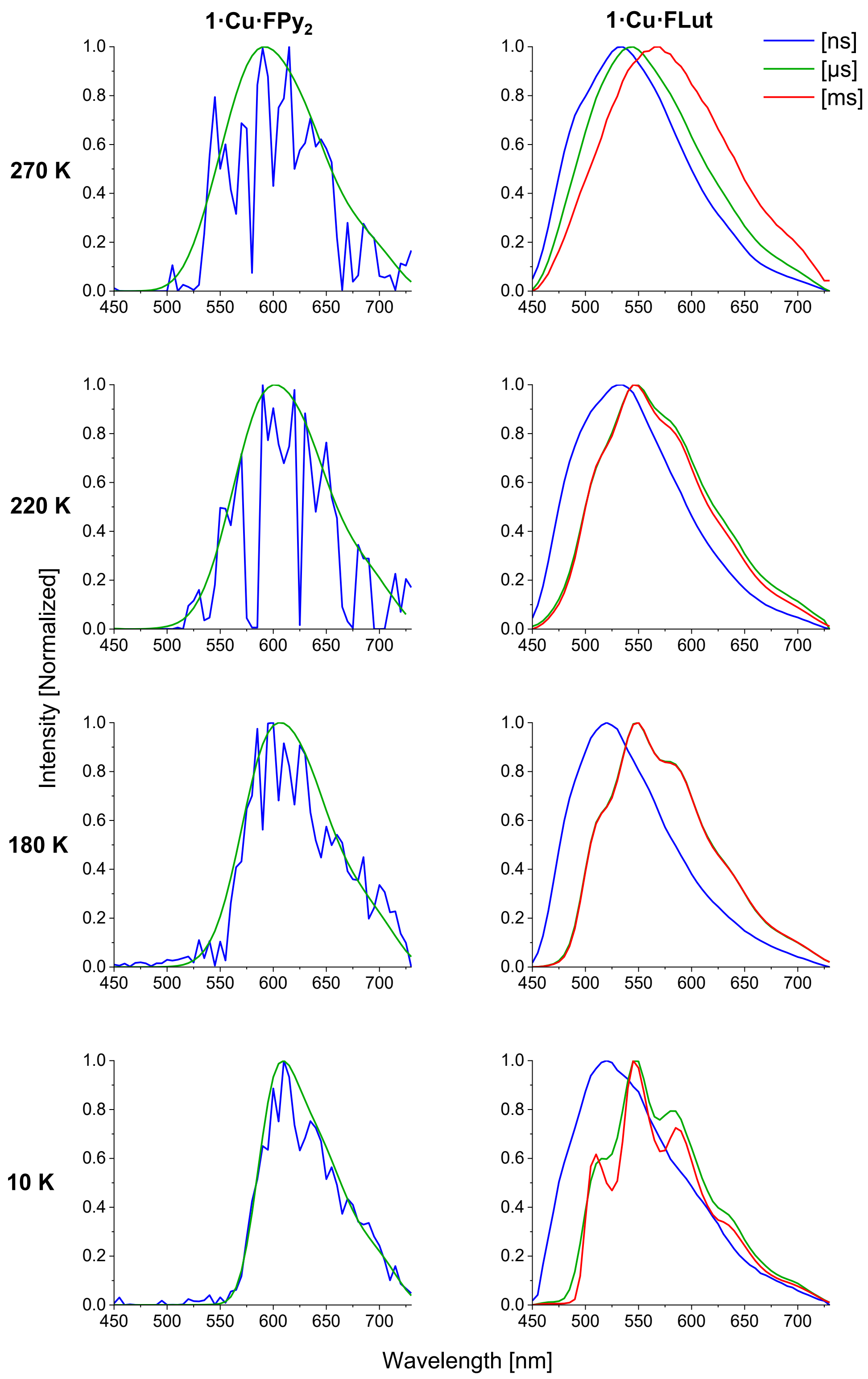

Figure 49. Dependence of the normalized time-resolved emission spectra of **1·Cu·FPy₂** and **1·Cu·FLut** per temperature on the time window.

Analysis for **1·Cu·FPy₂**

Compound **1·Cu·FPy₂** demonstrates a very weak and therefore noisy ns emission, in line with previous findings. Given that the observed emission in the ms range is entirely attributed to free ligand, all photons originating from the intact sample are emitted in the range of µs. Complementarily, the individual µs spectra experience a pronounced redshift from 590 nm (270 K) to 610 nm (10 K) with decreasing temperature, together with a reduction in width. This indicates a mixed emission from S_1 and T_1 at 270 K and thereafter a reduction of the S_1 emission with decreasing temperature, leaving behind almost exclusively T_1 emission at 10 K. Surprisingly though, the ns spectra are matched by the µs spectra almost perfectly at all four temperatures.

With these observations, the nature of the emission in **1·Cu·FPy₂** is presumably a mixture of TADF and phosphorescence at 270 K, both in the µs range, shifting to pure phosphorescence at very low temperatures. This assumption is supported by the redshift of the µs spectra that inevitably indicates two involved states, namely the S_1 from where TADF is produced and the T_1, responsible for the phosphorescence. The match of the ns spectra with the ones in µs range strongly suggests that the ns spectra do in fact not contain only prompt fluorescence, since then, no redshift with decreasing temperature could occur. An explanation might be given by a prompt fluorescence that is actually below the detection limit of the TCSPC, due to an unbeatably fast ISC after initial excitation. The obtained ns spectra are therefore presumably only a part of the µs spectra, possibly due to residual offset that was not fully subtracted from the ns decay curves, explaining the near perfect match. From Table 8 it is obvious that the offset of the ns decay curves contains precisely the information of the µs- and ms emission. Such an error is not unexpected and might arise due to statistical inaccuracies of the photon counting and the global fitting, but has a significant impact in this case, since the absolute photon count in the nanosecond range is very small. To verify this assertion, Figure 50 depicts a comparison between the tail spectra and the offset spectra in the nanosecond range of **1·Cu·FPy₂** (see Figure 46). The spectra match at all four temperatures, indicating that the respective emissions are of equal origin.

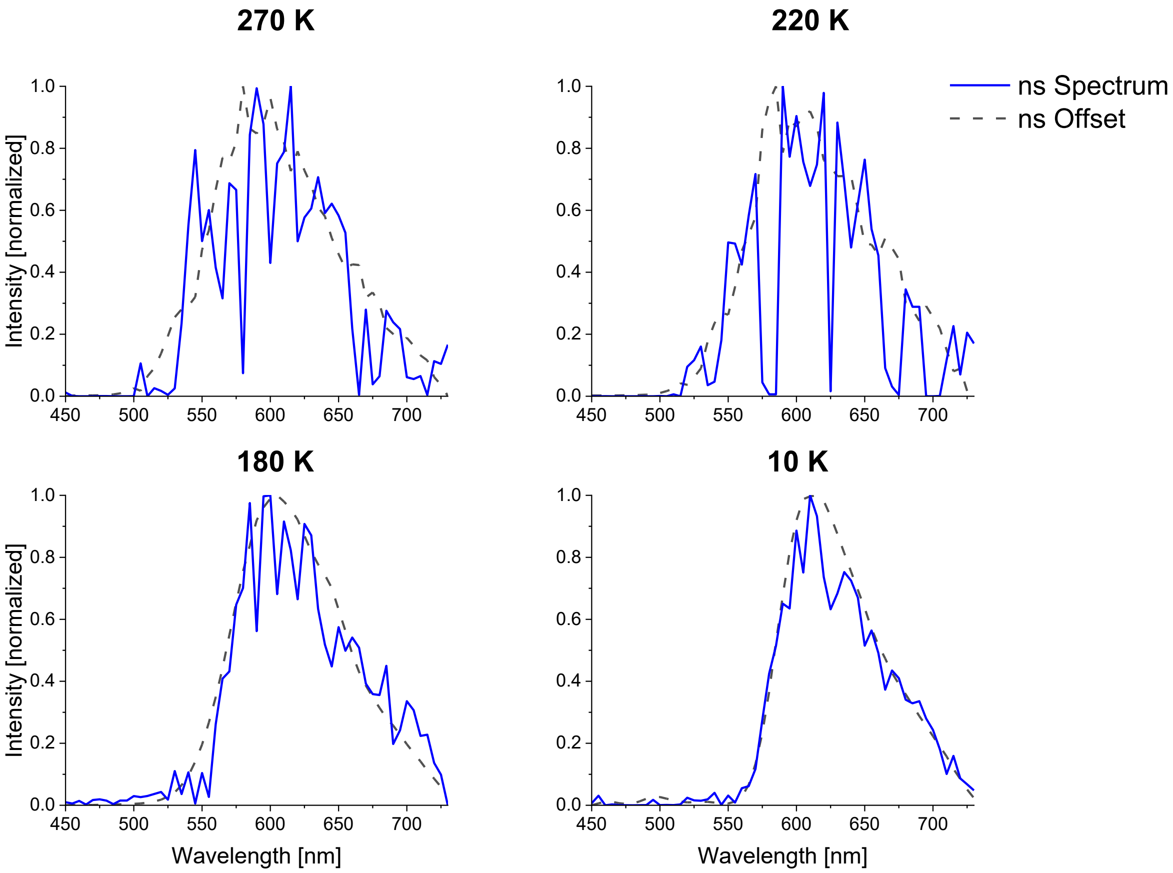

Figure 50. Comparison of the normalized spectra obtained in the nanosecond range of **1·Cu·FPy₂** with their respective normalized offset spectrum that is subtracted from them. Matching is observed at all four temperatures.

Analysis for 1·Cu·FLut

In **1·Cu·FLut**, a different picture is found since here, strong emission is observed in all three time ranges. The ns spectra again lose intensity with decreasing temperature, although this time without a pronounced shift of their emission maxima. In fact, only a slight blueshift from 530 nm to 520 nm is detected upon cooling, in line with a hampered stabilization of the S_1 via molecular movement at low temperature. Both the µs and the ms emission demonstrate an increased intensity at lower temperatures and no considerable shift of their emission maxima between 10 K and 220 K. Moreover, these two emission types show near perfect superimposition in that same temperature range. At 270 K though, the µs and ms emission are clearly separated with the µs spectrum approaching the one in ns.

Based on these findings, **1·Cu·FLut** most likely shows a distinct prompt fluorescence at 530 nm paired with a phosphorescence at 550 nm. At 220 K and below, the compound does not show TADF, but only prompt fluorescence and phosphorescence. At 270 K though, TADF becomes operative, since there is a clear separation between its spectrum in microseconds and the phosphorescence spectrum in milliseconds. In accordance with that, the absolute intensity of the phosphorescence spectrum at 270 K is very small, meaning that the rISC efficiently pumps the system back into the singlet manifold. The phosphorescence lifetime thereby decreases, leading to the decreased intensity of the resulting spectrum. The complete absence of TADF at low temperature is in line with the larger $\Delta E_{S1\text{-}T1}$ of this compound.

Presumably, this picture would be even clearer at higher temperature than 270 K, but note that the upper limit of 270 K was enforced by the melting point of cyclohexane. Only in the solid matrix, the compounds are stable over the long measurement period. Experiments in liquid cyclohexane under constant stirring were unsuccessful, because the compounds are dissociated during the measurements.

Further considerations

The intensities of the nanosecond spectra of **1·Cu·FLut** do not follow an obvious trend. While there is almost no change between 270 K and 220 K, the spectrum at 180 K shows the highest intensity, while at 10 K, the intensity again drops. A possible explanation might be given by an interplay of increased prompt fluorescence quantum yield (PFQY) due to less non-radiative decay caused by hampered molecular movement, but concomitantly decreased rISC and thereby decreased delayed fluorescence quantum yield (DFQY), which is also operative in the late nanosecond range. Another break of the intensity trend is visible in the ms spectrum at 10 K, which is lower than expected from the increase in intensity before. While there is no inherent physical explanation for this behaviour, this is most likely due to the subtraction of the ligand emission, that was done only in this spectrum, distorting a meaningful representation of the intensity.

The hypothesis that the underestimation of the $\Delta E_{S1\text{-}T1}$ by the *Arrhenius* plots is caused by a phosphorescence admixing with the TADF at 220 K and below (see 4.3.4.1) is verified by the analysis presented above. Indeed, phosphorescence with rate constants close to those of the TADF is found, resulting in the case shown in blue in Figure 45.

Finally, the last open question is why the admixed TADF and phosphorescence signals of **1·Cu·FPy$_2$** cannot be separated into individual spectra by the TRES, since this is exactly what it would be designed for. The answer is the inaccuracy of the detection wavelength of the TCSPC, which was ±20 nm for the presented measurements, caused by the slit size to the detector's monochromator. Given that the $\Delta E_{S1\text{-}T1}$ of 79 meV corresponds to a spectral shift between S_1 and T_1 of only 24 nm, the two emissions cannot be separated spectrally. In **1·Cu·FLut**, a separation between its TADF and phosphorescence could be achieved, because they possess very different time constants at 270 K, making them distinguishable regardless of their spectral proximity.

Summary of the TRES experiments

To summarize the results gathered by the TRES experiments, the key findings and explanations are compiled shortly.

1·Cu·FPy$_2$

- Emission is detected only in the microsecond range.
- The spectra in this time range are a mixture of TADF and phosphorescence at 270 K, shifting to pure phosphorescence upon cooling.
- Its prompt fluorescence is below the detection threshold, the spectra in the nanosecond range are an artifact from their offset.

1·Cu·FLut

- Emission is detected in all three time ranges.
- At 220 K and below, only prompt fluorescence and phosphorescence are operative.
- At 270 K, TADF becomes active.

5 Conclusion

The research presented in this work deals with the coordination chemistry of the anionic diamido NHC **1** towards copper(I) and thereafter the assessment of the photophysical properties of a selection of complexes showing promising emission upon excitation with ultraviolet light. Several heteroleptic linear as well as trigonal planar complexes have been synthesized, the coordination sphere being completed by either pnictogen- or chalcogen-based ligands, i.e., pyridines, triphenylphosphine and seleno ureas.

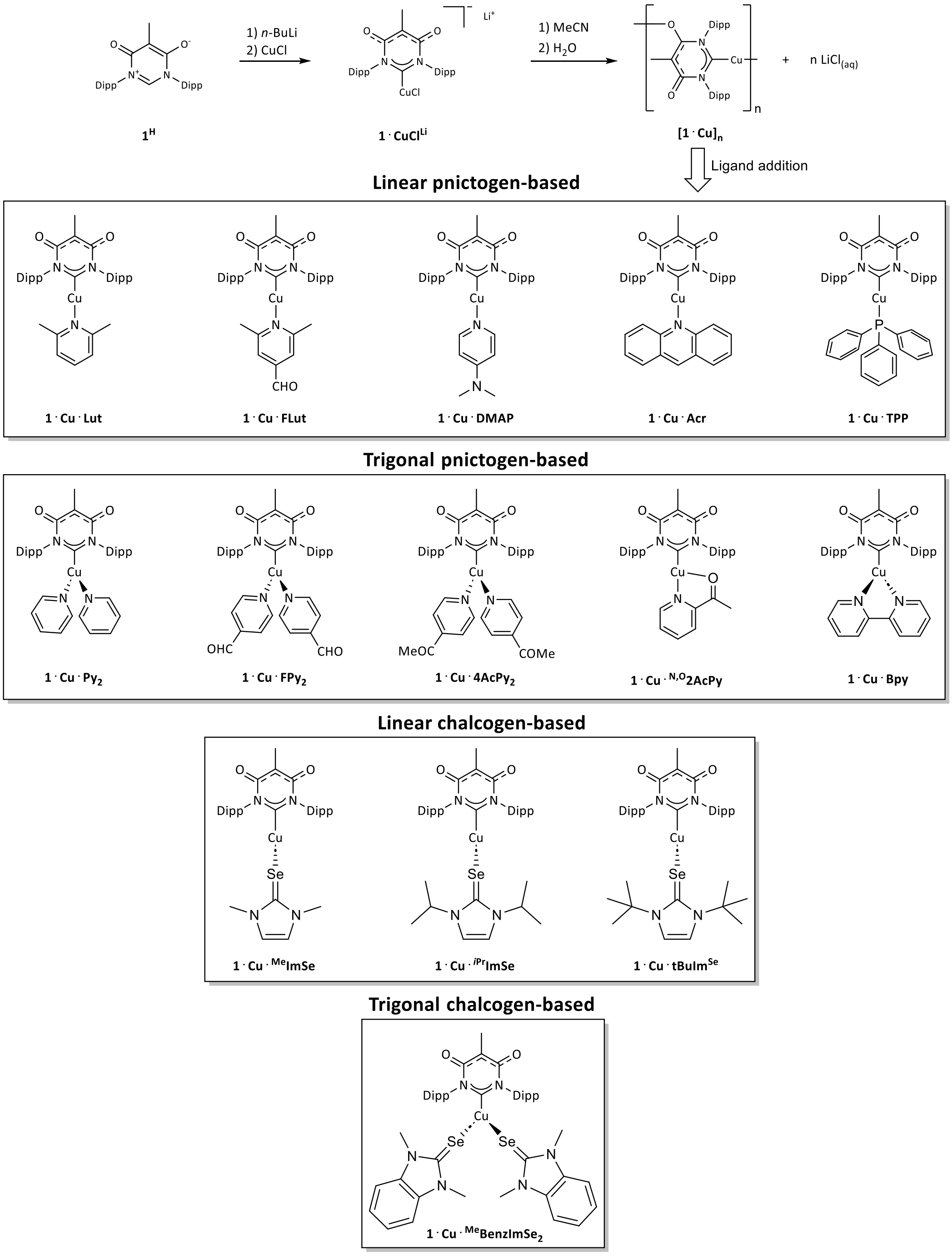

The direct precursor for this synthetic route is the water- and air-stable 1D coordination polymer **[1·Cu]$_n$** composed only of the NHC **1** and copper(I) ions, with the copper being linearly coordinated by the carbene carbon atom and one oxygen atom from the carbene's backbone.

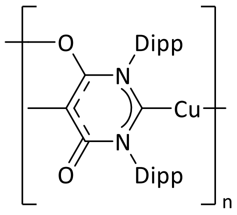

[1·Cu]$_n$

The copper-oxygen bond is easily cleaved by addition of a desired ligand, under concomitant formation of the respective mono-nuclear complex. The suitability of the ligands used decreases with their σ-donor capacity, which is evident from the amount of ligand required to ensure complete conversion of the polymer.

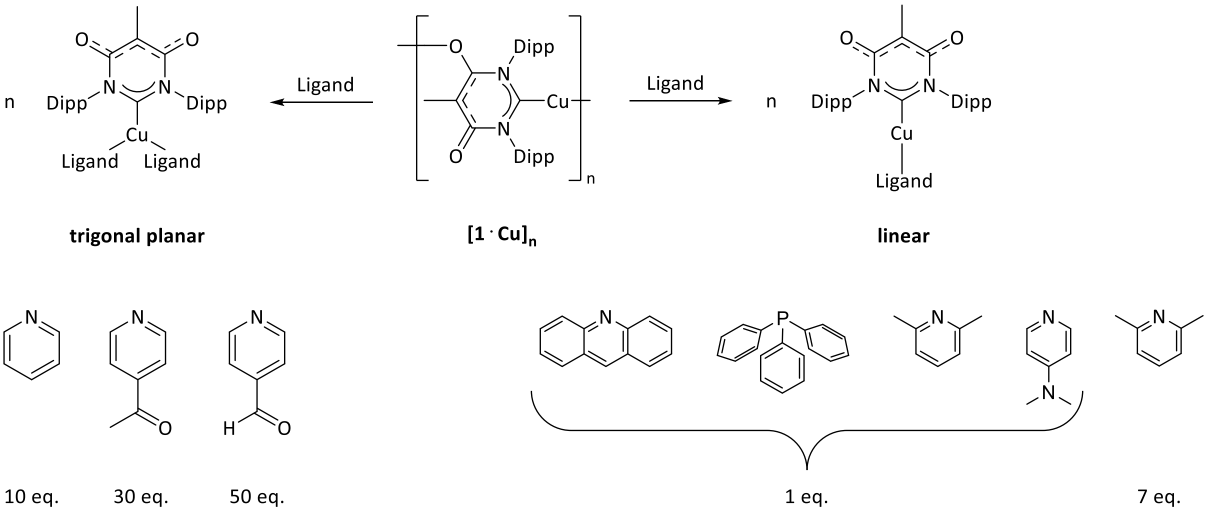

This process is governed by an equilibrium that is present in solution of all synthesized compounds, involving the monomeric complexes as well as oligo- and polymeric material of **[1·Cu]$_n$** besides free ligand. The respective concentrations of the participating species again depend on the electronic nature of the secondary ligands. In case of **1·Cu·FPy₂**, the equilibrium is far on the side of **[1·Cu]ₙ**, such that it spontaneously precipitates if **1·Cu·FPy₂** is dissolved, preventing any further analytical assessments in solution.

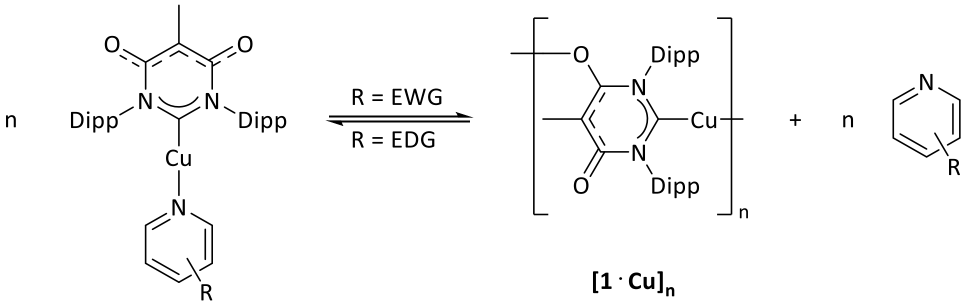

The coordination number of the heteroleptic complexes is directly affected by the necessity of an excess of ligand in many cases, e.g., the respective linear species of **1·Cu·Py₂**, **1·Cu·FPy₂**, **1·Cu·4AcPy₂** cannot be obtained, since complex formation does not commence with the addition of only one equivalent of ligand. The stoichiometric composition was therefore controlled by other means. Kinetic control is achieved with sterically demanding ligands, such as 2,6-lutidine, acridine or triphenylphosphine, allowing only the mono-coordination, but also thermodynamic control is possible. For example, **1·Cu·DMAP** is exclusively obtained in its linear form, a second DMAP molecule does not coordinate to the copper, regardless of its small size. This is caused by the strong σ-donating ability of DMAP, resulting in an electronic mismatch with the already strongly donating NHC **1**.

In solid state, the complexes feature surprising stability towards air and moisture, their integrity being unjeopardized even after months of storage under non-inert conditions. Upon inspection of the molecular structures, clarified for all presented compounds via SC-XRD, it becomes clear that the pnictogen-based complexes form sub-*Van-der-Waals*-radii intermolecular contacts in solid state, caused by their high dipole moments. These contacts form primarily between the electron-rich carbene backbone and the electron-deficient pyridine moieties, even involving atoms that are commonly only expected to undergo *Van-der-Waals* interactions, such as aromatic or aliphatic protons. The presence of these contacts has also been shown for the powdered samples via PXRD and by the same means, their thermal lability was shown by taking a PXRD histogram before and after heating solid **1·Cu·FPy$_2$**, yielding clear changes in its diffraction pattern.

For an in-depth photophysical analysis, a selection of four compounds was chosen. This choice was based on their promising light emission, visible to the naked eye, as well as suggestions stemming from rational design conducted in the department of theoretical chemistry. The four compounds, **1·Cu·Py$_2$**, **1·Cu·FPy$_2$**, **1·Cu·Lut** and **1·Cu·FLut**, were subjected to steady state as well as time resolved spectroscopy, focusing on the confirmation of possible TADF properties.

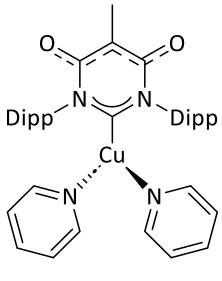

1·Cu·Py$_2$

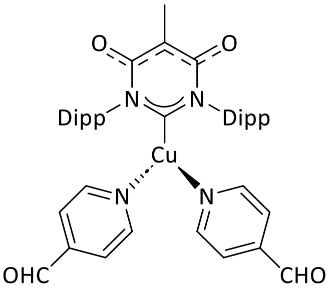

1·Cu·FPy$_2$

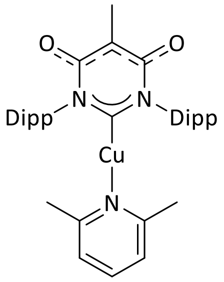

1·Cu·Lut

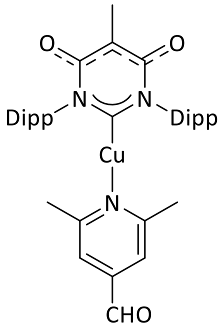

1·Cu·FLut

Due to the intricate situation encountered in solution, the spectroscopic methods had to be adapted, in order to guarantee defined and reproducible compositions of the samples. Solutions of the compounds were stabilized with an excess of ligand, shifting the equilibrium towards the monomeric complexes. Solid state measurements were conducted either with neat powdered samples or with suspensions of the compounds in cyclohexane. The latter allowed the experiments to be conducted in standard cuvettes and thereby ensured the compatibility with virtually all commonly available spectrometers, most importantly a TCSPC coupled with a cryostat that could be cooled down to 10 K. The obtained results from the cyclohexane suspensions were in very good agreement with the ones obtained from powdered samples, indicating the suitability of this technique in the scope of this work.

The excitation dynamics have been analysed via common UV-Vis absorption and excitation experiments as well as via the absolute reflectance of the samples. UV-Vis absorption was majorly affected by the chemical equilibrium in solution, since it usually requires homogeneous solutions for clean light transmission. Thus, they were partly recorded on ligand stabilized solutions, the ligand concentration being matched by the reference cuvette in order to subtract its absorption. The theoretically expected absorption bands were matched quite well by this technique. Absorption of the cyclohexane suspensions yielded meaningful results as well, after the light scattering by the particles was accounted for. Only for **1·Cu·FPy$_2$**, the S_1 band at 405 nm, predicted by calculations, was not observed, possibly due to its instability even in cyclohexane, once the concentration is in the micromolar range. The excitation in solid state and in suspension as well as the reflectance spectra are in good agreement with each other, confirming the expectations.

The emission maxima range from 451 nm in the blue for **1·Cu·Lut** to 591 nm in the orange region for **1·Cu·FPy$_2$**, covering almost half of the light spectrum visible to the human eye. A trend between the chemical nature and the emission colour can be observed. While the linear complexes emit at lower wavelengths than their trigonal counterparts, an electron withdrawing substituent on the pyridine moieties causes a red-shift of the emission.

Temperature dependant emission spectroscopy reveals a slight blue shift for **1·Cu·Py$_2$** and **1·Cu·Lut** upon cooling, in line with a rigidification of the excited states, but a strong red shift for **1·Cu·FPy$_2$** and **1·Cu·FLut**. This is a first hint towards TADF, since the bathochromic shift upon cooling indicates that the emission primarily stems from the triplet state, because rISC is sufficiently hampered. For **1·Cu·FPy$_2$**, its emission intensity in dependence on the energy fluence was analysed in order to obtain deeper insights in possible triplet-triplet-annihilation behaviour. This was ruled out though, since the kinetic of the emission was shown to be of first order, as expected for TADF, and not of second order, as for TTA.

The absolute photoluminescence quantum yields have been experimentally determined at room temperature using an *Ulbricht* integrating sphere. Values of 0.13, 0.04, 0.02 and 0.01 have been found for **1·Cu·FPy$_2$**, **1·Cu·Lut**, **1·Cu·Py$_2$** and **1·Cu·FLut**, respectively.

Time resolved spectroscopy shed light on the rate constants involved in the radiative transitions of the analysed compounds, generally indicating that **1·Cu·Lut** relaxes radiatively in the nanosecond range via the prompt fluorescence pathway while **1·Cu·Py$_2$** does so in the millisecond range via a long-lived phosphorescence. TADF was ruled out for both compounds, since the temperature dependence of both the steady state as well as the time resolved emission does not match the expectations. Calculations suggest a local excitation on the carbene, which was also experimentally indicated by a strong vibronic fine-structure of the emission bands of these compounds. For **1·Cu·FPy₂** and **1·Cu·FLut**, time-resolved spectroscopy reveals the temperature dependence expected for TADF in both cases, namely an elongation of the lifetimes in the microsecond range at low temperature.

Constructing an *Arrhenius* plot from these lifetime data in the microsecond range yields an energy separation of S_1 and T_1 of 52 meV (**1·Cu·FPy₂**) and 69 meV (**1·Cu·FLut**), which is systematically lower than the value extracted from the spectral shift of the emissions in the high and the low temperature edge case. This is attributed to a phosphorescence being operative at low temperature, that has a very similar rate constant compared to the rISC and subsequently the TADF.

Finally, time resolved emission spectroscopy gave the necessary spectral information about the involved emission types. It turned out, that in **1·Cu·FPy₂**, only emission in the microsecond range is observed. Presumably, the prompt fluorescence cannot compete with the rate of ISC. Emission that was observed in the millisecond range at lower temperature was proven to stem from dissociated ligand without exception. The observed redshift of the spectra obtained in the microsecond range indeed confirms the participation of both the S_1 and the T_1, confirming the abovementioned hypothesis. The condition of matching prompt and delayed fluorescence spectra can neither be verified nor falsified for **1·Cu·FPy₂**, since no prompt fluorescence was detected.

For **1·Cu·FLut** on the other hand, emission in all three time ranges was observed. Upon cooling, the prompt fluorescence intensity decreases with a concomitant increase in the intensity of the presumed phosphorescence in the microsecond and millisecond range. Again, presumably TADF and phosphorescence are operative with very similar rate constants. Comparing the spectra in the different time ranges, a clear match between the microsecond and the millisecond spectra is observed at temperatures below 220 K. At 270 K though, the microsecond spectrum clearly blueshifts towards the nanosecond spectrum, although no perfect match is established at this temperature. Presumably, this could be observed at higher temperatures, however, these experiments could only be performed in solid cyclohexane. Nevertheless, also for **1·Cu·FLut** TADF is operative, but only at higher temperature, which is in line with its larger $\Delta E_{S1\text{-}T1}$. Phosphorescence is most likely operative throughout the observed temperature range, becoming the primary source of emission at 220 K and below.

In the end, two copper(I) complexes were identified to fulfil all criteria expected for TADF, as far as the physical, chemical and instrumental restrictions allowed to do so. The statement given in the beginning, that TADF is a very unremarkable and therefore hard to verify property, was proven many times over. Even though TADF is highly likely to be operative in the two compounds **1·Cu·FLut** and **1·Cu·FPy$_2$**, there are still open questions that need answering. Mainly, the spectral resolution ultimately prevented a definite proof, since the emissions from S_1 and T_1 are apparently spectrally very close together. Nevertheless, this challenge underlines the close energetic proximity of these two states, which is vital for TADF to occur. Gaining a higher spectral resolution would then allow for the two distinct emissions to be separated.

5.1 Zusammenfassung

Die vorliegende Arbeit befasst sich mit der Koordinationschemie des anionischen Diamido-*N*-heterocylischen Carbens **1** gegenüber Kupfer(I) und der anschließenden Analyse der photophysikalischen Eigenschaften einiger Vertreter dieser Komplexklasse, die eine vielversprechende Emission bei Anregung mit ultraviolettem Licht zeigen. Mehrere heteroleptische, lineare und trigonal-planare Komplexe wurden synthetisiert, wobei die Koordinationssphäre entweder durch Pniktogen- oder Chalkogenliganden, d.h. Pyridine, Triphenylphosphin oder Selenoharnstoffe, vervollständigt wurde.

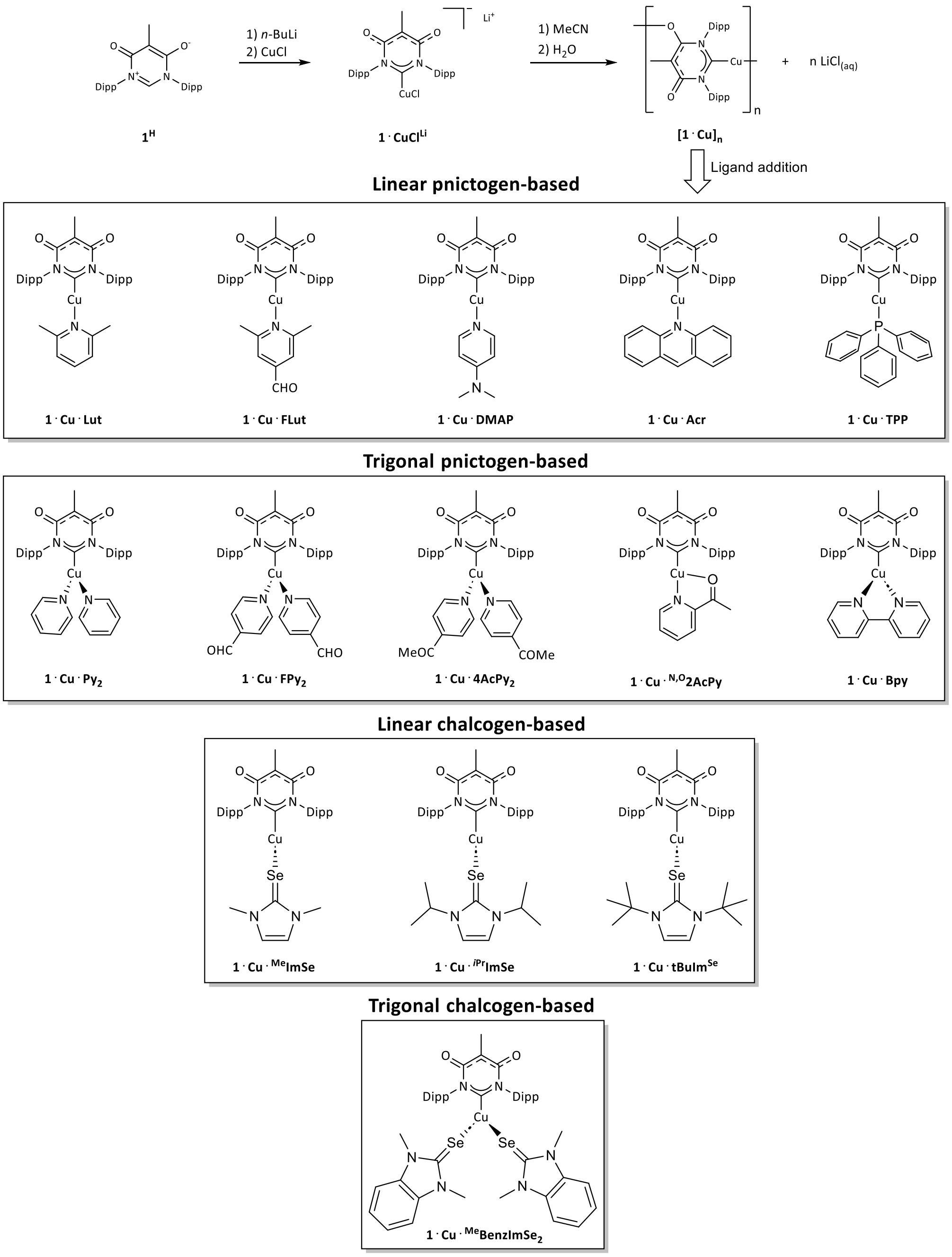

Der Vorläufer für diesen Syntheseweg ist das wasser- und luftstabile 1D-Koordinationspolymer **[1·Cu]$_n$**, das nur aus dem NHC **1** und Kupfer(I)-Ionen besteht, wobei das Kupfer linear durch das Carben-Kohlenstoffatom und ein Sauerstoffatom aus dem Carben-Rückgrat koordiniert wird.

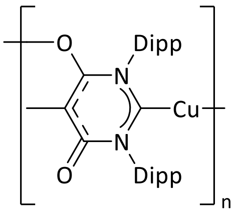

[1 · Cu]$_n$

Die Kupfer-Sauerstoff-Bindung lässt sich durch Zugabe eines gewünschten Liganden unter gleichzeitiger Bildung des entsprechenden einkernigen Komplexes leicht spalten. Die Eignung der verwendeten Liganden nimmt mit ihrer σ-Donor-Kapazität ab, was an der Menge des Liganden zu erkennen ist, die für eine vollständige Umsetzung des Polymers erforderlich ist.

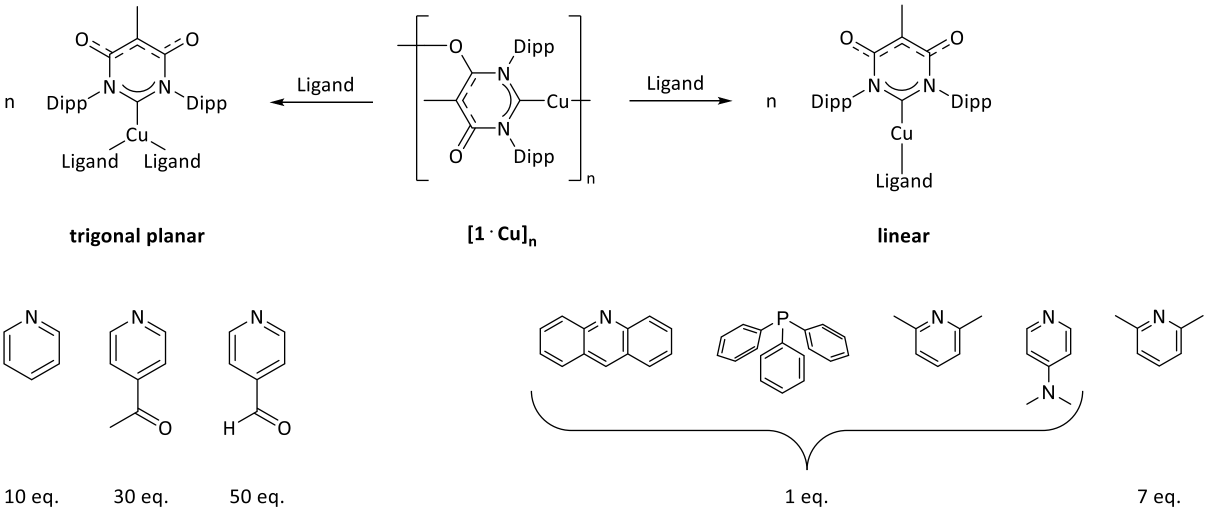

Dieser Prozess unterliegt einem Gleichgewicht, das in der Lösung aller synthetisierten Verbindungen aktiv ist und an dem neben dem freien Liganden sowohl die monomeren Komplexe als auch oligo- und polymeres Material von **[1·Cu]$_n$** beteiligt sind. Die jeweiligen

Konzentrationen der beteiligten Spezies hängen wiederum von der elektronischen Natur der sekundären Liganden ab. Im Falle von **1·Cu·FPy$_2$** liegt das Gleichgewicht weit auf der Seite von **[1·Cu]$_n$**, so dass dieses spontan ausfällt, wenn **1·Cu·FPy$_2$** in Lösung gebracht wird, was weitere Analysen in Lösung unmöglich macht.

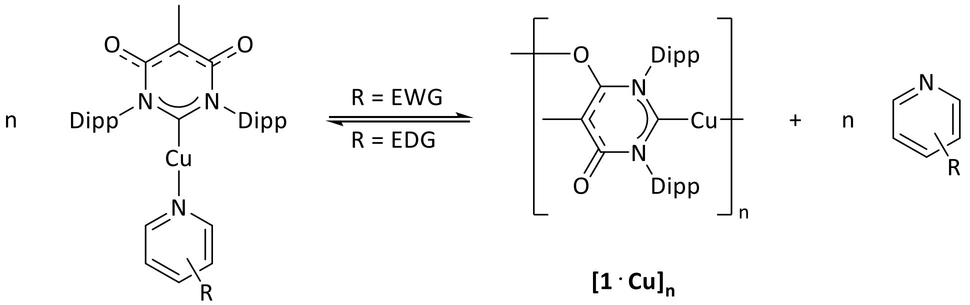

Die Koordinationszahl der heteroleptischen Komplexe wird in vielen Fällen direkt durch den notwendigen Ligandenüberschuss bestimmt, z. B. können die jeweiligen linearen Spezies von **1·Cu·Py$_2$**, **1·Cu·FPy$_2$** oder **1·Cu·4AcPy$_2$** nicht erhalten werden, da die Komplexbildung nicht mit der Zugabe von nur einem Äquivalent Ligand abläuft. Die stöchiometrische Zusammensetzung wurde daher mit anderen Mitteln kontrolliert. Kinetische Kontrolle ist mit sterisch anspruchsvollen Liganden wie 2,6-Lutidin, Acridin oder Triphenylphosphan möglich, die durch ihre Größe nur eine Monokoordination erlauben, aber auch thermodynamische Kontrolle ist möglich. Beispielsweise wird **1·Cu·DMAP** ausschließlich in seiner linearen Form erhalten, ein zweites DMAP-Molekül koordiniert nicht an das Kupfer. Dies ist auf die starke σ-Donizität von DMAP zurückzuführen, eine zweite Koordination wird aufgrund des bereits sehr elektronenreichen NHCs **1** nicht ausgebildet.

In festem Zustand weisen die Komplexe eine erstaunliche Stabilität gegenüber Luft und Feuchtigkeit auf, selbst nach monatelanger Lagerung unter nicht inerten Bedingungen kann keine Zersetzung festgestellt werden. Bei Betrachtung der Molekülstrukturen, die für alle vorgestellten Verbindungen mittels SC-XRD aufgeklärt werden konnten, wird deutlich, dass die Pniktogen-basierten Komplexe im festen Zustand aufgrund ihrer hohen Dipolmomente intermolekulare Kontakte ausbilden, deren Abstände teils deutlich unterhalb der vereinten Van-der-Waals Radien der beteiligten Atome sind. Diese Kontakte bilden sich vor allem zwischen dem elektronenreichen Carbenrückgrat und den elektronenarmen Pyridinliganden, auch unter Beteiligung von Atomen, von denen man normalerweise nur Van-der-Waals-Wechselwirkungen erwartet, wie z. B. aromatische oder aliphatische Protonen. Das Vorhandensein dieser Kontakte wurde auch für die Bulk-Phase mittels PXRD nachgewiesen, und auf die gleiche Weise wurde ihre thermische Labilität durch die Aufnahme eines PXRD-Histogramms vor und nach dem Erhitzen von festem **1·Cu·FPy$_2$** gezeigt, da deutliche Veränderungen in seinem Beugungsmuster zu sehen waren.

Für eine tiefgehende photophysikalische Analyse wurden vier Verbindungen ausgewählt. Diese Auswahl beruhte auf ihrer vielversprechenden, mit bloßem Auge sichtbaren Lichtemission sowie auf rationalem Design durchgeführt vom Institut für Theoretische Chemie. Die vier Verbindungen **1·Cu·Py$_2$**, **1·Cu·FPy$_2$**, **1·Cu·Lut** und **1·Cu·FLut** wurden sowohl durch steady-state als auch zeitaufgelöste Spektroskopie untersucht, wobei insbesondere Wert auf die Bestätigung von TADF in diesen Komplexen gelegt wurde.

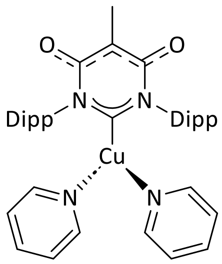

1 · Cu · Py$_2$

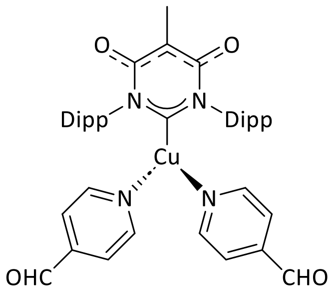

1 · Cu · FPy$_2$

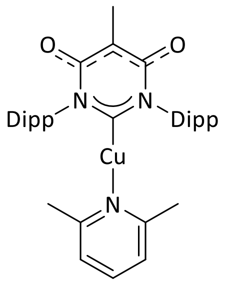

1 · Cu · Lut

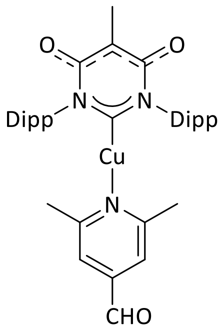

1 · Cu · FLut

Aufgrund des bestehenden Gleichgewichtes in Lösung mussten die spektroskopischen Methoden angepasst werden, um definierte und reproduzierbare Zusammensetzungen der Proben zu gewährleisten. Lösungen der Verbindungen wurden mit einem Überschuss des jeweiligen Liganden stabilisiert, wodurch sich das Gleichgewicht in Richtung der monomeren Komplexe verschob. Festkörpermessungen wurden entweder mit pulverförmigen Proben oder mit Suspensionen der Verbindungen in Cyclohexan durchgeführt. Letzteres ermöglichte die Durchführung der Experimente in Standardküvetten und gewährleistete damit die Kompatibilität mit praktisch allen handelsüblichen Spektrometern, insbesondere mit einem TCSPC-Setup, das mit einem auf 10 K kühlbaren Kryostaten ausgestattet ist. Die in

Suspension gewonnenen Ergebnisse stimmten sehr gut mit denen überein, die mit den pulverförmigen Proben erzeugt wurden, was die Eignung dieser Methode im Rahmen dieser Arbeit belegt.

Die Dynamik der Anregung wurde durch Aufnahme von UV-Vis-Absorptions- und Anregungsspektren sowie durch die absolute Reflektivität der Proben analysiert. Die UV-Vis-Absorption wurde in erster Linie durch das chemische Gleichgewicht in der Lösung beeinflusst, da sie in der Regel homogene Lösungen für eine ungehinderte Lichttransmission erfordert. Daher wurden teilweise ligandenstabilisierte Lösungen eingesetzt, wobei die selbe Ligandenkonzentration in der Referenzküvette eingestellt wurde, um die Absorption des freien Liganden zu ignorieren. Die theoretisch erwarteten Absorptionsbanden wurden durch diese Methodik gut wiedergegeben. Die Absorption der Cyclohexan-Suspensionen lieferte ebenfalls aussagekräftige Ergebnisse, nachdem für die Lichtstreuung an den Partikeln korrigiert wurde. Nur für **1·Cu·FPy$_2$** wurde die durch Berechnungen vorhergesagte S_1-Bande bei 405 nm nicht beobachtet, was möglicherweise auf dessen Instabilität selbst in Cyclohexan zurückzuführen ist. Die Anregung im festen Zustand und in Suspension sowie die Reflexionsspektren stimmen gut miteinander überein und bestätigen die Erwartungen.

Die Emissionsmaxima reichen von 451 nm im blauen Bereich für **1·Cu·Lut** bis 591 nm im orangen Bereich für **1·Cu·FPy$_2$** und decken damit fast die Hälfte des für das menschliche Auge sichtbaren Lichtspektrums ab. Es lässt sich ein Trend zwischen der chemischen Natur und der Emissionsfarbe beobachten. Während die linearen Komplexe, verglichen mit den trigonalen, bei niedrigeren Wellenlängen emittieren, bewirkt ein elektronenziehender Substituent an den Pyridinliganden eine Rotverschiebung der Emission.

Die temperaturabhängige Emissionsspektroskopie zeigt eine leichte Blauverschiebung für **1·Cu·Py$_2$** und **1·Cu·Lut** beim Abkühlen, was auf eine abgeschwächte molekulare Bewegung der angeregten Zustände zurückzuführen ist, aber eine starke Rotverschiebung für **1·Cu·FPy$_2$** und **1·Cu·FLut**. Dies ist ein erster Hinweis auf TADF, da die bathochrome Verschiebung beim Abkühlen darauf hindeutet, dass die Emission hauptsächlich aus dem Triplett-Zustand stammt, da der rISC weniger effizient wird. Für **1·Cu·FPy$_2$** wurde die Emissionsintensität in Abhängigkeit von der eingestrahlten Photonenenergie analysiert, um möglichen TTA auszuschließen. Es zeigte sich, dass die Emissionskinetik erster Ordnung ist, wie für TADF erwartet, und nicht zweiter Ordnung, wie für TTA.

Die absoluten Photolumineszenz-Quantenausbeuten wurden experimentell bei Raumtemperatur mit einer Ulbricht-Kugel bestimmt. Für **1·Cu·FPy$_2$**, **1·Cu·Lut**, **1·Cu·Py$_2$** und **1·Cu·FLut** wurden Werte von 0,13, 0,04, 0,02 bzw. 0,01 ermittelt.

Zeitaufgelöste Spektroskopie gab Aufschluss über die an den Emissionen der untersuchten Verbindungen beteiligten Geschwindigkeitskonstanten, die darauf hindeuten, dass **1·Cu·Lut** im Nanosekundenbereich über den Relaxationspfad der prompten Fluoreszenz emittiert, während **1·Cu·Py$_2$** dies im Millisekundenbereich über eine langlebige Phosphoreszenz tut. TADF wurde für beide Verbindungen ausgeschlossen, da die Temperaturabhängigkeit sowohl der steady-state als auch der zeitaufgelösten Emission nicht den Erwartungen entspricht. Die Berechnungen deuten auf eine lokale Anregung auf dem Carben hin, was auch experimentell durch eine starke vibronische Feinstruktur der Emissionsbanden dieser Verbindungen belegt wurde. Für **1·Cu·FPy$_2$** und **1·Cu·FLut** zeigt die zeitaufgelöste Spektroskopie in beiden Fällen die für TADF erwartete Temperaturabhängigkeit, nämlich eine Verlängerung der Lebensdauern im Mikrosekundenbereich bei niedriger Temperatur.

Die Arrhenius-Plots aus diesen Lebensdauern im Mikrosekundenbereich ergibt einen energetischen Abstand von S_1 und T_1 von 52 meV **(1·Cu·FPy$_2$)** und 69 meV **(1·Cu·FLut)**; systematisch niedriger als die Werte, die sich aus der spektralen Verschiebung der Emissionen im Hoch- und Tieftemperaturgrenzfall ergeben. Dies wird darauf zurückgeführt, dass bei niedriger Temperatur auch Phosphoreszenz aktiv ist, die eine sehr ähnliche Geschwindigkeitskonstante hat wie das rISC, bzw. das TADF.

Schließlich lieferte die zeitaufgelöste Emissionsspektroskopie die notwendigen spektralen Informationen über die beteiligten Emissionstypen. Es stellte sich heraus, dass in **1·Cu·FPy$_2$** nur Emission im Mikrosekundenbereich beobachtet wird. Vermutlich kann die prompte Fluoreszenz nicht mit der Rate des ISC konkurrieren. Die Emission, die bei niedrigeren Temperaturen im Millisekundenbereich beobachtet wurde, stammte nachweislich ausnahmslos von dissoziiertem Liganden. Die beobachtete Rotverschiebung der im Mikrosekundenbereich erhaltenen Spektren bestätigt in der Tat die Beteiligung sowohl des S_1 als auch des T_1, was die oben genannte Hypothese bestätigt. Die Bedingung der Übereinstimmung des prompten und des verzögerten Fluoreszenzspektrums kann für **1·Cu·FPy$_2$** weder verifiziert noch falsifiziert werden, da keine prompte Fluoreszenz nachgewiesen werden konnte.

Für **1·Cu·FLut** hingegen wurde Emission in allen drei Zeitbereichen beobachtet. Beim Abkühlen nimmt die Intensität der prompten FLuoreszenz ab, während gleichzeitig die Intensität der Phosphoreszenz im Mikrosekunden- und Millisekundenbereich zunimmt. Auch hier ist davon auszugehen, dass TADF und Phosphoreszenz mit sehr ähnlichen Geschwindigkeitskonstanten ablaufen. Vergleicht man die Spektren in den verschiedenen Zeitbereichen, so zeigt sich bei Temperaturen unter 220 K eine deutliche Übereinstimmung zwischen dem Mikrosekunden- und dem Millisekundenspektrum. Bei 270 K verschiebt sich das Mikrosekundenspektrum jedoch deutlich in Richtung des Nanosekundenspektrums. Vermutlich würde eine perfekte Deckung der beiden Spektren bei höheren Temperaturen beobachtet werden, allerdings konnte dieses Experiment aufgrund von Stabilitätsproblemen nicht durchgeführt werden. Dennoch ist auch für **1·Cu·FLut** TADF höchstwahrscheinlich wirksam, allerdings nur bei höheren Temperaturen, was mit dem größeren $\Delta E_{S1\text{-}T1}$ in Einklang steht. Die Phosphoreszenz ist im gesamten beobachteten Temperaturbereich aktiv, wobei sie bei 220 K und darunter die primäre Emissionsquelle ist.

Schließlich wurden zwei Kupfer(I)-Komplexe identifiziert, die alle für TADF erwarteten Kriterien erfüllen, soweit die physikalischen, chemischen und instrumentellen Restriktionen diese Analysen zulassen. Die eingangs gemachte Aussage, dass TADF eine sehr unauffällige und daher schwer zu erfassende Eigenschaft ist, wurde mehrfach bestätigt. Auch wenn TADF mit hoher Wahrscheinlichkeit in den beiden Verbindungen **1·Cu·FLut** und **1·Cu·FPy$_2$** aktiv ist, gibt es noch offene Fragen, die beantwortet werden müssen. Vor allem die spektrale Auflösung verhinderte letztlich einen eindeutigen Nachweis, da die Emissionen von S_1 und T_1 offenbar sehr nahe beieinander liegen. Dennoch unterstreicht dieses Problem die energetische Nähe dieser beiden Zustände, die für das Auftreten von TADF unerlässlich ist. Eine höhere spektrale Auflösung würde es dann ermöglichen, die beiden unterschiedlichen Emissionen zu trennen.

6 Experimental Section

6.1 Instruments and Software

NMR spectra were measured on a Bruker Avance - 300 or a Bruker Avance - 600. Mass spectra were obtained on a Bruker DALTONICS Ultraflex (MALDI-TOF), a Finnigan LCQ Ion-Trap-API (ESI) or a Bruker DALTONICS UHR-QTOF maXis 4g (HR-ESI). Elemental analyses were obtained on an Elementar vario MICRO cube.

X ray crystal structure data were collected on a Bruker Apex Duo diffractometer or a Rigaku XtaLAB-Synergy S diffractometer and refined using Olex2 by OlexSys Ltd. Thermal ellipsoid plots and simulated powder patterns were generated with Mercury by the Cambridge Crystallographic Data Centre.[128] PXRD histograms were recorded on a Rigaku MiniFlex.

Optical measurements on cyclohexane suspensions

Steady-state emission and excitation data were obtained on a Horiba Jobin Yvon Fluorolog FL3-22 or a PicoQuant FluoTime 300 equipped with an NKT Photonics SuperK Extreme White Light Laser. The samples were prepared in the respective concentration in 3.0 ml of cyclohexane and shock-frozen under constant mixing in a -20 °C ethanol bath to ensure homogeneity. UV-Vis absorption data were obtained on a Agilent Technologies Cary 4000 UV-Vis spectrophotometer in liquid suspension under constant stirring using a Hellma cuv-o-stirr model 333. Time resolved measurements were obtained on a PicoQuant FluoTime 300 equipped with an NKT Photonics SuperK Extreme White Light Laser (ns) or with a Cobolt 06-MLD laser with 375 nm (µs, ms). Measurements at low temperatures were carried out in a Sumitomo Cryostat powered with a Sumitomo HC-4E Helium compressor (Cryogenics of America).

Optical measurements on powdered samples

Steady-state emission and excitation data were obtained on an Edinburgh Instruments FLS1000 spectrofluorometer with a 450 W Xe lamp. All spectra were corrected for wavelength-dependent grating efficiency and detector sensitivity, while the excitation spectra were additionally corrected for potentially fluctuating lamp intensity.

Luminescence spectra at 80 K were obtained by placing powdered sample into a liquid N_2-cooled Linkam THMS600 temperature cell that was coupled to the above spectrometer with optical fiber bundles.

Time resolved measurements were obtained on the above device equipped with either a 375 nm EPL, a 450 nm VPL or a µF2 Flashlamp, all from Edinburgh Instruments, as excitation source. The samples were placed on a quartz dish and covered with a quartz lid. Absolute photoluminescence quantum yields and reflectance spectra were measured on the same device at room temperature with an integrating sphere coated with BenFlect®.

All Time-resolved emission data were fitted using ChiSurf.[129,130] Global fits of TRES data were obtained using BatchFitting.[131]

6.2 Syntheses and analytical data

6.2.1 General considerations

All syntheses were carried out under dry nitrogen using the Schlenk technique or under argon in a glovebox, unless otherwise stated. The oven dried glassware used was triple evacuated and flooded with inert gas. Solvents were dried by storing them over the appropriate, activated molecular sieve for two days prior to use and deoxygenated by evacuating them three times at room temperature under strong stirring and purging with dry nitrogen after each cycle.

6.2.2 Analytical assessments

The molecules synthesized were characterised by NMR spectroscopy, mass spectrometry, elemental analysis (CHNS) and SC-XRD. For NMR analyses, the sample was dissolved in 0.5 ml of a suitable deuterated solvent. The residual proton signals of the solvent served as internal standard for referencing. The ^{13}C-NMR-spectra were measured proton decoupled. The evaluation of the spectra is given according to the following pattern: chemical shift [ppm] (multiplicity, coupling constant [Hz], integral, assignment). The multiplicities are abbreviated as follows: s: Singlet, d: Doublet, t: Triplet, m: multiplet. The mass spectra were obtained either by ESI or MALDI-TOF. The evaluation of these spectra is given according to the following pattern: MS (type of measurement): m/z = [mass/charge ratio] (assignment).

6.2.3 Reagents

The following reagents were synthesized[a] or purified[b] according to literature procedures. All other chemicals were commercially purchased and used as received.

- *N*,*N*'-bis(2,6-Diisopropylphenyl)formamidine.132,[a]
- 2-Methylmalonyl dichloride.133,[a]
- Copper(I)-chloride.134,135,[b]
- Lithium (1,3-Bis(2,6-diisopropylphenyl)-5-methyl-6-oxo-6H-pyrimidin-2-ylidene-4-olate) copper(I) chloride.92,[a]
- 1,3-dimethyl-1,3-dihydro-2H-imidazole-2-selenone.136,[a]
- 1,3-diisopropyl-1,3-dihydro-2H-imidazole-2-selenone.136,[a]
- 1,3-di-*tert*-butyl-1,3-dihydro-2H-imidazole-2-selenone.136,[a]
- 1,3-dimethyl-1,3-dihydro-2H-benzo[d]imidazole-2-selenone.136,[a]

6.2.4 Syntheses

6.2.4.1 Modified synthesis of 1^H

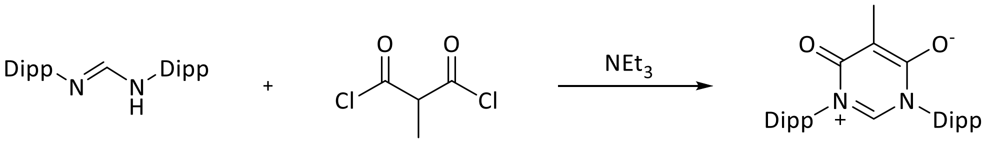

[446.64]

The synthesis reported in the literature is modified to improve upscaling. The synthesis is not carried out under exclusion of water or air. 63.2 mmol (23.04 g, 1 eq.) *N*,*N*'-bis(2,6-diisopropylphenyl)formamidine is dissolved in 100 ml dichloromethane in a 250 ml single-neck round-bottom flask. 158.2 mmol triethylamine (22 ml, 2.5 eq.) are added and the solution is cooled to 0 °C in an ice bath. A dropping funnel is filled with 69.6 mmol 2-methylmalonyl dichloride (10.78 g, 1.1 eq.) dissolved in 50 ml of dichloromethane. The solutions are combined dropwise and the ice bath is removed at the end of the addition. After 45 min the volatile components are removed with a rotary evaporator. The solid residue is ground up using mortar and pestle and is then applied to a packed 10 cm pad of silica gel under ethyl acetate. The crude product is eluted with ethyl acetate until the eluate no longer leaves a spot on a TLC plate. The volatile components are removed again and the residual solid is heated to reflux in 300 ml *n*-hexane. Just enough ethyl acetate is added to the boiling suspension until a complete dissolution of the product is observed. The solution is cooled to Rt and then stored at -20 °C for 16 h, during which time yellow crystals form. The supernatant is decanted and the crystals are washed several times with cold *n*-hexane. To remove incorporated ethyl acetate, the crystals are heated to 60 °C for 16 h in vacuo.

Yield 23.4 g light yellow solid (83%).

^{1}H-NMR (300 MHz, $CDCl_3$) δ = 8.06 (s, 1H, N2CH), 7.44 (t, J = 7.7 Hz, 2H, CH_{Dipp}), 7.26 (d, J = 7.7 Hz, 4H, CH_{Dipp}), 2.77 (sept, J = 6.8 Hz, 4H, CH_{iPr}), 2.08 (s, 3H, $CH_{3\ apical}$), 1.28 (d, J = 6.8 Hz, 12H, $CH_{3\ iPr}$), 1.18 (d, J = 6.8 Hz, 12H, $CH_{3\ iPr}$) ppm. (In agreement with original publication.[92])

Elemental analysis for $C_{29}H_{38}N_2O_2$

Calculated C 77.99, H 8.58, N 6.27

Found C 78.13, H 8.46, N 6.23

6.2.4.2 Synthesis of 4-formyl-2,6-lutidine

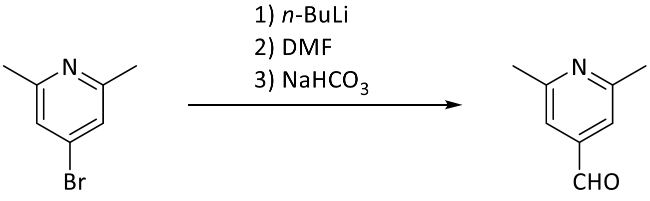

[135.17]

A 100 ml Schlenk flask is charged with 5.53 mmol of 4-bromo-2,6-lutidine (1.029 g, 1 eq.), dissolved in 20 ml of dry tetrahydrofuran. After cooling to -80 °C, 5.53 mmol (1 eq.) of *n*-butyl lithium solution (2.5 M in n-pentane) is added dropwise. After 15 min at -80 °C, 5.53 mmol of dry DMF (428 µl, 1 eq.) is added dropwise to the red solution and the mixture is stirred for 3 h in the cooling bath, during which time it slowly warms up and changes colour to yellow. The cooling bath is removed and 6 ml of saturated, aqueous $NaHCO_3$ solution, 10 ml of deionized water as well as 10 ml of dichloromethane are added. The mixture is extracted three times with dichloromethane and the combined organic phases are dried over anhydrous $MgSO_4$. After removal of the solvent, the residual brown oil might be stored overnight in a freezer or is directly subjected to a recondensation step. For this, the crude product is placed into a 50 ml Schlenk flask, which is connected via a short glass connector (120° angle) to a 50 ml pointed bottom Schlenk flask. The system is held in high vacuum for 10 min under stirring to remove residual volatiles. Condensation of the product is carried out thereafter from a 60 °C oil bath to the receiving flask cooled in LN_2 in high vacuum. The product is very sensitive to light (fast yellowing) and is stored at -24 °C under inert gas.

Yield 524 mg colourless oil (70 %).

^{1}H-NMR (300 MHz, $CDCl_3$) δ = 10.00 (s, 1H, CHO), 7.35 (s, 2H, H_{Ar}), 2.62 (s, 3H, H_{Me}) ppm. (In agreement with original publication.[110])

6.2.4.3 Synthesis of $[1\cdot\mathrm{Cu}]_n$

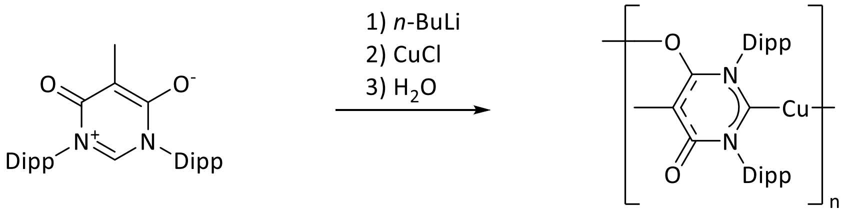

[509.17]

Into a 250 ml Schlenk flask 1.12 mmol (500 mg, 1 eq.) 1^{H} are added and dissolved in 50 ml tetrahydrofuran. To the yellow solution cooled to -20 °C, 1.175 mmol (470 µl, 1.05 eq.) n-butyllithium solution (2.5 M in n-pentane) is added dropwise. The cooling bath is removed and the resulting colourless solution is stirred for 15 min. 1.13 mmol (112 mg, 1.01 eq.) of copper(I) chloride is added as a solid and the mixture is stirred for 1 h, during which time the solid almost completely dissolves. All volatiles are removed in vacuo and the residue is taken up in 20 ml of dichloromethane. The suspension is filtered (Celite®, dichloromethane) and the solvent is again removed in vacuo. The resulting colourless solid is dissolved in 10 ml of acetonitrile and the product is completely precipitated by addition of 100 ml of deionized water. The product is collected by centrifugation and the supernatant is decanted. The solid is washed two times each with deionized water, methanol and diethyl ether, centrifuging it after each washing step. The product is obtained as a colourless powder after drying in vacuo overnight.

Yield 519 mg colourless solid (91%)

^{1}H-NMR (300 MHz, CD_3CN) δ = 7,40 – 7,33 (m, 2H, $H_{Dipp|para}$), 7,27 – 7,21 (m, 4H, $H_{Dipp|meta}$), 2,87 (sept, $^3J_{HH}$ = 7,0 Hz, 4H, CH_{iPr}), 1,76 (s, 3H, $CH_{3\ apical}$), 1,20 (d, $^3J_{HH}$ = 6,9 Hz, 12H, $CH_{3\ iPr}$), 1,15 (d, $^3J_{HH}$ = 6,8 Hz, 12H, $CH_{3\ iPr}$) ppm.

MS (ESI, CH_3CN) *m/z* = 550 (1-Cu-MeCN), 1058 ($[NHC\text{-}Cu]_2$-MeCN)

Elemental analysis for $C_{29}H_{37}CuN_2O_2$

Calculated	C 68,41; H 7,32; N 5,50
Found	C 68,20; H 7,32; N 5,43

Due to its poor solubility, the maximum concentration of the product in all common NMR solvents is too low for ^{13}C-NMR spectroscopy.

6.2.4.4 Synthesis of 1·CuI^{Na}

Free carbene route

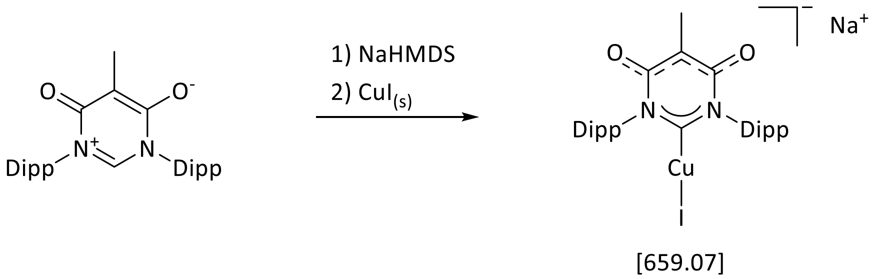

A 100 ml Schlenk flask is charged with 1.12 mmol of 1^H (500 mg, 1 eq.) and 1.34 mmol of copper(I) iodide (256 mg, 1.2 eq.). The solids are suspended in 35 ml of dry tetrahydrofuran and 1.34 mmol of NaHMDS solution in tetrahydrofuran (2M, 670 µl, 1.2 eq.) are added dropwise. A clear solution is obtained after treatment in an ultrasonic bath. After 1 h of stirring, all volatiles are removed in vacuo and the crude product is resolubilized in 20 ml of dichloromethane. A few drops of tetrahydrofuran are added and the solution is filtered (Celite®, dichloromethane). The volatiles are removed again and the product is dried in vacuo overnight.

Yield 642 mg colourless solid (87%), minus tetrahydrofuran coordinated to the Na$^+$.

[1·Cu]$_n$ route

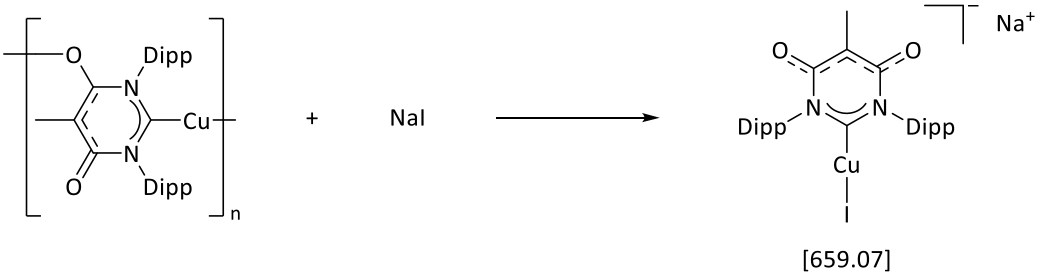

A 10 ml microwave vessel is charged with 0.198 mmol of **[1·Cu]$_n$** (101 mg, 1 eq.) and 0.200 mmol of anhydrous sodium iodide (30 mg, 1.01 eq.). 9 ml of tetrahydrofuran and 1 ml of acetonitrile are added, whereafter a clear solution is obtained. All volatiles are removed and the product is dried in vacuo overnight.

Yield 127 mg colourless solid (97%).

^{1}H-NMR (300 MHz, CD_3CN) δ = 7.40 – 7.34 (m, 2H, H_{Dipp}), 7.27 – 7.19 (m, 4H, H_{Dipp}), 2.86 (sept, 4H, H_{iPr}), 1.79 (s, 3H, $CH_{3,apical}$), 1.25 – 1.14 (m, 24H, $CH_{3,Dipp}$) ppm.

^{13}C{^{1}H}-NMR (75 MHz, CD_3CN) δ = 206.9 (s, carbene), 163.4 (s, CO), 146.9 (s, C_{Dipp}), 139.7 (s, C_{Dipp}), 129.5 (s, C_{Dipp}), 124.4 (s, C_{Dipp}), 90.8 (s, C_{apical}), 29.4 (s, CH_{iPr}), 24.4 (s, $CH_{3,Dipp}$), 24.2 (s, $CH_{3,Dipp}$), 9.8 ($CH_{3,apical}$) ppm.

General synthetic routes for complexes of the type 1·Cu·L$_n$

Method A

Complexes requiring a stoichiometric amount of ligand during synthesis.

[1·Cu]$_n$ is added to a 10 ml microwave vessel. In case of solid ligand, 1.02 equivalents of it are added at this point as well. The vessel is sealed with a crimp cap and 7 ml of dichloromethane are added via syringe through the septum. In case of liquid ligand, 1.02 equivalents of it are added via syringe at this point. The reaction mixture is treated in an ultrasonic bath, after which [1·Cu]$_n$ is dissolved. The mixture is taken up with a syringe and filtered through a PTFE syringe filter into a Schlenk flask. The volatiles are removed in vacuo and the resulting solid washed once with diethyl ether and dried overnight in vacuo.

Method B

Complexes requiring an excess of ligand during synthesis.

[1·Cu]$_n$ is added to a 10 ml microwave vessel. The vessel is sealed with a crimp cap and 7 ml of dichloromethane are added via syringe through the septum. The appropriate amount of ligand is added via syringe (see below) and the reaction mixture is treated in an ultrasonic bath, after which [1·Cu]$_n$ is dissolved. The mixture is taken up with a syringe and filtered through a PTFE syringe filter into a Schlenk flask. The volatiles are removed in vacuo and the resulting solid washed five times with diethyl ether and dried overnight in vacuo.

6.2.4.5 Synthesis of (1·Cu·Py$_2$)

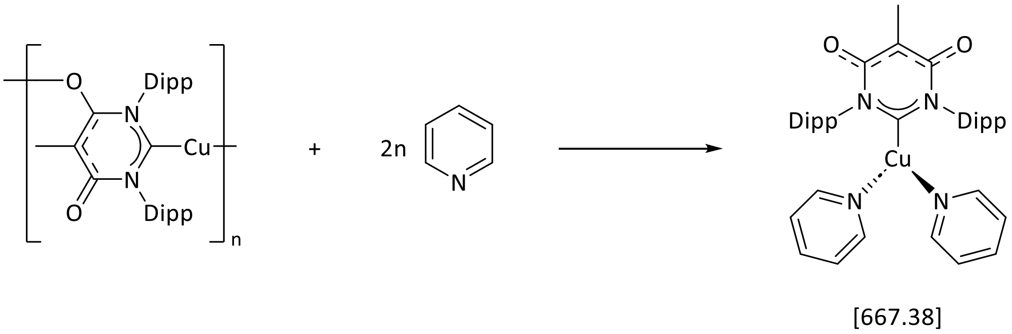

Starting from 0.20 mmol [1·Cu]$_n$ (102 mg) and following method B with 10 eq. of pyridine, this complex is isolated as a white solid. Crystals suitable for XRD studies were obtained by slow diffusion of diethyl ether in a saturated methanol solution containing excess pyridine.

Yield 121 mg colourless solid (91%).

^{1}H-NMR (300 MHz, CD$_3$CN) δ = 8,48 – 8,43 (m, 4H, H$_{\text{Py, ortho}}$), 7,75 (tt, $^3J_{HH}$ = 7,7 Hz, $^4J_{HH}$ = 1,8 Hz, 2H, H$_{\text{Py, para}}$), 7,40 – 7,30 (m, 6H, H$_{\text{Dipp, para}}$ + H$_{\text{Py, meta}}$), 7,27 – 7,22 (m, 4H, H$_{\text{Dipp, meta}}$), 2,88 (sept, $^3J_{HH}$ = 6,7 Hz, 4H, CH$_{i\text{Pr}}$), 1,78 (s, 3H, CH$_{3\text{ apical}}$), 1,19 (d, $^3J_{HH}$ = 6,8 Hz, 12H, CH$_{3\ i\text{Pr}}$), 1,15 (d, $^3J_{HH}$ = 6,9 Hz, 12H, CH$_{3\ i\text{Pr}}$) ppm.

^{13}C{^{1}H}-NMR (75 MHz, CD$_3$CN) δ = 197,6 (s, Carbene), 163,7 (s, C=O), 150,4 (s, Ar), 146,5 (s, Ar), 139,2 (s, Ar), 137,3 (s, Ar), 129,8 (s, Ar), 124,8 (s, Ar), 124,7 (s, Ar), 93,8 (s, C$_{\text{apical}}$), 29,4 (s, CH$_{i\text{Pr}}$), 24,7 (CH$_{3\ i\text{Pr}}$), 24,3 (s, CH$_{3\ i\text{Pr}}$), 10,0 (s, CH$_{3\text{ apical}}$) ppm.

MS (MALDI-TOF, DCM) m/z = 509.3 (NHC-Cu-H$^+$), 588.4 (NHC-Cu-Py-H$^+$), 1017.6 (NHC-Cu-H)$_2^+$, 1528.0 (NHC-Cu-H)$_3^+$.

Elemental analysis calculated for C$_{39}$H$_{47}$CuN$_4$O$_2$: C 70.19; H 7.10; N 8.40, Found: C 69,95; H 7,08; N 8,15.

6.2.4.6 Synthesis of 1·Cu·FPy$_2$

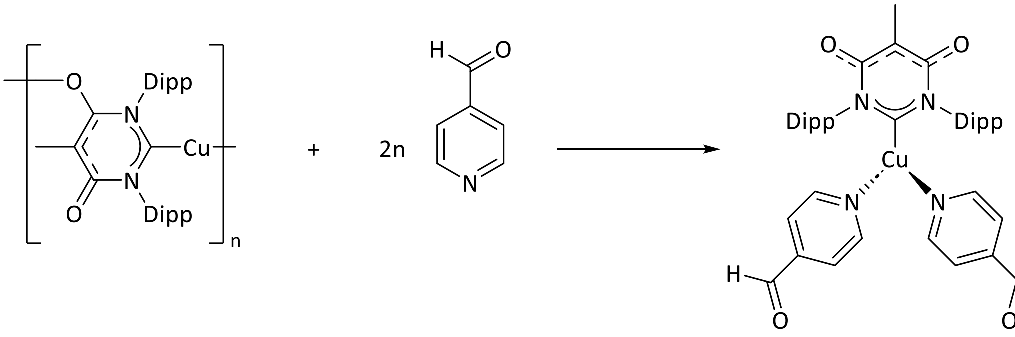

[723.40]

Starting from 0.20 mmol [1·Cu]$_n$ (102 mg) and following method B with 50 eq. of 4-formylpyridine, this complex is isolated as an orange solid. Crystals suitable for XRD studies were obtained by cooling down a saturated solution in dichloromethane with excess of ligand to -20 °C.

Yield 119 mg yellow solid (82%).

Elemental analysis calculated for $C_{41}H_{47}CuN_4O_4$: C 68.07; H 6.55; N 7.75, Found C 67.89; H 6.39; N 7.63.

Note. Due to fast degradation in solution, ^{1}H-NMR, ^{13}C-NMR and mass spectrometry data are not available.

6.2.4.7 Synthesis of 1·Cu·4AcPy$_2$

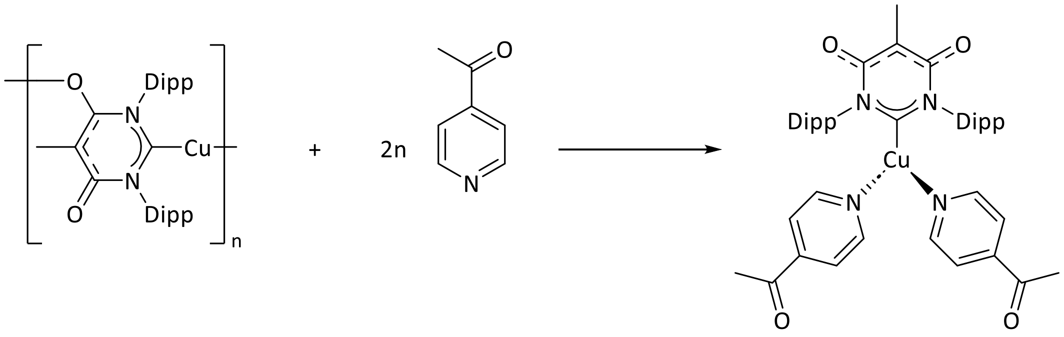

Starting from 0.20 mmol [1·Cu]$_n$ (102 mg) and following method B with 30 equivalents of 4-acetyl pyridine, this complex is isolated as a yellow solid. Crystals suitable for XRD studies were obtained by slow evaporation of a saturated dichloromethane solution with excess ligand.

Yield 108 mg yellow solid (72%).

Elemental analysis calculated for $C_{43}H_{51}CuN_4O_4$: C 68.73; H 6.84; N 7.46, Found C 68.71; H 6.64; N 7.39.

Note. Due to fast degradation in solution, ^{1}H-NMR, ^{13}C-NMR and mass spectrometry data are not available.

6.2.4.8 Synthesis of 1·Cu·^{N,O}2AcPy

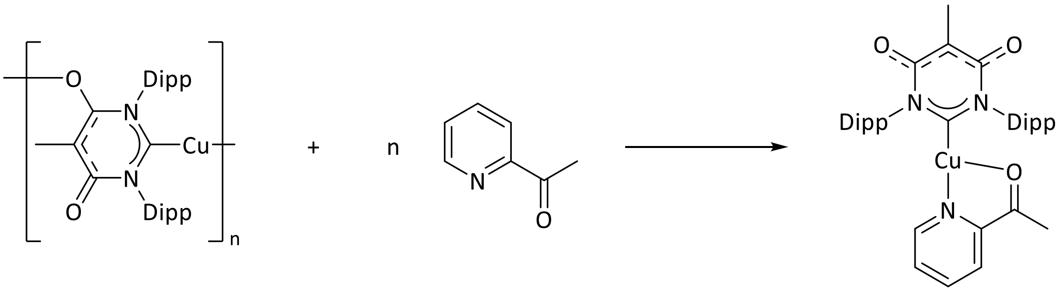

[630.31]

Starting from 0.10 mmol [1·Cu]$_n$ (51 mg) and following method B with 20 equivalents of 2-acetyl pyridine, this complex is isolated as a dark-red solid. Crystals suitable for XRD studies were obtained by slow evaporation of a saturated dichloromethane solution with excess ligand and a few drops of methanol.

Yield 56 mg red solid (89%).

MS (MALDI-TOF, DCM) m/z = 509.1 (NHC-Cu-H$^+$), 630.3 (NHC-Cu-(2-AcPy)-H$^+$), 1017.4 (NHC-Cu-H)$_2^+$, 1527.6 (NHC-Cu-H)$_3^+$.

MS (HR-ESI, DCM) calcd. m/z = 630.2751, found m/z = 630.2755 (NHC-Cu-(2-acpy)-H)$^+$.

*The general procedure was modified in that 6 ml of dichloromethane and 1 ml of methanol was used as solvent.

Note. Due to fast degradation in solution, ^{1}H-NMR and ^{13}C-NMR data are not available.

6.2.4.9 Synthesis of 1·Cu·Bpy

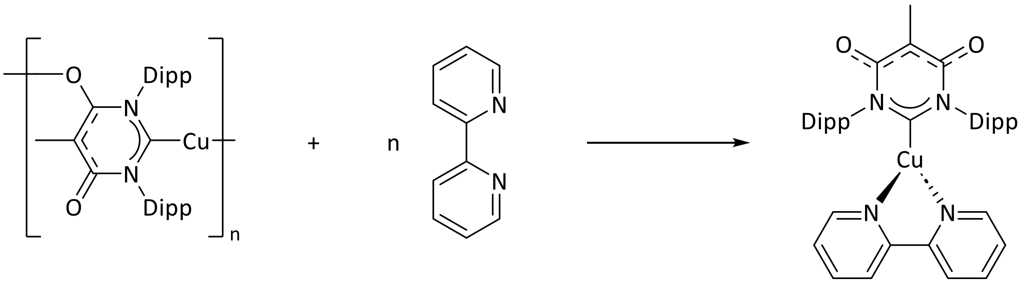

[665.36]

Starting from 0.10 mmol $[1\cdot Cu]_n$ (51 mg) and following method A, this complex is isolated as a yellow solid. Crystals suitable for XRD studies were obtained by layering a saturated dichloromethane solution with *n*-hexane.

Yield 62 mg yellow solid (93%).

^{1}H-NMR (300 MHz, CD_2Cl_2) δ = 7.92 (d, 2H, $^3J_{HH}$ = 8.1 Hz, NCH_{Bipy}), 7.82 (dt, J_{HH} = 7.7/1.6 Hz, Bipy), 7.42 – 7.35 (m, 2H, $H_{Dipp,\ para}$), 7.26 – 7.22 (m, 4H, $H_{Dipp,\ para}$), 7.21 – 7.16 (m, 2H, Bipy), 6.79 (d, J_{HH} = 4.9 Hz, $N\text{-}C^{C}\text{-}CH_{Bipy}$), 3.14 (sept, J_{HH} = 7.0 Hz, 4H, ^{iPr}CH), 1.94 (s, 3H, $CH_{3,\ apical}$), 1.22 (d, J_{HH} = 6.9 Hz, 12H, $CH_{3,\ Dipp}$), 1.05 (d, J_{HH} = 6.9 Hz, 12H, $CH_{3,\ Dipp}$) ppm.

^{13}C{^{1}H}-NMR (75 MHz, CD_2Cl_2) δ = 163.1 (s, CO), 151.4 (s, Bipy), 150.8 (s, Bipy), 147.0 (s, Bipy), 141.6 (s, Dipp), 139.3 (s, Dipp), 128.8 (s, Bipy), 125.6 (s, Dipp), 124.4 (s, Dipp), 121.0 (s, Bipy), 91.5 (s, C_{apical}), 28.9 (s, ^{iPr}C), 24.2 (s, $CH_{3,\ Dipp}$), 23.9 (s, $CH_{3,\ Dipp}$), 9.7 (s, $CH_{3,\ apical}$) ppm.

MS (MALDI-TOF, DCM) m/z = 665.2 $(NHC\text{-}Cu\text{-}(bipy)\text{-}H)^+$, 1173.5 $((NHC\text{-}Cu)_2\text{-}(bipy)\text{-}H)^+$.

Elemental analysis calculated for $C_{39}H_{45}CuN_4O_2$: C 70.40; H 6.82; N 8.42, Found C 70.44; H 6.89; N 8.41.

6.2.4.10 Synthesis of 1·Cu·Lut

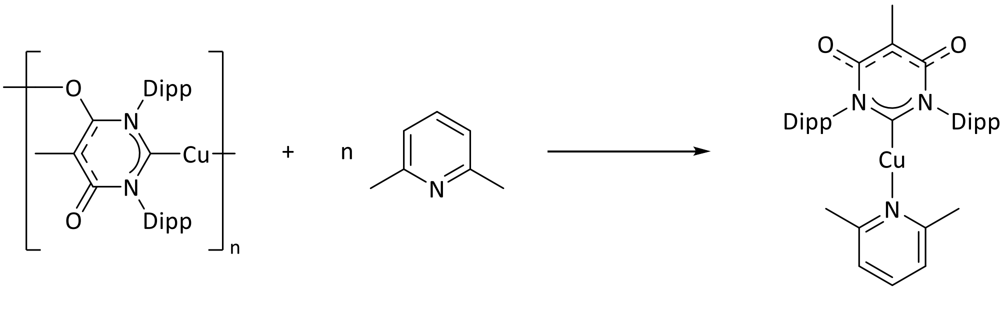

[616.33]

Starting from 0.20 mmol [1·Cu]$_n$ (102 mg) and following method A*, this complex is isolated as a white solid. Crystals suitable for XRD studies were obtained by slow diffusion of 2-methylpropane into a saturated dichloromethane solution.

Yield 67 mg colourless solid (54%).

^{1}H-NMR (600 MHz, CD_2Cl_2) δ = 7,54 (t, $^3J_{HH}$ = 7,7 Hz, 1H, $H_{Lut, para}$), 7,44 – 7,40 (m, 2H, $H_{Dipp, para}$), 7,28 – 7,25 (m, 4H, $H_{Dipp, meta}$), 6,91 (d, $^3J_{HH}$ = 7,7 Hz, 2H, $H_{Lut, meta}$), 3,01 (sept, $^3J_{HH}$ = 6,9 Hz, 4H, CH_{iPr}), 1,94 (s, 3H, $CH_{3\ apical}$), 1,48 (s, 6H, $CH_{3\ Lut}$), 1,23 (d, $^3J_{HH}$ = 6,7 Hz, 12H, $CH_{3\ iPr}$), 1,17 (d, $^3J_{HH}$ = 6,9 Hz, 12H, $CH_{3\ iPr}$) ppm.

^{13}C{^{1}H}-NMR (151 MHz, CD_2Cl_2) δ = 192,4 (s, carbene), 162,4 (s, C=O), 159,4 (s, $C_{Lut, ortho}$), 147,0 (s, C_{Lut}), 140,4 (s, Ar), 140,2 (s, Ar), 140,0 (s, C_{Lut}), 129,8 (s, Ar), 129,6 (s, Ar), 124,7 (s, Ar), 124,5 (s, Ar), 122,6 (s, Ar), 122,5 (s, Ar), 92,0 (s, C_{apical}), 29,0 (s, C_{iPr}), 24,6 (s, $C_{Lut, Methyl}$), 24,5 (s, $CH_{3\ iPr}$), 24,1 (s, $CH_{3\ iPr}$), 24,0 (s, $CH_{3\ iPr}$), 9,5 (s, $CH_{3\ apical}$) ppm.

MS (MALDI-TOF, DCM) m/z = 509.2 (NHC-Cu-H$^+$), 616.3 (NHC-Cu-(2,6-lut)-H$^+$), 1124.5 ((NHC-Cu)$_2$-(2,6-lut)-H)$^+$, 1634.7((NHC-Cu)$_3$-(2,6-lut)-H$^+$).

Elemental analysis calculated for $C_{36}H_{46}CuN_3O_2$: C 70.16; H 7.52; N 6.82, Found: C 69.93; H 7.46; N 6.74.

*The general procedure was modified in that the product was recrystallized by slow diffusion of 2-methylpropane into the obtained dichloromethane solution after filtration.

6.2.4.11 Synthesis of 1·Cu·FLut

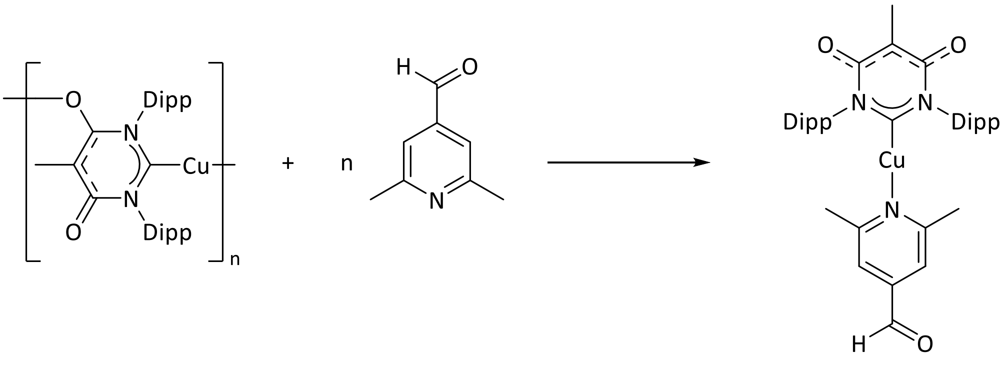

[644.34]

Starting from 0.20 mmol [1·Cu]$_n$ (102 mg) and following method B* with 7 eq. of 4-formyl-2,6-lutidine, this complex is isolated as a light-yellow solid. Crystals suitable for XRD studies were obtained by slow evaporation of a saturated dichloromethane solution with excess ligand.

Yield 72 mg light-yellow solid (56%).

Elemental analysis calculated for $C_{37}H_{46}CuN_3O_3$: C 68.97; H 7.20; N 6.52, Found C 68.61; H 7.28; N 6.38.

*The general procedure was modified in that the resulting product solution in dichloromethane with excess of ligand was allowed to slowly evaporate, resulting in the product recrystallizing.

Note. Due to fast degradation in solution, ^{1}H-NMR, ^{13}C-NMR and mass spectrometry data are not available.

6.2.4.12 Synthesis of 1·Cu·DMAP

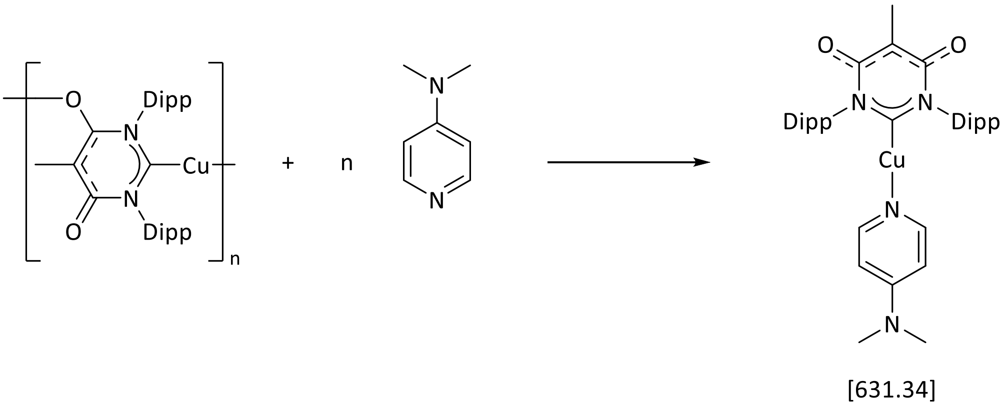

Starting from 0.20 mmol [1·Cu]$_n$ (102 mg) and following method A*, this complex is isolated as a white solid. Crystals suitable for XRD studies were directly yielded by the synthetic procedure.

Yield 40 mg colourless solid (32%).

^{1}H-NMR (300 MHz, CD_3CN) δ = 7.47 – 7.39 (m, 2H, $H_{Dipp, para}$), 7.34 – 7.26 (m, 4H, $H_{Dipp, meta}$), 7.05 – 6.92 (m, 2H, $H_{DMAP, ortho}$), 6.46 – 6.38 (m, 2H, $H_{DMAP, meta}$), 2.97 – 2.86 (m, 10H, CH_{iPr} + $CH_{3\ DMAP}$), 1.82 (s, 3H, $CH_{3\ apical}$), 1.22 – 1.14 (d, 24H, $CH_{3\ iPr}$) ppm.

^{13}C{^{1}H}-NMR (75 MHz, CD_2Cl_2) δ = 194.0 (s, carbene), 162.6 (s, CO), 146.7 (s, Dipp), 146.2 (s, DMAP), 139.9 (s, Dipp), 131.2 (s, DMAP), 129.2 (s, Dipp), 124.8 (s, DMAP), 124.2 (s, Dipp), 91.4 (s, C-Me_{apical}), 39.5 (s, N-$(CH_3)_2$), 29.0 (s, C-^{i}Pr), 24.4 (s, Dipp-CH_3), 24.3 (s, Dipp-CH_3), 9.6 (s, $CH_{3\ apical}$).

MS (MALDI-TOF, DCM) m/z = 631.3 (NHC-Cu-(DMAP)-H^+), 1139.5 ((NHC-Cu)$_2$-(DMAP)-H^+), 1649.7 ((NHC-Cu)$_3$-(DMAP)-H^+), 2157.9 ((NHC-Cu)$_4$-(DMAP)-H^+).

Elemental analysis calculated for $C_{36}H_{47}CuN_4O_2$: C 68.49; H 7.50; N 8.87, Found C 68.25; H 7.23; N 8.80.

*The general procedure was modified in that the product was recrystallized by cooling down its hot saturated acetonitrile solution.

6.2.4.13 Synthesis of 1·Cu·Acr

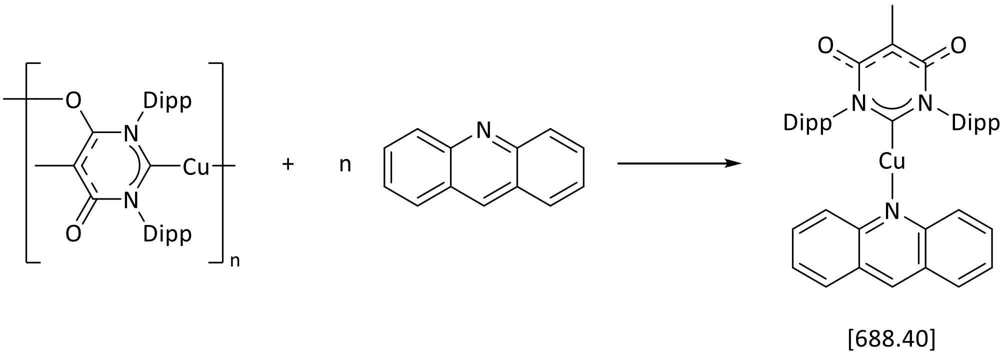

Starting from 0.14 mmol $[1\cdot Cu]_n$ (72 mg) and following method A, this complex is isolated as a yellow solid. Crystals suitable for XRD studies were obtained by slow evaporation of a saturated dichloromethane solution.

Yield 85 mg yellow solid (88%).

^{1}H-NMR (300 MHz, CD_2Cl_2) δ = 8.96 (s, 1H, $Acr_{para\text{-}H}$), 8.03 – 7.99 (m, 2H, Acr), 7.70 – 7.64 (m, 2H, $Dipp_{paraH}$), 7.59 – 7.53 (m, 4H, Acr), 7.48 – 7.41 (m, 4H, $Dipp_{meta\text{-}H}$), 6.42 – 6.14 (m, 2H, Acr), 3.12 (sept, J_{HH} = 6.8 Hz, 4H, ^{iPr}CH), 1.99 (s, 3H, $CH_{3,\,apical}$), 1.28 (d, J_{HH} = 6.8 Hz, 12H, Dipp CH_3), 1.12 (d, J_{HH} = 6.9 Hz, 12H, Dipp CH_3) ppm.

^{13}C{^{1}H}-NMR (75 MHz, CD_2Cl_2) δ = 192.1 (s, carbene), 162.4 (s, CO), 148.4 (brs, Acr), 147.5 (s, Dipp), 146.2 (brs, Acr), 139.5 (s, Dipp), 134.6 (brs, Acr), 130.2 (s, Acr para-C), 129.0 (brs, Acr), 127.1 (s, Dipp), 127.0 (brs, Acr), 126.2 (brs, Acr), 124.8 (s, Dipp), 92.2 (s, C_{apical}), 29.1 (s, ^{iPr}CH), 24.7 (s, $CH_{3,\,Dipp}$), 24.0 (s, $CH_{3,\,Dipp}$), 9.7 (s, $CH_{3,\,apical}$) ppm.

MS (MALDI-TOF, DCM) m/z = 509.2 (NHC-Cu-H^+), 688.3 (NHC-Cu-(acr)-H^+), 1017.4 ($(NHC\text{-}Cu)_2$-H^+), 1196.5 ($(NHC\text{-}Cu)_2$-(acr)-H^+).

Elemental analysis calculated for $C_{42}H_{46}CuN_3O_2$: C 73.28; H 6.74; N 6.10, Found C 73.28; H 7.01; N 5.98.

6.2.4.14 Synthesis of 1·Cu·TPP

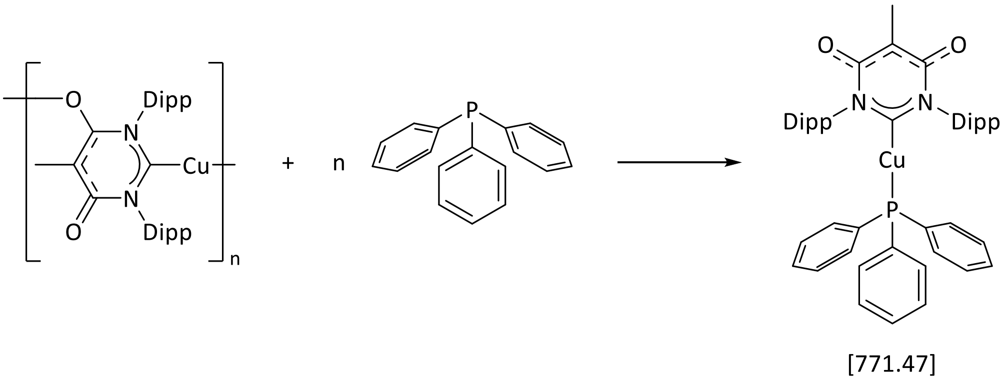

Starting from 0.093 mmol [1·Cu]$_n$ (47 mg) and following method A*, this complex is isolated as a white solid. Crystals suitable for XRD studies were obtained by slow evaporation of a saturated methanol solution.

Yield 71 mg colourless solid (99%).

^{1}H-NMR (300 MHz, CD_3OD) δ = 7.62 – 7.29 (brm, 21H, TPP + Dipp), 4.12 (sept, J_{HH} = 6.8 Hz, 4H, ^{iPr}CH), 1.96 (s, 3H, $CH_{3\ \mathrm{apical}}$), 1.23 (d, J_{HH} = 6.6 Hz, 12H, Dipp CH_3), 1.07 (d, J_{HH} = 6.6 Hz, 12H, Dipp CH_3) ppm.

^{13}C{^{1}H}-NMR (75 MHz, CD_3OD) δ = 164.0 (s, CO), 147.4 (s, Dipp), 146.9 (s, Dipp), 139.1 (s, Dipp), 134.8 (s, Dipp), 134.6 (s, Dipp), 132.0 (s, TPP), 131.1 (s, TPP), 130.4 (s, TPP), 130.3 (s, TPP), 125.6 (s, Dipp), 125.5 (s, Dipp), 95.1 (s, C_{apical}), 30.1 (s, ^{iPr}C), 25.1 (s, Dipp CH_3), 24.2 (s, Dipp CH_3), 9.3 (s, $CH_{3,\ \mathrm{apical}}$) ppm.

^{31}P-NMR (121 MHz, CD_3OD) δ = 32.4 (s, TPP) ppm.

MS (MALDI-TOF, DCM) m/z = 771.3 (NHC-Cu-(TPP)-H^+), 1281.5 ((NHC-Cu)$_2$-(TPP)-H^+), 1789.7 ((NHC-Cu)$_3$-(TPP)-H^+), 2298.0 ((NHC-Cu)$_4$-(TPP)-H^+).

Elemental analysis calculated for $C_{47}H_{52}CuN_2O_2P$: C 73.17; H 6.79; N 3.63, Found C 72.91; H 6.65; N 3.64.

*The general procedure was modified in that 6 ml of dichloromethane and 1 ml of methanol was used as solvent.

6.2.4.15 Synthesis of 1·Cu·^{Me}ImSe

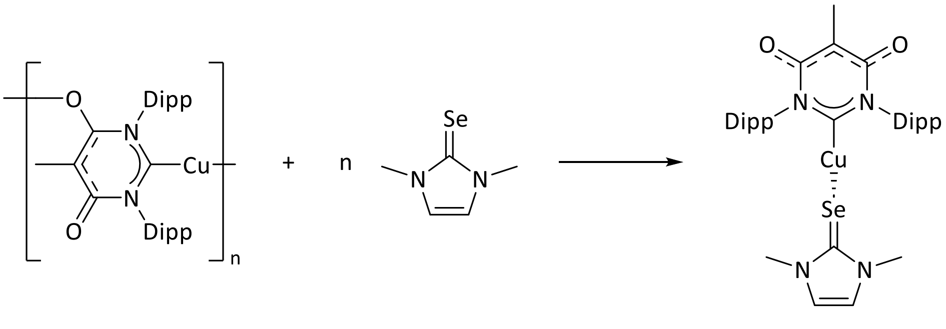

[684.28]

Starting from 0.49 mmol $[1\cdot Cu]_n$ (250 mg) and following method A, this complex is isolated as a white solid. Crystals suitable for XRD studies were obtained by cooling a saturated dichloromethane solution. The solvent during synthesis was a mixture of dichloromethane and methanol in a ratio of 1:6.

Yield 288.4 g colourless solid (86%)

^{1}H-NMR (300 MHz, CD_2Cl_2): δ = 7.33-7.41 (m, 2H, H_{Dipp}) 7.13-7.22 (m, 4H, H_{Dipp}), 6.90 (s, 2H, $H_{Se\ backbone}$), 3.33 (s, 6H, $H_{Me,Se}$), 2.73-2.89 (sept, 4H, H_{iPr}), 1.83 (s, 3H, $H_{Me,backbone}$), 1.13-1.17 (m, 24H, H_{Dipp}) ppm.

^{13}C-{^{1}H}-NMR (75 MHz, CD_2Cl_2): δ = 164.0 (s, C=O), 154.8 (s, C=Se) 147.7 (s, C_{Dipp}), 134.1 (s, C_{Dipp}), 130.6 (s, C_{Dipp}), 125.6 (s, C_{Dipp}), 123.2 (s, CH,Se backbone), 39,4 (s, CH_3,apical), 30.4 (s, CH_{iPr}), 26.0 (s, $CH_{3,iPr}$), 25.7 (s, $CH_{3,iPr}$), 11.1 (s, $CH_{3,Backbone}$) ppm.

Elemental analysis calculated for $C_{34}H_{46}CuN_4O_2Se$, calculated C 59.68; H 6.63; N 8.19 found C 59.00; H 6.65; N 7.69.

MS (ESI, CH_3CN) *m/z* = 685.3 $(M-H)^+$

6.2.4.16 Synthesis of 1·Cu·^{iPr}ImSe

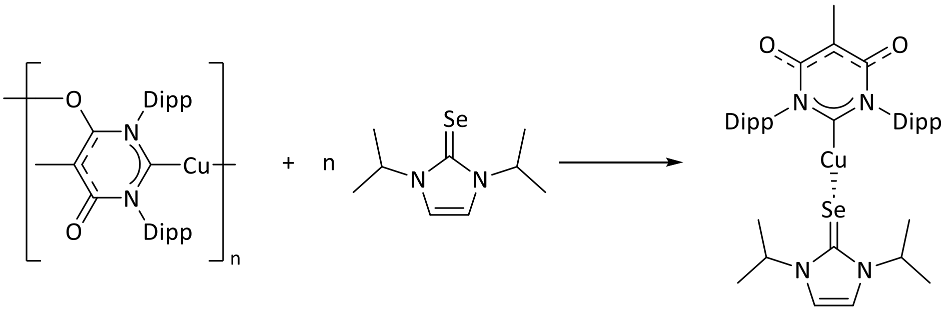

[740.40]

Starting from 0.10 mmol $[1\cdot Cu]_n$ (50 mg) and following method A, this complex is isolated as a white solid. The solvent during synthesis was a mixture of dichloromethane and methanol in a ratio of 1:6.

Yield 34 mg colourless solid (46%)

^{1}H-NMR (300 MHz, CD_2Cl_2): δ = 7.30-7.42 (m, 2H, H_{Dipp}) 7.14-7.22 (m, 4H, H_{Dipp}), 6.97 (s, 2H, $H_{Se,backbone}$), 4.93 (sept, 2H, $H_{iPr,Se}$), 2.71-2.97 (sept, 4H, $H_{iPr,Dipp}$), 1.88 (s, 3H, $CH_{3,apical}$), 1.26-1.29 (m, 12H, $H_{CH3,Se}$), 1.13-1.19 (m, 24H, $H_{CH3,Dipp}$) ppm.

^{13}C-{^{1}H}-NMR (75 MHz, CD_2Cl_2): δ = 162.6 (s, C=O), 156.9 (s, C=Se) 146.2 (s, C_{Dipp}), 139.3 (s, C_{Dipp}), 129.2 (s, C_{Dipp}), 124.1 (s, C_{Dipp}), 116.5 (s, $CH_{Se,backbone}$), 51.4 (s, $CH_{iPr,Se}$), 28.9 (s, $CH_{iPr,Dipp}$), 24.6 (s, $CH_{3,Dipp}$), 24.1 (s, $CH_{3,Dipp}$), 22.2 (s, $CH_{3,Se}$) 9.6 (s, $CH_{3,apical}$) ppm.

HR-MS (ESI, CH_3CN) m/z = 741.2711 (calculated for $C_{38}H_{53}CuN_4O_2Se$-H^+ m/z = 741.2730)

6.2.4.17 Synthesis of 1·Cu·^{tBu}ImSe

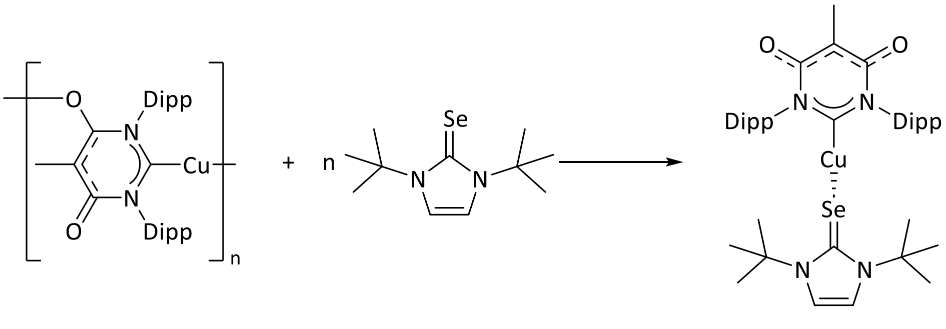

[768.44]

Starting from 0.10 mmol [1·Cu]$_n$ (50 mg) and following method A, this complex is isolated as a white solid. The solvent during synthesis was a mixture of dichloromethane and methanol in a ratio of 1:6.

^{1}H-NMR (300 MHz, CD_2Cl_2): δ = 7.57 – 7.27 (m, 8H, H_{Ar}), 2.94 – 2.74 (m, 6H, H_{iPr}), 2.00 (s, 3H, $CH_{3\ apical}$), 1.87 (brs, 12 H, H_{tBu}), 1.28 – 1.15 (m, 24H, H_{Dipp}) ppm.

^{13}C-{^{1}H}-NMR (75 MHz, CD_2Cl_2): δ = 162.7 (s, C=O), 146.4 (s, C=Se) 146.2 (s, C_{Dipp}), 139.6 (s, C_{Dipp}), 129.2 (s, C_{Dipp}), 124.2 (s, C_{Dipp}), 116.2 (s, $CH_{tBuImSe}$), 61.1 (s, $C_{iPr,Se}$), 29.1 (s, $CH_{3\text{-}tBuImSe}$), 28.9 (s, CH_{iPr}), 24.4 (s, $CH_{3,iPr}$), 24.2 (s, $CH_{3,iPr}$), 9.8 (s, $CH_{3,apical}$) ppm.

HR-MS (ESI, CH_3CN) m/z = 769.3019 (calculated for $C_{40}H_{57}CuN_4O_2Se\text{-}H^+$ m/z = 769.3016)

6.2.4.18 Synthesis of 1·Cu·^{Me}BenzImSe$_2$

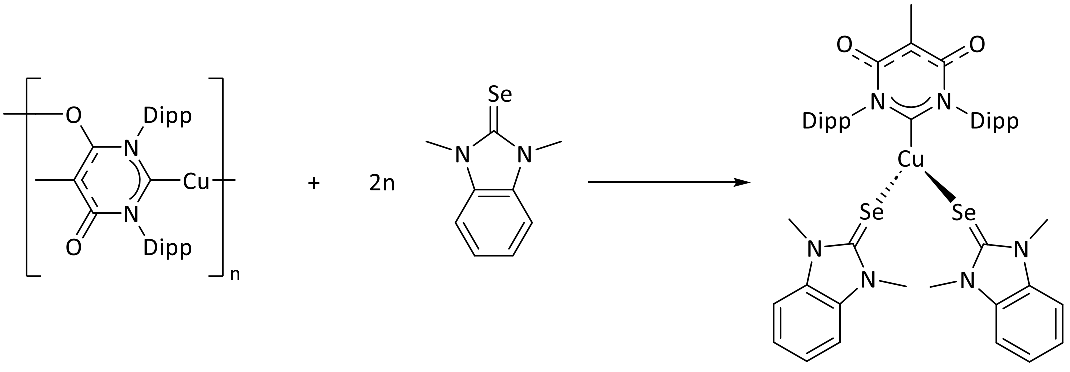

[959.50]

Starting from 0.49 mmol [1·Cu]$_n$ (250 mg) and following method A, this complex is isolated as a white solid. Crystals suitable for XRD studies were obtained by cooling a saturated dichloromethane solution. The solvent during synthesis was a mixture of dichloromethane and methanol in a ratio of 1:6.

Yield 197 mg colourless solid (42%)

^{1}H-NMR (300 MHz, CD_2Cl_2): δ = 7.31-7.37 (m, 8H, $H_{Se,Ar}$), 7.09-7.24 (m, 2H, H_{Dipp}) 6.94-7.08 (m, 4H, H_{Dipp}), 3.72 (s, 6H, $H_{Me,Se}$), 2.79-2.99 (m, 4H, $H_{iPr,Dipp}$), 1.87 (s, 3H, $CH_{3,apical}$), 1.03-1.17 (m, 24H, $CH_{3,Dipp}$) ppm.

^{13}C-{^{1}H}-NMR (75 MHz, CD_2Cl_2): δ = 208.3 (s, carbene), 154.6 (s, C=Se), , 164.0 (s, C=O), 147.7 (s, C_{Dipp}), 135.1 (s, C_{Dipp}), 132.7 (s, NCN_{Se}), 130.7 (s, C_{Dipp}), 125.9 (s, C_{Dipp}), 125.6 (s, $C_{ar,Se}$), 111.9 (s, $C_{ar,Se}$), 35.3 (s, $CH_{3,Se}$), 30.4 (s, CH_{iPr}), 26.0 (s, $CH_{3,iPr}$), 25.7 (s, $CH_{3,iPr}$), 11.1 (s, $CH_{3,acpical}$) ppm.

HR-MS (ESI, CH_3CN) m/z = 735.2238 (calculated for $C_{38}H_{47}CuN_4O_2Se$-H^+ m/z = 735.2233)

6.3 Spectroscopic data

6.3.1 Converting wavelengths to wavenumbers

The intensities I of a steady-state emission spectrum are corrected with the square of the respective wavelength λ and the cube of the respective wavenumber ν according to the following equation.

$$I_{corr} = \frac{I * \lambda^2}{\nu^3}$$

6.3.2 Smoothing of noisy data

For better visibility, a smoothing algorithm was applied to noisy data. The algorithm takes two adjacent intensities I_1 and I_2 and their arithmetic mean I_M.

$$I_M = \frac{I_1 + I_2}{2}$$

Two new intensity values I_{1N} and I_{2N} are generated.

$$I_{1N} = \frac{I_1 + I_M}{2}$$

$$I_{2N} = \frac{I_2 + I_M}{2}$$

The algorithm is employed 50 times with the pairs of intensities being chosen in an alternating fashion.

Smoothed data are shown in Figure 33. The original data are depicted in Figure E1.

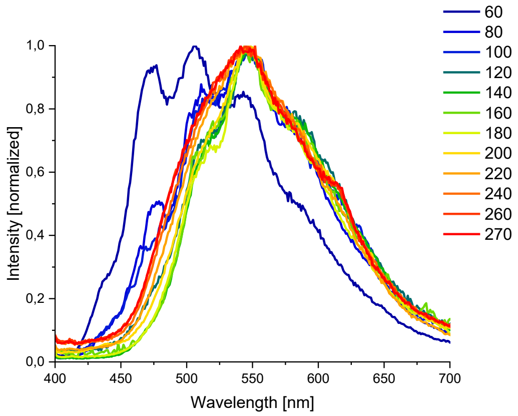

Figure E1. Original data of Figure 33.

6.3.3 Emission decay fitting

1·Cu·Py₂ Cyclohexane suspension

80 K, ms, Ex = 375 nm, Em = 500 nm

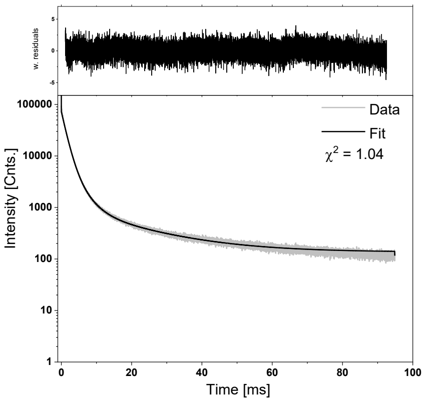

1·Cu·Py₂ Cyclohexane suspension

270 K, ms, Ex = 375 nm, Em = 500 nm

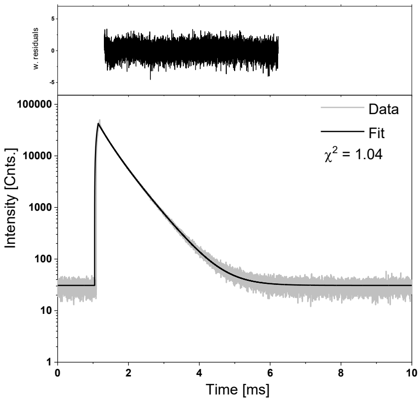

1·Cu·FPy₂ Cyclohexane suspension

80 K, µs, Ex = 375 nm, Em = 595 nm

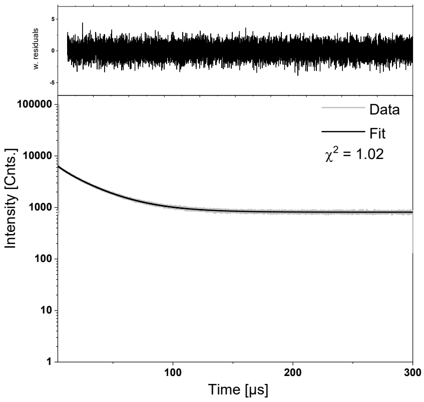

1·Cu·FPy₂ Cyclohexane suspension

270 K, µs, Ex = 375 nm, Em = 595 nm

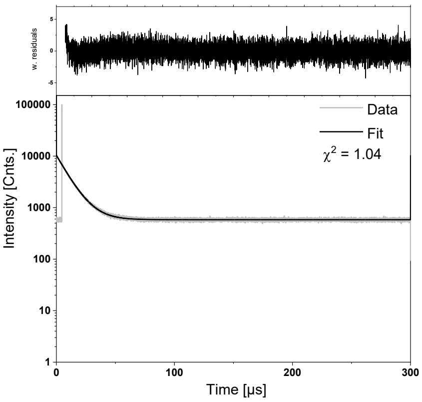

1·Cu·Lut Cyclohexane suspension

80 K, ns, Ex = 375 nm, Em = 450 nm

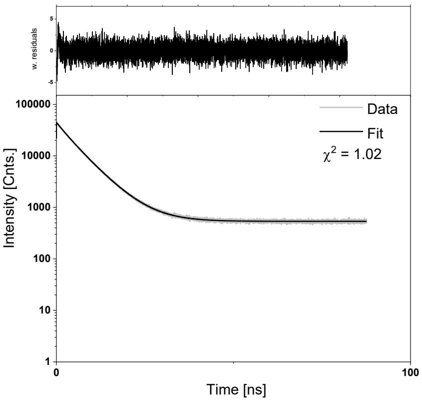

1·Cu·Lut Cyclohexane suspension

270 K, ns, Ex = 375 nm, Em = 450 nm

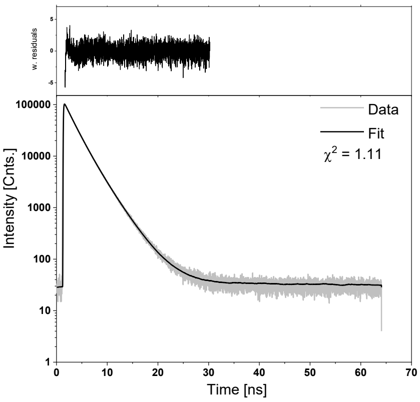

1·Cu·FLut Cyclohexane suspension

80 K, ms, Ex = 375 nm, Em = 540 nm

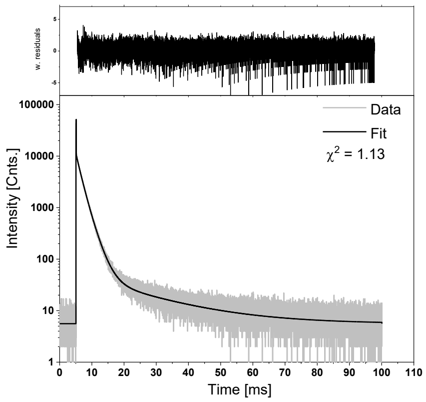

1·Cu·FLut Cyclohexane suspension

80 K, ns, Ex = 375 nm, Em = 540 nm

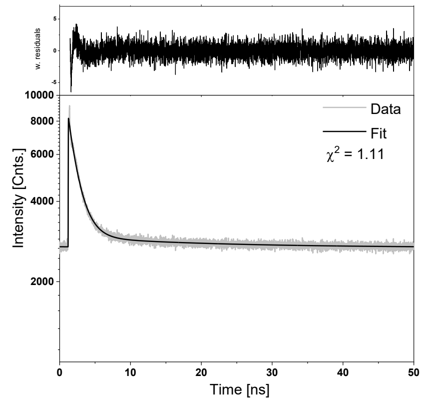

1·Cu·FLut Cyclohexane suspension

270 K, ns, Ex = 375 nm, Em = 540 nm

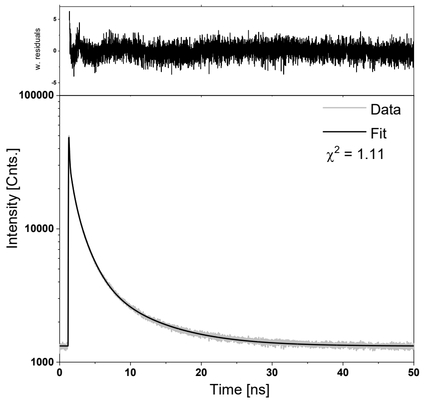

1·Cu·FLut Cyclohexane suspension

270 K, µs, Ex = 375 nm, Em = 540 nm

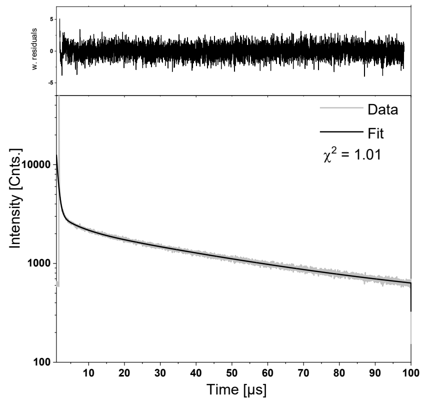

1·Cu·Py$_2$ Powder

80 K, ms, x = 375 nm, Em = 500 nm

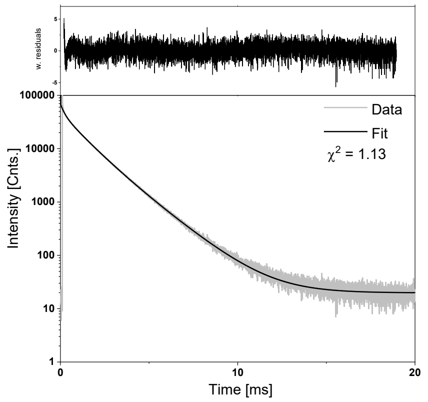

1·Cu·Py$_2$ Powder

80 K, ms, Ex = 375 nm, Em = 500 nm

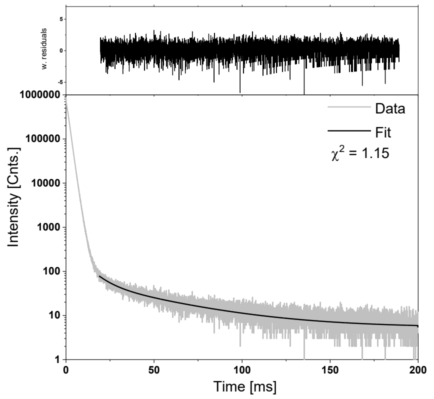

1·Cu·Py$_2$ Powder

298 K, ms, Ex = 375 nm, Em = 500 nm

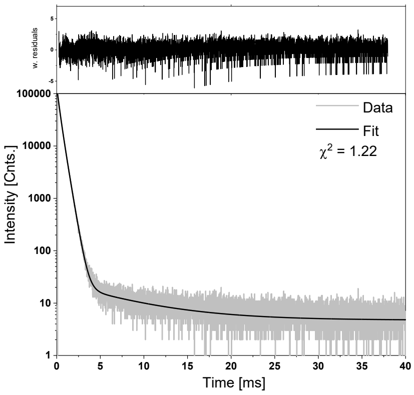

1·Cu·FPy$_2$ Powder

80 K, µs, Ex = 450 nm, Em = 595 nm

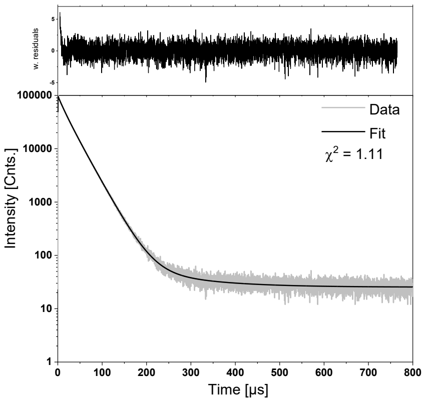

1·Cu·FPy$_2$ Powder

298 K, µs, Ex = 420 nm, Em = 595 nm

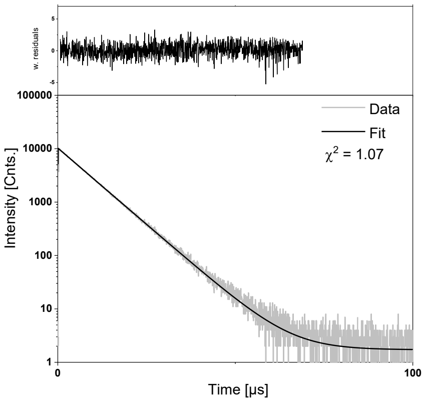

1·Cu·Lut Powder

298 K, ns, Ex = 375 nm, Em = 450 nm

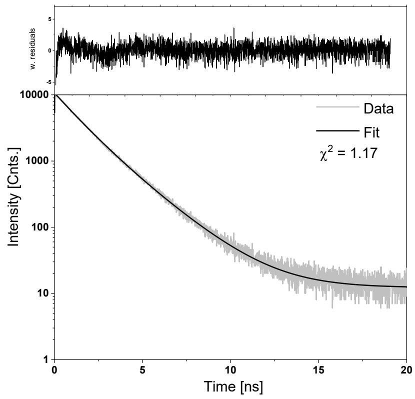

1·Cu·Lut Powder

80 K, ns, Ex = 375 nm, Em = 450 nm

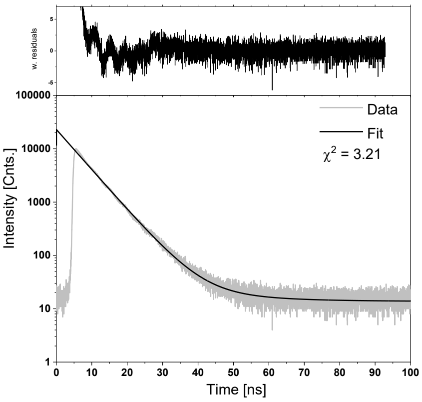

1·Cu·FLut Powder

80 K, ns, Ex = 375 nm, Em = 540 nm

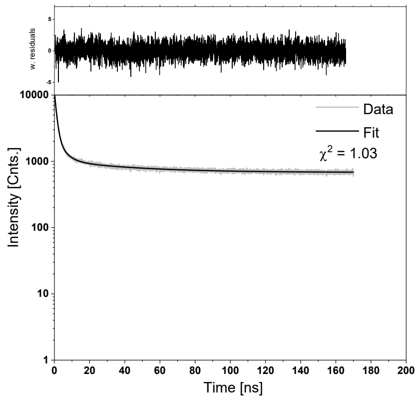

1·Cu·FLut Powder

80 K, ms, Ex = 375 nm, Em = 540 nm

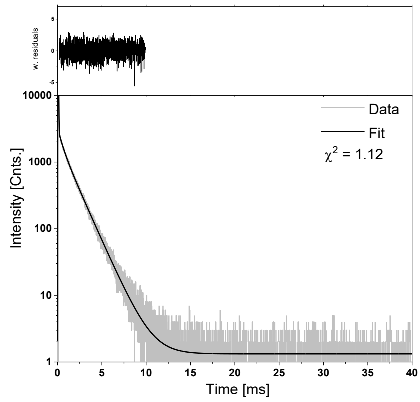

1·Cu·FLut Powder

298 K, µs, Ex = 420 nm, Em = 480 nm

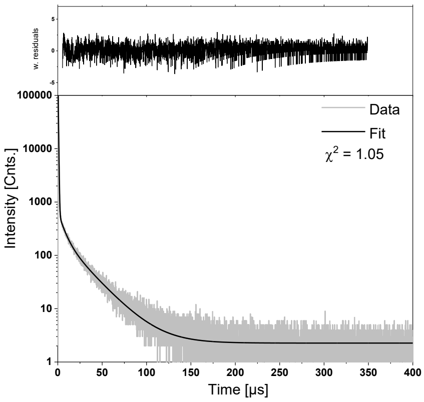

1·Cu·FLut Powder

298 K, ns, Ex = 375 nm, Em = 540 nm

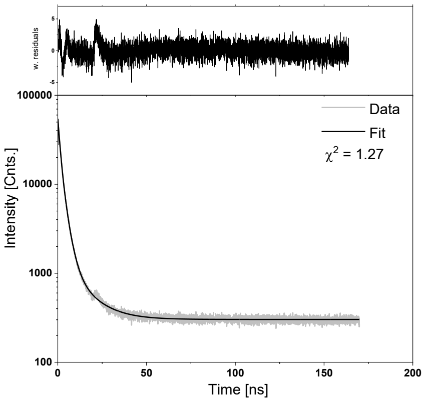

Table E1. Fit results for the temperature series of **1·Cu·FPy$_2$** in cyclohexane suspension.

T [K]	τ [µs]	χ^2
60	29.87	1.05
80	28.79	1.18
100	27.93	1.07
120	26.79	1.06
140	25.51	1.07
160	24.23	1.07
180	22.06	1.07
200	20.41	1.06
220	17.60	1.04
240	14.97	1.04
260	11.69	1.03
270	10.44	1.04

Table E2. Fit results for the temperature series of **1·Cu·FLut** in cyclohexane suspension.

T [K]	τ [µs]	χ^2
60	8.69	1.07
80	8.65	1.11
100	7.42	1.15
120	6.52	1.18
140	8.72	1.10
160	7.74	1.06
180	7.03	1.10
200	5.70	1.08
220	5.35	1.10
240	4.76	1.16
260	4.28	1.18
270	4.15	1.11

6.4 Crystallographic data

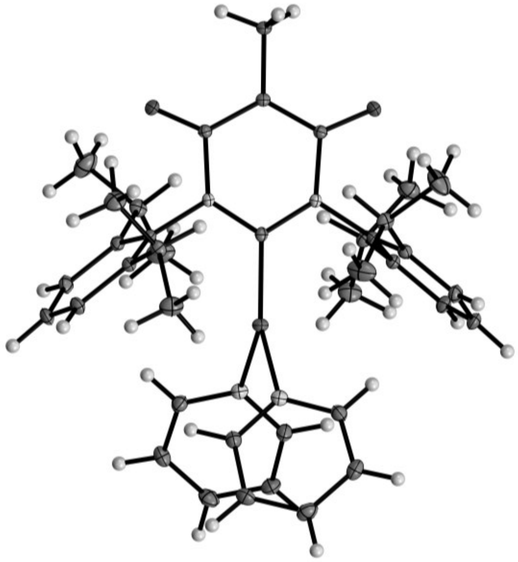

Compound	**1·Cu·Py$_2$**
Ligand	**pyridine**
CCDC No.	2256219
Empirical formula	$C_{19.5}H_{23.5}Cu_{0.5}N_2O$
Formula weight [g/mol]	333.67
Crystal shape and colour	block, colourless
Size [mm^3]	0.1 × 0.1 × 0.05
Temperature [K]	140
Crystal system	monoclinic
Space group	C2/c
Lattice parameters [Å]	a = 15.7393(13)
	b = 13.6942(11)
	c = 15.9958(14)
	β = 97.987(4)
Volume [Å^3]	3414.2(5)
Z	8
ρ_{calc} [g/cm^3]	1.298
Abs. coeff. [mm^{-1}]	0.680
F(000)	1416.0
2Θ range [°]	3.96 to 57.066
Index ranges	$-21 \le h \le 21$, $-18 \le k \le 18$, $-21 \le l \le 21$
Reflections collected	27050
Independent reflections	4284
Final R-value (I>2σ(I))[a]	$R_1 = 0.0438$
	$wR_2 = 0.1142$
R-value (whole data)[a]	$R_1 = 0.0540$
	$wR_2 = 0.1191$
Completeness	99.5
Data/restraints/ parameters	4284/0/215
Flack parameter	-
Goodness-of-fit on F^2 [b]	1.068

Compound	**1·Cu·FPy$_2$**
Ligand	**4-formyl pyridine**
CCDC No.	2256220
Empirical formula	$C_{20.5}H_{23.5}Cu_{0.5}N_2O_2$
Formula weight [g/mol]	361.68
Crystal shape and colour	block, yellow
Size [mm^3]	0.1 × 0.05 × 0.05
Temperature [K]	100
Crystal system	monoclinic
Space group	C2/c
Lattice parameters [Å]	a = 14.8386(2)
	b = 16.4904(3)
	c = 15.9004(3)
	β = 101.238(2)
Volume [Å^3]	3816.14(12)
Z	8
ρ_{calc} [g/cm^3]	1.259
Abs. coeff. [mm^{-1}]	1.163
F(000)	1528.0
2Θ range [°]	8.102 to 157.15
Index ranges	-16 ≤ h ≤ 18, -19 ≤ k ≤ 19, -19 ≤ l ≤ 20
Reflections collected	14598
Independent reflections	3754
Final R-value (I>2σ(I))[a]	R$_1$ = 0.0349
	wR$_2$ = 0.0950
R-value (whole data)[a]	R$_1$ = 0.0373
	wR$_2$ = 0.0969
Completeness	100
Data/restraints/ parameters	3754/0/233
Flack parameter	-
Goodness-of-fit on F^2 [b]	1.083

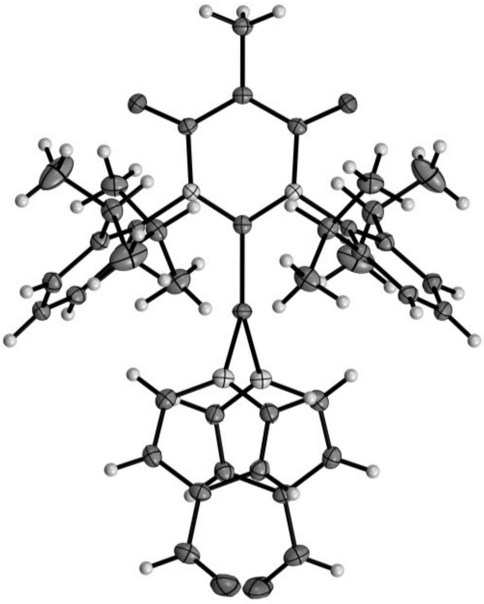

Compound	**1·Cu·4AcPy$_2$**
Ligand	**4-acetyl pyridine**
CCDC No.	2256222
Empirical formula	$C_{43}H_{51}CuN_4O_4$
Formula weight [g/mol]	751.41
Crystal shape and colour	block, yellow
Size [mm^3]	0.3 × 0.1 × 0.1
Temperature [K]	100
Crystal system	orthorhombic
Space group	$P2_12_12_1$
Lattice parameters [Å]	a = 10.10330(10) b = 18.36820(10) c = 21.4085(2)
Volume [Å^3]	3972.98(6)
Z	4
ρ_{calc} [g/cm^3]	1.256
Abs. coeff. [mm^{-1}]	1.135
F(000)	1592.0
2Θ range [°]	6.34 to 158.306
Index ranges	$-12 \le h \le 12$, $-21 \le k \le 23$, $-25 \le l \le 26$
Reflections collected	72398
Independent reflections	8012
Final R-value (I>2σ(I))[a]	R_1 = 0.0347 wR_2 = 0.0948
R-value (whole data)[a]	R_1 = 0.0355 wR_2 = 0.0955
Completeness	100
Data/restraints/ parameters	8012/139/481
Flack parameter	-0.022(6)
Goodness-of-fit on F^2 [b]	1.041

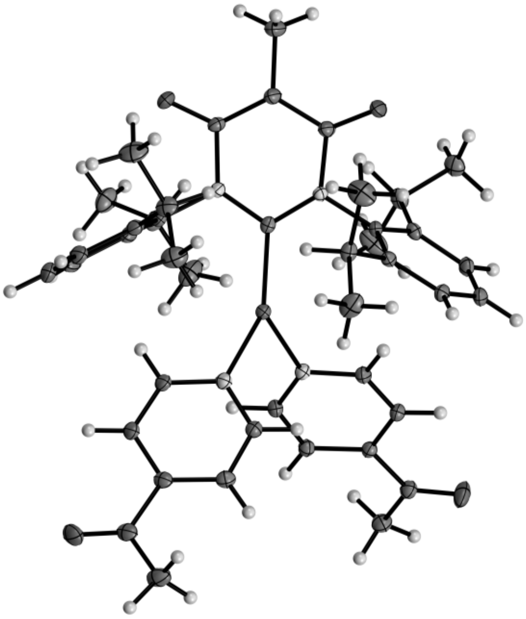

Compound	**1·Cu·2AcPy**
Ligand	**2-acetyl pyridine**
CCDC No.	2256223
Empirical formula	$C_{36}H_{44}CuN_3O_3$
Formula weight [g/mol]	630.28
Crystal shape and colour	block, yellow
Size [mm^3]	0.1 × 0.1 × 0.1
Temperature [K]	100
Crystal system	monoclinic
Space group	$P2_1/c$
Lattice parameters [Å]	a = 14.2718(3) b = 10.7805(2) c = 21.8146(4) β = 98.305(2)
Volume [Å^3]	3321.13(11)
Z	4
ρ_{calc} [g/cm^3]	1.261
Abs. coeff. [mm^{-1}]	1.224
F(000)	1336.0
2Θ range [°]	6.258 to 157.168
Index ranges	-21 ≤ h ≤ 21, -18 ≤ k ≤ 18, -21 ≤ l ≤ 21
Reflections collected	24404
Independent reflections	6551
Final R-value (I>2σ(I))[a]	R_1 = 0.0545 wR_2 = 0.1423
R-value (whole data)[a]	R_1 = 0.0623 wR_2 = 0.1465
Completeness	99.8
Data/restraints/ parameters	6551/0/398
Flack parameter	-
Goodness-of-fit on F^2 [b]	1.048

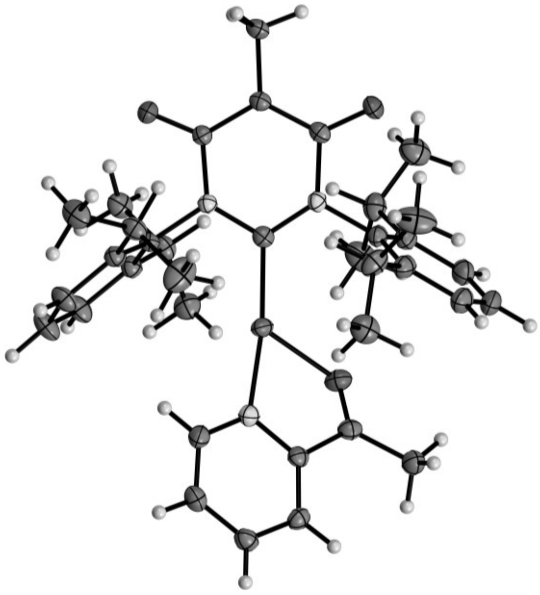

Compound	**1·Cu·Bpy**
Ligand	**2,2'-bipyridine**
CCDC No.	2256224
Empirical formula	$C_{39}H_{45}CuN_4O_2$ x CH_2Cl_2
Formula weight [g/mol]	750.25
Crystal shape and colour	block, yellow
Size [mm^3]	0.31 × 0.16 × 0.12
Temperature [K]	100
Crystal system	monoclinic
Space group	$P2_1/n$
Lattice parameters [Å]	a = 11.21210(10) b = 21.4513(3) c = 16.3875(2) β = 99.5840(10)
Volume [Å^3]	3886.41(8)
Z	4
ρ_{calc} [g/cm^3]	1.282
Abs. coeff. [mm^{-1}]	2.355
F(000)	1576.0
2Θ range [°]	6.848 to 158.336
Index ranges	$-8 \le h \le 14$, $-26 \le k \le 24$, $-20 \le l \le 19$
Reflections collected	29297
Independent reflections	7791
Final R-value (I>2σ(I))[a]	R_1 = 0.0378 wR_2 = 0.1026
R-value (whole data)[a]	R_1 = 0.0404 wR_2 = 0.1044
Completeness	100
Data/restraints/ parameters	7791/2/471
Flack parameter	-
Goodness-of-fit on F^2 [b]	1.086

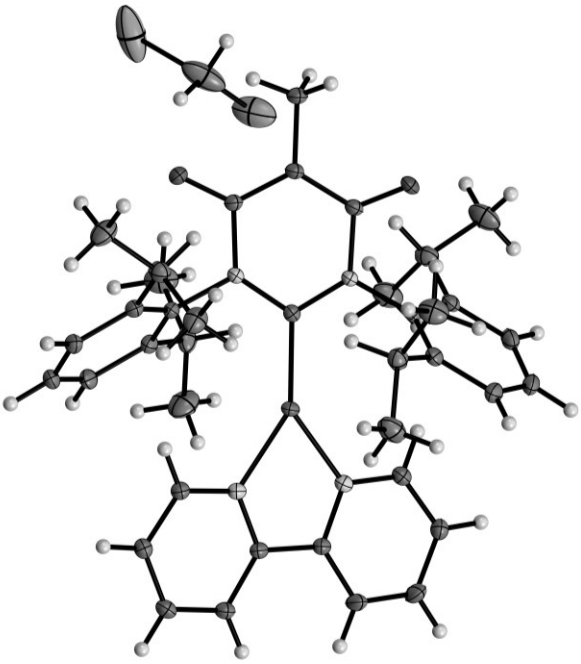

Compound	**1·Cu·Lut**
Ligand	**2,6-lutidine**
CCDC No.	2256225
Empirical formula	$C_{72}H_{92}Cu_2N_6O_4$
Formula weight [g/mol]	1232.59
Crystal shape and colour	block, colourless
Size [mm^3]	0.05 × 0.05 × 0.05
Temperature [K]	100
Crystal system	triclinic
Space group	P-1
Lattice parameters [Å]	a = 11.0787(2)
	b = 11.1412(2)
	c = 28.2628(4)
	α = 90.1010(10)
	β = 90.8170(10)
	γ = 106.0810(10)
Volume [Å^3]	3351.58(10)
Z	2
ρ_{calc} [g/cm^3]	1.221
Abs. coeff. [mm^{-1}]	1.177
F(000)	1312.0
2Θ range [°]	6.256 to 158.276
Index ranges	-13 ≤ h ≤ 13, -14 ≤ k ≤ 14, -36 ≤ l ≤ 29
Reflections collected	44491
Independent reflections	13496
Final R-value (I>2σ(I))[a]	R_1 = 0.0603
	wR_2 = 0.1477
R-value (whole data)[a]	R_1 = 0.0657
	wR_2 = 0.1493
Completeness	99.2
Data/restraints/ parameters	13496/0/779
Flack parameter	-
Goodness-of-fit on F^2 [b]	1.233

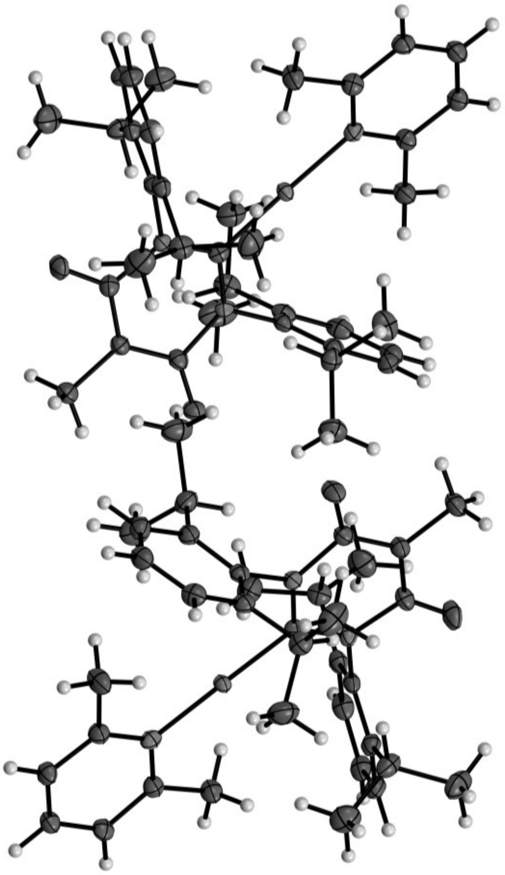

Compound	**1·Cu·FLut**
Ligand	**4-formyl-2,6-lutidine**
CCDC No.	2256226
Empirical formula	$C_{37}H_{46}CuN_3O_3$
Formula weight [g/mol]	644.31
Crystal shape and colour	plate, yellow
Size [mm^3]	0.2 × 0.2 × 0.05
Temperature [K]	100
Crystal system	monoclinic
Space group	$P2_1/c$
Lattice parameters [Å]	a = 11.4918(3)
	b = 14.1551(3)
	c = 21.1762(5)
	β = 92.579(2)
Volume [Å^3]	3441.19(14)
Z	4
ρ_{calc} [g/cm^3]	1.244
Abs. coeff. [mm^{-1}]	1.192
F(000)	1368.0
2Θ range [°]	7.514 to 140
Index ranges	$-13 \leq h \leq 13$, $-12 \leq k \leq 17$, $-25 \leq l \leq 25$
Reflections collected	21990
Independent reflections	6354
Final R-value (I>2σ(I))[a]	$R_1 = 0.0683$
	$wR_2 = 0.1727$
R-value (whole data)[a]	$R_1 = 0.0838$
	$wR_2 = 0.1843$
Completeness	98.9
Data/restraints/ parameters	6354/0/408
Goodness-of-fit on F^2 [b]	1.129

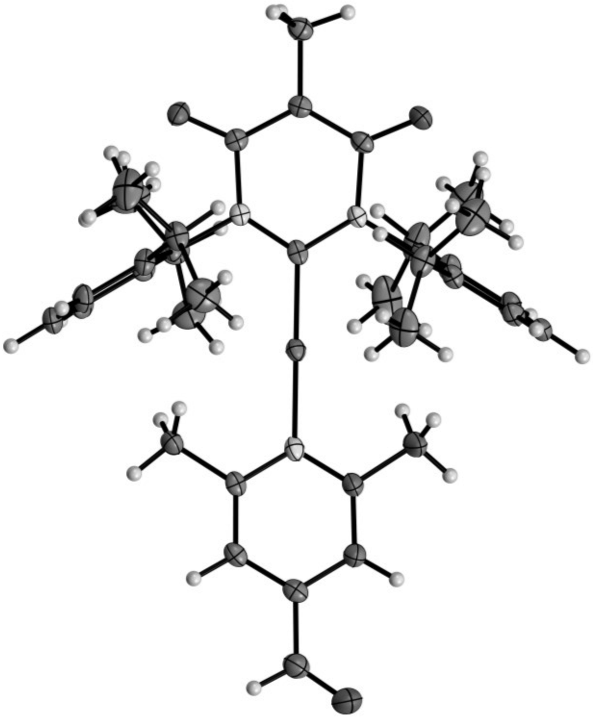

Compound	**1·Cu·DMAP**
Ligand	**4-dimethylamino pyridine**
CCDC No.	2256227
Empirical formula	$C_{18}H_{23.5}Cu_{0.5}N_2O$
Formula weight [g/mol]	148.54
Crystal shape and colour	block, colourless
Size [mm^3]	0.1 × 0.1 × 0.05
Temperature [K]	100
Crystal system	orthorhombic
Space group	Pbcm
Lattice parameters [Å]	a = 13.6625(2) b = 20.2132(2) c = 13.88800(10)
Volume [Å^3]	3835.35(7)
Z	8
ρ_{calc} [g/cm^3]	1.093
Abs. coeff. [mm^{-1}]	1.047
F(000)	1344.0
2Θ range [°]	6.47 to 158.214
Index ranges	$-17 \leq h \leq 16$, $-24 \leq k \leq 25$, $-17 \leq l \leq 7$
Reflections collected	25518
Independent reflections	4196
Final R-value (I>2σ(I))[a]	$R_1 = 0.0380$ $wR_2 = 0.0952$
R-value (whole data)[a]	$R_1 = 0.0392$ $wR_2 = 0.0958$
Completeness	100
Data/restraints/ parameters	4196/0/237
Goodness-of-fit on F^2 [b]	1.124

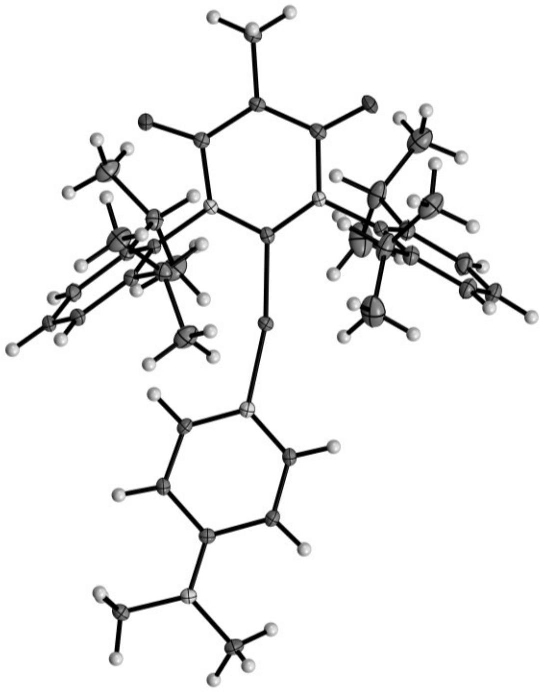

Compound	**1·Cu·Acr**
Ligand	**acridine**
CCDC No.	2256228
Empirical formula	$C_{42}H_{46}CuN_3O_2$ x CH_2Cl_2
Formula weight [g/mol]	773.28
Crystal shape and colour	Block, yellow
Size [mm^3]	0.3 × 0.1 × 0.05
Temperature [K]	100
Crystal system	monoclinic
Space group	$P2_1/c$
Lattice parameters [Å]	a = 9.0341(2)
	b = 22.8317(4)
	c = 19.2670(4)
	β = 98.822(2)
Volume [Å^3]	3927.07(14)
Z	4
ρ_{calc} [g/cm^3]	1.308
Abs. coeff. [mm^{-1}]	2.340
F(000)	1624.0
2Θ range [°]	6.044 to 157.986
Index ranges	$-11 \le h \le 7$, $-28 \le k \le 25$, $-23 \le l \le 24$
Reflections collected	28594
Independent reflections	7667
Final R-value (I>2σ(I))[a]	$R_1 = 0.0344$
	$wR_2 = 0.0868$
R-value (whole data)[a]	$R_1 = 0.0401$
	$wR_2 = 0.0898$
Completeness	99.8
Data/restraints/ parameters	7667/0/499
Goodness-of-fit on F^2 [b]	1.033

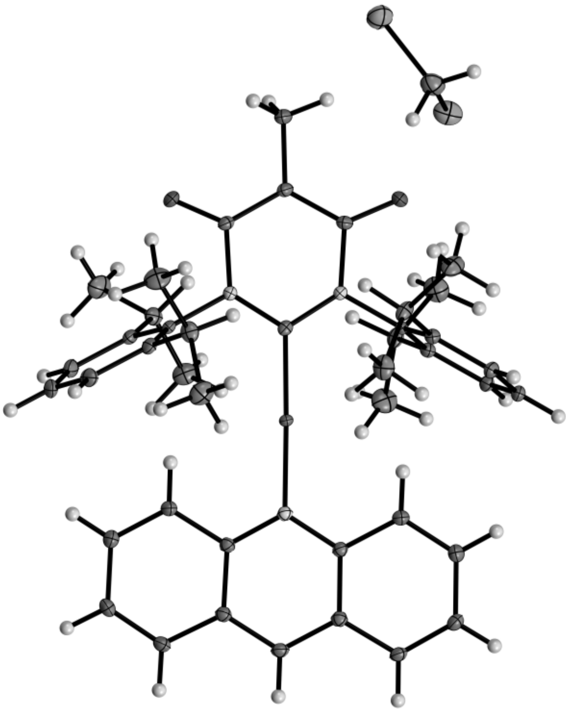

,

Compound	**1·Cu·TPP**
Ligand	**triphenylphosphine**
CCDC No.	2256230
Empirical formula	$C_{47}H_{52}CuN_2O_2P$ x 2 CH_3OH
Formula weight [g/mol]	835.50
Crystal shape and colour	Block, colourless
Size [mm^3]	0.1 × 0.05 × 0.05
Temperature [K]	100
Crystal system	orthorhombic
Space group	$Pna2_1$
Lattice parameters [Å]	a = 25.4211(2) b = 12.74610(10) c = 13.64160(10)
Volume [Å^3]	4420.15(6)
Z	4
ρ_{calc} [g/cm^3]	1.256
Abs. coeff. [mm^{-1}]	1.390
F(000)	1776.0
2Θ range [°]	6.954 to 158.304
Index ranges	$-31 \le h \le 32$, $-15 \le k \le 16$, $-17 \le l \le 17$
Reflections collected	144848
Independent reflections	9182
Final R-value (I>2σ(I))[a]	R_1 = 0.0479 wR_2 = 0.0865
R-value (whole data)[a]	R_1 = 0.0528 wR_2 = 0.0876
Completeness	100
Data/restraints/ parameters	9182/1/538
Flack parameter	-0.013(8)
Goodness-of-fit on F^2 [b]	1.051

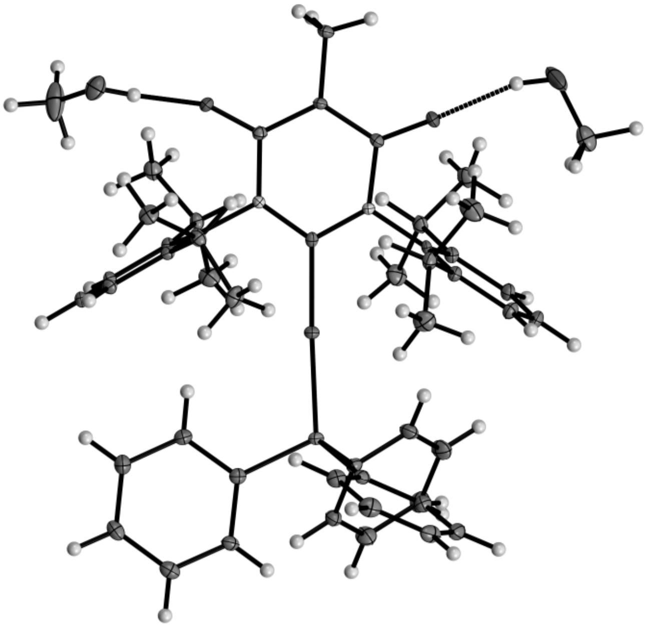

Compound	**1·Cu·^{Me}ImSe**
Ligand	1,3-Dimethylimidazole-selenourea
CCDC No.	
Empirical formula	$C_{34}H_{46}CuN_4O_2Se$ x CH_3OH
Formula weight [g/mol]	716.28
Crystal shape and colour	Block, colourless
Size [mm^3]	0.1 × 0.05 × 0.05
Temperature [K]	100
Crystal system	Orthorhombic
Space group	$P2_12_12_1$
Lattice parameters [Å]	a = 12.65500(10)
	b = 16.2539(2)
	c = 16.9570(2)
Volume [Å^3]	3487.94(7)
Z	4
ρ_{calc} [g/cm^3]	1.364
Abs. coeff. [mm^{-1}]	2.380
F(000)	1496.0
2Θ range [°]	7.534 to 158.218
Index ranges	$-14 \le h \le 16$, $-20 \le k \le 19$, $-21 \le l \le 18$
Reflections collected	53205
Independent reflections	7330
Final R-value ($I>2\sigma(I)$)[a]	R1 = 0.0259
	wR2 = 0.0625
R-value (whole data)[a]	R1 = 0.0276
	wR2 = 0.0630
Completeness	99.9
Data/restraints/ parameters	7330/0/410
Flack parameter	-0.029(7)
Goodness-of-fit on F^{2} [b]	1.045

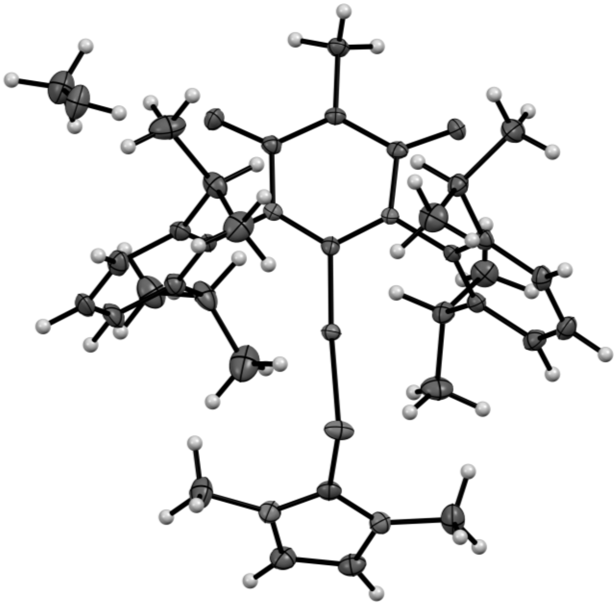

Compound	**1·Cu·^{Me}BenzImSe$_2$**
Ligand	1,3-dimethylbenzimidazole-selenourea
CCDC No.	
Empirical formula	$C_{47}H_{57}CuN_6O_2Se_2$ x 2 MeOH
Formula weight [g/mol]	185.53
Crystal shape and colour	Block, colourless
Size [mm^3]	0.1 x 0.05 x 0.2
Temperature [K]	100
Crystal system	Triclinic
Space group	P-1
Lattice parameters [Å]	a = 14.2343(3)
	b = 14.3492(3)
	c = 15.5307(4)
	α = 83.566(2)°
	β = 63.570(2)°
	γ = 68.261(2)°
Volume [Å^3]	2633.26(12)
Z	2
ρ_{calc} [g/cm^3]	0.234
Abs. coeff. [mm^{-1}]	1.256
F(000)	170.0
2Θ range [°]	6.368 to 158.628
Index ranges	$-15 \le h \le 18$, $-15 \le k \le 18$, $-18 \le l \le 19$
Reflections collected	37430
Independent reflections	10683
Final R-value (I>2σ(I))[a]	R1 = 0.0483, wR2 = 0.1198
R-value (whole data)[a]	R1 = 0.0565, wR2 = 0.1238
Completeness	99.8
Data/restraints/ parameters	10683/0/577
Goodness-of-fit on F^2 [b]	1.079

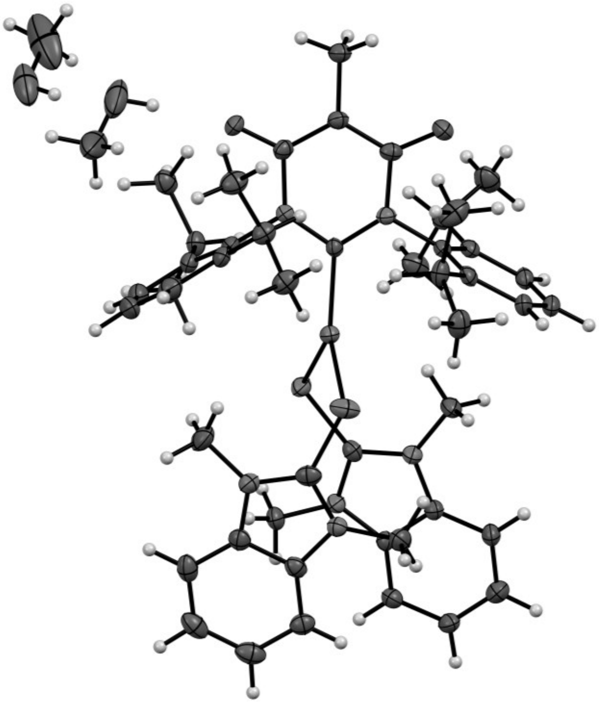

7 References

[1] IEA, Lighting, *IEA* **2022**, Paris https://www.iea.org/reports/lighting, 28.06.2023.

[2] IEA, Electricity Information: Overview, *IEA* **2021**, Paris https://www.iea.org/reports/electricity-information-overview, 28.06.2023.

[3] F. Grum, R. Becherer, *Optical Radiation Measurements*, Vol 1., New York: Academic Press, **1979**.

[4] DIAL (Deutsches Institut für Angewandte Lichttechnik), *Efficiency of LEDs: The Highest Luminous Efficacy of a White LED*, Retrieved from https://www.dial.de/en-GB/projects/efficiency-of-leds-the-highest-luminous-efficacy-of-a-white-led, June 30, **2023**.

[5] High Efficiency Incandescent Lighting, MIT Technology Licensing Office https://tlo.mit.edu/technologies/high-efficiency-incandescent-lighting, 28.06.2023.

[6] K. D. Edwards, Light Emitting Diodes, *University of California, Irvine* **2005**.

[7] Philips Lighting, LED bulb specifications, https://www.lighting.philips.co.uk/consumer/p/led-bulb/8719514343801/specifications, accessed: 28.06.**2023.**

[8] OLEDWorks, *OLED and LED Technology: What's the Difference?*, https://www.oledworks.com/news/blog/oled-and-led-technology-whats-the-difference/, accessed June 30, **2023**.

[9] S. F. Wu, S. H. Li, Y. K. Wang, C. C. Huang, Q. Sun, J. J. Liang, L. S. Liao, M. K. Fung, *Adv. Funct. Mater.* **2017**, *27*, 1701314.

[10] Microsoft Bing Image Creator, retrieved from https://www.bing.com/create, accessed: 3.07.**2023**.

[11] Inductiveload (creator), *LED, 5mm, green [Illustration]*, retrieved from https://commons.wikimedia.org/wiki/File:LED,_5mm,_green_(en).svg, accessed: 30.06.**2023**.

[12] Welt der Physik, OLED. Retrieved from https://www.weltderphysik.de/gebiet/materie/halbleiter/oled/, accessed: 30.06.**2023**.

[13] C. Adachi, A. S. D. Sandanayaka, *CCS Chem.* **2020**, *2*, 1203.

[14] M. Pope, P. H. Kallmann, P. Magnante, *J. Chem. Phys.* **1963**, *38*, 2042.

[15] C. Adachi, A. M. Baldo, E. M. Thompson, R. S. Forrest, *J. Appl. Phys.* **2001**, *90*, 5048.

[16] H. Uoyama, K. Goushi, K. Shizu, H. Nomura, C. Adachi, *Nature* **2012**, *492*, 234.

[17] Edinburgh Instruments, *Identifying Thermally Activated Delayed Fluorescence (TADF) Using an FS5 Spectrofluorometer*, retrieved from https://www.edinst.com/identifying-thermally-activated-delayed-fluorescence-tadf-using-an-fs5-spectrofluorometer/, 30.06.**2023**.

[18] M. Vijayakumar, *J. Mol. Structure* **1996**, *361*, 15.

[19] R.H. Grubbs, T.M. Trnka, Ruthenium-Catalyzed Olefin Metathesis, Wiley-VCH, **2004.**

[20] S. Würtz, F. Glorius, *Acc. Chem. Res.* **2008**, *41*, 1523.

[21] M. S. Viciu, R. A. Kelly III, E. D. Stevens, F. Naud, M. Studer, S. P. Nolan, *Org. Lett.* **2003,** *5*, *9*, 1479.

[22] E. A. B. Kantchev, C. J. O'Brien, M. G. Organ, *Angew. Chem. Int. Ed.* **2007**, *46*, 2768.

[23] J. B. Dumas, E. Peligot, *Annales de Chimie et de Physique* **1835**, *58*, 5.

[24] J. U. Nef, *Justus Liebigs Ann. Chem.* **1892**, *270*, 267.

[25] L. Chugaev, M. J. Skanavy-Grigorieva, *Russ. Chem. Soc.* **1915**, *47*, 776.

[26] L. Chugaev, M. J. Skanavy-Grigorieva, A. Posnjak, *Z. Anorg. Allg. Chem.* **1925**, *148*, *1*, 37.

[27] G. Rouschias, B. L. Shaw, J. Chem. Soc., *Chem. Commun.* **1970**, 183.

[28] H.-W. Wanzlick, E. Schikora, *Angew. Chem.* **1960**, *72*, 494.

[29] D. M. Lemal, R. A. Lovald, K. I. Kawano, *J. Am. Chem. Soc.* **1964**, *86*, 2518.

[30] H. E. Winberg, J. E. Carnahan, D. D. Coffman, M. Brown, *J. Am. Chem. Soc.* **1965**, *87*, 2055.

[31] E. O. Fischer, A. Maasböl, *Angew. Chem. Int. Ed. Engl.* **1964**, *3*, 580.

[32] P. de Frémont, N. Marion, S. P. Nolan, *Coord. Chem. Rev.* **2009**, *253*, 862.

[33] H.-W. Wanzlick, H.-J. Schönherr, *Angew. Chem. Int. Ed. Engl.* 1968, 7, 141.

[34] K. Öfele, *Journal of Organometallic Chemistry* **1968**, *12*, 42.

[35] D. J. Cardin, B. Cetinkaya, M. F. Lappert, L. Manojlović-Muir, K. W. Muir, *J. Chem. Soc. D* **1971**, *0*, 400.

[36] D. J. Cardin, B. Cetinkaya, E. Cetinkaya, M. F. Lappert, *J. Chem. Soc., Dalton Trans.* **1973**, 514.

[37] A. Igau, H. Grutzmacher, A. Baceiredo, G. Bertrand, *J. Am. Chem. Soc.* **1988**, *110*, 6463.

[38] T. Kato, H. Gornitzka, A. Baceiredo, A. Savin, G. Bertrand, *J. Am. Chem. Soc.* **2000**, *122*, 998.

[39] A. J. Arduengo, R. L. Harlow, M. Kline, *J. Am. Chem. Soc.* **1991**, *113*, 361.

[40] References search for "N-heterocyclic carbene”, https://scifinder-n.cas.org, retrieved 22.06.2023

[41] R. Hoffmann, G. D. Zeiss, G. W. Van Dine, *J. Am. Chem. Soc.* **1968**, *90*, 1485.

[42] F. E. Hahn, M. C. Jahnke, *Angew. Chem.* **2008**, *120*, 3166.

[43] T. Mehdoui, J. C. Berthet, P. Thuéry, M. Ephritikhine, *Chem. Commun.* **2005**, 2860.

[44] C. A. Tolman, *Chem. Rev.*, **1977**, *77*, 313.

[45] W. Strohmeier, F. J. Müller, *Chem. Ber.* **1967**, *100*, 2812.

[46] G. Bouquet, A. Loutellier, M. Bigorgne, *J. Mol. Struct.* **1968**, *1*, 211.

[47] A. Liske, K. Verlinden, H. Buhl, K. Schaper, C. Ganter, *Organometallics* **2013**, *32*, *19*, 5269.

[48] K. Verlinden, H. Buhl, W. Frank, C. Ganter, *Eur. J. Inorg. Chem.* **2015**, 2416.

[49] O. Back, M. Henry-Ellinger, C. D. Martin, D. Martin, G. Bertrand, *Angew. Chem., Int. Ed.* **2013**, *52*, 2939.

[50] A. Poater, B. Cosenza, A. Correa, S. Giudice, F. Ragone, V. Scarano, L. Cavallo, *Eur. J. Inorg. Chem.* **2009**, *2009*, 1759.

[51] A. C. Hillier, W. J. Sommer, B. S. Yong, J. L. Petersen, L. Cavallo, S. P. Nolan, *Organometallics* **2003**, *22*, 4322.

[52] H. Clavier, S. P. Nolan, *Chem. Commun.* **2010**, *46*, 841.

[53] C. A. Tolman, *Chem. Rev.* **1977**, *77*, 313.

[54] T. Sugimoto, K. Fukutani, *Nature Phys* **2011**, *7*, 307.

[55] J. R. Lakowicz, Principles of Fluorescence Spectroscopy, 3rd Edition, *Springer*, Baltimore, Maryland, USA, **2010**, p. 5.

[56] D. A. McQuarrie, J. D. Simon, Physical Chemistry, a Molecular Approach, University Science Books, **1997**.

[57] G. L. Miessler, P. J. Fischer, D. A. Tarr, Inorganic Chemistry, 5th ed., Boston: Pearson, **2014**.

[58] P. Schmeinck, *Lumineszente, cyclometallierte Iridiumkomplexe mit Bis(NHC)-Chelatliganden*, Master Thesis, HHU Düsseldorf, **2019**, p 16.

[59] H. Yersin, A. F. Rausch, R. Czerwieniec, T. Hofbeck, T. Fischer, *Coord. Chem. Rev.* **2011**, *255*, 2622.

[60] D. R. Lide, CRC Handbook of Chemistry and Physics, 85. ed., *CRC Press*, Boca Raton, Florida, **2005**, *sec. 14*.

[61] D. R. McMillin, J. R. Kirchhoff, K. V. Goodvin, *Coord. Chem. Rev.* **1985**, *64*, 83.

[62] C. T. Cunningham, J. J. Moore, K. L. H. Cunningham, P. E. Fanwick, D. R. McMillin, *Inorg. Chem.* **2000**, *39*, *16*, 3638.

[63] G. Blasse, D. R. McMillin, *Chem. Phys. Lett.* **1980**, *70*, 1.

[64] A. Tsuboyama, K. Kuge, M. Furugori, S. Okada, M. Hoshino, K. Ueno, *Inorg. Chem.*, **2007**, *46*, 1992.

[65] A. F. Rausch, H. H. H. Homeier, H. Yersin, *Top. Organomet. Chem.* **2010**, *29*, 193.

[66] T. Hofbeck, H. Yersin, *Inorg. Chem.* **2010**, *49*, 9290.

[67] W. Li, D. Liu, F. Shen, D. Ma, Z. Wang, T. Feng, Y. Xu, B. Yang, Y. Ma, *Adv. Funct. Mater.* **2012,** *24*, 1609.

[68] W. Li, Y. Pan, R. Xiao, Q. Peng, S. Zhang, D. Ma, F. Li, F. Shen, Y. Wang, B. Yang, Y. Ma, *Adv. Funct. Mater.* **2014**, *24*, 1609.

[69] Y. Tao, K. Yuan, T. Chen, P. Xu, H. Li, R. Chen, C. Zheng, L. Zhang, W. Huang, *Adv. Mater.* **2014**, *26*, 7931.

[70] F. B. Dias, K. N. Bourdakos, V. Jankus, K. C. Moss, K. T. Kamtekar, V. Bhalla, J. Santos, M. R. Bryce, A. P. Monkman, *Adv. Mater.* **2013**, *25*, 3707.

[71] K. C. Moss, K.N. Bourdakos, V. Bhalla, K.T. Kamtekar, M.R. Bryce, M.A. Fox, H.L. Vaughan, F.B. Dias, A.P. Monkman, *J. Org. Chem.* **2010**, *75*, 6771.

[72] T. J. Penfold, *J. Phys. Chem. C* **2015**, *119*, 13535.

[73] F. B. Dias, T. J. Penfold, A. P. Monkman, *Methods Appl. Fluoresc.* **2017**, *5*, 012001.

[74] J. Perrin, *Lumière et réactions chimiques, rapport au 2^{e} Conseil des Chimie Solvay, Bruxelles*, Gauthier-Villars, Paris, **1926**, pp 322 of Structure et activité chimique.

[75] M. N. Berberan-Santos, eds.: B. Valeur, J. C. Brochon, *Pioneering Contributions of Jean and Francis Perrin to Molecular Luminescence*, in book: *New Trends in Fluorescence Spectroscopy. Applications to Chemical and Life Sciences*, Springer, **2001**, 7.

[76] A. Endo, K. Sato, K. Yoshimura, T. Kai, A. Kawada, H. Miyazaki, C. Adachi, *Appl. Phys. Lett.* **2011**, *98*, 2009.

[77] J. R. Kirchhoff, R. E. Gamache Jr., M. W. Blaskie, A. A. Del Paggio, R. K. Lengel, D. R. McMillin, *Inorg. Chem.* **1983**, *22*, *17*, 2380.

[78] P. Pander, F. B. Dias, *Display and Imaging* **2017**, *2*, 249.

[79] N. J. Turro, V. Ramamurthy, K. S. Schanze, Modern Molecular Photochemistry of Organic Molecules, **2010**, 1st ed., New York, *Oxford University Press*.

[80] C. E. Housecroft, E. C. Constable, *J. Mater. Chem. C*, **2022**, *10*, 4456.

[81] Y. M. Wang, F. Teng, Y. B. Hou, Z. Xu, Y. S. Wang, W. F. Fu, *Appl. Phys. Lett.* **2005**, *87*, 233512.

[82] N. Armaroli, G. Accorsi, M. Holler, O. Moudam, J. F. Nierengarten, Z. Zhou, R. Wegh, R. Welter, *Adv. Mater.* **2006**, *18*, 1313.

[83] R. Czerwieniec, J. Yu, H. Yersin, *Inorg. Chem.* **2011**, *50*, 8293.

[84] A. A. Danopoulos, T. Simler, P. Braunstein, *Chem. Rev.* **2019**, *119*, *6*, 3730.

[85] N. Lüdtke, J. Föller, C. M. Marian, *Phys. Chem. Chem. Phys.* **2020**, *22*, 23530.

[86] A. Liske, L. Wallbaum, T. Hölzel, J. Föller, M. Gernert, B. Hupp, C. Ganter, C. M. Marian, A. Steffen, *Inorg. Chem.* **2019**, *58*, 5433.

[87] O. Nolden, J. Kremper, W. Haselbach, M. Morshedi, J. Guhl, P. Schmeinck, C. M. Marian, C. Ganter, P. Gilch, ChemPhotoChem **2023**, *7*, e20220023.

[88] J. Föller, C. Ganter, A. Steffen, C. M. Marian, *Inorg. Chem.* **2019**, *58*, 5446.

[89] T. Hölzel, A. Belyaev, M. Terzi, L. Stenzel, M. Gernert, C. M. Marian, A. Steffen, C. Ganter, *Inorg. Chem.* **2021**, *60*, 18529.

[90] S. Shi, M. C. Jung, C. Coburn, A. Tadle, D. M. R. Sylvinson, P. I. Djurovich, S. R. Forrest, M. E. Thompson, *J. Am. Chem. Soc.* **2019**, *141*, 3576.

[91] F. Chotard, A. S. Romanov, D. L. Hughes, M. Linnolahti, M. Bochmann, *Eur. J. Inorg. Chem.* **2019**, 4234.

[92] V. César, C. Barthes, Y. C. Farré, S. V. Cuisiat, B. Y. Vacher, R. Brousses, N. Lugan, G. Lavigne, *Dalton Trans.* **2013**, *42*, 7373.

[93] U. Kernbach, M. Ramm, P. Luger, W. P. Fehlhammer, *Angew. Chem. Int. Ed.* **1996**, *35*, 310.

[94] R. Fränkel, U. Kernbach, M. Bakola-Christianopoulou, U. Plaia, M. Suter, W. Ponikwar,

H. Nöth, C. Moinet, W. P. Fehlhammer, *J. Organomet. Chem.* **2001**, *617 – 618*, 530.

[95] A. Nasr, A. Winkler, M. Tamm, *Coord. Chem. Rev.* **2016**, *316*, 68.

[96] L. Benhamou, V. César, H. Gornitzka, N. Lugan, G. Lavigne, *Chem. Commun.* **2009**, 4720.

[97] A.T. Biju, K. Hirano, R. Fröhlich, F. Glorius, *Chem. Asian J.* **2009**, *4*, 1786.

[98] V. César, J. C. Tourneux, N. Vujkovic, R. Brousses, N. Lugan, G. Lavigne, *Chem. Commun.* **2012**, *48*, 2349.

[99] P. K. Majhi, G. Schnakenburg, Z. Kelemen, L. Nyulaszi, D. P. Gates, R. Streubel, *Angew. Chem. Int. Ed.* **2013**, *52*, 10080.

[100] T. D. Forster, K. E. Krahulic, H. M. Tuononen, R. McDonald, M. Parvez, R. Roesler, *Angew. Chem. Int. Ed.* **2006**, *45*, 6356.

[101] V. César, N. Lugan, G. Lavigne, *J. Am. Chem. Soc.* **2008**, *130*, 11286.

[102] V. César, N. Lugan, G. Lavigne, *Chem. Eur. J.* **2010**, *16*, 11432.

[103] M. Ruamps, N. Lugan, V. César, *Eur. J. Inorg. Chem.* **2017**, 4167.

[104] C. Dash, A. Das, H. V. R. Dias, *Molecules*, **2020**, *25*, *16*, 3741.

[105] M. Jonek, J. Diekmann, C. Ganter, *Chem. Eur. J.* **2015**, *21*, 15759.

[106] S. Bastin, C. Barthes, N. Lugan, G. Lavigne, V. César, *Eur. J. Inorg. Chem.* **2015**, 2216.

[107] C. Sivasankar, N. Sadhukhan, J. K. Bera, A. G. Samuelson, *New J. Chem.* **2007**, *31*, 385.

[108] D. R. Lide, CRC Handbook of Chemistry and Physics, 60. ed., Cleveland, *Cleveland Rubber Publishing Co.*, B91-92, B123-129.

[109] M. Saab, D. J. Nelson, N. V. Tzouras, T. A. C. A. Bayrakdar, S. P. Nolan, F. Nahra, K. Van Hecke, *Dalton Trans.* **2020**, *49*, 12068.

[110] K. J. Arm, W. Leslie, J. A. G. Williams, *Inorg. Chim. Act.* **2006**, *359*, 1222.

[111] J. C. Boehm, J. M. Smietana, M. E. Sorenson, R. S. Garigipati, T. F. Gallagher, P. L. Sheldrake, J. Bradbeer, A. M. Badger, J. T. Laydon, J. L. Lee, L. M. Hillegass, D. E.

Griswold, J. J. Breton, M. C. Chabot-Fletcher, J. L. Adams, *J. Med. Chem.* **1996**, *39*, 3929.

[112] H. Yamanaka, H. Abe, T. Sakamoto, H. Hiranuma, A. Kamata, *Chem. Pharm. Bull.* **1977**, *25*, 1821.

[113] M. Joost, M. Nieger, M. Lutz, A. W. Ehlers, J. C. Slootweg, K. Lammertsma, *Organometallics* **2020**, *39*, 1762.

[114] G. Roy, P. N. Jayaram, G. Mugesh, *Chem. Asian J.* **2013**, *8*, 1910.

[115] J. Leopold, Y. Popkova, K. M. Engel, J. Schiller, *Biomolecules* **2018**, *8*, 173.

[116] G. R. Desiraju, T. Steiner, The Weak Hydrogen Bond. Structural Chemistry and Biology, *Oxford University Press*, New York, **1999**.

[117] A. Bondi, *J. Phys. Chem.* **1964**, *68*, *3*, 441.

[118] J. S. Murray, G. Resnati, P. Politzer, *Faraday Discuss.* **2017**, *203*, 113.

[119] G. P. Junor, J. Lorkowski, C. M. Weinstein, R. Jazzar, C. Pietraszuk, G. Bertrand, *Angew. Chem. Int. Ed.* **2020**, *59*, 22028.

[120] P. Schmeinck, D. Sretenovic, J. Guhl, R. Kühnemuth, C. A. M. Seidel, C. M. Marian, M. Suta, C. Ganter, *Eur. J. Inorg. Chem.* **2023**, e202300416.

[121] Louisiana State University, Department of Chemistry, *UV Cutoffs of Common Solvents*, retrieved from https://macro.lsu.edu/HowTo/solvents/UV%20Cutoff.htm (24.06.2023).

[122] L. N. M. Duysens, *Biochimica et Biophysica Acta* **1956**, *19*, 1.

[123] F. M. Mirabella, *Modern Techniques in Applied Molecular Spectroscopy*, ISBN 0-471-12359-5, John Wiley & Sons, Inc., **1998**, pp. 185.

[124] P. Kubelka, F. Munk, *Z. Tech. Phys.* **1931**, *12*, 593.

[125] K. Shizu, H. Kaji, Comms. Chem. **2022**, *5*, *53*, 1.

[126] R. C. Weast, CRC Handbook of Chemistry and Physics, 55. ed., Cleveland, *CRC Press*, pp. F224.

[127] L. M. Hirvonen, K. Suhling, *Meas. Sci. Technol.* **2017**, *28*, 012003.

[128] C. F. Macrae, I. Sovago, S. J. Cottrell, P. T. A. Galek, P. McCabe, E. Pidcock, M. Platings, G. P. Shields, J. S. Stevens, M. Towler, P. A. Wood, *J. Appl. Cryst.* **2020**, *53*, 226.

[129] T. O. Peulen, ChiSurf v. 17.03.24, **2019**, *GitHub repository*, https://github.com/Fluorescence-Tools/chisurf

[130] T. O. Peulen, O. Opanasyuk, C. A. M. Seidel, *J. Phys. Chem. B* **2017**, *121*, *35*, 8211.

[131] S. Felekyan, BatchFitting, **2023**, not publicly available.

[132] K. M. Kuhn, R. H. Grubbs, *Org. Lett.* **2008**, *10*, *10*, 2075.

[133] K. M. E. Ng, T. C. McMorris, *Can. J. Chem.* **1984**, *62*, 1945.

[134] W. L. F. Armarego, C. L. L. Chai, *Purification of Laboratory Chemicals*, Elsevier Inc., Oxford, **2009**.

[135] J. Österlof, *Acta Chem. Scand.* **1950**, *4*, 375.

[136] A. Liske, *Selen-Addukte N-Heterocyclischer Carbene,* Düsseldorf **2013**, Heinrich-Heine-Universität.